FRACTION-SPECIFIC GEOCHEMISTRY ACROSS THE ASBESTOS HILLS BIF OF THE TRANSVAAL SUPERGROUP, SOUTH AFRICA

IMPLICATIONS FOR THE ORIGIN OF BIF AND THE HISTORY OF ATMOSPHERIC OXYGEN

A thesis submitted in fulfilment of the
requirements for the degree of

DOCTOR OF PHILOSOPHY

of

RHODES UNIVERSITY

By

Paul Bernardus Hendrikus Oonk

April 2017

Supervisors

Prof. dr. H. Tsikos, *Rhodes University - Grahamstown, South Africa*

Prof. dr. P. R. D. Mason, *Universiteit Utrecht - Utrecht, The Netherlands*

Members of the examination committee:

Prof. dr. K. Konhauser, *University of Alberta - Edmonton, Canada*

dr. S. V. Lalonde, *European Institute for Marine Studies - Brest, France*

dr. C. T. Reinhard, *Georgia Institute of Technology - Atlanta, United States*

The sampling and basic geochemistry were conducted at Rhodes University, South Africa, together with a part of the writing. The major part of the analytical work was done at Utrecht University, the Netherlands and the final writing stage was concluded there. Iron isotopes were measured at various other institutes.

Synopsis (EN)

Banded iron formations (BIF), deposited prior to and concurrent with the Great Oxidation Event (GOE) at ca. 2.4 Ga, record changes in oceanic and atmospheric chemistry during this critical time interval. Four previously unstudied drill-cores from the Griqualand West Basin, South Africa, capturing the rhythmically mesobanded, deep-water Kuruman BIF and the overlying granular, shallower Griquatown BIF, were sampled every ca. 10 m along core depth. Mineralogically, these BIFs consist of three iron-bearing fractions: (1) Fe-Ca-Mg-Mn carbonates, (2) magnetite with/without minor hematite and (3) Fe-silicates. These fractions are typically fine-grained on a sub-µm scale and their co-occurrence in varying amounts means that bulk-rock or microanalytical geochemical and stable isotope data are influenced by mineralogy.

Fraction specific variations in geochemistry have the potential to reveal diagenetic versus primary precipitative controls on BIF mineralogy and give insight into redox conditions at the time of deposition. An existing sequential extraction scheme for Fe-phases (Poulton and Canfield, 2005) was adapted for the high Fe-content in, and the specific mineralogy of BIF. The first step, an acid acetate leach was tested to ensure that all micro-crystalline Fe-carbonates were effectively dissolved, resulting in an optimum extraction for 48 hr at 50 °C under an inert atmosphere. The second step, dissolution of magnetite by NH_4-oxalate was also tested and resulted in a 24 hr extraction under an ambient atmosphere. Finally, a HF-$HClO_4$-HNO_3 leach was added to dissolve the residual silicate fraction which has to date not been considered in any detail in BIF. Subsequent processing of the extracts enabled stable Fe-isotope analysis (Henkel, et al., 2016).

Various transition metal abundances and their isotopic ratios have been used in BIF as proxies to deduct redox conditions. Among the most frequently used proxies to date are Mo, Cr and U. Based upon the speciation of U and Cr their behaviour is shown here to be linked to varying fluxes of detrital input. Molybdenum isotopic variation has traditionally been linked to Mn-oxide formation and hence indicative of oxidizing conditions, however no relationship between Mn and Mo was observed in the Kuruman and Griquatown BIF were the $\delta^{98/95}$Mo signal is more likely to be influenced by bulk-rock mineralogy.

Because of the similarities between shale-normalized bulk-rock rare earth element + yttrium (REY_{SN}) patterns in BIFs and modern seawater, arguments have been made that BIFs quantitatively capture seawater signals. A decreasing REY_{SN} slope from the relatively oxide-rich Kuruman to the carbonate-dominated Griquatown BIF was observed here for both bulk-rock and fraction specific

patterns. The carbonate fraction mimics the contemporaneous seawater pattern whereas the oxide fraction is relatively middle REE (MREE) enriched. The silicate fraction was found to be dominated by detrital material.

Bulk Fe-isotopic values of 50 samples show an apparent relationship with their mineralogy. Lower $\delta^{56}Fe$ values correlate with carbonate-rich samples, whereas higher $\delta^{56}Fe$ correspond to magnetite dominated samples. Furthermore, there is a clear negative exponential correlation between $\delta^{56}Fe$ and Mn content. Manganese, the most abundant transition metal in BIFs after Fe, is solely bound to the carbonates and stratigraphically increases in abundance. When extended to other BIFs around the GOE, the correlation indicates that seawater Mn/Fe ratios increased globally due to preferential sequestration of Fe over Mn. The Mn enrichment eventually resulted in the deposition of the Hotazel Mn-ores.

Fraction specific Fe-isotopes in combination with bulk-rock $\delta^{13}C$ and REY_{SN} patterns argue for a primary geochemical signal in the Fe-carbonates. The difference between the carbonate and oxide fraction $\delta^{56}Fe$ ($\Delta\delta^{56}Fe_{OX\text{-}CAR}$) is small for ferrous-Fe dominated samples and tends to be larger for the mixed valence oxide-rich samples. This is best explained by varying degrees of dissimilatory iron reduction (DIR). If DIR was near-complete, ferrous minerals would have dominated and only minor oxides would have been present. During partial DIR the isotopically lighter iron would be preferentially reduced, creating a significantly lower $\delta^{56}Fe$ for the small ferrous fraction compared to the residual ferric particulates, from which eventually the oxide fraction formed.

All the aforementioned proxies were integrated into a conceptual deposition model for the Kuruman and Griquatown BIFs. A basin with depth gradients in Fe^{2+}, O_2, $\delta^{56}Fe$, $\delta^{13}C_{DIC}$ and Yb/Ce became more manganiferous over time. Oxygenic photosynthesis produced O_2 that oxidized ferrous iron to insoluble ferric (oxy)hydroxides. During transport to the sediment column the MREEs preferentially adsorbed onto these particulates. An active and laterally extensively dissimilatory iron reducing (DIR) microbial community existed in the benthic zone. After Fe-reduction (either partial or near-quantitative), primary carbonate precipitated, capturing the seawater gradient signals at its depth of formation and included Mn(II) as a redox-passive species. Residual non-reduced ferric (oxy) hydroxide eventually recrystallized as magnetite.

This thesis shows that banded iron formations can be used to track ancient seawater signatures, although interpreting and assessing them remains challenging. The new sequential extraction technique opens up future possibilities to better interpret the various proxies and to increase our understanding of marine sediments in general, and BIFs in particular.

Synopsis (NL)

Gebande ijzersteenformaties (banded iron formations; BIF's), afgezet voorafgaand en ten tijde van de Great Oxidation Event (GOE), ongeveer 2.4 miljard jaar geleden, registreren de chemische veranderingen in de oceaan en atmosfeer tijdens deze essentiële tijd in de aardgeschiedenis. De Asbestos Hills subgroup afgezet in het Griqualand West Basin in Zuid-Afrika bestaat uit twee zulke BIF's: de diep-marine Kuruman BIF, gekenmerkt door ritmische banding, is overlegen door de granulaire, ondieper afgezette Griquatown BIF. Vier niet eerder bestudeerde boorkernen van deze BIFs werden circa elke 10 meter bemonsterd. Mineralogisch gezien bestaan deze monsters uit 3 ijzerrijke fracties: (1) Fe-Ca-Mg-Mn carbonaten, (2) Fe-oxides (magnetiet met soms een beetje hematiet) en (3) Fe-silicaat mineralen. Het verschil in mineralogische compositie beïnvloedt de geochemische en stabiele isotoop data van de bulkmonsters en de erg fijne, sub-µm korrelgrootte van de mineralen maakt micro-analytische meettechnieken minder geschikt.

Geochemische fractie-specifieke variaties hebben de potentie om onderscheid te maken tussen secundaire diagenese- en primaire precipitatie-processen op de mineralogie. Dit geeft daarmee inzicht in de redoxcondities ten tijde van de afzetting. Een bestaand sequentiële-extractie schema voor ijzer-sedimenten (Poulton en Canfield, 2005) werd geoptimaliseerd voor de hoge ijzerconcentraties en de specifieke mineralogie van BIF's. De zure acetaat-extractie werd getest om zeker te zijn dat alle microkristallijne ijzercarbonaten compleet oplosten. Dit resulteerde in een optimale extractie van 48 uur, bij 50 °C onder een zuurstofloze stikstof-atmosfeer. Ook werd de ammonium-oxalaat extractie voor magnetiet getest, resulterend in een langere extractietijd van 24 uur. Ten slotte werd het silicaat-residu opgelost met een totaal ontsluiting. Verdere behandeling van de extracten maakte het mogelijk om fractie-specifieke ijzerisotopen te meten (Henkel, et al., 2016).

Om redoxcondities in BIF's te reconstrueren worden verscheidene transitiemetaal concentraties en isotoop ratio's als proxy gebruikt. Vooral molybdeen (Mo), chroom (Cr) en uranium (U) zijn hiervoor gebruikt in BIF's. De U en Cr distributie over de drie fracties kan worden gelinkt aan wisselende fluxen van erosiemateriaal. Molybdeen isotoop variatie wordt vaak gekoppeld aan de vorming van mangaan-oxides, welke indicatief zijn voor oxiderende condities. Bij de bestudeerde BIF's werd echter geen relatie tussen Mn en Mo gevonden. Daarnaast zijn er aanwijzingen dat het isotoop signaal juist beïnvloed wordt door de bulk mineralogie.

Schalie-genormaliseerde, zeldzame aarde element en yttrium (REY_{SN}) concentraties in BIF's komen goed overeen met hedendaags zeewater. Hierdoor wordt betoogd dat BIF's kwantitatief

zeewaterpatronen kunnen overnemen. De fractie specifieke data kan deze bulk trends verder ontbinden. De carbonaat-fractie reproduceert het hedendaagse zeewaterpatroon, terwijl de oxide-fractie relatief verrijkt is in de midden zeldzame aarde elementen (MREE). De silicaat-fractie wordt gedomineerd door erosiemateriaal. In zowel de bulk-monsters als in de individuele fracties wordt een afnemende steilheid in het REY_{SN} patroon waargenomen vanaf de oxide-rijke Kuruman naar de carbonaat-gedomineerde Griquatown monsters.

Bulk ijzerisotoop ratio's van 50 monsters kunnen worden gerelateerd aan de mineralogie. Lage $\delta^{56}Fe$ waarden correleren met carbonaat-rijke monsters, terwijl hogere $\delta^{56}Fe$ waarden corresponderen met magnetiet gedomineerde monsters. Verder is er een negatieve correlatie tussen de $\delta^{56}Fe$ en de Mn-concentratie. Mangaan, na ijzer het meest voorkomende transitiemetaal in BIF's, is uitsluitend gebonden aan de carbonaat-fractie en de concentratie neemt toe met de stratigrafie. Als ook andere BIF's van rond de GOE in ogenschouw worden genomen, wijst deze correlatie op een progressieve ontwikkeling van de globale zeewater Mn/Fe ratio. Deze ontwikkeling kan gekoppeld worden aan een Mn verrijking door het preferentieel neerslaan van Fe ten opzichte van Mn. De Mn-verrijking resulteert uiteindelijk in het afzetten van de Hotazel Mn-ertsen. Doordat de lichtere ^{54}Fe-isotoop eerder oxideerd dan ^{56}Fe is de Mn/Fe ratio ook gelinkt aan $\delta^{56}Fe$.

Fractie-specifieke Fe-isotopen samen met bulk-monster $\delta^{13}C$ en REY_{SN} patronen duiden op primaire geochemische signalen in de Fe-carbonaat fractie. Het verschil tussen de carbonaat- en oxide-fractie $\delta^{56}Fe$ ($\Delta\delta^{56}Fe_{OX\text{-}CAR}$) is klein voor Fe(II) gedomineerde monsters en is over het algemeen groter voor de oxide-rijke monsters bestaande uit zowel Fe(II) als Fe(III). Dit kan het beste worden verklaard door een verschillende mate van bacteriële ijzerreductie (dissimilatory iron reduction; DIR). Wanneer DIR bijna-kwantitatief is zullen Fe(II)-mineralen het monster domineren en zal de hoeveelheid oxides gering zijn. Ten tijde van gedeeltelijke DIR wordt bij voorkeur het isotopisch lichtere ijzer gereduceerd. Dit resulteert in een significant lagere $\delta^{56}Fe$ voor de kleine Fe(II) fractie vergeleken met de resterende Fe(III)-(oxy)hydroxiden, die voorlopers van de oxide-mineralen zijn.

Alle voorgaande indicatoren zijn geïntegreerd in een conceptueel depositiemodel voor de Kuruman en Griquatown BIF's. Een bekken met diepte-afhankelijke zeewater-gradiënten in Fe^{2+}, O_2, $\delta^{56}Fe$, $\delta^{13}C_{DIC}$ en Yb/Ce werd meer mangaanhoudend naar verloop van tijd. Zuurstof, geproduceerd door fotosynthese, oxideert oplosbaar Fe(II) tot onoplosbare Fe(III)-(oxy)hydroxiden. Tijdens het zinken door de waterkolom worden de MREE preferentieel geadsorbeerd op deze hydroxiden. Een actieve en lateraal uitgebreide DIR gemeenschap, in de bentische zone, reduceert de hydroxiden. Na ijzerreductie (gedeeltelijk dan wel bijna-kwantitatief) vormen primaire carbonaat-mineralen,

die de lokale zeewatersignalen overnemen en Mn(II) als een redox-passief element incorporeren. De resterende niet-gereduceerde Fe(III)-(oxy)hydroxiden rekristalliseren na verloop van tijd tot magnetiet.

BIF's kunnen gebruikt worden om vroegere zeewater-signaturen te ontrafelen, hoewel het interpreteren en beoordelen hiervan een uitdaging blijft. Het nieuwe sequentiële-extractie schema opent toekomstige mogelijkheden om de interpretatie van de verschillende proxies te verbeteren en ons begrip van mariene sedimenten in het algemeen, en BIF's in het bijzonder, te vergroten.

TABLE OF CONTENTS

CHAPTER 3: TRANSITION METALS

CHAPTER 4: RARE EARTH ELEMENTS

CHAPTER 5: IRON ISOTOPES

CHAPTER 6: SYNTHESIS

REFERENCES

APPENDICES

Acknowledgements

This thesis would not be here without the help and support of many people.

First and foremost I would like to thank my supervisors, Hari Tsikos and Paul Mason. Without their support, ideas and guidance completing this project would not have been possible. Looking for an exciting PhD position somewhere in the world I walked into Paul's office sometime during the final months of my MSc-project. A couple of months, a few skype-interviews and Paul's recommendation later, Hari took the leap of faith and offered me a place in his recently formed PRIMOR (Post-graduate Research in Iron and Manganese Ore Recources) group. Subsequent online discussions helped shaping the project which would keep me busy for the majority of the past three years. Without ever setting a foot on the African continent my journey started early February 2014. After missing my flight in Jo'burg, I finally arrived in a thunderstorm late in the evening in Grahamstown, where I finally met Hari and his family. It took some time, a change in apartment and the sports sign-up before I settled in the new surroundings. Since then we've (including Paul when on visit in G'town) spend quite a bit of time braaiing, discussing science over "proper" coffee, looking at core, driving long straight stretches of empty road and having good times in general. The stints in the Netherlands were predominantly used for lab-work. I greatly benefited from Paul's expertise and during the last couple of months and his direct involvement in the writing part was highly appreciated.

Without financial support this project wouldn't have been possible. The main funding for this project, and PRIMOR, comes from ASSMANG Ltd. I would like to thank Philip Crous, Willem Grobbelaar, Christelle van der Merwe and Christo Kuhl for their involvement in PRIMOR in general and my project in particular. It was really great to present our progress to all of you, and your co-workers on the yearly colloquium. Furthermore, I would like to thank the Netherlands Research Centre for Integrated Solid Earth Sciences (ISES, grant number 2.2.3) which covered all the lab costs in Utrecht. And I would like to thank SOUTH32 in Hotazel, by names of Thomas Rambuda and EP Ferreira, for giving access to the various drill-cores studied here.

For this project I've visited numerous laboratories, which eventually resulted in a number of close collaborations. I would like to personally thank Susann Henkel and Michael Staubwasser for hosting me in Cologne and helping me to kick-start the laboratory-part of the project. Thanks to them I learned the various lab-protocols first hand and their tips and tricks definitely made my lab-work more efficient. I'm also indebted to Helen Williams, she taught me the basics of iron isotope measurement in Durham and the data we collected were excellent, which made their interpretation much easier. Next, I would like to thank Geerke Floor for her time and guidance when Margriet and I visited the GFZ in Potsdam for additional Fe-isotope measurements.

Lastly I would like to thank Michael Bau for his constructive comments and ideas on the rare earth element chapter, which helped greatly with the interpretation of the data.

I've spend quite a bit of time the last three years measuring samples, which would not have been possible without the assistance of the technical and support staff. At Rhodes University I would like to thank Goonie Marsh, John Hepple, Chris Pikoli, Thulani Royi, Jonathan Britton, Andrea King, Ashley Goddard and Vuyokazi Nkayi, for their various contributions. At Utrecht University I would like to thank first and foremost Helen de Waard for her general assistance in the lab and her practical solutions. Furthermore, I need to mention Ton Zalm, Coen Mulder, Jan van Tongeren and Bernadette Marchand. Peter Kraal and Niels van Helmond are thanked for the various discussions regarding sequential extractions. Lastly I would like to thank Jochen Scheld (Cologne) and Darren Gröcke (Durham).

Next I would like to thank my colleagues and fellow-students. The PRIMOR-group is thanked for their enthusiastic discussions during the Friday afternoon meetings. "X" (Xolane), Vlassis, Dave, Sihle, Wiliam, James, Stephen and Donald; thanks I really enjoyed spending time and beers with you guys! Keep up the good work. When in Utrecht I would like to thank my office-mates Ale, Claudia, Özlem and Aleks for the coffee breaks, lunch discussions and office BBQ's. Furthermore I would like to thank the rest of the petrology-group for their active and fun discussions during the group-meetings.

I would like to thank my friends from "*Jaartje 007*" for their general support, great parties, lovely dinners and interesting 007-weekends. Especially the "*Help Paul de winter door! actie*" was heartwarming and very thoughtful. I've properly experienced the hills around G'town on that mountainbike. When working in Utrecht I enjoyed the various lunches, coffee breaks and general discussions with WiBa, Nienke, Jan, Ingrid, Sander en Hugo. Although I'm not actively playing football anymore I would like to give my regards to the "*Roze Rakkers*" for the numerous drinking-sessions, scouting-trips and for keeping me up to date with *Eredivisie*-news all the time.

I'm much indebted to my family. My parents (Johan and Ine), sisters (Nicol, Christel and Marieke) supported me from the start to end and, although not always understanding what I was doing, they were there when I needed them. Also I would like to thank Hans, Rita and Mark for their support to me and to Imke when we lived separated. I was very lucky to show all of you around Grahamstown during your various holidays, to try to introduce you into South Africa and to make some great memories along the way. Lastly I would like to thank Imke. Life hasn't been easy for us the last three years. Nonetheless, you've always supported me, cheered me up when I was down and you were always there when I needed you.

“Imagination is more important than knowledge. For knowledge is limited, whereas imagination embraces the entire world, stimulating progress, giving birth to evolution. It is, strictly speaking, a real factor in scientific research.“

Albert Einstein (1931) *Cosmic Religion : With Other Opinions and Aphorisms* p. 97

1

INTRODUCTION

1.1. THE EVOLUTION OF ATMOSPHERIC OXYGEN

The present atmospheric level (PAL) of oxygen (21%) has not been constant through time. Prevailing opinion argues that for the first 2 billion years of Earth history the atmosphere was thought to be anoxic with oxygen levels below 0.001% of PAL (Figure 1.1a; Lyons, et al., 2014). Although there are studies suggesting that the atmosphere contained free oxygen as far back as 3.8 Ga (Ohmoto, et al., 2006a; 2006b; 2014), the current general consensus is that at circa 2.4 Ga pO_2-levels rose to above 10^{-5} PAL, in what is now known as the Great Oxidation Event (GOE) (Holland, 2002).

The most direct evidence for early anoxic conditions followed by a rise in atmospheric oxygen is based on the mass-independent fractionation of sulfur isotopes (MIF-S), which signal starts to disappear at 2.45 Ga and is gone by 2.32 Ga (Figure 1.1b; Farquhar and Wing, 2003; Bekker, et al., 2004; Farquhar, et al., 2011). Gas phase photolytic reactions in an anoxic atmosphere with $O_2 < 10^{-5}$ PAL led to strong anomalous variability in the ^{33}S and ^{36}S isotopes, which is recorded in pyrite and barite minerals in Archean sedimentary rocks (Farquhar and Wing, 2003). When oxygen levels reach $>10^{-5}$ PAL, ozone and to a lesser extent oxygen start to adsorb ultraviolet radiation at wavelengths less than 300 nm (Farquhar and Wing, 2003). This ozone-shield restricts penetration of UV-radiation through the atmosphere and thereby prevents volcanically emitted sulfur-gasses from undergoing mass-independent fractionation. The disappearance of MIF-S in the geological record around 2.4 Ga thus indicates that pO_2-levels rose above 0.001% of PAL. Other less direct proxies for atmospheric oxygenation include the disappearance of redox-sensitive detrital grains of uraninite and pyrite after the GOE (Johnson, et al., 2014), shifts in some transition metal abundances and their stable isotope ratios (e.g. Cr, Mo) indicative of oxidative weathering (Wille, et al., 2007; Frei, et al., 2009; Kendall, et al., 2010; Czaja, et al., 2012) and the Zn/Fe ratio in marine carbonates (Liu, et al., 2016).

The evolution of oxygenic photosynthesis is considered to be one of the key biological

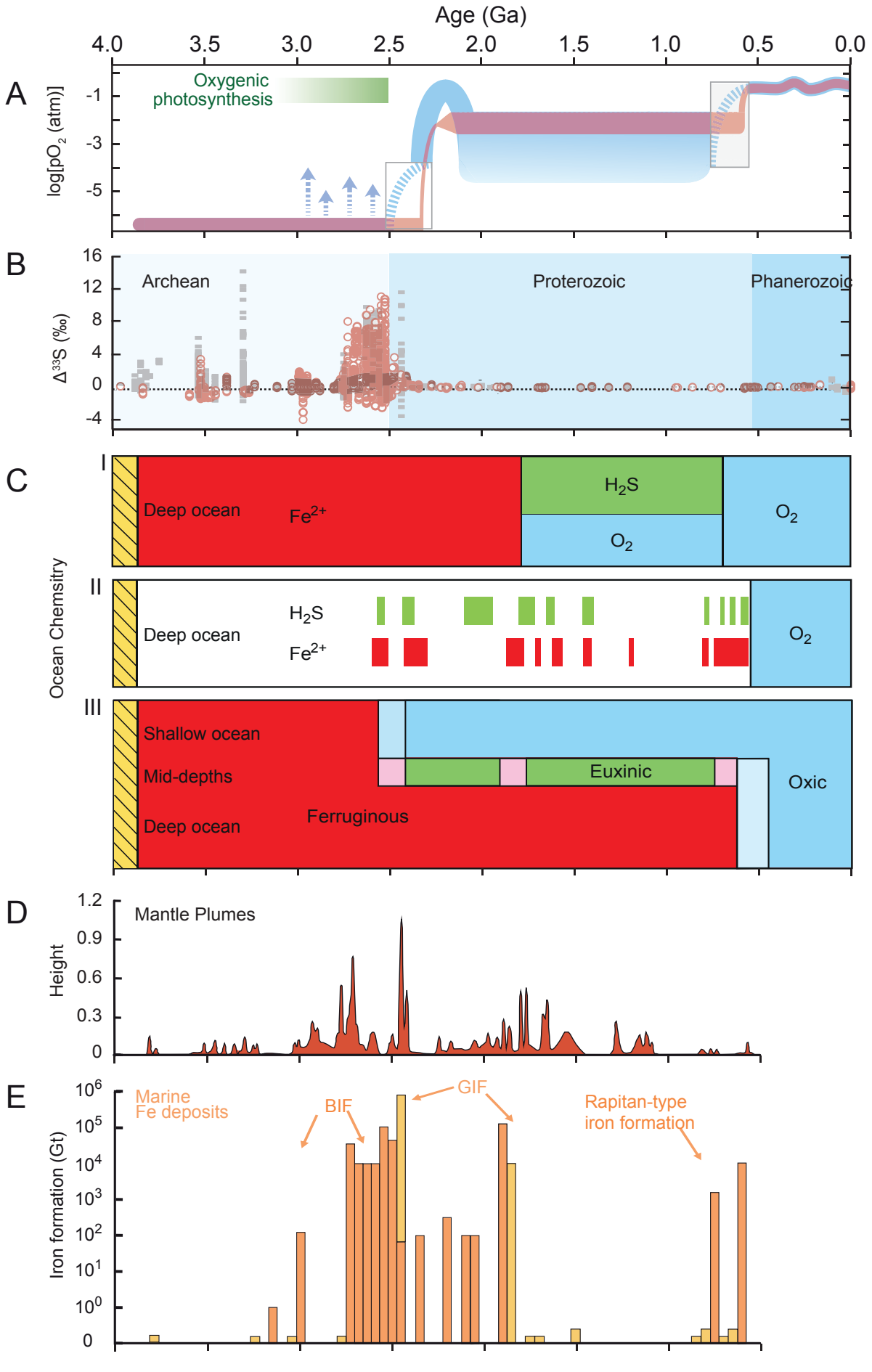
Age (Ga)
4.0
3.5
3.0
2.5
2.0
1.5
1.0
0.5
0.0
A
log[pO2 (atm)]
-1
-3
-5
Oxygenic photosynthesis
B
Δ33S (‰)
16
12
8
4
0
-4
Archean
Proterozoic
Phanerozoic
C
Ocean Chemsitry
I
Deep ocean
Fe2+
H2S
O2
O2
II
Deep ocean
H2S
Fe2+
O2
III
Shallow ocean
Mid-depths
Deep ocean
Ferruginous
Euxinic
Oxic
D
Height
1.2
0.9
0.6
0.3
0
Mantle Plumes
E
Iron formation (Gt)
10^6
10^5
10^4
10^3
10^2
10^1
10^0
0
Marine Fe deposits
BIF
GIF
Rapitan-type iron formation

innovations in Earth history. Although the timing of the onset is still debated, evidence suggests that there were cyanobacteria by 2.7 Ga (e.g. Canfield, 2005; Eigenbrode and Freeman, 2006; Buick, 2008; Crowe, et al., 2013; Planavsky, et al., 2014; Satkoski, et al. 2015). The time-gap between the evolution of oxygenic photosynthesis and the GOE is considerable and has been estimated to be up to hundreds of millions of years (Lyons, et al., 2014). It has been explained by the time required to titrate the reducing surface environment in the Archean with O_2. Methane and other greenhouse gasses are considered to be important constituents of the Archean atmosphere required to counteract the effects of the faint young sun (Pavlov, et al., 2000; Lyons, et al., 2014). In such an atmosphere, O_2 is unstable and would readily react with methane to form CO_2 and H_2O. This and other O_2-sinks (i.e. oxidative weathering) in the Archean prevented a build-up of atmospheric oxygen until the GOE. The transition from methane to CO_2 as the dominant greenhouse gas has been used to explain the Huronian (2.4-2.1 Ga) "Snowball Earth" (Kopp, et al., 2005). An alternative explanation for the time-gap has been sought in limited primary production due to low nutrient availability (e.g. Bjerrum and Canfield, 2002). In addition to photosynthesis, the evolution of atmospheric oxygen was also likely to have been influenced by different magmatic and tectonic processes related to the stabilization of plate-tectonics (Kump and Barley, 2007) and changing oxidation states of volcanic gasses (Holland, 2002).

The relationship between atmospheric and ocean oxygenation remains unclear. Pre-GOE oxygen produced by cyanobacteria might have caused large scale, steady state, "oxygen oases" (e.g. Olson, et al., 2013) in shallow photic waters with high primary productivity in otherwise predominantly anoxic basins. These oases might have accumulated enough oxygen to produce the

Figure 1.1: Temporal evolutions of various phenomena. A) Atmospheric oxygen content as log-function of present day atmospheric levels (PAL) (Lyons, et al., 2014). B) Disappearance of mass-independent fractionation (as $\Delta^{33}S$) at the GOE (Lyons, et al., 2014, and references therein). Grey data were generated by secondary ion mass spectrometry (SIMS); red circles designate all other bulk and small sample data. C) Generalized ocean chemistry, showing the major redox players. I is the classical model of the deep ocean; II is the distribution of Precambrian euxinic and ferruginous deep waters, based on the shale record (Planavsky, et al., 2011); III vertical stratification during the Proterozoic with oxygenated surface waters, underlain by euxinic and ferruginous conditions (Lowenstein, et al., 2014). D) Mantle plume activity through time, vertical axis is the sum of Gaussian time series for high Mg-rocks, layered intrusions, flood basalts, and dikes (Abbott and Isley, 2002; Bekker, et al., 2010). E) BIF deposition in billions of metric tonnes with 50 Myr bar-widths (Bekker, et al., 2010) (*including Isua Group).

short-lived atmospheric "whiffs of oxygen" (Anbar, et al., 2007). The importance of these events is difficult to constrain, not at least due to the lack of preservation of Archean rocks. Furthermore, there are essentially no constrains on paleo-bathymetry, so how widespread or localized these features are and how the different basins were connected remains unclear. Only after the second oxygen rise in the Neoproterozoic did the oceans become fully oxic (Figure 1.1c). So, instead of oxygen being the dominant redox-player in the oceans around the GOE, the basins were dominated by another one: iron (e.g. Bekker, et al., 2010).

1.2. Banded iron formations

Banded iron formations (BIF) have been defined as: "*a chemical sediment, typically thin bedded or laminated, whose principal chemical characteristic is an anomalously high content of iron, commonly but not necessarily containing layers of chert*." – Klein (2005), after James (1954) and Trendall (1983), which excludes the original arbitrary lower limit of 15 wt% Fe.

Intrinsic links to surface oxygenation and increased magmatic plume activity (Figure 1.1) have been used to explain BIF formation (e.g. Bekker, et al., 2010). In the classic model, ferric iron oxidizes to form insoluble ferrous Fe-(oxy)hydroxides which would over time be transformed into BIF minerals through dehydration and diagenetic reactions (e.g. Ayres, 1972). However the oxidation mechanisms, the role of biology, diagenesis and possible primary mineral precipitation remain debated (see Section 1.2.3). In addition to Fe, the Archean oceans were enriched in Si (Siever, 1992). Both Fe and Si could have originated from enhanced magmatic activity (Isley, 1995; Isley and Abbott, 1999; Abbott and Isley, 2002). Based on positive Eu anomalies in BIF, Bau and Dulski (1996) concluded that a high-temperature hydrothermal component was present in Transvaal seawater. In the hydrothermal model of Isley (1995), plumes transported the Fe (and Si) from the mid-ocean ridge vents to the upper water column and transferred it laterally to the continental margins where BIF deposition took place. Another view is that the hydrothermal fluids were released into the deep sea in a density stratified ocean (Klein, 2005) and transported vertically by upwelling. Nd-isotope systematics and rare-earth element (REE) data favour this deep-water "storage" of a hydrothermal input (Bau, et al., 1997).

BIFs have been found on all Paleoproterozoic cratons (Figure 1.2). Ages range from the 3.8 Ga

Archean Isua BIF in Greenland to the Neoproterozoic (0.6 Ga) Rapitan (Canada) and Urucum (Brazil) Iron Formations (Bekker, et al., 2010; Klein, 2005). The majority of BIF deposition took place between 2.8 and 2.1 Ga, with the Hamersley BIFs (2.6-2.4 Ga) in Australia and the Transvaal Supergroup

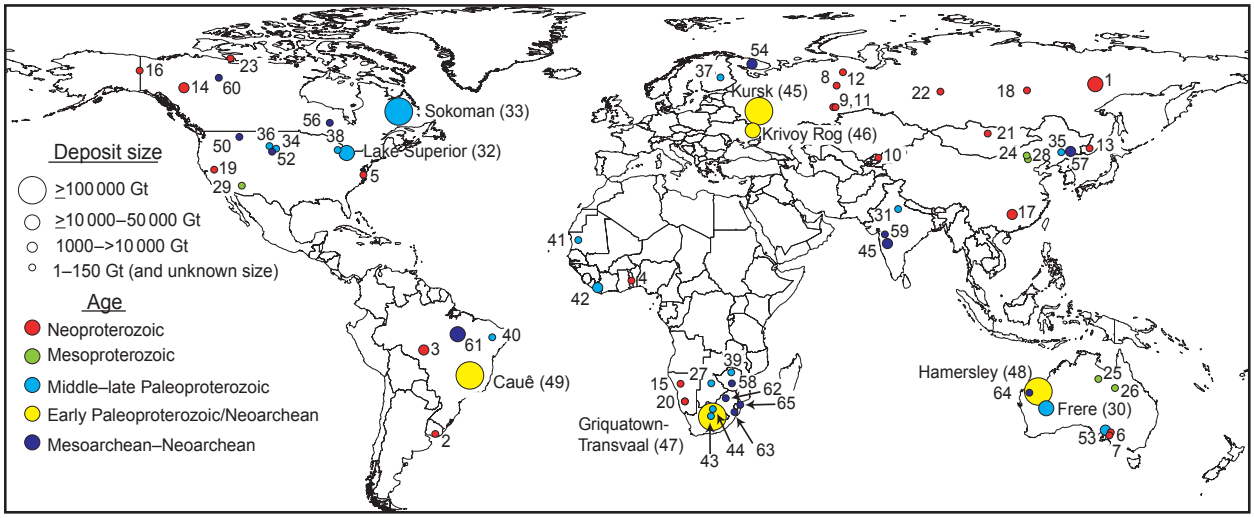

#	Formation/Group/Deposit	Location	Age (Ma)
1	*Maly Khinghan Formation*	Russia	560
2	Yerbel Formation	Uruguay	560
3	*Jacadigo Group (Urucum district)*	Brazil	600
4	*Bisokpabe Group*	Togo	600
5	Chestnut Hill Formation	USA	600
6	*Holowilena Ironstone*	Australia	650
7	*Braemar Iron Formation*	Australia	650
8	*Vil'va and Koyva Formations*	Russia	650
9	Bakeevo (Tolparovo) Formation	Russia	650
10	*Dzhetymtau Suite*	Kyrgyzstan	650
11	UK Formation	Russia	700
12	Yamata Formation	Russia	700
13	Lake Khanka Formation	Russia	700
14	*Rapitan Formation*	Canada	715
15	*Chuos Formation*	Namibia	715
16	*Tindir Group*	USA	715
17	*Fulu Formation*	China	741
18	*Medvezhevo Formation*	Russia	700-750
19	*Kingston Peak Formation*	USA	700-750
20	*Numees Formation*	Namibia	700-750
21	*Mugur Formation*	Mongolia	767
22	Nizhne-Angara Formation	Russia	800
23	Aok Formation (Shaler Supergr.)	Canada	840
24	Xiamaling Formation	China	1368
25	Roper Group	Australia	1490
26	South Nicholson Group	Australia	1500
27	Shoshong Formation	Botswana	1600
28	Chuanlinggou Iron Formation	China	1650-1600
29	Pike's Peak Iron Formation	USA	1728
30	Frere Formation	Australia	1890
31	Alwar Group (North Delhi fold belt)	India	1850-2000
32	Lake Superior region	USA+CAN	
-	Gunflint Iron Formation	Canada	1878-1850
-	Negaunee Iron Formation	USA	1874-1850
-	Biwabik Iron Formation	USA	1880-1850
-	Ironwood Iron Formation	USA	1880-1850
-	Riverton Iron Formation	USA	1880-1850
33	Sokoman Iron Formation	Canada	1877
34	Rochford Formation	USA	1884
35	Liaohe Group	China	1950-2050
36	Estes Formation	USA	2020-2100
37	Pääkkö Iron Formation	Finland	2080
38	Glen Township Formation	USA	2100
39	Lomagundi Group	Zimbabwe	2100-2200
40	Caldeirão belt	Brazil	>2078 - <2687
41	Ijil Group	Mauritania	2200
42	Nimba Itabirite	Liberia	>2100 - <2615
43	Hotazel Iron Formation	South Africa	>2200 - <2426
44	Timeball Hill Formation	South Africa	2320
45	Kursk Supergroup	Russia	2450
46	Krivoy Rog Supergroup	Ukraine	2450
47	Transvaal Province	South Africa	
-	Griquatown Iron Formation	South Africa	2431
-	Kuruman Iron Formation	South Africa	2465
-	Penge Iron Formation	South Africa	2480
48	Hamersley Basin	Australia	
-	Boolgeeda Iron Formation	Australia	2445
-	Weeli Wolli Formation	Australia	2449
-	Brockman IF (Joffre Mbr)	Australia	2461
-	Brockman IF (Dales Gorge Mbr)	Australia	2461-2495
-	Mt. Sylvia Formation	Australia	2505
-	Marra Mamba Iron Formation	Australia	2597
49	Cauê Formation	Brazil	2450
50	Indian Creek Metamorphic Suite	USA	2470
51	Ruker Series	Antarctica	2450-2480
52	Benchmark Iron Formation	USA	2480-2560
53	Hutchison Group (Middleback)	Australia	2500
54	Nemo Iron Formation	USA	2560-2890
55	Chitradurga Group	India	2614
56	Beardmore-Geraldton assemblage	Canada	2700
57	Anshan Iron Formation	China	2700
58	Manjeri Iron Formation	Zimbabwe	2700-2830
59	Bababudan Group	India	2720
60	Central Slave Cover Group	Canada	2730-2920
61	Carajás Formation	Brazil	2740-2750
62	West Rand Group	South Africa	2960
63	Pongola Supergroup	South Africa	2960
64	Jack Hills belt	Australia	>3080
65	Moodies Group	South Africa	3230

Figure 1.2: Geographical distribution of the Mesoarchean-Neoproterozoic BIFs (Bekker, et al., 2014 and references therein). Most iron formations ca. 2.4 Ga and older consist largely of banded iron formation (BIF); those ca. 2.3–0.8 Ga are predominantly granular iron formation (GIF); Neoproterozoic Rapitan-type iron formation (0.80–0.56 Ga) associated with glacial deposits are in italics. *The figure is reproduced from Bekker, et al., 2014*

BIFs (2.5-2.3 Ga) in South Africa as the largest ones (Figure 1.1). Although BIFs are generally not of economic significance due to abundant carbonate and chert, volumetrically minor but high-grade (>60 wt% Fe) BIF-hosted iron ore deposits make up the vast majority of all Fe mined annually (Smith and Beukes, 2016).

Based on their respective tectono-sedimentary environments BIFs have been divided into two groups, the Algoma and Lake Superior types (Gross, 1983). Lake Superior-type BIFs formed along the passive margins of cratons or platforms over extended periods of time and include the Transvaal and Hamersley BIFs. Algoma-type BIFs were deposited in association with volcanic rocks in various tectonic-volcanic systems. These tectonic conditions were more dynamic, with rapid periods of deposition of only 10,000 to a few millions of years (Gross, 1983). Due to more stable depositional environments the Lake Superior-type is typically laterally more extensive and generally thicker than the smaller Algoma-type BIF.

1.2.1. Banding in BIF

One of the outstanding questions regarding BIFs is the origin of their banding (Figure 1.3). The banding has been classified based on average thickness, from coarse macrobands (metres in thickness) to mesobands (centimetre scale) and microbands (mm to sub-mm thick) (Trendall and Blockey, 1970). Generally the larger bands are made up of numerous smaller ones. The banding is created by an alternation of chert-rich and iron-rich intervals, although various carbonate and Fe-silicate minerals can also produce discrete bands.

One of the key problems in linking banding to natural phenomena is the general lack of datable minerals in BIF, making the compacted sedimentation rates and hence the relationship between time and band-thickness difficult to constrain. However based on estimations from sedimentology and the few dated volcanic bands that are available a general picture emerges. The macroband alternation between BIF and shale (S-bands) in the Hamersley province for example has been related to long-term eustatic cycles (Krapež, et al., 2003). Chert-band precipitation within these BIF has been suggested to be linked to Milankovitch cycles (Rasmussen, et al., 2015a). The general premise for the microbands is that they are seasonal although this remains speculative (Trendall and Blockey, 1970; Posth, et al., 2013). A seasonal variation between Fe-rich and Fe-poor bands can be related

Figure 1.3: Three types of iron formation found in a single core (GAS) from the Asbestos Hills Subgroup, Griqualand West Basin, South Africa; (left) Granular IF (219-225 m), (centre) mesobanded BIF (207-213 m) and (right) microbanded BIF (415-423 m).

to biological primary productivity of ferric iron in the upper water column (e.g. Johnson, et al., 2008a). Fe-rich sediment layers could have formed when the supply or the oxidization rate of Fe(II) overwhelmed the precipitation rate of silica due to seasonal cycling or temperature fluctuations (Posth, et al., 2008). In constrast, silica-rich layers could have formed at times when Fe(II) oxidation was unfavourable. The silica source for Fe-silicates minerals in BIF bands has been linked to sorption of Si onto ferric-particulates during precipitation in a silica-saturated ocean (Fischer and Knoll, 2009).

Another explanation is that the banding is not related to primary processes in the ocean, but was depositional or diagenetic in origin. In one such model the Fe-rich sediments were delivered by

deep-sea density currents (Krapež, et al., 2003; Lascelles, 2007), which led to sorting linked to the internal banding. By contrast, the chert dominated sections could represent *in situ* silicification of the pre-existing sediment (Krapež, et al., 2003; Rasmussen, et al., 2015a). The top of the depositional sequences has been placed at the bedded cherts, because of the sharp contact with overlying rocks and the gradational contacts into underlying BIF. The bedded cherts can contain multiple relics of the shaly intervals which indicate that the ambient suspension sediments during low-stands were not BIF, and that BIF deposition ceased prior to the end of the depositional cycles (Krapež, et al., 2003; Bekker, et al., 2010).

Not all iron formations are banded and another common type is the granular iron formation (GIF, Figure 1.3). These are the clastic counterparts of BIF, which range in grain size from fine to coarse sand (Simonson, 2003). The "granules" consist internally of finely crystalline Fe-minerals. Generally GIFs do show some sort of banding, but less regular than in BIF, and microbands are virtually absent (Klein, 2005). Granular iron formations are deposited in shallower water than their banded counterparts. In this higher energetic environment the original sediments were reworked by wave-action. The GIFs are volumetrically subordinate to BIFs, the Algoma-type iron formations are almost exclusively banded and most of the Superior-type are as well (Simonson, 2003). GIFs were rare in the Archean but they became more common in Proterozoic times (Klein, 2005).

1.2.2. BIF mineralogy

Banded iron formations have a limited mineralogy, especially those that are pristine and nearly unmetamorphosed like the Asbestos Hills Subgroup BIFs, which were studied here (Section 1.3). With the exception of chert, all the major minerals are Fe-bearing. The iron is distributed over various carbonate, oxide and silicate minerals, which are described below.

1.2.2.1. Carbonates

The carbonate minerals found in BIFs are predominantly siderite ($FeCO_3$) and the dolomite-ankerite series ($CaMg(CO_3)_2$ - $CaFe(CO_3)_2$) with minor amounts of calcite ($CaCO_3$) (Klein, 2005). Chemically the carbonate minerals vary significantly with Fe substitution by Mg and Mn, however a complete range in solid-solution end-members is not found (Figure 1.4). Electron Micro Probe

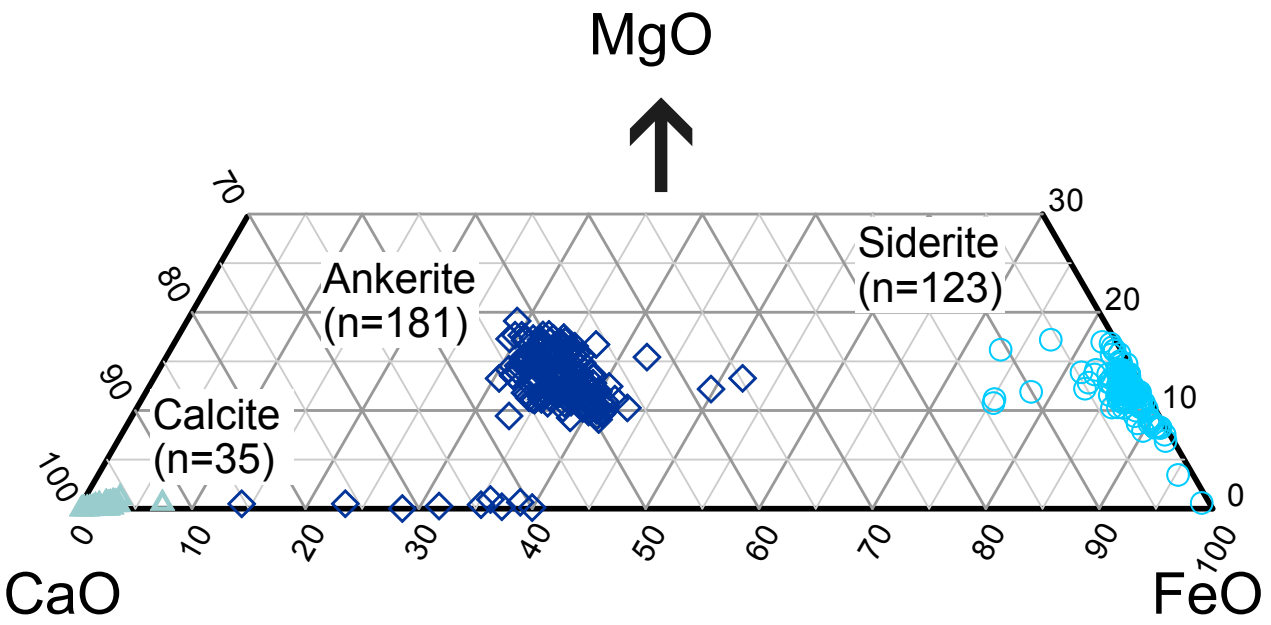

Figure 1.4: CaO, FeO and MgO distribution in the carbonates of the ERIN core based on EMP analyses. Renormalized for no MnO (up to 10 wt%) content and only pure (< 3.0wt% SiO_2) analyses are included. The dolomite-ankerite solid-solution tilts to the ankeritic end-member. Data from Rafuza (2015).

(EMP) analyses on the carbonates of one of the cores studied here (ERIN) show a wide variability in composition (Table 1.1; Rafuza, 2015). These ranges are similar to published values for the Asbestos Hills BIF (Klein and Beukes, 1989; Beukes and Klein, 1990), although those studies detected dolomite as well in the Kuruman IF, which was not found here.

Textually the carbonates in the Asbestos Hills Subgroup occur as microcrystalline siderite to coarse-grained, rhombohedral ankerites (Figure 1.5; Klein and Beukes, 1989). In general the larger crystals are ankeritic, although siderite rhombohedra are present as well. In the Griquatown Formation carbonate-filled pelloids are sometimes present. Calcite occurs within secondary veins in the BIF and rarely as massive, bedding-parallel layers. With increasing waterdepth and increasing Fe(II)-content calcite precipitation was probably inhibited and siderite-supersaturation was reached, explaining the lack of calcite in BIFs (Sumner, 1997).

Table 1.1: EMP ranges (wt%) for the carbonate minerals in BIF. Data from the ERIN-core (Rafuza, 2015).

	Ankerite (n=181)			Calcite (n=35)			Siderite (n=123)		
	Min.	Mean	Max.	Min.	Mean	Max.	Min.	Mean	Max.
CaO	21.81	28.10	43.43	46.46	51.56	55.87	0.12	1.04	8.19
FeO	7.18	19.61	33.01	0.13	1.12	3.57	41.70	49.38	54.35
MgO	0.03	7.08	9.99	0.01	0.20	0.58	0.30	6.85	9.72
MnO	0.26	1.85	5.54	0.04	1.90	6.08	0.19	2.05	6.97

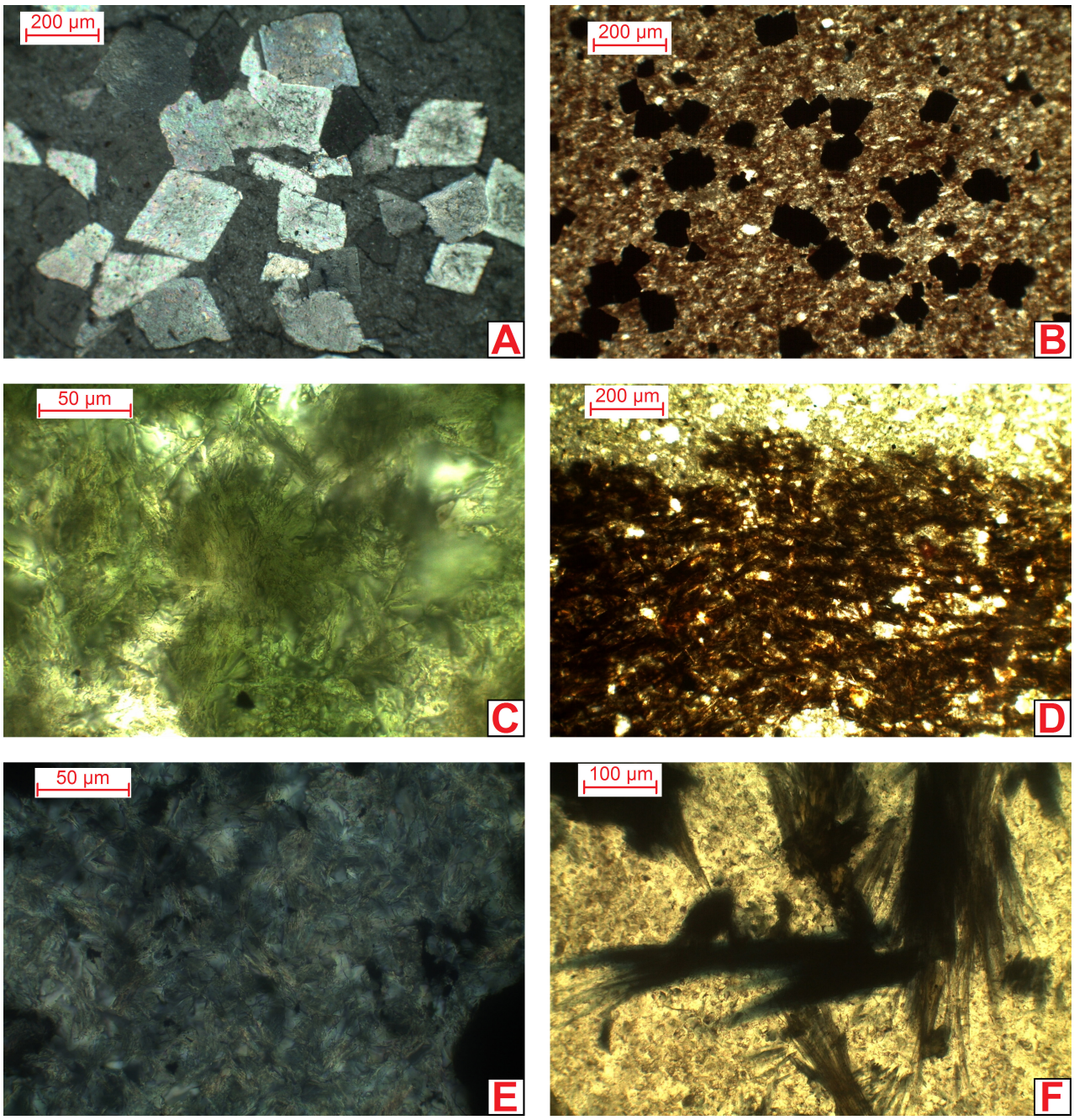

Figure 1.5: Microscope images minerals of the Asbestos Hills BIF minerals. A: Rhombohedral carbonates in a carbonate matrix (XPL, HEX836), B: Euhedral magnetite crystals in a stilpnomelane-quartz matrix (PPL, HEX836), C: Platy, fine grained greenalite (PPL, ERI387), D: Massive stilpnomelane aggregate with carbonate band above it (PPL, ERI470), E: Bow-tie minnesotaite in quartz (XPL, ERI603) F: Blue riebeckite feathers in chert-carbonate matrix (PPL, ERI572).

1.2.2.2. Oxides

Magnetite ($Fe^{2+}Fe^{3+}_2O_4$) is the major Fe-oxide mineral in the Asbestos Hills BIFs (Beukes and Klein, 1990). Tiny hematite particles are present, sometimes forming pigmented chert bands (Klein and Beukes, 1989). The oxides are the major sink for ferric Fe in BIFs and are responsible for the

Table 1.2: Literature EMP ranges (wt%) for the silicate minerals (Beukes and Klein, 1990; Dymek and Klein, 1988; Floran and Papike, 1975; 1978; Klein, 1974; Klein and Gole, 1981; Gole, 1980; Miyano and Beukes, 1984).

	Minnesotaite (n=32)			Greenalite (n=37)			Stilpnomelane (n=47)			Riebeckite (n=25)		
	Min.	Mean	Max.	Min.	Mean	Max.	Min.	Mean	Max.	Min.	Mean	Max.
SiO_2	48.9	52.0	61.2	31.8	34.9	37.7	39.2	46.1	51.3	51.1	53.2	55.5
Al_2O_3	0.0	0.6	1.5	0.0	0.8	3.0	1.3	4.2	6.7	0.0	0.1	0.6
FeO	22.2	34.1	42.6	45.8	49.7	53.4	23.4	32.4	40.3	24.6	30.3	36.2
MnO	0.0	0.2	1.5	0.0	0.4	3.2	0.0	0.3	5.2	0.0	0.1	0.7
MgO	2.0	6.2	16.9	0.6	2.8	5.3	2.3	5.4	10.5	1.4	5.4	9.2
CaO	0.0	0.0	0.2	0.0	0.1	0.6	0.0	0.2	1.9	0.1	0.3	0.8
Na_2O	0.0	0.0	0.2	0.0	0.1	1.4	0.0	0.2	1.1	5.0	6.4	7.7
K_2O	0.0	0.3	0.6	0.0	0.0	0.5	0.0	1.5	4.7	0.0	0.1	0.5

average BIF oxidation state of $Fe^{2.4+}$ (Klein and Beukes, 1992).

The euhedral magnetite grains (Figure 1.5) are generally made up of pure Fe-oxides since EMP analyses of different BIFs shows <0.1 wt% of other oxides present (Klein, 1974; Gole, 1980; Pecoits, et al., 2009). Iron formation hosted magnetite is typically also depeleted in other trace elements based on Laser Ablation Inductively Coupled Plasma Mass Spectrometry (LA-ICP-MS) data (Nadoll, et al., 2014; Chung, et al., 2015; Alibert, 2016).

1.2.2.3. Silicates

There are 4 major Fe-bearing silicates present in unmetamorphosed BIF (Gole, 1980; Klein, 2005). These are the phyllosilicates, greenalite [$(Fe^{2+},Fe^{3+})_{2-3}Si_2O_5(OH)_4$] and stilpnomelane [$K(Fe^{2+},Mg,Fe^{3+})_8(Si,Al)_{12}(O,OH)_{27} \times n(H_2O)$], the talc-mineral minnesotaite [$(Fe^{2+},Mg)_3Si_4O_{10}(OH)_2$] and the amphibole riebeckite [$Na_2(Fe^{2+}_3Fe^{3+}_2)Si_8O_{22}(OH)_2$]. Published BIF-hosted compositional ranges as are presented in Table 1.2.

Both greenalite and stilpnomelane occur as very fine grained (sub-µm) matrix minerals together with chert. Depending on their ferric/ferrous Fe ratio they are greenish to brown under plane polarized light, and both are slightly pleochroic, making them hard to distinguish from each other when dealing with small grainsizes. These minerals have been suggested as primary phases (e.g. Rasmussen, et al. 2013; 2015b). Both minerals, but stilpnomelane especially, also exist as bigger, platy crystals, generally associated with euhedral magnetite grains.

Minnesotaite is considered a diagenetic mineral based on the cross-cutting relationships with

other minerals (Floran and Papike, 1975; Gole, 1980; Klein and Gole, 1981; Klein, 2005). It generally occurs in its very fine grained "bow-tie" needle sprays associated with chert. Riebeckite forms blueish feathers which are easily identified under the microscope. It is the only mineral to accommodate Na in BIFs (Beukes and Klein, 1990). The general consensus is that it formed diagenetically with the Na being derived from pore-fluids or from alkali-rich hydrothermal fluids (Trendall and Blockey, 1970). The distinct blue riebeckite bands in the Griquatown and Kuruman IF (e.g. Horstmann and Hälbich, 1995) are often asbestiform (crocidolite). The name of the Asbestos Hils Subgroup refers to the presence of crocidolite.

1.2.2.4. Trace minerals

Although there are sulphur-bearing BIFs which contain abundant pyrite, the Asbestos Hills BIFs are nearly pyrite-free. Other trace minerals which have been described in the Hamersley BIFs include apatite, xenotime, monazite and vivianite (Alibert, 2016). The phosphorus contents of the Transvaal BIFs (ca. 0.1 wt%, Klein and Beukes, 1989) indicate that trace amounts phosphate minerals may be present.

1.2.3. Fe incorporation in BIF minerals

The processes responsible for the transfer of aqueous ferrous iron into the precursor forms of the BIF minerals we see today has been an ongoing discussion for nearly half a century (e.g. Ayres, 1972; Chan, et al., 2016). The mixed valence magnetite or the ferric hematite requires at least partial oxidation of Fe^{2+}. Post-GOE deposited BIFs could have been oxidized by free oxygen; however, even the oldest ca. 3.8 Ga Isua BIFs contain abundant magnetite (e.g. Dauphas, et al., 2004), when free oxygen was not readily available.

Other oxidizing mechanisms, both abiotic and biological, have been proposed to explain the average oxidation state of $Fe^{2.4+}$ in BIF (Klein and Beukes, 1992). The three most persistent are abiotic photochemical oxidation (Cairns-Smith, 1978), anoxygenic photosynthesis (Garrels, et al., 1973), or oxidation by free O_2 provided by oxygenic photosynthesis (Cloud, 1965). A recent review of these mechanisms is given in Bekker, et al. (2010) and Posth, et al. (2013).

The oxidized Fe(III)-oxyhydroxides are insoluble at pH >7 and eventually sink through the water

column providing a source of Fe for BIF. Since the Fe-carbonates and Fe-silicates contain ferrous Fe, this has to come directly from seawater through an alternative pathway or the ferric Fe-particulates need to be (partially) reduced. Just as for the oxidation pathway, multiple hypotheses are proposed to form the more reduced ferrous minerals. Direct precipitation of the ferrous carbonates and silicates from porewater Fe(II) diffused into the sedimentary environment or dissimilatory iron reduction (DIR) are the prime candidates.

Evidence for these mechanisms has been sought by looking at microfossils, bulk-rock chemical evidence, isotopic ratios and detailed petrography. The following section describes the different oxidation and reduction mechanisms followed by the primary precipitation pathway. All the mechanisms described below are not mutually exclusive. They can all act in the same water column and interfere with each other. A combination of these various mechanisms is most likely the answer to BIF precipitation.

1.2.3.1. Abiotic photochemical oxidation

An abiotic pathway to oxidize ferrous iron is through photochemical oxidation (Cairns-Smith, 1978). Due to the absence of an ozone-layer in the Archean atmosphere, UV-radiation could reach Fe^{2+}-rich seawater. An intense UV-flux could result in the oxidation of ferrous Fe and production of H_2 (reaction 1.1). The reduced species, H_2 and to a lesser extent CO would be lost to the atmosphere, resulting in a net oxidation of the seawater (Cairns-Smith, 1978).

$$2Fe^{2+}_{(aq)} + 2H^{+}_{(aq)} + h\nu \rightarrow 2Fe^{3+}_{(aq)} + H_2 \qquad \text{(reaction 1.1)}$$

Experiments on Fe-rich solutions have focussed on the oxidation rates and determined the viability of this mechanism (Braterman, et al., 1983). This pathway can also explain the low Mn/Fe ratios in BIF, since Mn-precipitation from irradiated solutions containing both Fe^{2+} and Mn^{2+} is insignificant (Anbar and Holland, 1992). A major criticism for these photo-chemical Fe-oxidation experiments is the inability to simulate the complex, disequilibrium water chemistry that would have contained significant amounts of dissolved Si and HCO_3^- (Konhauser, et al., 2007). In the experiments of Konhauser, et al. (2007), supersaturation of greenalite and siderite meant that mineral precipitation

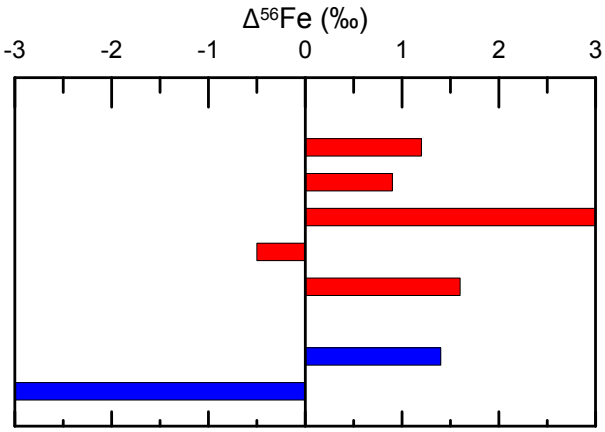

Process:	Reaction:	Ref:
UV photo-oxidation	$Fe(II)_{aq}$ -> $Fe(III)_{aq}$	[1]
Abiotic oxidation by free O_2	$Fe(II)_{aq}$ -> $Fe(III)_{aq}$	[2]
Equi. frac. - partial oxidation	$Fe(II)_{aq}$ -> $Fe(III)_{aq}$	[3]
Abiotic siderite precipitation	$Fe(II)_{aq}$ -> siderite	[4]
Abiotic magnetite precipitation	$Fe(II)_{aq}$ -> magenetite	[5]
Anoxygenic photosynthesis	$Fe(II)_{aq}$ -> $Fe(III)_{aq}$	[6]
Dissimilatory iron reduction	$Fe(III)_{aq}$ -> $Fe(II)_{aq}$	[7]

Figure 1.6 Schematic overview of various abiotic (red) and biological (blue) isotope fractionation processes discussed in this thesis, with $\Delta^{56}Fe$ (‰) as $\delta^{56}Fe_{product}$ - $\delta^{56}Fe_{reactant}$. Experimental data are from [1] Nie, et al. (2017), [2] Bullen, et al. (2001), [3] Johnson, et al. (2008b), [4] Wiesli, et al. (2004), [5] Frierdich, et al. (2014), [6] Croal, et al. (2004) and [7] Johnson, et al. (2005).

was dominant over photo-oxidation, indicating that the latter might have only played a minor role in BIF deposition. The lack of chemical constraints on Archean seawater makes the experimental results controversial and open for interpretation (Nie, et al., 2017). The $\delta^{56}Fe$-fractionation by photo-oxidation between the initial solution and the ferric precipitate (1.2 ± 0.1 ‰, Nie, et al., 2017) are in line with the other oxidation processes (Figure 1.6). Based on these results photo-oxidation remains a viable pathway to oxidize Fe before the rise in atmospheric oxygen.

1.2.3.2. Anoxygenic photosynthesis (photoferrotrophy)

Light can couple the iron and carbon cycles through anoxygenic photosynthesis (Garrels, et al., 1973). Here photoferrotrophs use ferrous iron instead of H_2O as an electron donor, which produces ferric Fe instead of O_2 (reaction 1.2) and transforms CO_2 into organic matter [CH_2O].

$$4Fe^{2+}_{(aq)} + 11H_2O + CO_2 + h\nu \rightarrow [CH_2O] + 4Fe(OH)_3 + 8H^+_{(aq)} \quad \text{(reaction 1.2)}$$

Laboratory cultivation of photoferrotrophs under anoxic conditions showed that this is a possible oxidation pathway (Widdel, et al., 1993). Photoferrotrophs have been found in the photic zone of the sulphur-poor, ferrous Lake Matano in Indonesia (Crowe, et al., 2008). Physical or chemical evidence for the presence of photoferrotrophs in the Archean is still missing, but phylogenetic evidence classifies six of the seven known strains of photoferrotrophs as Proteobacteria (Posth, et

al., 2013).

Experimental studies show that these photoferrotrophs produce ferric Fe even under very low light conditions, down to a few hundreds of meters water-depth (Kappler, et al., 2005), although their oxidation rate decreased significantly with depth. These authors state that, even in the presence of cyanobacteria in the upper water column, anoxygenic phototrophs are the most likely explanation for Fe-oxidation. Similar conclusions have been reached by Konhauser, et al. (2002), who calculated that photoferrotrophy (and/or micro-aerobic Fe-oxidizers) can account for all of the ferric iron contained in BIFs. Similar to Fe, Mn-oxidizing phototropic bacteria have been favoured over oxidation by free O_2 based on relative rates and coupled sulfur isotope evidence (Johnson, et al., 2013).

1.2.3.3. Oxygenic photosynthesis

The last mechanism discussed here is oxygenic photosynthesis, generally associated with cyanobacteria (Cloud, 1965). In oxygenic photosynthesis, CO_2 and water are converted into organic matter and free oxygen (reaction 1.3), which can directly oxidize aqueous Fe(II) (reaction 1.4). The emergence of oxygenic photosynthesis has been directly linked to the increase in atmospheric oxygen, which ultimately resulted in the GOE (Canfield, 2005).

$$CO_2 + H_2O \rightarrow [CH_2O] + O_2 \qquad \text{(reaction 1.3)}$$

$$4Fe^{2+}_{(aq)} + O_2 + 10H_2O \rightarrow 4Fe(OH)_3 + 8H^+_{(aq)} \qquad \text{(reaction 1.4)}$$

Instead of direct Fe oxidation by O_2, the most likely pathway for oxidation was a microbially mediated one. The microaerophilic Fe(II) oxidizers utilize oxygen, CO_2 and water to form organic matter and ferric Fe particulates (reaction 1.5; Konhauser, et al., 2002). At low oxygen levels, these microaerophilic microbes can dominate the Fe-cycle, since microbial oxidation rates are significantly faster than abiotic ones (Bekker, et al., 2010; Chan, et al., 2016).

$$12Fe^{2+}_{(aq)} + O_2 + 2CO_2 + 32\,H_2O \rightarrow 2[CH_2O] + 12Fe(OH)_3 + 24H^+_{(aq)} \qquad \text{(reaction 1.5)}$$

The age of the onset of oxygenic photosynthesis and its timing with respect to the GOE remain

debated (Buick, 2008). Previously published bio-marker evidence (Brocks, et al., 1999) for active photosynthesis at ca. 2.7 Ga. has been refuted as a contaminant (Rasmussen, et al., 2008; Brocks, 2011; French, et al., 2015) and these rocks, in the Hamersley Basin, are considered too mature for syngenetic hydrocarbon biomarker preservation (French, et al., 2015). Other, less direct, lines of evidence such as microfossils and stromatolites still support oxygenic photosynthesis at 2.7 Ga (Buick, 1992). Based on Cr-isotopes in paleosols and iron formations, Crowe, et al. (2013) concluded that oxygen levels at 3.0 Ga. were above levels which can be produced abiotically via photochemical reactions in the atmosphere, from which it follows that oxygenic photosynthesis should have already evolved and been active.

1.2.3.4. Abiotic Fe reduction

To form ferrous minerals either a part of the precipitated oxidized iron needs to be reduced again or dissolved iron needs to be directly incorporated. If microbes had been present the lack of organic carbon in BIFs (e.g. Klein, 2005) can be explained through a process in which organic carbon was the electron acceptor to reduce Fe(III). In short this reaction can be summarized as follows (reaction 1.6, Johnson, et al., 2008b):

$$4Fe(OH)_3 + [CH_2O] + 8H^+_{(aq)} \rightarrow 4Fe^{2+}_{(aq)} + CO_2 + 11H_2O \qquad \text{(reaction 1.6)}$$

Steinhoefel, et al. (2009; 2010) argued for abiotic Fe(III) reduction during low-grade metamorphism based on *in situ* Fe and Si isotopes, although they cannot exclude the role of microbial reduction mechanisms.

1.2.3.5. Dissimilatory iron reduction

Based on reaction rates, microbially mediated reduction is much faster than abiotic mechanisms (Lovley, et al., 1991). Thus when present, Fe-reducing bacteria should be the dominant reduction pathway for Fe(III) as given in reaction 1.6. Dissimilatory iron reduction (DIR) was present on the early Earth, as Archaea and Bacteria that are most closely related to the last common ancestor can reduce Fe(III) to support growth (Vargas, et al., 1998). Here, micro-organisms obtain energy by

the complete reduction of organic matter to CO_2 (Lovley, 1991). The importance of DIR to BIF has been inferred based on varying Fe-isotopic ratios in co-existing siderite and magnetite (Johnson, et al., 2003; 2008a). These authors have argued for a biological reduction mechanism to explain the ferrous component in BIF. Follow up studies with multiple isotopic systems (Fe, O, C, Nd) support this conclusion (Heimann, et al., 2010; Li, et al., 2015). They explain the relationship between C and Fe isotopes in siderite to be the result of microbial iron reduction.

Experimental work on DIR (Johnson, et al., 2005) shows the fractionation of Fe-isotopes into an isotopically heavy residual Fe(III) and a light Fe(II)-product pool (Figure 1.6). In combination with sorbed Si, this isotopically light Fe(II) can be incorporated into silicates (Percak-Dennett, et al., 2011) or react with HCO_3^- to form Fe-carbonates.

Dissimilatory iron reduction is generally treated as a diagenetic process occurring below the sediment-water interface (e.g. Johnson, et al., 2008a; Li, et al., 2015). In this case DIR would act locally which would explain small-scale variations in $\delta^{56}Fe$ and $\delta^{13}C$ (e.g. Heimann, et al., 2010). In modern systems DIR has been described in marine and lake sediments (e.g. Staubwasser, et al., 2006; Percak-Dennett, et al., 2013). Recently a model transferred the DIR process to the water column (Tsikos, et al., in prep.) to explain co-varying bulk-rock $\delta^{13}C$ on a regional scale. Water column DIR has not yet been proven but, Busigny, et al. (2014) inferred DIR from sinking Fe(III) particles at the oxic-anoxic interface in the water column of Lake Pavin. In this thesis, the water column DIR model is further explored. An assumption made here is that DIR can exist anywhere within the Paleoproterozoic water column, but the focus will lie on the benthic zone. This is slightly different than the “benthic DIR shuttle” (Li, et al., 2015), in which large quantities of isotopically light Fe(II), produced by DIR in coastal sediments, are shuttled to the benthic zone. Where relevant a clear distinction is made between “diagenetic DIR” and “water column DIR”.

1.2.3.6. Primary precipitation

Another way to incorporate iron into the minerals is by primary precipitation of the ferrous minerals. Petrological studies infer that very fine grained crystals of oxides, siderite and silicates (greenalite and stilpnomelane) are primary (Ayres, 1972; Klein, 1974; Gole, 1980; Beukes, 1984; Rasmussen, et al., 2013; 2015b; Tosca, et al., 2016). In their experiments to constrain the viability

of photo-chemical Fe(II)-oxidation, Konhauser, et al. (2007) found that greenalite and siderite are primary precipitates, when their saturation levels are reached. Primary deposition of ferrous minerals does not exclude an oxidative pathway to form Fe-oxyhydroxides which can remineralize to form the mixed-valence oxides.

The larger, euhedral crystals (magnetite, ankerite) have overgrown primary minerals during early diagenesis, generally maintaining the overall geochemical signals, such as carbon and oxygen isotope ratios (Kaufman, et al., 1990), REE signatures (e.g. Derry and Jacobsen, 1990) and δ^{56}Fe values (Frost, et al., 2007). However, due to possible inclusions of other minerals during growth the individual euhedral crystals can still differ from the original very fine grained crystals. This could affect the results of micro-analytical techniques as the larger crystals are more readily measureable. The exact replacement by larger crystals is dependent on the oxidation-state of the precipitate; in more oxidized permeable zones primary siderite and greenalite can be replaced by hematite and ankerite, where in less permeable intermediate oxidized zones this should be magnetite (Kaufman, et al., 1990).

An argument against primary precipitation and for formation during early diagenesis is the presence of Fe-isotope heterogeneities on different scales, from adjacent microbands to samples <15 kyr apart. This cannot be readily explained by the seawater residence time of Fe(II) (Johnson, et al., 2008a). Additional evidence against primary carbonate precipitation is based on Sr-isotopes from carbonate lamina (Johnson, et al., 2013).

1.3. Regional geology and sampling strategy

Deposition of Superior-type BIFs culminated around the GOE at circa 2.4 Ga. At that time the large Krivoy Rog-Kursk, Cauê, Hamersley and Transvaal BIFs were formed (Figure 1.2; Bekker, et al., 2010). The latter two systems are the best studied and due to similarities in deposition the Southern African Kaapvaal and the Australian Pilbara cratons have been linked to a single cratonic block called “Vaalbara” (e.g. Pickard, 2003; Beukes and Gutzmer, 2008; Kampmann, et al., 2015). Direct correlation between the iron formations on both cratons remains open for debate, however, recent age dating correlates the Kuruman IF to the Brockmann and the 2.45 Ga Weeli Wolli IFs in the Hamersley basin (Trendall, et al., 2004; Kampmann, et al., 2015). The Brockman Formation consist

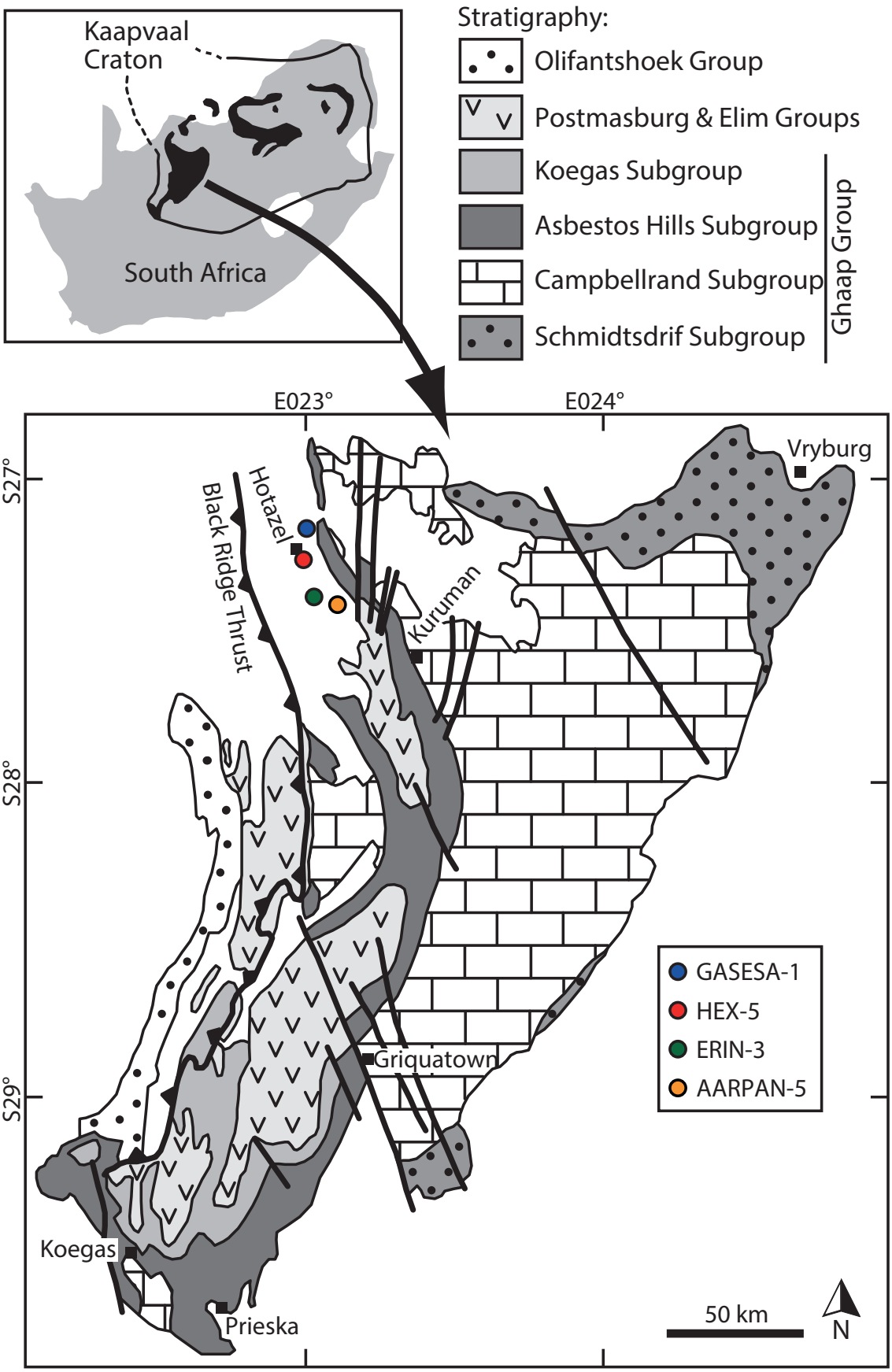

Figure 1.7: Regional geology of the Griqualand West Basin in the Kaapvaal Craton (modified from Schröder, et al., 2011) showing the location of the drill cores selected for this study (see Section 1.3.3) .

of two major IFs, the 2.48 Ga Dales Gorge member and the 2.46 Ga Joffre member (Trendall, et al., 2004). The Griquatown Formation is correlated with the lower Bolgeeda IF (Kampmann, et al., 2015). Comparing the various BIFs helps to better constrain their depositional environment.

The Paleoproterozoic Transvaal Supergroup situated on the Kaapvaal craton comprises three basins, the Griqualand West, Transvaal and the smaller Kanye basin (Moore, et al., 2001; 2012; Pickard, 2003). The stratigraphic correlation between the two major basins is still an ongoing debate due to the lack of datable minerals, lack of outcrop and previously published contradictory ages (Pickard, 2003; Eriksson, et al., 2006; Moore, et al., 2012; Gumsley, et al., 2017).

The study area in this thesis is the Griqualand West basin (Figure 1.7), where the Transvaal Supergroup represents a continuous depositional event for approximately 250 Ma (Polteau, et al., 2006). The Supergroup is subdivided in the Ghaap and Postmasburg Groups (Figure 1.8). The sedimentary Ghaap Group comprises of the Schmidtsdrift, Campbellrand, Asbestos Hills (*Asbesheuwels* in Afrikaans) and Koegas Subgroups and is overlain by the Postmasburg Group, consisting of the Makganyene diamictite, Ongeluk lava, Hotazel BIF and Mooidraai carbonate Formations (Moore, et al., 2012). This study focuses on the Asbestos Hills Subgroup, which hosts of the Kuruman and Griquatown Formations.

1.3.1. Kuruman Iron Formation

In the northern part of the Griqualand West basin a large thick carbonate platform (Campbellrand-Malmani) was developed, which is much thinner in the southern parts (Figure 1.9). The top of the Campbellrand Subgroup, the stromatolitic Gamohaan formation has been used to argue for the presence of oxygen-producing cyanobacteria based on N-isotopes (Godfrey and Falkowski, 2009). The transition into the Asbestos Hills Subgroup is continuous and indicates a deepening of the basin from the stromatolites to the micro-banded BIFs of the Kuruman Formation (Klein and Beukes, 1989; Sumner, 1997). The rhythmically banded Kuruman BIF was largely deposited in an open-shelf environment below wave base and contains multiple cycles of shallowing upward sequences (Beukes, 1984).

The thickness of the Kuruman IF varies significantly, from <150 m on the carbonate platform to >750 m in the southern part of the basin (Figure 1.9; Beukes, 1984; Beukes and Gutzmer, 2008).

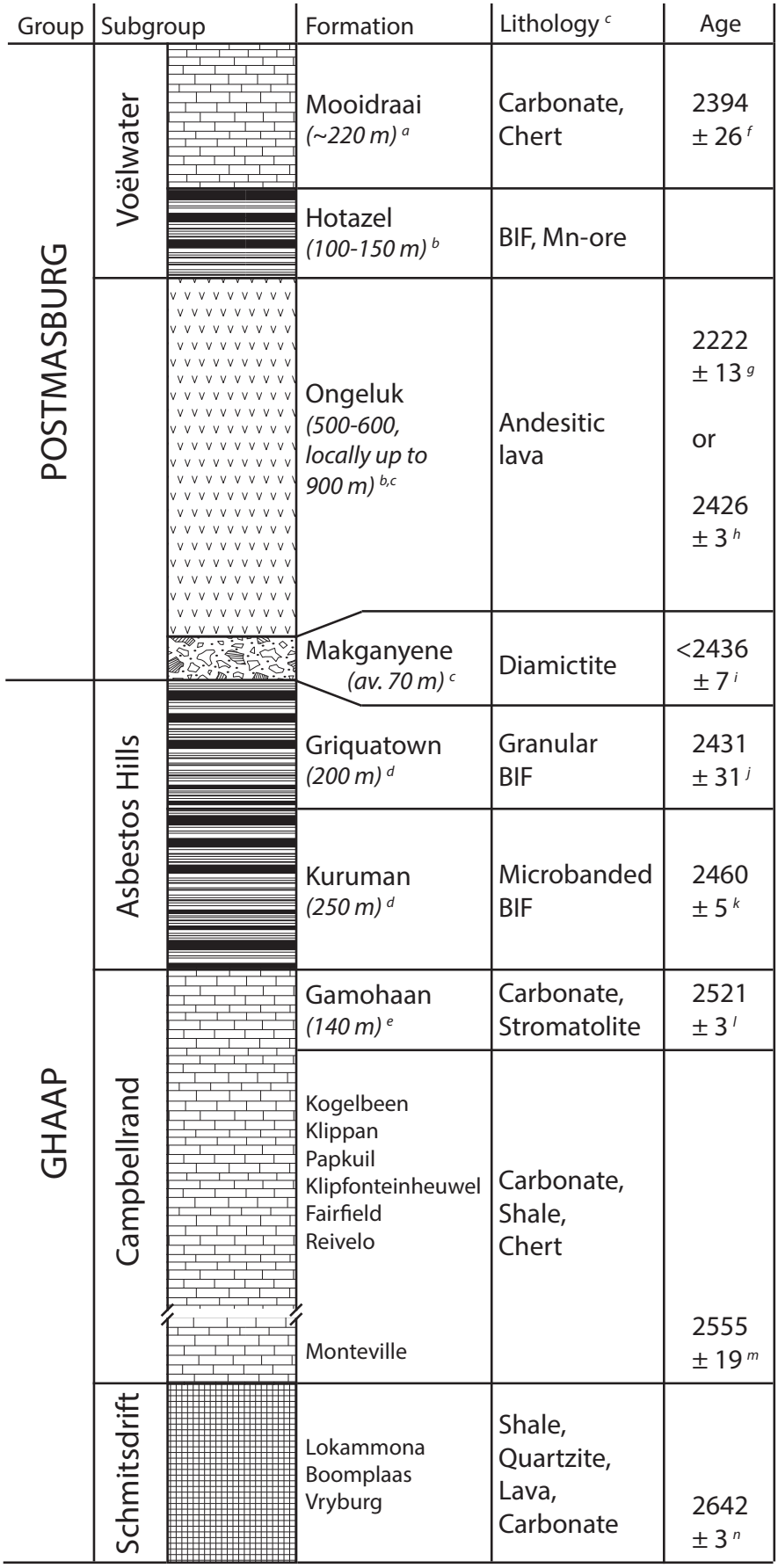

Figure 1.8: Regional stratigraphy of the Kuruman-Hotazel area.

Thickness and age data from:
a: Kunzmann, et al., 2014
b: Tsikos, et al., 2003
c: Polteau, et al., 2006
d: this study
e: Sumner, 1997
f: Bau, et al., 1999
g: Cornell, et al., 1996
h: Gumsley, et al., 2017
i: Moore, et al., 2012
j: Trendall, et al., 1990
k: Pickard, 2003
l: Sumner and Bowring, 1996
m: Altermann and Nelson, 1998
n: Walraven and Martini, 1995

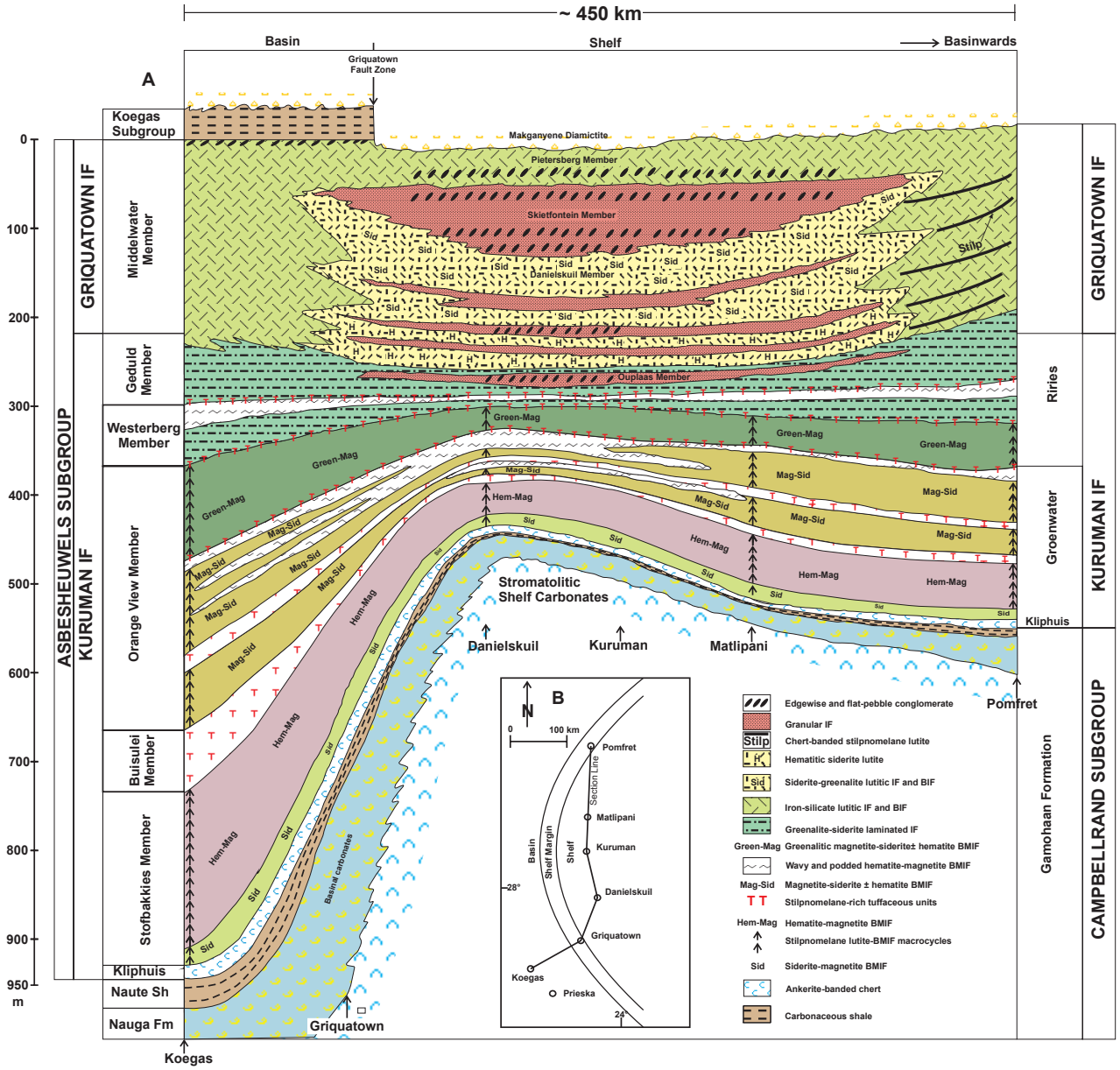

Figure 1.9: North-south cross section through the Asbestos Hills Subgroup (A) with the trajectory plotted in (B). *Reproduced from Beukes and Gutzmer (2008).* **The cores studied fit between the Kuruman and Matlipani section. Note the unconformity between the Griquatown and Makganyene diamictite interpreted here is challenged in recent years (e.g. Moore, et al., 2012)**

Multiple sedimentological members have been described in the Kuruman Formation; these are based on outcrop in the basinal part of the formation (Beukes, 1984). They are harder to distinguish at the top of the carbonate platform, and in drill core-sections. The Kuruman Formation studied here is ca. 200m thick.

A SHRIMP U/Pb zircon age based on stilpnomelane-rich tuffaceous mudrocks, dates the Kuruman IF at 2460 ± 5 Ma (Pickard, 2003). Depositional rates for banded-iron formations are hard to establish due to lack of datable material within the chemical sediments. Based upon a date for the

Gamohaan Formation and the 2460 ± 5 Ma for the mudrock the entire compacted deposition rate for the Kuruman IF was calculated to be 3-4 m per million years (Pickard, 2003). Altermann and Nelson (1998) deducted a similar range (2-6 m/Myr) for the Kuruman IF. However the Riries member shows sedimentation rates of circa 22 m/Myr which fit better with those of 30m/Myr described in the Hamersley BIFs (Pickard, 2003 and references therein). Taking these various rates into consideration, the 430 m of Asbestos Hills BIF studied here (Section 1.3.3) was deposited over a time period of between 20 and 100 Myr.

The base of the Kuruman Formation hosts multiple, dm-scale dark stilpnomelane lutite bands (Beukes, 1984). They have been linked to volcanic input into deep waters (Klein and Beukes, 1989), based on their lateral continuity, close association with deep-shelf carbonates and the preservation of fine microbanding (Beukes and Gutzmer, 2008). The Kuruman IF is also cross-cut by two basaltic andesitic sills, a thinner one (3 m thick) in between mesobanded BIF and a thicker interval near the Kuruman-Griquatown transition. The BIFs immediately around these sills are carbonate depleted due to contact metamorphism.

1.3.2. Griquatown Iron Formation

The predominantly clastic-textured Griquatown BIF indicates a shallower-water, storm-dominated depositional environment (Beukes, 1984; Beukes and Klein, 1990). The transition from the Kuruman to the Griquatown is in itself intriguing, since transitions from microbanded to granular BIFs are uncommon (Beukes and Klein, 1990). Although this transition is based on sedimentological indicators, the geochemical signal might prove to be even more robust (Tsikos, et al., in prep). The Griquatown IF has been dated at 2431 ± 31 Ma (zircon U–Pb SHRIMP age; Trendall, et al., 1990) and its thickness varies between 200-300 m (Tsikos, et al., 2003).

The clastic texture in the Griquatown Formation is clear; there are soft-sediment deformation features, chert pods, granules of varying composition in the same bed and even well sorted grainstones (Figure 1.3; Beukes and Gutzmer, 2008). The central part of the Griquatown IF consists of three, thick, laterally continuous stilpnomelane lutites, which are excellent marker beds (Figure 1.10). These lutites are also interpreted to represent volcanic pyroclastic beds as they do in the Kuruman IF and might be correlated to the shale-macrobands in the Hamersley basin (e.g. Beukes

and Gutzmer, 2008).

In the cores studied here, the Griquatown Formation is directly overlain by the Makganyene diamictite. The transition seems continuous, as there are dropstones found across the boundary and into the Griquatown and the bottom of the Makganyene is Fe-rich. This is at odds with the previously proposed major regional unconformity suggested between the Ghaap and Postmasburg Groups (e.g. Beukes, 1983; Hoffman, et al., 1998; Eriksson, et al., 2006; Beukes and Gutzmer, 2008) and favours of the regional statigraphy proposed by Moore, et al. (2001; 2012) and Polteau, et al. (2006). The main argument for an unconformity has been a 2222 ± 13 Ma Pb-Pb whole-rock isochron age of the submarine Ongeluk lavas (Cornell, et al., 1996) which overly the Makganyene diamictite and the absence of the Koegas IF in the northern part of the basin.

In recent years this 2222 Ma age has been questioned (Kampmann, et al., 2015) and recently a 2426 ± 3 Ma age for the Ongeluk has been measured using the U-Pb *in situ* SIMS technique on baddeleyite (Gumsley, et al., 2017). Furthermore, this age fits better with the 2394 ± 26 Ma for the Mooidraai dolomites (Bau, et al., 1999) at the top of the Postmasburg Group (Figure 1.8). The new Ongeluk age combined with the 2521 Ma age of the Gamohaan (Sumner, 1997) brackets the Asbestos Hills BIFs deposition to less than 100 Myr. The disappearance of mass-independent sulfur fractionation between 2.45 and 2.32 Ga (Farquhar and Wing, 2003; Bekker, et al., 2004) in combination with the new 2426 Ma age implicates that the Asbestos Hills BIFs were precipitated right before the GOE, and that the Hotazel Mn-BIFs were precipitated syn-GOE.

The Koegas Subgroup was only developed in the deep Prieska sub-basin, in the south west part of the Griqualand West Basin (Figure 1.9). The supposed presence of an unconformity, due to the absence of the Koegas Subgroup in the northern part of the basin, could also be explained by paleo-bathymetry. The Koegas Subgroup would then have precipitated in the sub-basin synchronous with the onset of the Makganyene on top of the platform (Moore, et al., 2001; Polteau, et al., 2006).

1.3.3. Drill cores selected for this study

The Kuruman and Griquatown BIFs were sampled from four drill-cores (Figure 1.10): Gasesa-1 (*GAS*), HEX-5 (*HEX*), Erin-3 (*ERI*) and Aarpan-5 (*ARP*) which cover a ca. 25 km NW-SE trajectory near the town of Hotazel (Figure 1.7). The cores were drilled as part of an exploration-programme in the

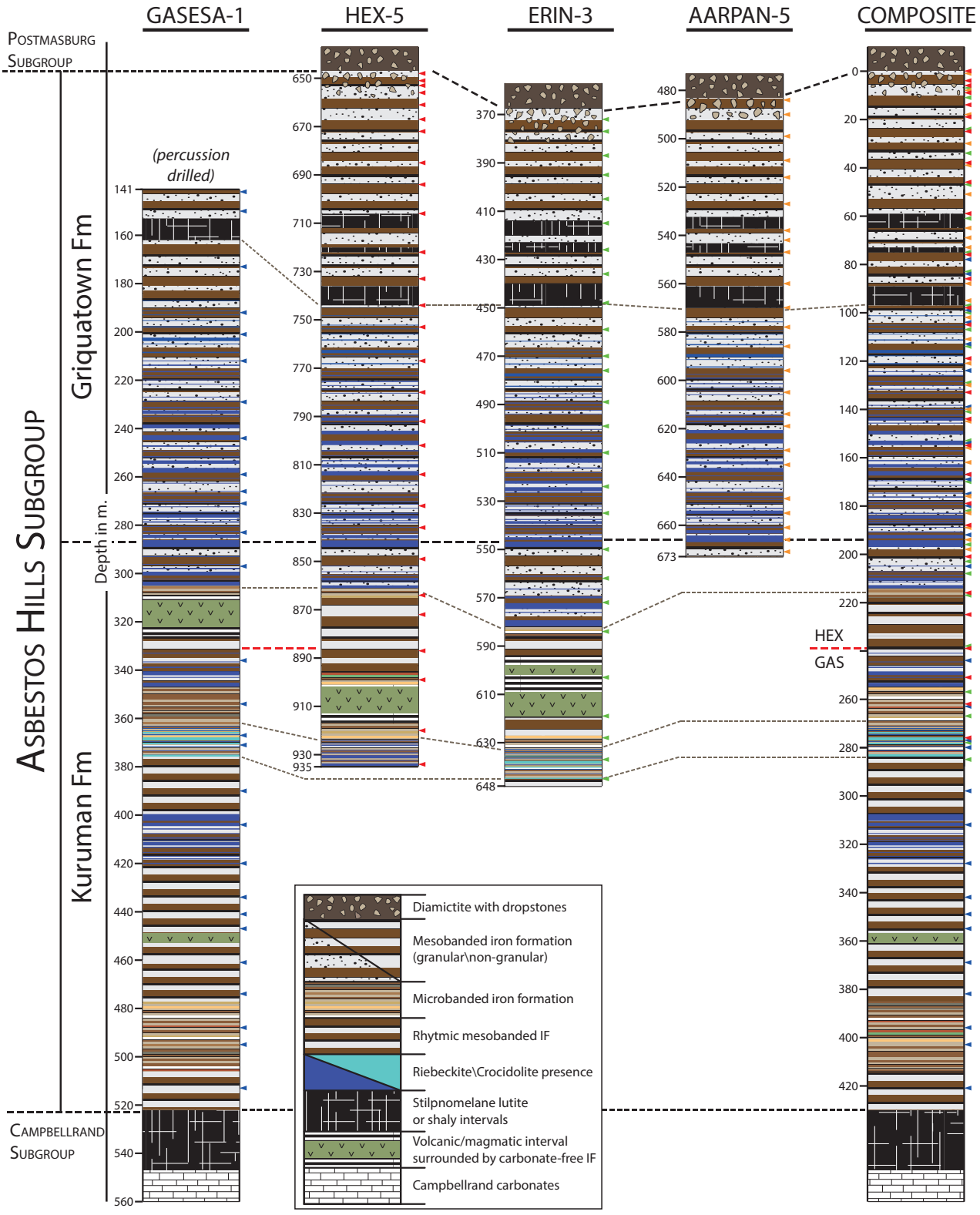

Figure 1.10: The four drillcores studied in this thesis and the composite log based on the GAS and HEX cores. The small triangles indicate the sample depths, their colors are coded per core (similar as in Figure 1.7) and are replotted on the composite log. On this log the sample depths are recalculated based on multiple marker beds within the different cores

mid-1990's and stored in the South32 core yard in Hotazel.

The top of Gasesa-1 was percussion drilled and therefore the contact between the BIFs and the Makganyene diamictite is missing. This core captures most of the Griquatown, the entire Kuruman and part of the Gamohaan Formations. The HEX and ERI cores capture part of the Kuruman IF, whereas the ARP core stops around the Griquatown-Kuruman transition. However, these last three cores capture the Griquatown-Makganyene contact. Using marker-beds the cores could be correlated and a composite log was made through ca. 430 m of BIF-stratigraphy (Figure 1.10).

Samples were taken circa every 15 m for the GAS, 10 m for the HEX and ERI and 7 m for the ARP cores. They consisted of 5-15 cm half-core fragments, capturing the diversity of BIF, giving a total of 106 samples (Figure 1.10). No samples were taken within a few meters of the volcanic sills present in the Kuruman IF. The samples were halved into quarter-core pieces, of which one was kept as a reference piece at Rhodes University, and the other was used to make a petrographical thin section and its offcuts were pulverised. The samples are labelled by their core-abbreviation (GAS, HEX, ERI, ARP) followed by their depth in meters. Brief sample descriptions including bulk-rock mineralogy and the XRD spectra are presented in Appendices I and II.

1.3.4. Previous/active work on the drill-cores

The 4 drill-cores studied here have been used in multiple MSc-theses at both Rhodes and Utrecht Universities. The results of these theses complement the work of this project and have aided the discussion and synthesis. The following section describes briefly the main conclusions and the implications of these various projects for my thesis. The full theses can be requested at the respective university libraries.

Fryer (2015) investigated the HEX and GAS cores focussing on their petrography and geochemistry. This study was a pilot-study that provided samples and results that are integrated into my work. Although the focus laid on Mn and Fe speciation, bulk-rock C and Fe isotope data were produced. The major result of this study was to question a diagenetic origin for the Fe-carbonates.

The origin of the carbonate minerals was also the main focus of the study by Rafuza (2015). Following high resolution (3-4 m) sampling of the ERI core, the carbonate minerals were characterized by petrography and Electron Microprobe (EMP) analysis. The stratigraphical bulk-rock $\delta^{13}C$ signal

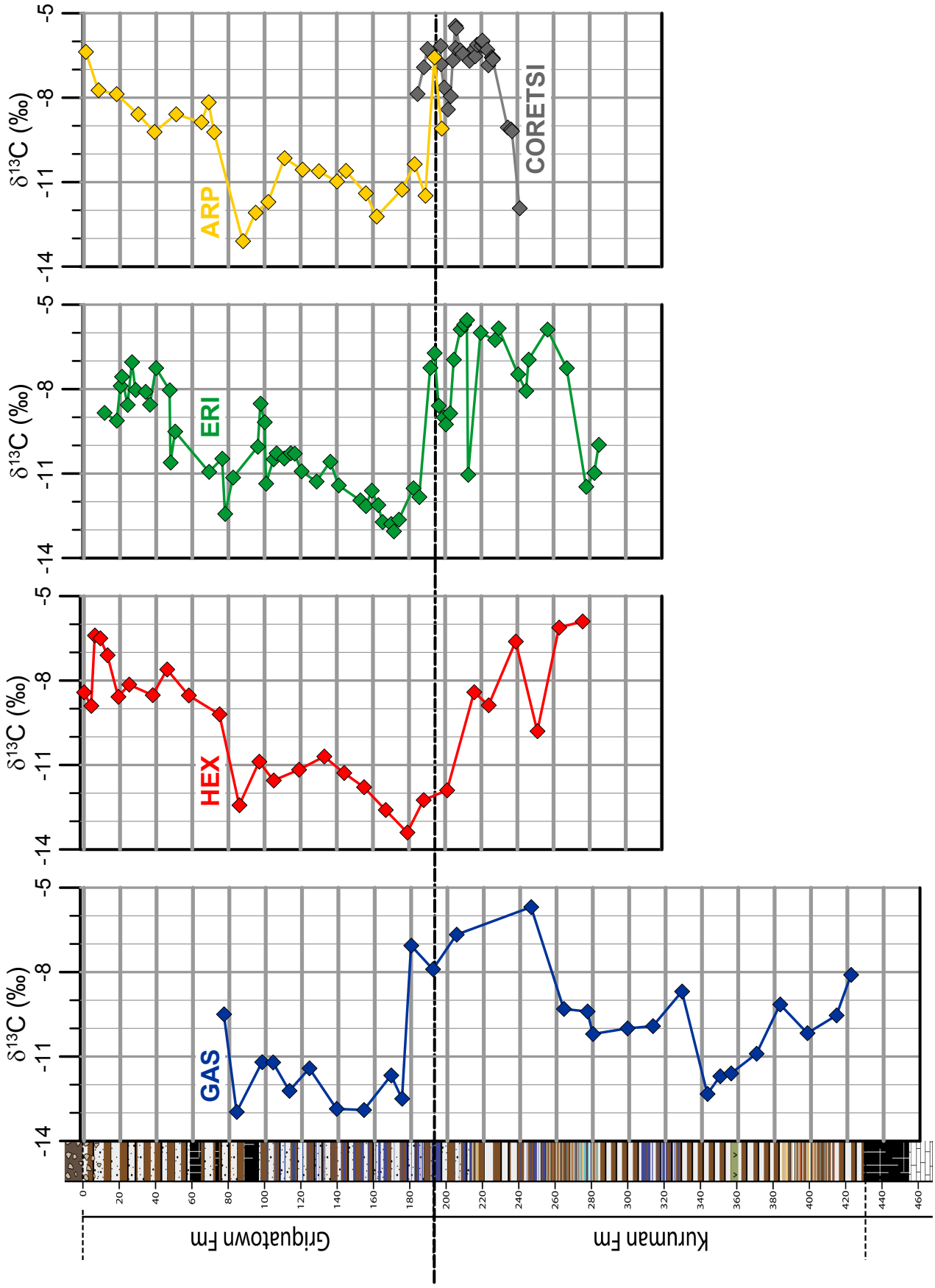

Figure 1.11: The reproducible stratigraphic bulk-rock $\delta^{13}C$ values from Tsikos, et al. (in prep) for the four drillcores studied in this project. Additional bulk-rock $\delta^{13}C$ values from the CORETSI-core are from Beukes, et al. (1990).

(Figure 1.11; Tsikos, et al., in prep.) found in the GAS and HEX cores (Fryer, 2015) was reproduced for the ERI core, (Rafuza, 2015) and the ARP core (this study) and could be integrated with the CORETSI-data (Beukes, et al., 1990). Furthermore, in a subset of samples Rafuza (2015) showed that the $\delta^{13}C$ co-varied predictably, generally within 1 ‰ between ankerite and siderite. This implies that variations in bulk-rock $\delta^{13}C$ values are independent of the ankerite/siderite ratio.

BIF deposition in the Griqualand West Basin was not restricted to the the Kuruman and Griquatown Formations, since the Hotazel Formation also contains significant amounts of BIF. The transition from the Ongeluk lavas into the Hotazel Formation was studied by Lantink (2016). This study used micro-drilled hematite samples to determine the influence of the underlying Ongeluk lavas in the overlying basin. Based on the REE + Y and Fe isotope characteristics acquired here the hydrothermal component was only restricted to the first few meters of the Hotazel deposition. The hematite higher up unequivocally represent a primary signal, relating to the initial process of ferric oxyhydroxide formation from oxidation of dissolved Fe(II) in the water column (Lantink, 2016).

Mhlanga (in prep.) focussed on the entire Hotazel stratigraphy. Using various sampling strategies, including high-resolution, centimetre-scale sampling of the three key lithologies, the redox behaviour of Fe and Mn was constrained. Bulk-rock geochemistry, petrology and stable-Fe isotopes combined with Fe and Mn speciation helped to unravel the deposition of the Mn-rich BIFs and Mn-ore.

Basin wide Rayleigh-effects have been suggested as an explanation for the low $\delta^{56}Fe$ values in the Hotazel Formation (Tsikos, et al., 2010). In combination with the aforementioned studies and this current work, the stratigraphical $\delta^{56}Fe$ record of the Transvaal Supergroup, present in the Griqualand West Basin will be complete. This will help to further constrain redox-changes in the basin right up to, and including the GOE.

A few other studies have investigated other aspects of the Asbestos Hills BIF. Similar to the carbonate minerals, the origin of the riebeckite-bands also remains unclear. Van der Burg (in prep.) used detailed petrography and *in situ* geochemical analyses, including REE, to better understand the various forms of riebeckite present. Although nothing conclusive about the origin of the riebeckite could be stated, the *in situ* data is used in the relevant sections of this thesis.

The presence of the lutite bands in the Asbestos Hills BIFs is generally related to a volcanic ash

input (e.g. Beukes, 1984). Based on bulk-rock trace elemental analyses of the lutite-samples, Van der Waal (2016) confirmed a volcanological origin of the lutites, thus giving additional confidence to use these bands as marker beds (Figure 1.10). Multiple-sulfur isotope analyses found that mass-independent fractionation of sulfur was present in the lutites, indicating that the Asbestos Hills were deposited before the GOE (Van der Waal, 2016).

Where the lutite bands are good marker beds, the intervals of magmatic rocks at the top of the Kuruman Formation are not. A petrological and microprobe study of the lower contact of the igneous rock with the BIF in the HEX-core (ca. 910 m depth, Figure 1.10) was carried out in order to determine the nature of its emplacement. Metamorphic mineralogy, cross-cutting relationships and the presence of porphyroblasts indicated that this unit was intrusively emplaced (Molendijk, 2016).

1.4. Problem statement and research objective

BIFs have been studied using a wide variety of sampling strategies and techniques, each with its own advantages and drawbacks. Bulk-rock data include REE which have been used to argue for the hydrothermal source of the iron (e.g. Bau and Dulski, 1996) and Fe-isotopes to infer the oxidation state of the atmosphere (e.g. Planavsky, et al., 2012). Furthermore, bulk-rock abundances of transition metals (e.g. Liu, et al., 2016) and their isotopic ratios have been used to attempt to identify evidence for oxidative weathering in the Paleoproterozoic environment (e.g. Frei, et al., 2009; Czaja, et al., 2012).

A major disadvantage of bulk-rock techniques is the poorly constrained role of mineralogy on bulk-rock chemistry, so that changes within a mineral-group might be masked by bulk-rock signals. Furthermore, bulk-rock techniques rely on the assumption that all minerals formed via a similar pathway and that diagenesis took place in a closed system. Another frequent assumption is that the different minerals are in isotopic equilibrium with each other.

Valid interpretations can be made even if these assumptions do not hold. This can be done, for example, by comparing only samples within a specific BIF facies with one other (e.g. Beukes and Klein, 1990), or working with mono-mineralogical samples (e.g. Johnson, et al., 2003; Craddock and Dauphas, 2011). In these cases sampling bias may affect the results. Small-scale heterogeneities in BIF make micro-drilled samples susceptible for erroneous interpretations when scaling-up to basin

wide trends across time and/or space. Similar drawbacks exist for *in situ* techniques, such as LA-ICP-MS, which are used to determine grain-specific δ^{56}Fe (Steinhoefel, et al., 2009; 2010) or REE signatures (Alibert, 2016). In these instances only the larger grains can be analysed, due to analytical limitations. Although averaging multiple grains from the same horizon gives some confidence, the translation to large scale variability remains challenging.

Another potential method that may solve many of these issues is a sequential extraction procedure in which various solvents can be used to target different Fe-bearing fractions. The advantage of this technique is that it averages out the chemistry of the different fractions on a bulk-rock level and allows comparison of the various fractions independent of their abundance, so chemo-stratigraphic profiles can be made for each of them. Sequential extraction of various Fe-phases has been successfully applied on BIFs before (e.g. Poulton, et al., 2004; Frost, et al., 2007; Halverson, et al., 2011) to interpret Fe-speciation as a function of the oxidation state of the ocean. These studies focused either on Neoproterozoic BIFs or investigated the effects of post-depositional metamorphism. No speciation work has yet been done on the BIFs leading up to the GOE. Additionally, to date, there has not been a universal and widely accepted technique developed for the sequential extraction of BIF.

Due to the presence of crystalline siderite, high concentrations of magnetite and the occurence of multiple Fe-silicates, the previously developed protocols for shales (Poulton and Canfield, 2005) should be tested and where necessary opitimized and adapted for BIF. Getting a clean, uncontaminated extraction is absolute vital for this work, in order to address key questions around BIF deposition and its relationship to the GOE.

As stated before, bulk-rock transition metal abundances and isotopes have been used to infer the onset of oxidative weathering in the Paleoproterozoic and Archean. In most instances little attention was given to the distribution of the targeted element across different minerals in bulk-rock samples. There might be similar processes at work as for iron, where the carbonate δ^{56}Fe is generally lower than oxide-bound δ^{56}Fe (e.g. Johnson, et al., 2008b). Once the optimized protocol is applied to all our samples this should enrich our understanding of the distribution of these trace metals, and elucidate on their bulk-rock applicability.

To this end the objectives of this PhD can be summarized as follows:

- The development of an existing laboratory protocol (Poulton and Canfield, 2005) for the sequential extraction of the three key mineral fractions in the Asbestos Hills BIFs; namely Fe-carbonates, magnetite and Fe-silicates, with further processing to allow species-specific Fe-isotope analysis (Henkel, et al., 2016). (Chapter 2)
- Examination of the stratigraphic behaviour of the transition metals and their partitioning in the different fractions of the Asbestos Hills BIF (Chapter 3)
- Focus on the Rare Earth Element (REE) speciation to investigate the role of primary versus secondary processes on mineral formation in BIF (Chapter 4).
- Produce a bulk as well as species-specific iron isotope stratigraphy and interpret the respective signals in the context of species-specific controls against postulated secular trends in ocean chemistry of iron (Chapter 5).
- The latter three objectives can then be combined and put in perspective with respect to the changing atmospheric and oceanic conditions leading up to the GOE (Chapter 6).

“By failing to prepare you are preparing to fail.“

Attributed to Benjamin Franklin

2

PROTOCOL DEVELOPMENT

Abstract

Banded iron formations (BIF) record changes in ocean chemistry through the Archean and Paleoproterozoic and their abundance and composition can be linked to oxygenation of the atmosphere across the Great Oxidation Event (GOE). Mineralogically, BIF consists of three main iron-bearing fractions: (1) Fe-Ca-Mg-Mn carbonates, (2) magnetite and/or hematite and (3) Fe-silicates. These fractions are typically fine-grained on a sub-µm scale and their co-occurrence in varying amounts means that bulk-rock or microanalytical geochemical and stable isotope data can be controlled by mineralogy.

Fraction specific variations in Fe isotopes have the potential to reveal diagenetic versus primary precipitative controls on BIF mineralogy. Here we adapt an existing sequential extraction scheme for Fe-phases (Poulton and Canfield, 2005) to the high Fe-content in BIF and the specific three-fraction mineralogy and subsequently process the extracts for stable Fe-isotope analysis (Henkel, et al., 2016). We use samples from the Asbestos Hills Subgroup BIF, Transvaal Supergroup, South Africa.

The commonly used hydroxylamine-HCl and dithionite leaches were omitted since ferric oxides are quantitatively insignificant in these BIF samples. The acid acetate leach was tested at variable temperatures, reaction times and extracting atmospheres in order to ensure that all micro-crystalline Fe-carbonates are effectively dissolved, resulting in an optimum extraction for 48 hr at 50 °C under inert conditions. The dissolution of magnetite by NH_4-oxalate was also tested and resulted in a 24 hr extraction under an ambient atmosphere. Finally, a HF-$HClO_4$-HNO_3 leach was added to dissolve the residual silicate fraction which has to date not been considered in any detail in BIF. The application of this modified protocol in future work will enable more detailed assessments of Fe fractionation in ancient sediments and rocks which will potentially provide new insights into the evolution of atmosphere and ocean chemistry.

2.1. INTRODUCTION

Banded iron formations (BIF) are key sedimentary archives that constrain the history of oxygenation in the early atmosphere and oceans (e.g. Klein, 2005; Rouxel, et al., 2005; Pecoits, et al., 2009; Bekker, et al., 2010). Several key aspects of BIF formation remain open to interpretation: the composition and structure of the oceans from which precursor sediments precipitated; the mode of primary precipitation of iron and silica; and the potential relationship between secular changes in BIF chemistry and the rise in atmospheric oxygen concentrations. Answers have been sought in recent years through the use of novel stable isotope geochemistry, including Fe or Cr isotopes (Rouxel, et al., 2005; Frei, et al., 2009; Planavsky, et al., 2014).

BIFs are composite rocks containing three major Fe-bearing fractions; Fe-carbonates, Fe-oxides and Fe-silicates of a very fine-grained textural nature. This poses significant challenges for geochemical research, especially with regard to phase-specific isotope studies. Physical separation of individual minerals in BIF is practically unattainable. Therefore, mainly bulk-rock analyses have been employed to BIF samples to date (Johnson, et al., 2003; Anbar, 2004; Rouxel, et al., 2005; Yamaguchi, et al., 2005; Tsikos, et al., 2010; Planavsky, et al., 2012). Bulk-rock data potentially reflect differences in modal mineralogy, as Fe-carbonates (e.g. siderite) are known to record lower δ^{56}Fe values compared to Fe-oxides (e.g. magnetite) (Johnson, et al., 2008b). Furthermore, to interpret bulk-rock δ^{56}Fe values, isotopic equilibrium between the different mineral fractions needs to be assumed. Bulk-rock δ^{56}Fe values do not represent direct precipitation from seawater, instead the isotopic composition is affected by post-depositional modification during diagenesis and/or metamorphism (Johnson, et al., 2008a; Heimann, et al., 2010).

Some studies have focussed on mono-mineralogical bands (siderite or magnetite) where possible (Johnson, et al., 2008a; Heimann, et al., 2010; Craddock and Dauphas, 2011) or single mineral grains (if large enough) using femto-second laser ablation inductively coupled plasma mass spectrometry (Steinhoefel, et al., 2009). However, the mono-mineralogical band and micro-analytical techniques focus on small-scale variations that are unsuitable for the elucidation of broader-scale trends across time and/or space. Furthermore, most bands in BIF are not mono-mineralogical and the very fine-grained nature makes micro-analytical techniques focus on the larger grains. The geochemical relations between different minerals and the bulk-rock to the original environment

of deposition remain unclear. An important first step to address this is to develop a technique for identifying isotopic variability within different mineral fractions and its relationship to the bulk-rock.

Chemical separation of BIF-samples into different mineralogical fractions has a clear potential to allow the monitoring and evaluation of phase-specific effects on bulk-rock Fe-isotope values. Sequential extraction techniques use consecutive solvents, where each solvent dissolves a specific mineral group and has been widely developed for a variety of sample types and elements (e.g. Schilling, et al., 2014; Siebert, et al., 2015). Multiple schemes have been developed using different solvents, varying reaction times and a wide range of sample types including BIFs (Poulton, et al., 2004; Reinhard, et al., 2009), but these studies did not include stable isotope analyses. Pioneering work has been performed on the Fe isotopic signatures for specific mineralogical fractions in modern anoxic sediments and soils (Staubwasser, et al., 2006; Wiederhold, et al., 2007; Guelke, et al., 2010; Henkel, et al., 2016). A few BIF samples have been included in a basic scheme using acetic acid, HCl and HF (Frost, et al., 2007). There is, however, the need for a cost-effective yet mineral-specific analysis protocol tailored to the key mineral fractions found in BIF but comparable to the method commonly applied in studies of the Archean and Proterozoic shale record (Poulton, et al., 2004).

This study builds on the sequential Fe extraction method developed by Poulton and Canfield (2005, hereafter referred to as P&C 2005) and its adaptation for subsequent Fe-isotope analysis by Henkel, et al. (2016). The P&C 2005-protocol was optimized for the very high Fe content in BIF and since there are only three key Fe-bearing mineral fractions, the number of different extracted fractions could be reduced. By varying the leaching times and conditions, using BIF samples from the Transvaal Supergroup of South Africa with highly contrasting modal mineralogy and bulk-rock $\delta^{56}Fe$ values, the optimum BIF-extraction protocol was obtained. Samples were subsequently purified for Fe isotope analysis by multiple collector ICP-MS (Henkel, et al., 2016).

2.2. Sample location and selection

The Asbestos Hills Subgroup in the Griqualand West section of the Transvaal Supergroup, South Africa, is dominated by two sequences of BIF, the rhythmically micro-banded Kuruman BIF Member and the overlying predominantly clastic-textured Griquatown BIF Member (Beukes, 1984). These BIFs have been captured by two complementary drill-cores, GAS1 and HEX-5, drilled 60 km

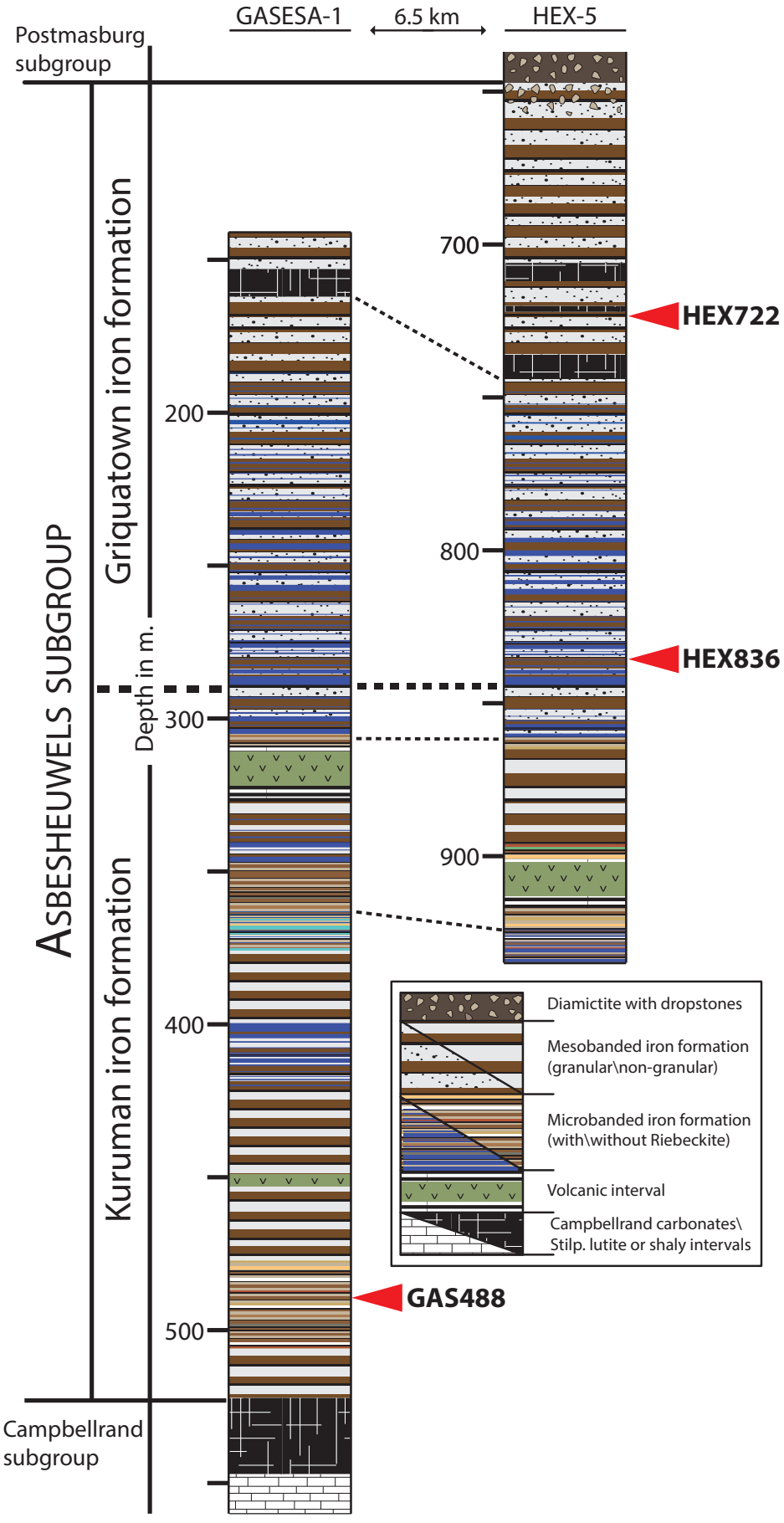

Figure 2.1: The drill cores and the three samples used for the tests (depths in m).

Table 2.1: Bulk-rock compositions of the samples in wt%; $\delta^{56}Fe$ in ‰ relative to IRMM-014. Typical external reproducibilities for $\delta^{56}Fe$ were 0.1‰ (2SD)

	SiO_2	Al_2O_3	FeO	MnO	MgO	CaO	K_2O	LOI	Total	C	S	$\delta^{56}Fe$
GAS488	37.2	b.d.l.	52.9	0.1	2.1	0.8	b.d.l.	6.0	99.4	0.4	0.1	0.42
HEX722	22.4	0.5	32.7	4.9	4.3	4.8	0.3	29.2	99.6	7.9	0.2	-1.77
HEX836	38.2	0.3	40.1	0.3	4.8	0.3	1.0	14.3	99.7	3.2	0.1	-0.60

TiO_2, P_2O_5, Na_2O and H_2O- < 0.1 wt%; All Fe as FeO; oxide data from XRF (b.d.l. = below detection limit), bulk-rock C and S from LECO CS

NW of the town of Kuruman. The complete, ca. 400 m thick interval of these BIFs was sampled every 10-15 m on average. After thin section preparation, quarter-core samples of 5-15 cm in length were powdered and geochemically characterized (see section 2.3). The bulk composition ranges (i.e. FeO 10-53 wt%, SiO_2 20-79 wt% and S <<1 wt%) match those measured by Beukes and Klein (1990).

Based on our initial bulk mineralogical, geochemical and iron isotope work, three samples (HEX722, GAS488 and HEX836; Figure 2.1) with highly contrasting compositions (Table 2.1) were selected for detailed sequential extraction analysis in order to assess the limitations of existing protocols. The carbonate-dominated HEX722-sample was taken from the upper part of the Griquatown BIF (Beukes, 1984) and consists of Fe-carbonate pelloids in a microcrystalline stilpnomelane/quartz matrix. Minnesotaite and calcite are also present in some pelloids. In thin section, magnetite appears only as a minor to trace mineral. Based on the XRD spectrum, siderite is the dominant carbonate, followed by ankerite and calcite in order of decreasing abundance.

In contrast to sample HEX722, GAS488 is dominated by magnetite. This sample represents the rhythmically microbanded Kuruman BIF, and is typified by alternating bands of microcrystalline quartz and magnetite (grain size up to 100 µm). At the edges of these bands, minute sub-µm hematite flakes are also present. Although peaks of carbonate minerals were not detected in the XRD spectrum, minor rhombohedral carbonates were observed in thin section. Dispersed riebeckite needles and stilpnomelane flakes were also identified microscopically but were undetectable in the XRD-spectra.

Sample HEX836 consists of the three Fe-hosting mineralogical fractions in approximately equal proportions. The thin section reveals an alternation of stilpnomelane-magnetite-quartz, riebeckite-quartz and carbonate-dominated bands. XRD revealed that the carbonate fraction is dominated by siderite in its typical very fine-grained rhombohedral habit.

The Fe-distribution of the first two samples is dominated by a single mineralogical fraction (Fe-carbonate or Fe-oxide). Consequently, the very bulk of the contained Fe ought to be leached in a single chemical reaction step. In contrast to this, HEX836 consists of the three fractions in approximately even proportions and could therefore be used to further assess the optimum geochemical leaching conditions and possibly as a standard for future work (see Table 2.1).

With increasing carbonate content, bulk-rock Fe-isotope values decrease in the selected samples (Table 2.1): GAS488 has a δ^{56}Fe value of 0.42 ± 0.1 ‰ (see section 2.4.3.1), but this decreases to -0.60 ± 0.1 ‰ for HEX836 and is lowest for the carbonate-dominated sample HEX722 (-1.77 ± 0.1 ‰).

2.3. Analytical techniques

Bulk-rock sample characterization took place at Rhodes University, South Africa. Chemical composition was determined by XRF, using the method of Norrish and Hutton (1969), and mineralogy was resolved by optical microscopy and XRD. Furthermore, bulk-rock C and S were measured on a LECO CS-300 analyser at Utrecht University, The Netherlands.

The extracted and processed solutions were analysed by inductively coupled plasma optical emission spectrometry (Spectro Arcos ICP-OES) at Utrecht University, with uncertainties <5 % (2SD) for duplicate measurements on major elements. Following the leachate-destruction and before the column chromatography the iron concentrations were confirmed colorimetrically using the 1,10-phenanthroline method (APHA, 2005).

Iron-isotopic ratios were measured on three ThermoFinnigan Neptune MultiCollector Inductively Coupled Plasma Mass Spectrometers (MC-ICP-MS) at three different laboratories. Bulk-rock and species-specific samples were measured at Durham University, UK, the protocol verification samples at the Steinmann Institute in Bonn, Germany, and a selection of the species-specific samples were verified at the "Helmholtz Laboratory for the Geochemistry of the Earth Surface'' at GFZ, Germany. Prior to any Fe-isotope measurement, the samples were matched to the lab-specific IRMM-014 standard concentration. IRMM-014 was used for sample-standard bracketing. The reported δ^{56}Fe values ($\delta^{56}Fe = [(^{56}Fe/^{54}Fe)_{sample}/(^{56}Fe/^{54}Fe)_{IRMM\text{-}014}\text{-}1] \times 10^3$) were calculated as the mean of replicates (n= 3 - 8) during the same measurement sequence. The uncertainty was estimated by multiple runs

of treated Fe standard and reference materials in different laboratories.

All measurements followed established analytical procedures. In Durham we used wet plasma (ESI Cinnabar spray chamber) and an ESI 50 µl/min PFA concentric nebulizer with samples (ca. 8 ppm Fe) aspirated in 0.1 M HNO_3 (Williams, et al., 2004; 2012). At the Steinmann Institute the setup followed Schoenberg and von Blanckenburg (2005) and Henkel, et al. (2016), using the ThermoFinnigan stable introduction system (SIS) with a glass MicroMist nebulizer and a nominal sample (ca. 1 ppm Fe in 0.3 M HNO_3) uptake rate of 80–110 µl/min. At GFZ the uptake system was also an SIS, however, a PFA-ST Nebulizer (nominal uptake of 100 µL/min) and a concentration of ca. 5 ppm Fe in 0.3 M HNO_3 was used (Schoenberg and von Blanckenburg, 2005).

Accuracy was monitored using international reference standards (BHVO-1 and IF-G) and a lab-specific in-house standard. This was the FeCl salt standard for Durham ($\delta^{56}Fe$ = -0.71 ± 0.06 ‰; Williams and Bizimis, 2014), the JM Fe Puratronic wire for Bonn ($\delta^{56}Fe$ = 0.42 ± 0.05 ‰; Schoenberg and von Blankenburg, 2005) and the HanFe for the GFZ ($\delta^{56}Fe$ = 0.29 ± 0.05 ‰; Von Blanckenburg, et al., 2014). For all labs the reference standards matched the literature values and same solutions measured at different labs were within uncertainty of each other.

Siderite dissolution in Na-acetate with and without atmospheric oxygen was thermodynamically modelled using PHREEQC (version 2.18.5570; Parkhurst and Appelo, 1999) in combination with the minteq.v4 database included in the software-package. In this process, 50 mg of siderite was equilibrated with 10 ml 1 M Na and H-acetate at a fixed pH of 4.5 and temperature of 50 °C with and without the presence of 5 ml air (where the 21 % O_2 is the only reactive species).

2.4. Optimization of the sequential extraction scheme for BIF samples

2.4.1. Sequential extraction schemes

The sequential extraction scheme used here is a modified version of the protocol designed by Poulton and Canfield (2005). The original protocol was developed to extract seven Fe phases, from “loosely sorbed” Fe to pyrite Fe, and calculate the unreactive silicate Fe by subtracting the sum of the extracted Fe from the bulk-rock Fe. The method has been successfully applied to ancient sediments (e.g. Poulton, et al., 2004; März, et al., 2008; 2012; Reinhard, et al., 2009) and further developed and

Table 2.2: Fractions and solvents used in this study and based on Poulton and Canfield (2005)

Target fraction	Solvent	Duration
Carbonates	1 M Na-acetate at pH 4.5 adjusted with acetic acid	24/48 hrs
Easily reducible oxides	1 M Hydroxylamine-HCl in 25% v/v acetic acid (pH 2.0)	48 hrs
Reducible Fe-oxides	50 g/L Na-dithionite buffered to pH 4.8 with 0.35 M acetic acid/0.02 M Na-citrate*	2 hrs
Magnetite	0.2 M ammonium oxalate/0.17 M oxalic acid solution (pH 3.7)	6 hrs
Silicates	5:3:2 v/v of HF (48%), HClO4 (72%) and HNO3 (65%) resp.	12 hrs

* The P&C2005 protocol uses 0.2 M Na-citrate, here reduced to 0.02 M due to matrix effects during MC-ICP-MS measurements (Henkel, et al., 2016).

applied for additional iron isotope analysis on shallow marine sediments (Henkel, et al., 2016). In the case of the Precambrian sediments (shales and BIF) only four phases were extracted: carbonate-Fe, ferric oxide-Fe, magnetite-Fe and pyrite-Fe, the other phases were either not present (sediment-sorbed Fe, ferrihydrite and goethite) or of no interest in the studies (poorly reactive sheet silicate Fe) (Poulton, et al., 2004; Reinhard, et al., 2009).

Here we further modified the P&C 2005-protocol for BIFs which contains three Fe- phases: Fe-carbonates, magnetite and Fe-silicates. No sediment-sorbed Fe, ferrihydrite or goethite are present in these 2.5 Ga rocks. Furthermore, the Asbestos Hills BIFs are generally sulfur-poor (<< 1 wt%, Beukes and Klein, 1990), making the pyrite-Fe fraction negligible.

The first two sequential extraction (SE) tests consisted of 4 original P&C 2005 steps and a final HF-$HClO_4$-HNO_3-step that was added to dissolve the silicate residue (Table 2.2). The dissolution of crystalline siderite in acetate might not be quantitative (Poulton and Canfield, 2005; Reinhard, et al., 2009). This was assessed using the two different extraction conditions mentioned in P&C 2005; 24 hr extraction at room temperature and a 48 hr extraction at 50 °C. To prevent contamination of the oxide fractions we included the original hydroxylamine-HCl step to collect any undissolved carbonate-Fe**.** Ideally we would combine the two oxide extractions into one leach, since hematite is only a trace constituent of the rocks and a clear separation of hematite from magnetite using the dithionite step might not be achieved (Henkel, et al., 2016). In P&C 2005, NH_4-oxalate was used to dissolve the magnetite, but it may also dissolve hematite if Fe(II), initially bound to magnetite, acts as a catalyst (Suter, et al., 1988; Panias, et al., 1996; Taxiarchou, et al., 1997). To confirm this we ran several tests with and without the dithionite step.

The setup of the six different SE-tests is presented in Table 2.3. The effectiveness of the different

Table 2.3: Setup for sequential extraction (SE) tests

	SE1	SE2	SE3	SE4	SE5	SE6
Laboratory	Cologne	Utrecht	Utrecht	Utrecht	Utrecht	Utrecht
Atmosphere	Inert	Inert	Oxic	Inert	Oxic	Inert
Acetate	24 hr/20 °C	24 hr/20 °C	24 hr/20 °C	48 hr/50 °C	48 hr/50 °C	48 hr/50 °C
Hydroxylamine	Yes	Yes	Yes	Yes	-	-
Dithionite	Yes	Yes	-	Yes	-	-
Oxalate	Yes	Yes	Yes	Yes	Yes	Yes[2]
Hydrofluoric acid	Yes[1]	Yes	Yes	Yes	Yes	Yes

[1]HF-step performed at Utrecht University; [2]Leached in darkness at 30°C

extractions was also tested with regard to atmospheric conditions. Several tests (SE1, 2, 4, 6) were performed under an inert N_2-atmopshere, whereas the remaining (SE3, 5) were performed under an ambient atmosphere. The setup of a preliminary extraction (SE1) done in Cologne was copied and an extraction under similar conditions (SE2) was performed at Utrecht, with the exception that the amount of reagents was increased from 5 to 10 ml. Sequential extraction 3 took place in an oxic atmosphere and the dithionite step was omitted. For the last three extraction tests (SE4-6), the acetate step was changed from 24 hours at 20 °C to 48 hours at 50 °C, following the recommendations by Poulton and Canfield (2005). With the exception of the acetate step conditions, SE4 was identical to SE2. SE5 and SE6 both omitted the hydroxylamine and dithionite steps. SE5 was performed under oxic and SE6 under inert conditions. The tests were performed in batches containing the test samples (GAS488 and HEX722) in triplicate as well as a blank and carbonatite standard, SARM-40 (Ring, 1993), in duplicate.

Following these tests, the optimum durations for the acetate and oxalate steps were tested using either the carbonate- or oxide-rich sample, respectively. The acetate step (SE-Ac) was performed under oxic conditions at 50 °C for 7, 24, 48 and 72 hours, followed by the 6-hour oxalate leach and the silicate digestion. For the oxalate step (SE-Ox) the extraction was tested, following the 48 hour, 50 °C acetate leach, at 6 and 24 hours for both atmospheric conditions, one extraction was completed in darkness and one was performed at 50 °C. These optimization tests included a duplicate sample (HEX722 for acetate and GAS488 for oxalate) and a control sample for each of the conditions tested. The results of these tests yielded a working protocol. This final protocol (SE_{final}) was then applied to the samples. In order to measure fraction specific Fe-isotopes these samples required further processing for matrix removal and Fe-purification after Henkel, et al. (2016) (see

section 2.4.3).

2.4.2. Sequential extraction methodology

For each extraction step, the extracting reagent was pipetted into a 15 ml Greiner® tube containing ca. 50 mg of homogenized sample. The tubes were placed horizontally on a shaker (150 rpm) for the indicated reaction time. In case of extractions at elevated temperatures, a shaking incubator was used. After centrifuging (2500G, 15 min), the supernatants were syringe-filtered (0.45 µm), transferred to another 15 ml Greiner® tube and stored in a fridge at 5 °C. Due to extremely high Fe concentrations in the samples, the residue was always washed with MilliQ® water, centrifuged and decanted before the next reagent was added. Addition of extracting solutions and filtrations was performed in a N_2-filled glove bag where indicated ('inert conditions', Table 2.3).

After the oxalate extraction, the residue was transferred with several rinses of MilliQ® from the Greiner® tube to a 30 ml Savillex® PFA-vial. After evaporation 5.0 ml HF-HClO4-HNO3 were added to the vial to dissolve the residue overnight at 90°C. This dissolution was followed by an evaporation step, after which the sample was re-dissolved in 10 ml 1.0 M HNO_3. The solution was then transferred to a 15 ml Greiner® tube, and also stored in the fridge. After the extractions all solutions were analysed for major elements by ICP-OES.

2.4.3. Leachate destruction and Fe-purification

To avoid matrix-induced bias on isotope ratio measurements, the leachates were broken down via a multi-step scheme (Figure 2.2; Henkel, et al., 2016). This involved multiple cycles of acid addition, evaporation, and thermal decomposition, followed by Fe-precipitation with 25 % ammonia. For the silicate fraction, the bulk-rock Fe-isotope protocol of Williams, et al. (2004) was applied. After the final evaporation step, the residue was dissolved in 6 M HCl, making a solution with maximum 600 ppm Fe to avoid overloading the chromatography columns. Iron concentrations were confirmed colorimetrically (APHA, 2005) and compared to the ICP-OES results of the extracted solutions, to check for any Fe-loss during leachate destruction.

Following the leachate breakdown, iron was purified to remove major elements, Ni and Cr using the protocol of Williams, et al. (2004). From the 6 M HCl solutions, 0.45 ml were added to

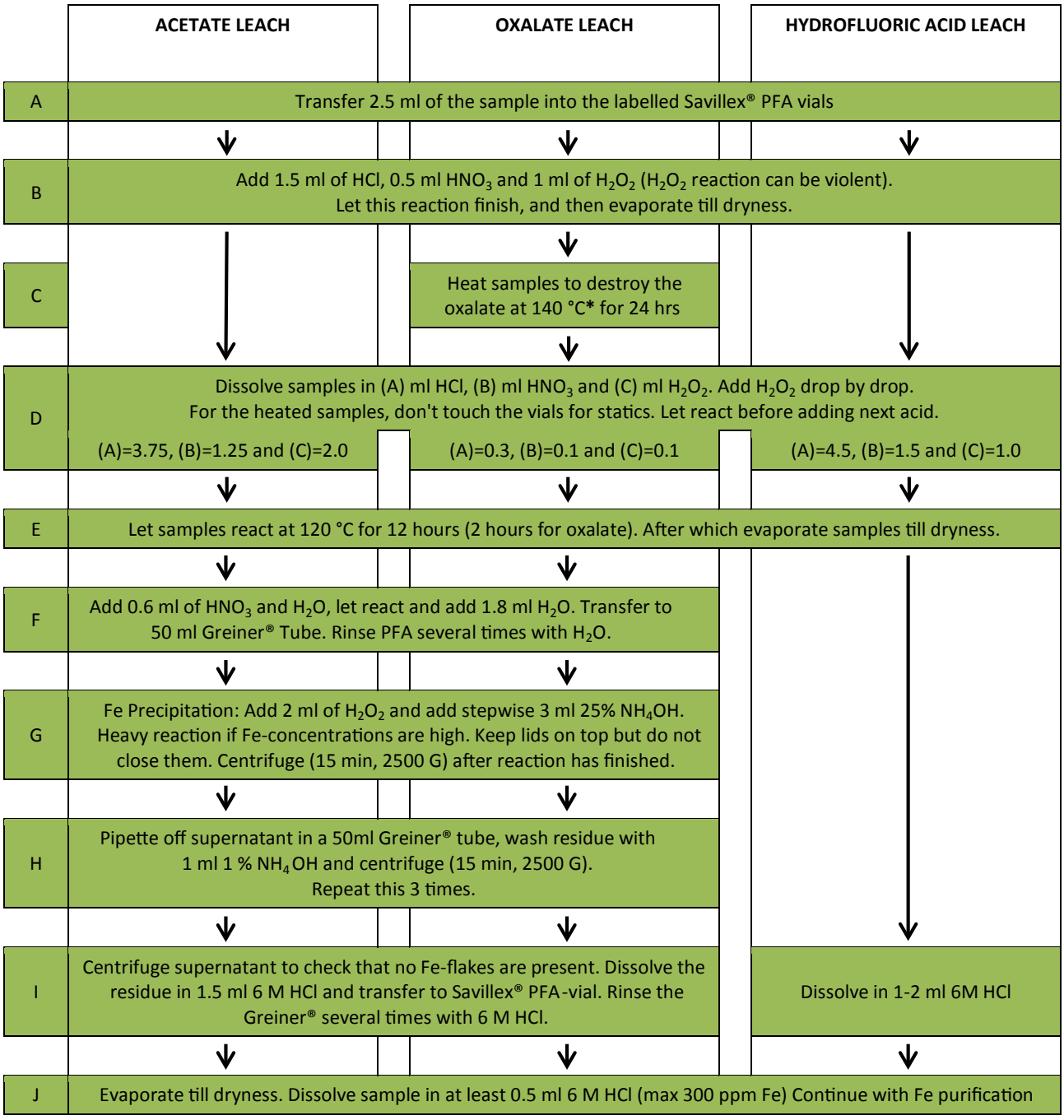

Concentrated acids are used unless stated otherwise * Remove growing oxalate crystals with H_2O

Figure 2.2: Flow diagram of the leachate destruction protocol, based on Henkel, et al. (2016)

a cleaned and pre-conditioned chromatography column (Bio-Rad, Micro Bio-Spin™) filled with AG 1-X4 Resin (0.8 ml, 200-400 mesh). After elution of the matrix with 4 passes of 1 ml 6M HCl, the Fe was eluted with 4 passes of 0.5 ml 0.05M HCl. The eluted Fe was collected, evaporated to dryness, oxidized (using H_2O_2 and HNO_3) and re-evaporated, before being taken up in 0.3 ml HNO_3. Recovery was assessed by ICP-OES and is discussed further below.

Table 2.4: MC-ICP-MS results of the certified reference materials (CRMs) and the SCP-Fe standard.

Sample		δ^{56}Fe		Number of repetitions				GeoREM values
		Mean	2SD	Sample prep.	Column chemistry	Measure-ments	Labs	
CRMs	BHVO-1	0.08	0.05	2	6	6	2	0.10 ± 0.04
	IF-G	0.63	0.05	2	7	8	3	0.64 ± 0.07
Processed SCP-Fe	Unprocessed	-0.24	0.09	3	3	3	1	
	Acetate	-0.22	0.04	4	4	4	2	
	Oxalate	-0.22	0.06	4	4	5	3	
	HF	-0.26	0.11	4	4	4	2	

2.4.3.1. Verification of destruction and purification protocols

The column chromatography was evaluated using international reference materials BHVO-1 and IF-G following digestion with HF-$HClO_4$-HNO_3 (Williams, et al., 2004). The destruction protocol was monitored with the addition of 0.5 ml of a 1000 mg/l Fe ICP-standard (PlasmaCAL, SCP Science, Canada; hereafter SCP-Fe) to 9.5 ml of either the acetate or the oxalate solution. For the HF step, 0.5 ml were added in an empty PFA-container. All fractions were processed to achieve matrix removal (Henkel, et al., 2016) and Fe purification (Williams, et al., 2004). To compare the processed fractions against the SCP-Fe standard, the latter was evaporated and re-dissolved in 0.3 ml HNO_3.

The measured δ^{56}Fe values for BHVO-1 and IF-G (Table 2.4) show excellent agreement with their respective GeoReM-database values (Jochum, et al., 2005). Table 2.4 also shows the δ^{56}Fe values of the processed SCP-Fe solutions. The yields were low for one acetate and one HF sample (91 % and 89 % resp.), but despite this all δ^{56}Fe results (using the different extraction reagents) were within uncertainties of the unprocessed standards and we can conclude that there was no significant fractionation during processing or matrix effects during measurements. Based on the repeated measurements of the standard and the two reference materials a typically overall analytical uncertainty (including sample preparation, excluding the extraction processes) was estimated to be 0.1 ‰. This value was used throughout the study.

2.5. Sequential extraction optimization results and implications

The absolute recoveries calculated against the bulk-rock XRF data are within analytical uncertainty (>95 %) for the major elements. Full results for the individual extractions are given in

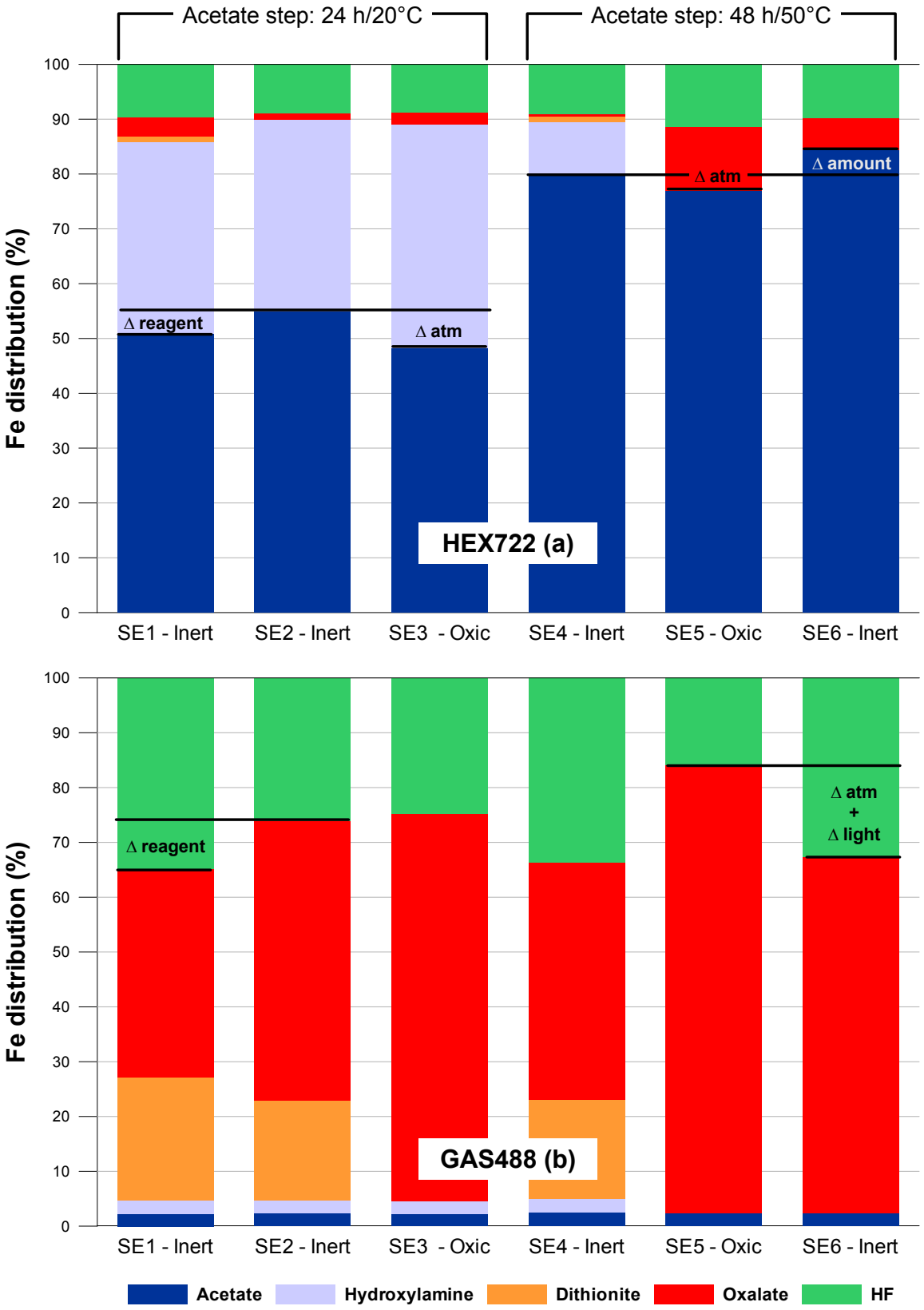

Figure 2.3: Fe distribution for the different tests for the samples HEX722 (a) and GAS488 (b). Δ reagent is the difference between the amount of reagent used (SE1: 5 ml; rest 10 ml), Δ atm is the difference between extraction under inert and oxic atmospheres, Δ amount is the difference between 50 and 30 mg of sample used and Δ light the light and dark conditions. See text for discussion.

the supplementary table (Appendix III). In the following sections we report elemental distributions normalized to total recovery of that specific element, with percentages averaged over the duplicate or triplicate samples.

2.5.1. Acetate-extracted iron

Tests with sample HEX722 (SE1-3) reveal that a 24 hr acetate treatment at room temperature was not sufficient to completely extract carbonate-Fe from carbonate-rich BIF samples. In the absence of ferrihydrite, the measured Fe in the hydroxylamine-step could only be from carried-over carbonate. Based on SE1-SE4, approximately 90 % of the bulk-rock Fe appears to be carbonate-bound (Figure 2.3a). A near complete extraction was achieved with a 48 hr treatment at 50 °C as proposed for crystalline samples by Poulton and Canfield (2005). In these longer duration tests the Fe recovery increased to 80-85 %, but 5-10 % was still transferred to the subsequent step.

To evaluate whether extending the duration further would lead to the full carbonate-bound Fe extraction, the SE-Ac test was performed up to 72 hours (Figure 2.4). This test, under oxic conditions at 50 °C, showed that not only Fe recovery increased to 84 %, but also that more Si was extracted suggesting that silicates were partially digested. Since most samples are not as carbonate-rich as HEX722, a reaction time of 48 hours was adopted to prevent undesirable silicate dissolution. We suggest using smaller sample sizes (30 mg) for carbonate-dominated BIF.

There was a small increase in Fe extracted (max. 5 %) when using an inert atmosphere compared to an oxic one (Figure 2.3a). The optimum acetate extraction adopted in the final protocol (SE_{final}) was thus for 48 hours at 50 °C under an inert atmosphere with sample sizes of 50 mg, which were decreased to 30 mg for carbonate-dominated samples.

2.5.2. Oxalate-extracted iron

The magnetite-rich GAS488-sample was used to optimize the oxalate extraction and test the necessity of the dithionite step. The sample contains negligible amounts of hematite but still approximately 20 % of the extracted Fe was present in the dithionite leach for SE1, 2 and 4. The amount of Fe in the dithionite leach indicated significant magnetite dissolution during the dithionite step. These values were much higher than initially suggested by Poulton and Canfield (2005), but

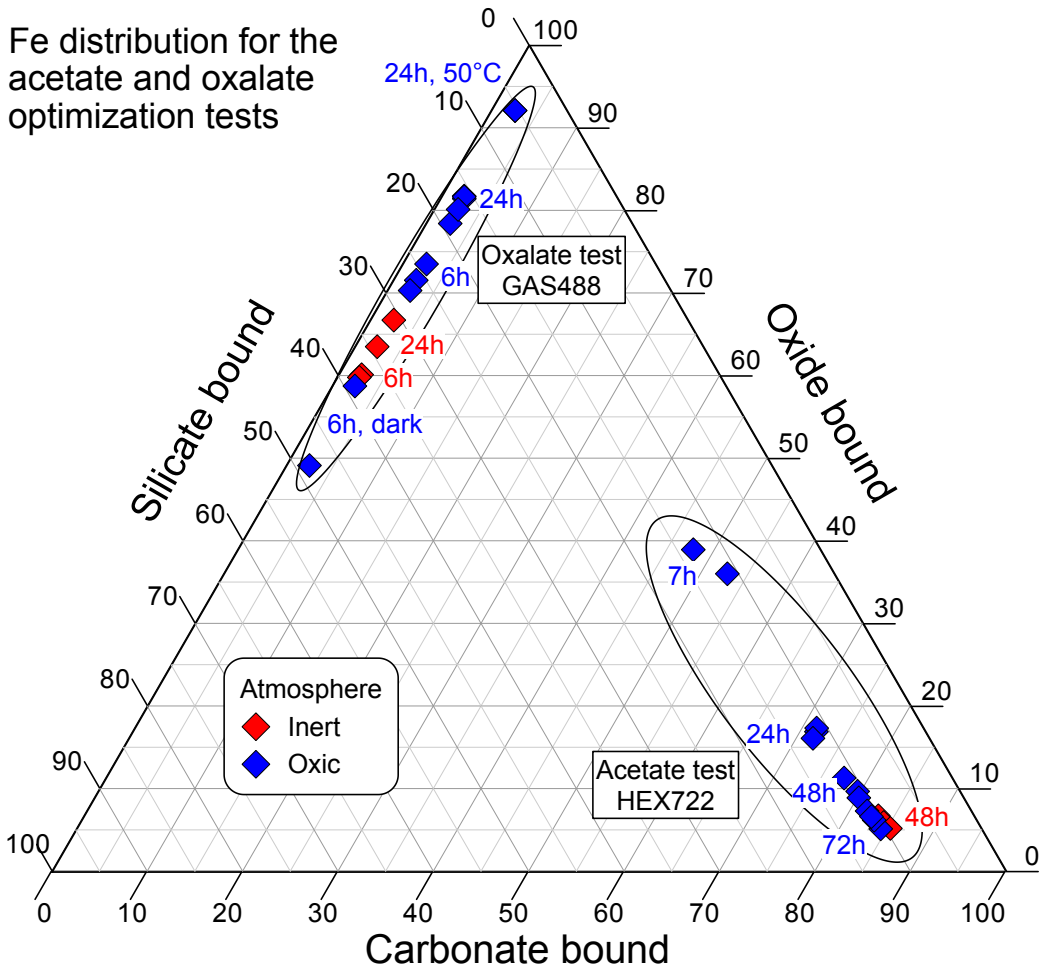

Figure 2.4: Fe distribution (normalized to total Fe extracted) for the SE-Ac and SE-Ox tests. The colors indicate the type of atmosphere and the durations for the extractions are mentioned. The inert samples (48 hr) in the acetate test are the results from SE6. For acetate tests, sample HEX722 was used. GAS488 was used for oxalate tests.

match those found by Henkel, et al. (2016).

The dithionite leach was shown to be unnecessary for magnetite-rich, hematite-poor BIFs, since the total amount of Fe leached by dithionite and oxalate did not exceed that of the oxalate treatment alone (Figure 2.3b). In case a sample contains minor amounts of hematite these will probably dissolve completely, although our oxalate leach was not optimized for hematite dissolution (Taxiarchou, et al., 1997).

The amounts of Fe extracted during the oxalate leach of SE6 was lower than expected based on previous extractions. This extraction took place in the incubator at 30 °C; as a consequence, this extraction took place in darkness whereas the previous extractions were performed in daylight. The effect of light on Fe dissolution was confirmed by the SE-Ox tests (Figure 2.4). The SE-Ox test also revealed that a leaching duration of 24 instead of 6 hours increased the amount of extracted Fe

without increasing the Si concentration. Furthermore, leaching under oxic atmosphere resulted in higher Fe dissolution compared to treatment under inert conditions.

The oxalate extraction at 50 °C increased the recovery from 79 % to 90 % of bulk-rock Fe, but it also almost doubled the amount of Si leached (from 2.5 % to 4.6 % in sample HEX836). Although for magnetite-dominated samples leaching at 50 °C is considered favourable, the silicate leaching poses a dilemma for samples of mixed mineralogy. There was no clear cut extraction possible, so in the final protocol (SE_{final}) the sample size was reduced to approximately 30 mg for samples with more than 40 wt% Fe (i.e. magnetite-rich samples) to achieve more complete dissolution at room temperature. Based on these results, I suggest that optimal extraction of the oxides in magnetite-dominated BIF samples should be performed at daylight, room temperature and under oxic conditions for 24 hours.

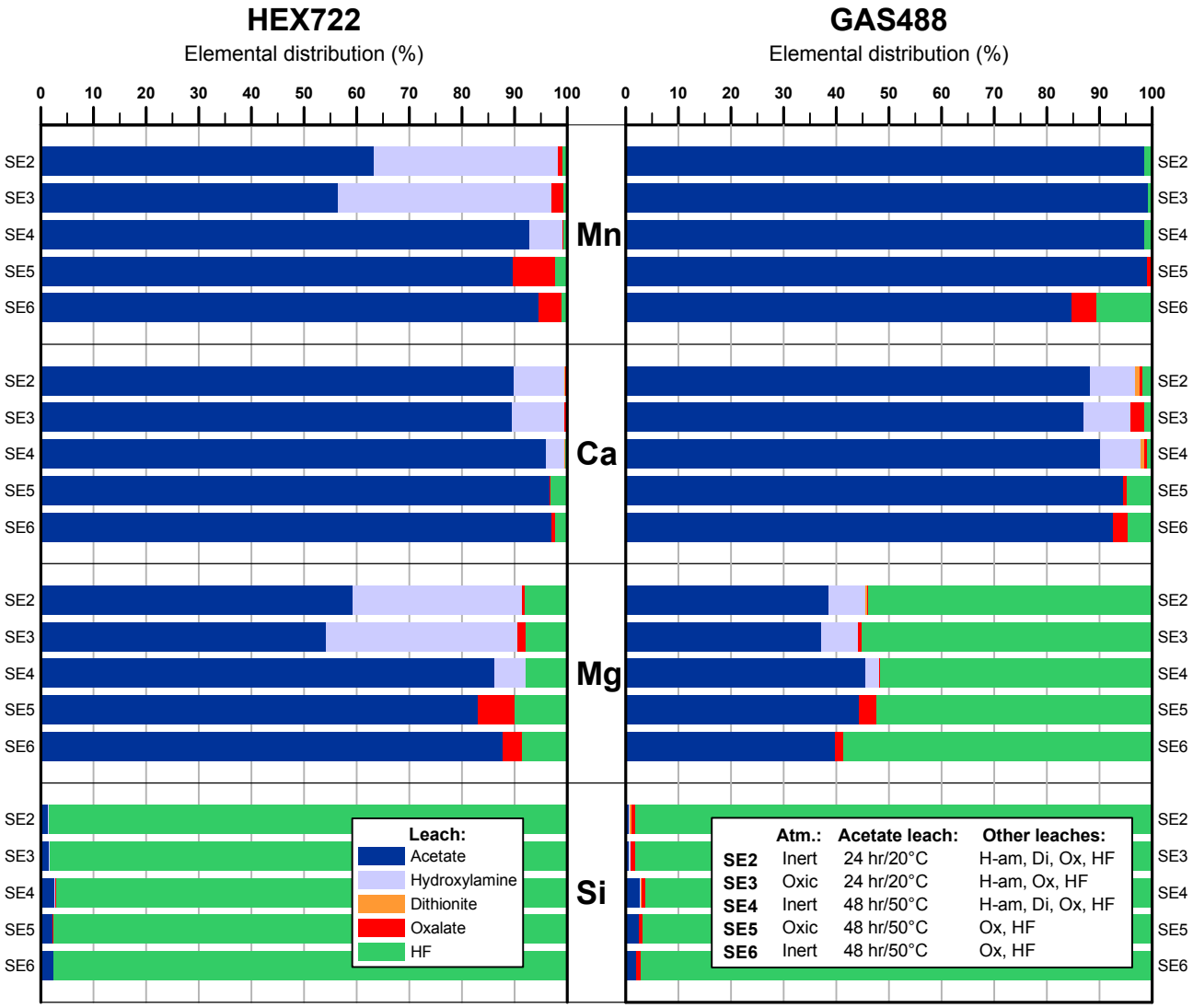

Figure 2.5: Elemental distribution among the five fractions for the different tests (averaged over triplicate samples), as percentages of total extracted. Silicon is quantitatively lost during HF-evaporation, so percentages based on bulk-rock values.

2.5.3. Distribution of major elements

Various other major elements could be used in addition to Fe to help assessing the quality of the different extractions (Figure 2.5). Based on the different BIF minerals, the only ones which incorporate Ca are the carbonates; ankerite, calcite and, to a lesser extent, siderite (Gole, 1980; Klein, 1974; Pecoits, et al., 2009). Manganese has been shown to be incorporated into the carbonate fraction in the Asbestos Hills BIF (Johnson, et al., 2013), although minor amounts can also be present in stilpnomelane (Klein, 1974; Gole, 1980). The percentages of these elements increase with the extended duration and temperatures of the acetate step, similar to that of iron discussed above, indicating improved carbonate dissolution during the longer leaches. Magnesium is distributed between the carbonate and silicate minerals, depending on the mineralogy. For the carbonate-rich HEX722 sample, only a small part is hosted in the silicates (8-10 %). The decrease of Mg present in the leaches following the acetate step from 35 % to 6 % confirms that the 48 hr acetate extraction at 50 °C was more suitable than the shorter extraction to dissolve the carbonates quantitatively.

Ideally, Si should only be present in the HF step. However, during the HF treatment Si was lost as gaseous silica-tetrafluoride complexes and thus could not be measured. Subtraction of the measured Si in the other steps from the bulk-rock XRF value shows >96 % of the Si to be present in the HF step (Figure 2.5), implying that the silicates were practically unaffected by preceding reagents. This is confirmed by the virtual absence of Mg in the oxalate step of the magnetite-rich GAS488. The small amount of Mg in the carbonate-rich HEX722 can be explained by incomplete carbonate dissolution (see 2.5.1).

2.6. Species-specific Fe isotopes for BIF samples

The optimized extraction protocol outlined above was applied to the 3 selected BIF samples (SE_{final}), GAS488 (n=9), HEX836 (n=9) and HEX722 (n=1), with ca. 30 mg for the 2 single fraction-dominated samples and ca. 50 mg for the HEX836 duplicates. The acetate extraction was performed for 48 hours at 50 °C under inert conditions, followed by the 24 hour oxic oxalate extraction and the digestion of the residue with HF-$HClO_4$-HNO_3. The resulting Fe-distributions are shown in Figure 2.6. The GAS488-samples plot in the same area as during tests SE1-6, whereas the carbonate-rich

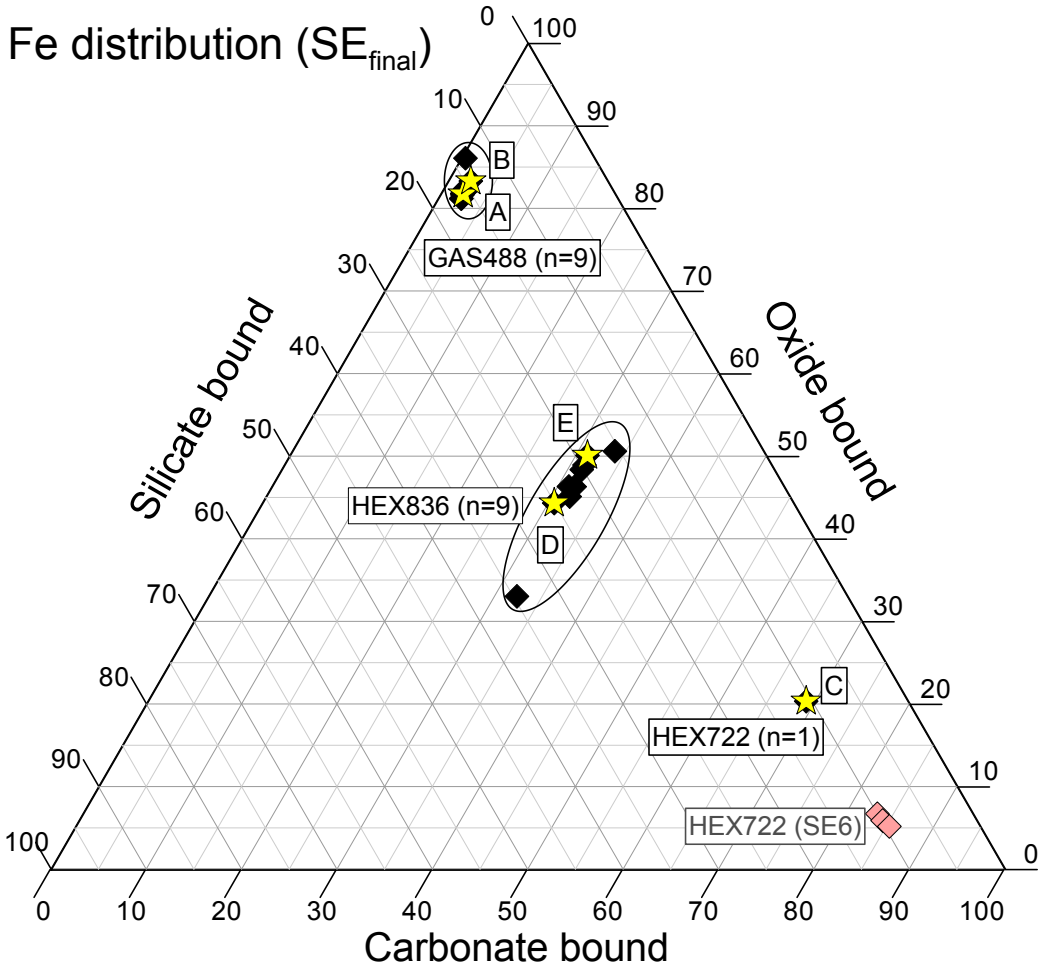

Figure 2.6: Fe distribution (normalized to total Fe extracted) for the SEfinal. To illustrate the offset of HEX722, the HEX722 values of SE6 are included as well. The yellow stars (A-E) represent the samples which were used to analyse fraction specific Fe-isotopes.

HEX722 shows an offset from the expected values for the carbonate-bound Fe based on SE-Ac (70 % instead of 85 %). This offset cannot be explained by the recovery values (100.4 %). A direct explanation is also missing for the single outlying HEX836 sample (33 % instead of 48 % oxide bound Fe). Sample heterogeneity is unlikely due to the fine grain size of the powder and the fact that the other duplicates plot in the same area. The summed fractional abundances for the major elements of all samples lie above 95 % of their bulk-rock values.

Of the 19 extracted samples, 5 were selected for species-specific Fe-isotopes following the protocol of Henkel, et al. (2016). The 5 selected were two from the samples GAS488 (A-B) and HEX836 (D-E) and the single one from HEX722 (C), each consisting of the three fractions (i.e. acetate, oxalate and HF). The Fe yields of the leachate destruction and Fe purification processing combined have an average of 98.5 %, with lower values (93 %) for the oxalate processing and >100 % for

Table 2.5: Sequentially extracted Fe isotopes and the respective Fe distribution.

Sample	GAS488		HEX722		HEX836		
Fe Distribution (%)							
Acetate	2.4	2.4	69.5		30.7		31.3
Oxalate	81.8	83.8	20.6		44.6		50.4
HF	15.9	13.8	9.8		24.7		18.3
Fe Isotopes (‰):							
Solution series	A	A	B	C	C	D	D	E
Lab	Potsdam	Durham	Durham	Potsdam	Durham	Potsdam	Durham	Durham
δ^{56}Fe Ac.	-0.43	-0.47	-0.39	-1.77	-1.76	-1.22	-1.25	-1.23
δ^{56}Fe Ox.	0.44	0.38	0.51	-2.07	-2.03	0.17	0.15	-0.11
δ^{56}Fe HF	0.54	0.48	-0.56	-2.01	-1.70	-1.52	-1.69	-0.99
δ^{56}Fe Calc.	0.43	0.38	0.34	-1.86	-1.81	-0.67	-0.74	-0.62
δ^{56}Fe B.R.	0.42			-1.77		-0.60		

Ac., Ox., HF., Calc and B.R. are the acetate, oxalate, HF, calculated and bulk-rock values (the latter presented in section 2.2). Typical uncertainties for measurements are 0.1 ‰. The Fe-distribution is normalized to the total extracted, so uncertainties are difficult to quantify, for an indication see the difference in the replicate samples (Figure 2.6).

the acetate samples. These yields were calculated from ICP-OES results of the extractions and the solutions as prepared for isotopic analyses. The low values for the oxalate can be explained by matrix suppression on the ICP-OES and/or material loss during the thermal degradation of oxalate.

All fractions of solutions series (A-E) were measured at Durham University and a selection (A, C, D) were repeated (same solution) for inter-laboratory comparison at "Helmholtz Laboratory for the Geochemistry of the Earth Surface'' at GFZ Potsdam. The SCP-Fe solutions and the certified reference materials used to monitor the post-extraction processing and column purification, respectively, were all within the typical uncertainty of 0.1 ‰ (Table 2.4). The isotope results of the sequentially extracted samples are shown in Table 2.5. Based on the Fe-distribution of each sample respective bulk-rock values could be calculated. These values are all within uncertainty of the measured bulk-rock values.

There are some discrepancies between duplicate HF-fractions. For both GAS488 and HEX836 the HF-solutions with the lower percentage of Fe (B, E) have more negative δ^{56}Fe values then their more Fe-rich duplicates (A, D; Table 2.5). The only discrepancy between solutions measured in both labs is the HF fraction of sample C (HEX722), there is no apparent reason for this. Re-measurement of this solution in Durham yielded a value of -1.66 ± 0.1 ‰.

2.7. Discussion

2.7.1. Limitations of the sequential extraction technique

The most critical aspect of any sequential extraction scheme is the complete dissolution of the targeted mineral fraction, leaving the other fractions unaffected. Using the single-mineral dominated samples, the different extraction combinations outlined above were setup to test the boundary conditions of each leach. Incomplete extraction for these samples is undesired, but almost unavoidable since increasing target fraction recoveries also increased the dissolution of neighbouring fractions. Consequently, a sequential extraction applied to samples dominated by a specific mineral group will almost always lead to contamination of the step following the dominated target fraction.

2.7.1.1. Acetate extraction

An explanation for incomplete iron recoveries by acetate might be the re-precipitation of Fe-(hydr)oxides during the leach. Precipitation is enhanced by the presence of oxygen, since the soluble ferrous iron oxidizes to insoluble ferric iron. The latter precipitates would consequently be transferred to the next extraction step. The Fe-concentrations of the inert extractions were indeed slightly higher than their oxic counterparts (Figure 2.3), indicating re-precipitation. Precipitation of ferric Fe-(hydr)-oxides is thermodynamically favourable, as supported by PHREEQC calculations. Despite this, no visual evidence for precipitation was observed.

For carbonate-rich samples or crystalline carbonate minerals, the acetate extraction might not quantitatively dissolve all Fe-carbonates (Reinhard, et al., 2009). A 24 hr, 10 % HCl extraction at room temperature should quantitatively extract all the microcrystalline siderite and ankerite (Raiswell, et al., 1994; 2011). However, this method also extracts several percent of the silicate and magnetite bound iron (Raiswell, et al., 1994) and was therefore considered unsuitable for Fe-oxide-rich BIF samples. Sample HEX722 is an exceptionally carbonate-rich sample and most bulk-rock BIF samples have lower modal carbonate abundances. Therefore, we prefer the acetate leach since it leaves the oxide and silicate fractions intact. However, this means that for carbonate-rich samples, the Fe concentration in the step succeeding the acetate might be overestimated, due to transfer of

undissolved/re-precipitated carbonate-bound iron. Another option could have been to repeat the extraction step for the carbonate-rich samples and combining the extracts. For consistency with the others we preferred a decrease in sample size of the carbonate-dominated samples.

2.7.1.2. Oxalate extraction

The dissolution of oxides in oxalate depends for major part on the pH and temperature of the solution (Taxiarchou, et al., 1997; 1998). We worked with a constant pH (3.7) following the original protocol (Poulton and Canfield, 2005), which is slightly above the optimum of 3 suggested by (Taxiarchou, et al., 1997; 1998). For the increased temperature experiments, the amount of Fe dissolved was higher, but as noted earlier unwelcome silicate dissolution was observed.

The combined total Fe dissolved in the dithionite and oxalate extractions (i.e. SE1, 2 and 4) was generally lower than their counterparts which excluded the dithionite step (SE3, 5, and 6; Figure 2.3). This might be explained by promotion of Fe oxide dissolution in oxalate in the presence of $Fe^{2+}_{(aq)}$ (Suter, et al., 1988; Panias, et al., 1996; Taxiarchou, et al., 1997). If a part of the oxides was already removed by dithionite leaching, the reaction during oxalate treatment might not have been catalysed and, accordingly, the magnetite dissolution may have been incomplete for those extractions.

For the dissolution of hematite in oxalate the atmosphere is important (Taxiarchou, et al., 1997) since $Fe^{2+}_{(aq)}$ needs to be present to catalyse the reaction. The dissolution of hematite is therefore enhanced by an inert atmosphere (Taxiarchou, et al., 1997). For magnetite it might be less important, since ferrous iron is present in the structure and can be used from there (Taxiarchou, et al., 1997; 1998).

2.7.2. Species-specific Fe-isotopes

2.7.2.1. General trends

If Fe dissolution is incomplete during leaching of a specific fraction, it may be transferred to the subsequent fraction. This might lead to flawed values for both fractions, as follows: 1) if the dissolution is not congruent, isotopic fractionations occur and thereby the results of the initial fraction are compromised, and 2) the transferred Fe contaminates the subsequent fraction to be extracted. In

this study, we tested the capabilities of the different extractions and ultimately optimized those using largely single-mineral-dominated samples. For the carbonate test sample (HEX722, C) it becomes apparent that, when looking at the Fe-distribution of the sample used for Fe-isotopes (Figure 2.6), not all carbonate-bound Fe was extracted during the acetate leach. This resulted in the subsequent oxalate-leach being contaminated by carbonate-bound Fe, thereby explaining its low δ^{56}Fe values of -2.03 ‰. However, these values were lower than the measured ones for the acetate-bound Fe (-1.70 ‰), which based on the other samples and anticipated from the literature (Johnson, et al., 2008a; Frost, et al., 2007) should have shown the opposite. This not only implies that the oxalate fraction is contaminated, but also that the acetate extraction fractionated the carbonate-bound Fe, whereby lighter Fe was preferentially transferred to the subsequent step. Based on these results, I cannot conclude whether this fractionation was due to incongruent dissolution or preferential re-precipitation of lighter Fe-hydroxides during the extraction. However, as previously stated this would only apply to extremely carbonate-rich samples.

2.7.2.2. Duplicate discrepancies

The δ^{56}Fe values of the HF-fraction of sample GAS488 (A) were positive and similar to the isotopic value of the oxalate fraction. The duplicate (B), however, had a significantly lower δ^{56}Fe value (Table 2.5, Figure 2.7). The only published δ^{56}Fe-data available of BIF Fe-silicates is for greenalite,

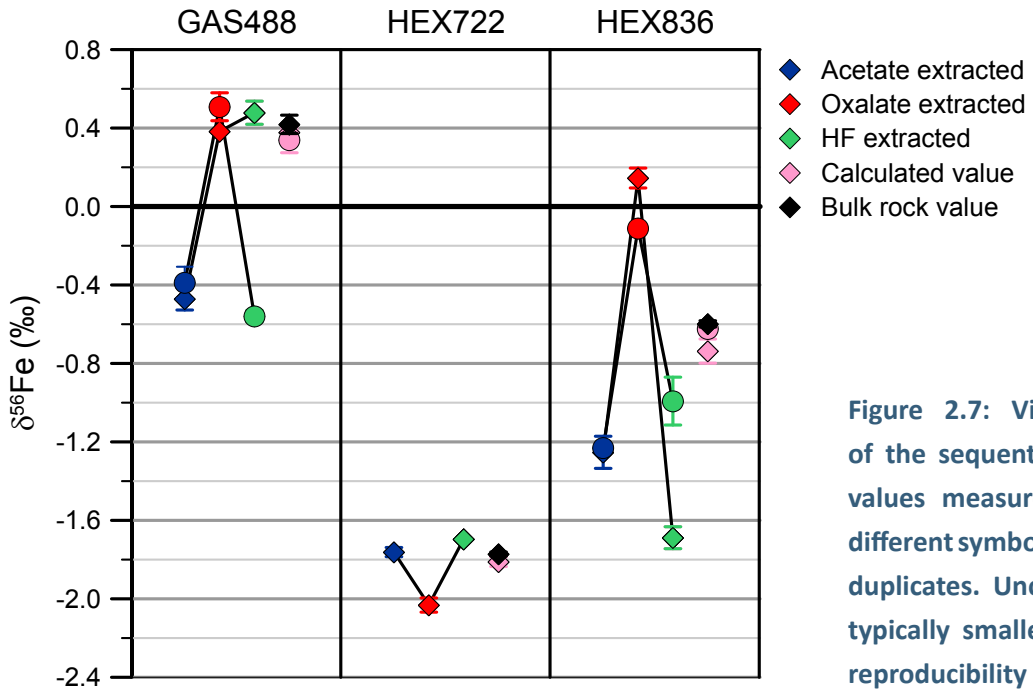

Figure 2.7: Visual representation of the sequentially extracted δ^{56}Fe values measured in Durham. The different symbols are the full process duplicates. Uncertainties (2SD) are typically smaller than the external reproducibility of 0.1 ‰.

which shows lighter Fe isotopic values (-0.1 ‰) compared to coexisting magnetite (0.7 ‰, Frost, et al., 2007). Based on microscopy, the silicates in this sample are riebeckite and stilpnomelane and not greenalite, but if those Fe-silicates formed diagenetically from greenalite (Rasmussen, et al., 2013; 2015b) they could still exhibit the original isotopic values. This would indicate, combined with the Fe-distribution, that the magnetite dissolution of this very magnetite-rich sample was incomplete during the first leach (A).

When assuming the B-series as end-member, it is possible to calculate the δ^{56}Fe value of the magnetite transferred to the silicate fraction in A. The difference between the two GAS488 samples in terms of percentage of Fe-extracted in the oxalate fraction was approximately 2.0 % (81.8 % for A vs. 83.8 % for B; Figure 2.6, Table 2.5). This final two percent would have to be substantially heavier in δ^{56}Fe (5-7 ‰) in order to explain the discrepancies for the oxide and silicate fractions. Incongruent dissolution of Fe-oxides (goethite) in oxalate has been demonstrated (Wiederhold, et al., 2006). Here, the δ^{56}Fe values of the dissolved phase increased with increasing leaching time, meaning that the isotopically lighter Fe was preferentially dissolved. The larger fractionation we calculated here however, seems out of that range.

Variation in the Fe-distribution was also present for duplicate sample HEX836. Similar to GAS488, the main discrepancy between the duplicates could be explained by the percentage of Fe extracted during the oxalate leach. This is also reflected in the variation of δ^{56}Fe for the HF-fraction, albeit not as extreme as for GAS488 (Figure 2.7).

2.7.3. Optimum sampling of BIF

BIF consists of a fine-grained mixture of the three Fe-bearing fractions we identified above, which are difficult to mechanically separate. This especially applies to microbanded BIF, which is a common facies in the Archean and Paleoproterozoic (Klein, 2005; Beukes and Klein, 1990). Fine-grain size often makes it difficult to estimate the relative abundances of the carbonate-, oxide- and silicate-bound iron. The proposed sequential extraction scheme here is less informative for samples dominated by a single mineral fraction. To avoid these samples in future work, bulk-rock samples should consist of multiple, mineralogically distinct bands that typically requires an increase in the sample size.

2.8. Conclusions

In this study, I evaluated and adapted an existing sequential extraction procedure for sulfur-poor banded iron formation samples. The adaptation was needed for two key reasons: to optimize for the very high FeO-content in BIF samples (well over 50 wt% in many instances) and to reduce the number of different fractions in the original scheme (Poulton and Canfield, 2005) to only the three key mineralogical fractions pertinent to BIF, in order to facilitate lab-work and machine-time for species-specific Fe-isotope measurements.

The final extraction scheme consists of three steps. Firstly, the micro-crystalline Fe-carbonates were dissolved in a pH 4.5 buffered 1.0 M Na-acetate solution, under inert conditions at 50 °C in a shaking incubator for 48 hours. Then, the Fe-oxides were digested using a 0.2 M ammonium oxalate/0.17 M oxalic acid solution for 24 hours at room temperature, under oxic and illuminated conditions. The final silicate residue was digested using a standard HF-digestion protocol.

Although optimized for BIF samples, no clear-cut sequential extraction was achieved. A balance was therefore sought between incomplete extraction and undesirable cross-dissolution of subsequent fractions. For the final scheme, the elemental recoveries were good and the distribution of major elements (e.g. Mn, Ca, Mg and Si) showed no significant cross-contaminations. However, full dissolution of siderite or magnetite was impossible to check, since these fractions essentially contain only Fe and the Fe-distribution is the major unknown.

To determine species-specific Fe-isotopes, the organic leachates needed to be broken down to avoid matrix-effects. The protocol designed by Henkel, et al. (2016) was for the first time successfully applied to BIFs. Corresponding δ^{56}Fe values were reproduced in multiple labs. In all cases, the calculated bulk-rock values based on the Fe-distribution matched, within uncertainty, the measured bulk-rock value. As expected by Johnson, et al. (2008a; 2008b), the Fe-isotope composition of the carbonate fraction was generally much lighter than the oxide fraction and broadly similar to the silicate one.

For samples dominated by a single mineralogical group, the species-specific isotopic values should be treated cautiously since the uncertainties for the small fractions are large, due to possible contamination by and/or incomplete dissolution of the dominant phase. However, the main fraction will invariably be close to the bulk-rock value, so in these cases a bulk-rock approach is a valid

alternative.

BIF precipitation is intrinsically linked to the redox evolution of the oceans and atmosphere. Therefore, application of the adapted protocol presented in this paper on larger stratigraphic scales of BIF occurrence, accompanied by careful interpretation of mineral-specific $\delta^{56}Fe$ distributions across space and time, have great potential in interrogating further the behaviour of iron isotopes during primary BIF deposition, and ultimately in constraining better the redox-conditions in the Paleoproterozoic oceans.

“Audentes Fortuna iuvat“

(Fortune favours the bold)

Virgil, *Aeneid; Book X,* 29-19 BC.

3

TRANSITION METALS

Abstract

Superior-type banded iron formations (BIFs) represent an important repository of marine chemical sediments which precipitated immediately prior to, and during the onset of the Great Oxidation Event (GOE). Transition metal abundances and their isotopic ratios have been widely used in BIF as proxies to constrain redox conditions in the depositional near-surface environment. To date, most geochemical proxies have been applied to bulk-rock BIF samples, where variable mineralogy potentially has a strong influence on geochemistry. Among the most frequently used geochemical proxies in BIF are U, Mo and Cr. In contrast to the other redox proxies, mono-isotopic Mn, the most abundant transition metal in BIFs after Fe, has received relatively little attention.

In this study, a three-step sequential extraction technique was applied to 106 samples from the Kuruman and Griquatown BIFs to determine transition element speciation over carbonate, oxide and silicate fractions. The accuracy of the extraction technique was verified by using 1) the elemental recoveries, 2) comparison of major and trace element distributions to expected mineralogy, and 3) by comparison to results from micro-analytical techniques. Uranium is predominantly bound to the silicate fraction and shows clear correlations with Zr and Sc implying detrital reworking and hence anoxic conditions. Molybdenum abundances in the Kuruman and Griquatown BIF are low and show an apparent correlation with mineralogical variability, as determined by the sequential extraction. This suggests that changes in bulk-rock mineralogy, rather than redox chemistry might significantly affect $\delta^{98/95}$Mo. For Cr a minor bulk-rock stratigraphic increase can be related to the oxide and silicate fraction. However, a positive relationship with Zr indicates that this was also controlled by detrital or volcanic ash input.

Manganese is solely bound to the carbonates and increases in abundance on going upwards through the stratigraphy. The absence of Ce anomalies indicates Mn(II) incorporation in primary carbonate minerals in a basin which became more manganiferous over time. There are no indicators for an active Mn-redox cycle, signifying that the surface waters remained reducing with respect to Mn in these BIFs precipitated immediately prior to the GOE.

3.1. Introduction

The deposition of banded iron formations (BIF) is intrinsically linked to the oxygenation of the Earth's near-surface environments (e.g. Bekker, et al., 2010), although the precise details of this complex relationship remain poorly understood. Small localized Algoma-type BIF deposition spans 2 Gyr from 3.8 to 1.8 Ga (e.g. Klein, 2005), the large laterally extensive Superior-type BIF deposition culminated around the Great Oxidation Event (GOE) at ca. 2.4 Ga. As chemical precipitates, BIFs can be used to reconstruct the composition of the oceans and atmosphere, using a variety of different techniques, proxies and models. Amongst these proxies are elemental abundances of various transitional metals and their stable isotope ratios.

By definition a transition metal is "*an element whose atom has a partially filled d sub-shell, or which can give rise to cations with an incomplete d sub-shell*" (McNaught and Wilkinson, 1997). This means that the entire "d-block" (groups 3-12) on the periodic table is included. In this chapter I will focus on the most common transition metals Sc, Ti, V, Cr, Mn, Co, Ni, Cu, Zn, Zr, Mo and U. Iron will be discussed in detail in Chapter 5, whereas the lanthanide series and Y will be discussed in Chapter 4.

Atmospheric oxygen is predominantly produced by oxygenic photosynthesis (e.g. Lyons, et al., 2014), however the timing of its onset and the relationship with the GOE remain enigmatic (e.g. Buick, 2008). Various redox-sensitive isotope systems have been used to argue for an early onset of oxygenic photosynthesis and include Mo-isotopes (e.g. Planavsky, et al., 2014), Fe-isotopes (e.g. Dauphas, et al., 2004) and Cr-isotopes (Crowe, et al., 2013). Based on decreasing molar Ni/Fe ratios in BIF samples through time, Konhauser, et al. (2009) have proposed that methanogens suffered from declining volcanic Ni-input in seawater, so facilitating the rise of photosynthetic bacteria.

The only direct proxy to put a constraint on Archean atmospheric O_2 concentrations has been the disappearance of mass-independent fractionation of S-isotopes (Farquhar and Wing, 2003). Beyond this, the GOE has been recorded in the Mo abundance and Cu-isotope record in marine black shales (Kendall, et al., 2010; Chi Fru, et al., 2016), the Zn/Fe ratio of marine carbonates (Liu, et al., 2016) and Co abundance in marine sediments (Swanner, et al., 2014). As a consequence of atmospheric oxygenation, the weathering patterns changed and oxidative weathering commenced. Proxies for oxidative weathering in the Archean include U concentrations in BIF (Partin, et al., 2013) and Cr-isotopes (Frei, et al., 2009).

One drawback of these techniques is that they generally rely on bulk-rock samples which have varying modal mineralogies, making them difficult to compare directly, or are selectively sampled/microdrilled in order to control the mineralogy. With the exception of S and Fe none of the aforementioned isotope ratios have been measured by micro-analytical techniques. For example, Fe isotopic fractionation occurs between different mineral species in BIF (e.g. Johnson, et al., 2003) and preliminary data indicate that this might also be the case for Mo (Thoby, et al., 2016).

As well as their role as redox-indicators, various other transition elements have been utilized to determine the input of allochtonous material, either detrital or volcanic ash. These trace elements are immobile in aqueous solutions and therefore can be used to represent clastic input. Commonly used elements to check for clastic-contaminated BIF samples are Sc, Ti, and Zr (e.g. Bau, 1993; Pecoits, et al., 2009).

In this chapter, I apply the sequential extraction technique outlined in the previous chapter to all 106 samples taken from the four different drill cores used in this study (Chapter 1). After briefly discussing the major element distribution, the focus of this chapter will shift to the transition metals and their speciation. Although the transition metal isotope ratios are not explored here, their speciation will give insight into the applicability of bulk-rock techniques for the stable isotope analysis of BIF-samples.

3.2. Methods

The granular Griquatown and rhythmically microbanded Kuruman IF were deposited immediately before the GOE around 2.4 Ga (Pickard, 2003). Based upon sedimentological features the Kuruman IF was deposited on an open-shelf environment below the wave base, whereas the Griquatown Formation was deposited in a shallower environment (Beukes, 1984). The BIF deposition is interspersed with stilpnomelane lutite bands, which are considered to represent ash layers (Beukes, 1984). These iron formations were sampled from four drill-cores: Gasesa-1, HEX-5, Erin-3 and Aarpan-5 (for sampling locations, core logs and regional geology see Chapter 1). Samples were taken every 10-15 m core depth and consisted of 5-15 cm quarter-core fragments, capturing the diversity of BIF in a total of 106 samples.

Of every sample a thin section was prepared, and the remnant was powdered. Major element

chemistry of the bulk powdered sampled was resolved using XRF, following the method of Norrish and Hutton (1969) at Rhodes University. Bulk-rock C and S were measured on a LECO CS-300 analyser and the minor and trace element chemistry was determined with a Thermo Scientific X-Series 2 ICP-MS after a standard bulk-rock digestion procedure using HF-HNO_3-$HClO_4$ at Utrecht University.

Chemical separation of the samples was done in batches of 17-18 samples including one blank, two monitoring (GAS488 and HEX836) and two duplicate samples and following a sequential extraction procedure described in detail elsewhere (Chapter 2). In summary, 30-50 mg of sample was transferred into a 15 ml Greiner© tube. Each extraction step used 10 ml of reagent, and after each step the sample was centrifuged and the supernatant filtered (0.2 µm). The extraction was started with 1 M Suprapur® Na-acetate (pH adjusted with acetic acid to 4.5) under an inert N_2-atmosphere and allowed to react for 48 hours at 50 °C in a shaking incubator. The acetate step targeted the carbonates, and at this duration and temperature the crystalline siderite present should have been extracted quantitatively (Chapter 2, Poulton and Canfield, 2005). The next step was the 0.2 M NH_4-oxalate (Normapur®)/0.17 M oxalic acid (Extra pure) extraction for 24 hours, to dissolve the magnetite and minor amounts of hematite present. The final residue was transferred to a PFA-vial (Savillex, USA) for total digestion using HF-HNO_3-$HClO_4$, targeting the silicate minerals.

Major and minor elements were determined using a Spectro Arcos ICP-OES and trace elements using a Thermo Scientific X-series 2 ICP-MS at Utrecht University. For ICP-MS analysis the samples were standardized using a 10 ppb In-spike and run-quality (QC) and drift were monitored every 6 samples. The low trace element concentrations encountered in BIF forced the use of a lower than optimum dilution factor (10x instead of 50x). To counteract any matrix effects and the low dilution factor both the standards and the independent QC were prepared 3 times to match either the acetate, oxalate and HNO_3 (after HF-extraction) matrix of the samples. Because the measured concentrations ranged over several orders of magnitude, the calibration curves were weighted (weighing factors of 1/concentration) to increase accuracy close to the detection limit. Blank values were negligible and below the detection limit for most elements. However for some transition metals (e.g. Cr, Zn, Cu and to a lesser extent Ni) the average blank values were anomalous for the acetate extraction, indicating reagent contamination, calibration or interference problems. Various transition metals (incl. Cr) are difficult to measure on ICP-MS due to spectroscopic-interferences (Jarvis, et al., 1992) and others

are prone to contamination in reagents or lab-environments (e.g. Zn). The average blank values for Cr, Zn, Cu and Ni could represent up to 30 % of the average measured concentration (1-2 ppb range) in the samples. Furthermore, blank values for these elements varied unpredictably within a run. To account for this, fraction-average blank corrections were applied for all elements.

The results for the sequential extractions were compared to mineralogical data determined by two *in situ* techniques, electron microprobe (EMP) and laser ablation inductively coupled plasma mass spectrometry (LA-ICP-MS). The EMP focussed mainly on the the major element composition of different carbonate minerals of the ERIN-core (Rafuza, 2015). EMP analyses were performed at the University of Cape Town on a JEOL JXA 8320 Superprobe, using 4 wave-dispersive spectrometers and a beam spot size smaller than 1 µm. LA-ICP-MS was performed at Utrecht University with a 193 nm wavelength COMPex 102 ArF excimer laser ablation system (Lambda Physik, Göttingen, Germany) connected to an Element 2 sector field ICP-MS (Thermo Scientific, Bremen, Germany). The ICP-MS was operated in low resolution mode, and the laser with an energy density of 10 J/cm^2 and a pulse repetition rate of 10 Hz. The laser crater diameter (80 µm) was relatively large but was optimized to give low detection limits and high analytical precision. Data reduction of laser ablation data was performed using the GLITTER software.

The goal of this study was to compare sequential extraction data for samples with highly contrasting mineralogies, for which a normalization factor was required. For the acetate fraction the major elements were converted to oxides (all Fe was assumed to be ferrous iron) and summed together with the bulk-rock carbon as CO_2 in wt%. Normalizing to 100% enabled the comparison of carbonate-poor and carbonate-rich samples as well as mineral-specific literature data. A similar strategy was applied to the oxide fraction, with all Fe assumed to be hosted in magnetite (Fe_3O_4). The remaining portion was the silicate fraction, which could not be calculated directly since Na_2O (carbonate extraction in Na-acetate) and H_2O were not measured and the oxidation state of Fe potentially varied. A complication for the silicate fraction was that all samples contained chert, with the result that the other minerals in the fraction were 'diluted' in various amounts with SiO_2. Fractions which were below 10 wt% of the total suffered from high degrees of uncertainty, since their measured trace element values were generally at or near the detection limit and the multiplication factor was high. These samples were not used further for interpretation.

3.3. RESULTS

For the full data tables the reader is referred to Appendix IV: bulk-rock and sequentially extracted data and Appendix V: LA-ICP-MS data.

3.3.1. Bulk-rock data

The SiO_2 concentrations in the Griquatown and Kuruman banded iron formations ranged from 19.9 to 78.8 wt%. SiO_2 anti-correlates (R^2= 0.43) with iron (FeO= 9.1-52.9 wt%). No other correlations were present between any of the major element oxides. The relative abundance of the carbonate fraction was inferred from the bulk-rock CO_2 values which varied between 0.2 and 30.4 wt%. The remaining major element oxides were all below 7.6 wt% except for CaO with values up to 15.6 wt% (Figure 3.1). The BIFs sampled here were found to be sulfur-poor with values below 0.9 wt% except one sample, ERIN637, with 3.7 wt% S. All these results are in line with those previously published for the bulk-rock Kuruman and Griquatown IF samples (Beukes, 1984; Beukes and Klein, 1990; Horstmann and Hälbich, 1995).

The average bulk-rock Mn concentration showed stratigraphically-resolved increases upwards from ca. 0.2 wt% in the Kuruman IF to 0.6 wt% in the Griquatown Formation (Table 3.1). This is consistent with the stratigrapichal increase in average MnO content based on the data of Horstmann

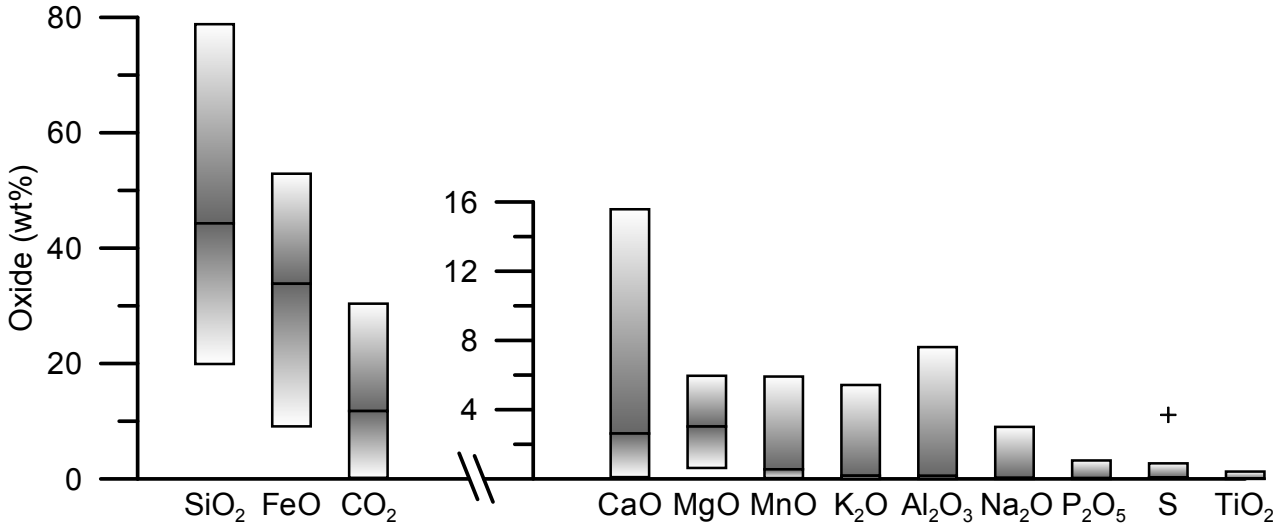

Figure 3.1: Bulk-rock oxide ranges and median values of the 106 BIF samples. Note the two different vertical scales. All Fe was converted to FeO. A single sample (ERIN637) contains 3.5 wt% S whereas the remaining contained <0.9 wt% S.

Table 3.1: Average bulk-rock transition metal concentrations for all samples and the mean Griquatown (incl. lutites; n=74) and mean Kuruman (n=32) subsets in ppm (except Mn* in wt%). The lower part shows the interelement correlations (R^2) of all samples in color codes.

	Sc	Ti	V	Cr	Mn*	Co	Ni	Cu	Zn	Y	Zr	Mo	U
Average	0.8	193.	9.9	18.1	0.5	1.8	7.2	7.0	7.2	4.0	7.1	0.8	0.13
Average Gri.	1.0	260.	11.2	19.8	0.6	2.1	7.9	7.6	6.6	3.8	9.0	0.8	0.18
Average Kur.	0.5	52.	7.1	14.4	0.2	1.2	5.5	6.0	8.6	4.6	3.1	0.9	0.05
Sc		0.97	0.93	0.65	0.02	0.90	0.84	0.57	0.38	0.26	0.90	0.00	0.92
Ti	0.97		0.91	0.70	0.02	0.91	0.82	0.62	0.31	0.21	0.94	0.00	0.95
V	0.93	0.91		0.77	0.01	0.87	0.91	0.68	0.39	0.23	0.84	0.03	0.86
Cr	0.65	0.70	0.77		0.00	0.69	0.81	0.80	0.22	0.04	0.66	0.24	0.68
Mn	0.02	0.02	0.01	0.00		0.02	0.00	0.00	0.00	0.03	0.01	0.11	0.01
Co	0.90	0.91	0.87	0.69	0.02		0.84	0.69	0.33	0.20	0.88	0.00	0.89
Ni	0.84	0.82	0.91	0.81	0.00	0.84		0.73	0.38	0.17	0.79	0.06	0.78
Cu	0.57	0.62	0.68	0.80	0.00	0.69	0.73		0.22	0.07	0.67	0.20	0.62
Zn	0.38	0.31	0.39	0.22	0.00	0.33	0.38	0.22		0.41	0.32	0.00	0.31
Y	0.26	0.21	0.23	0.04	0.03	0.20	0.17	0.07	0.41		0.22	0.08	0.21
Zr	0.90	0.94	0.84	0.66	0.01	0.88	0.79	0.67	0.32	0.22		0.00	0.95
Mo	0.00	0.00	0.03	0.24	0.11	0.00	0.06	0.20	0.00	0.08	0.00		0.00
U	0.92	0.95	0.86	0.68	0.01	0.89	0.78	0.62	0.31	0.21	0.95	0.00	

and Hälbich (1995). Carbonate-rich samples near the top of the Griquatown Formation were found to contain up to 2.6 wt% Mn. The majority of Mn is bound to carbonates in BIF (Johnson, et al., 2013; Rafuza, 2015; Alibert, 2016) so the relative abundance of carbonate minerals has a strong influence on the bulk-rock data. By plotting the Mn over the bulk carbon, it is apparent that the carbonates become more manganiferous stratigraphically upwards (see section 3.4.2.4).

The bulk-rock values of the other transition metals were found to vary from below the detection limit up to tens of ppm, with the highest average value for Cr (18.1 ppm) and the lowest for Mo (0.8 ppm; Table 3.1). Most of the transition metals correlated strongly with each other (R^2 >0.6) with a few notable exceptions: Mn, Y, Mo and to a lesser extent Zn. The latter three were the only transition metals with higher average abundances in the Kuruman compared to the Griquatown Formation (Table 3.1). With the exception of Mn, no strong correlation with stratigraphy was found for any of the transition metals.

3.3.2. Sequentially extracted data

The external reproducibility for the sequential extraction was based on multiple extractions

of the same sample that were measured independently, including eight duplicate samples and two samples replicated nine times. The average relative standard deviation (RSD) was 10.9 % for the major elements determined by ICP-OES (Si, Fe, Mg, Mn, Ca, K), which reduced to 3.7 % when more than 1.0 wt% of an element was present, and increased to 13.3 % in the case that less than 1.0 wt% was present. No systematic variation was found in the reproducibilities for the different fractions. For the ICP-MS (Al, Sc, Ti, V, Cr, Mn, Co, Ni, Cu, Zn, Y, Zr, Mo, U) the average RSD was 22.5 %, which also varied based on the abundance of an element in a sample. The average RSD of element concentrations >10 ppm was 10.8 %, which increased to 25.6 % for concentrations <10 ppm. Overall there was no trend in the average RSD per fraction, however for some elements there was a clear difference in RSD per fraction. For example the Sc RSD was 15.9 % for the acetate, 37.6 % for oxalate

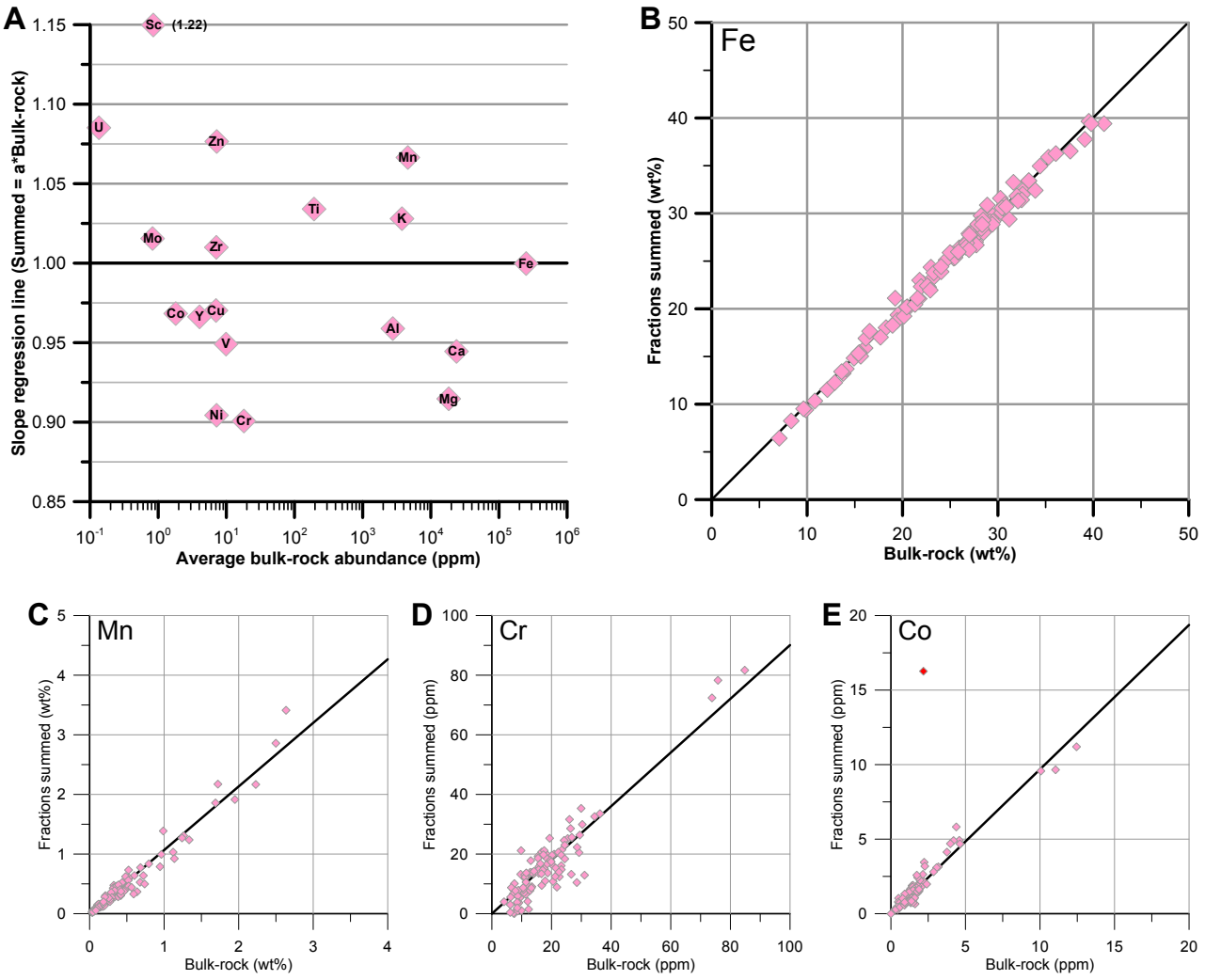

Figure 3.2: Recoveries as slope of the regression line for the major elements and transition metals. A) Regression line slope versus the bulk-rock abundance (ppm). Regression lines for individual element Fe (B), Mn (C), Cr (D) and Co (E) analyses.

Table 3.2: Fraction normalized concentration ranges with 5th percentile, average, 95th percentile and maximum values. Ca-Al in wt% and Sc-Mo in ppm. Only samples included when more than 10 wt% of the sample is the specific fraction.

	Carbonate fraction				Oxide fraction				Silicate fraction			
	5th	Av.	95th	Max.	5th	Av.	95th	Max.	5th	Av.	95th	Max.
Ca	0.68	7.74	18.21	28.34	0.02	0.04	0.09	0.11	0.01	0.15	0.51	1.67
Fe	15.15	27.47	36.30	37.18	61.24	69.03	71.57	71.76	2.74	12.40	23.79	31.78
Mg	2.15	3.70	4.85	6.30	0.05	0.89	3.27	4.76	0.10	0.95	2.24	2.80
Mn	0.20	1.41	3.84	5.11	0.00	0.10	0.33	0.63	<0.01	0.05	0.14	0.34
Si	0.39	1.52	3.73	5.30	0.38	1.05	3.24	4.30	26.59	35.92	43.85	45.70
Al	0.01	0.10	0.20	1.10	0.01	0.20	0.60	2.40	0.01	0.37	1.32	4.54
Sc	0.5	2.7	7.0	19.7	0.1	0.9	3.5	6.4	0.1	0.7	2.6	7.2
Ti	0.6	4.5	11.0	17.8	11.1	144.1	456.4	656.9	7.5	284.1	1372.	2684.
V	1.5	7.6	23.3	49.1	4.0	17.3	40.9	112.4	0.2	6.5	29.4	70.2
Cr	2.0	27.5	95.9	228.2	1.0	21.3	74.3	126.4	0.5	8.2	26.8	80.3
Co	0.6	2.3	6.1	17.1	0.1	1.9	3.7	58.6	0.1	1.8	7.7	9.8
Ni	2.2	9.4	27.5	66.4	0.7	6.5	17.2	26.6	0.7	5.3	16.7	45.2
Cu	2.6	15.2	36.0	67.5	2.1	8.3	15.3	24.0	0.9	5.6	16.6	23.1
Zn	2.5	13.3	34.4	70.5	0.7	5.7	16.9	27.9	0.5	6.4	15.1	61.3
Y	2.7	7.4	12.9	18.1	0.7	4.4	12.8	24.6	0.1	1.9	6.1	11.0
Zr	<0.1	0.2	0.7	3.2	0.5	4.8	16.2	21.8	0.6	10.2	38.0	121.9
Mo	0.3	1.4	3.8	13.8	0.6	1.8	4.1	7.1	0.1	0.3	1.0	2.4
U	<0.1	0.1	0.4	1.1	<0.1	0.1	0.2	0.5	<0.1	0.2	0.6	2.4

and 7.4 % for the HF fractions respectively.

If the recoveries (sum of extracted fractions vs. bulk-rock value) were calculated per sample and then averaged for all 106 samples, the values around the detection limit would introduce a significant uncertainty. To counter-act this, the recoveries were calculated by using the slope of the regression line (forced through zero) in the summed extractions vs. bulk-rock value plots (Figure 3.2b). This meant that the lower values had less influence on the average recovery. For the transition metals the recoveries were excellent (0.90-1.10) with slightly higher recoveries for Sc (1.22; Figure 3.2). The R^2 values of the linear regression lines were >0.95 for all but Cu (0.79), Zn (0.86), Mo (0.87) and Sc (0.90).

The transition metals were found to be unevenly distributed over the three fractions (Table 3.2). Since the recoveries were excellent, everything was normalized to the summed abundances in the discussion below. As stated above, Mn was bound to the carbonate fraction, with 89% of the Mn extracted during the acetate leach. Titanium and Zr were bound to the silicate fraction, with 86%

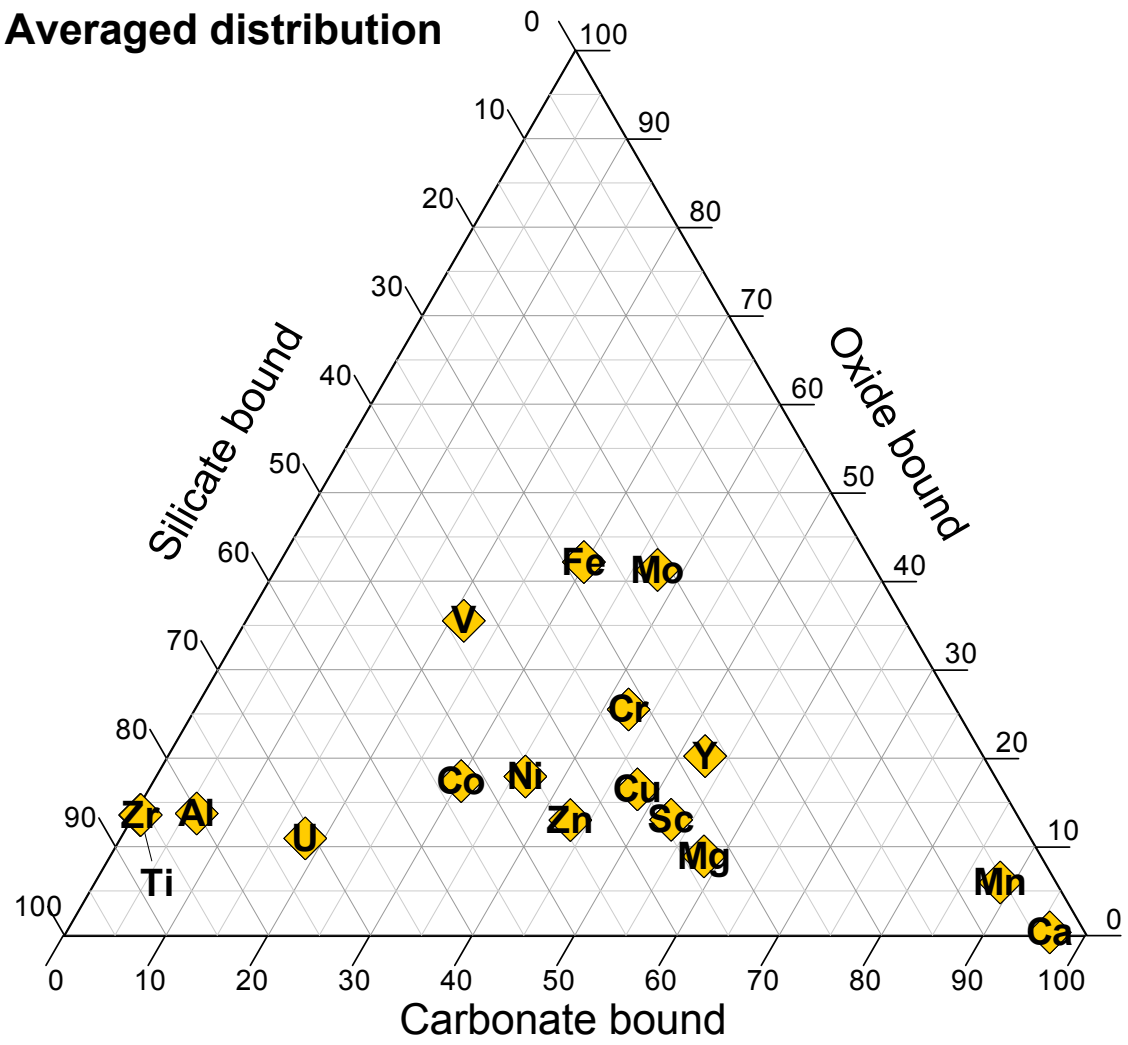

Figure 3.3: Averaged distribution of the major and transition elements over the three different fractions

extracted during the HF-step. Based on the distribution of the other elements it became evident that the oxide fraction was relatively depleted in transition metals (Figure 3.3).

In the carbonate fraction a clear negative correlation (R^2= 0.91) was present between Fe (10-37 wt%) and Ca (0-28 wt%), related to the relative amounts of ankerite versus siderite. Magnesium (0.7-6.3 wt%) was slightly more abundant than Mn (0.1-5.1 wt%). In the oxide fraction an anti-correlation (R^2= 0.77) between Mg (up to 4.8 wt%) and Fe (59-71 wt%) indicated mineralogical exchange. Trace elements were generally below 10ppm in all fractions except for Ti and Cr.

3.3.3. Micro-analytical techniques

For the ERIN core, multiple EMP analysed grains of each carbonate mineral were averaged per sample and compared to the acetate extracted data of the respective sample powder in Figure

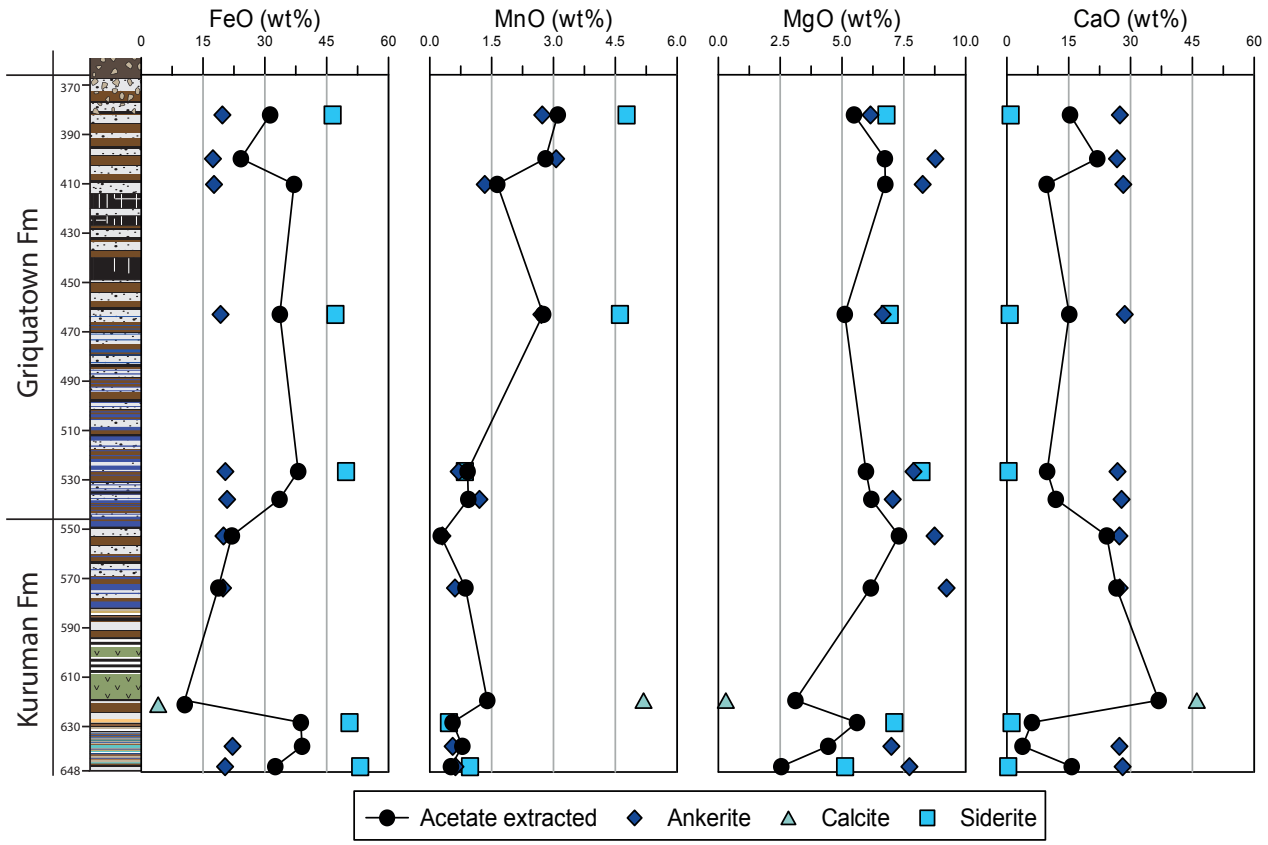

Figure 3.4: Fraction normalized acetate extracted data compared to averaged mineral specific EMP data for the ERIN core.

3.4. The EMP data (Rafuza, 2015) confirms the extracted data, which is a mixture of the different carbonate phases present.

The results of the LA-ICP-MS analyses are plotted in Figure 3.5, together with the ranges of the chemically extracted, fraction normalized data. The colored diamonds are *in situ* concentrations of the targeted mineral in ppm. Every diamond is the average of 1-4 accepted microanalyses in a single thin section. The blue diamonds are the carbonates (ankerite and siderite), the red ones are magnetite analyses and the green diamonds are the various Fe-silicates. These colored diamonds overlie their respective fraction normalized concentration average and ranges for all the accepted extractions (see section 3.2).

The variation within the extracted data was larger than the mineral trace element data, but they generally matched within an order of magnitude (Figure 3.5). However, for some of the transition metals the average extracted amounts in the carbonate fraction were higher than the microanalytical data (e.g. V, Cr, Co, Cu Mo).

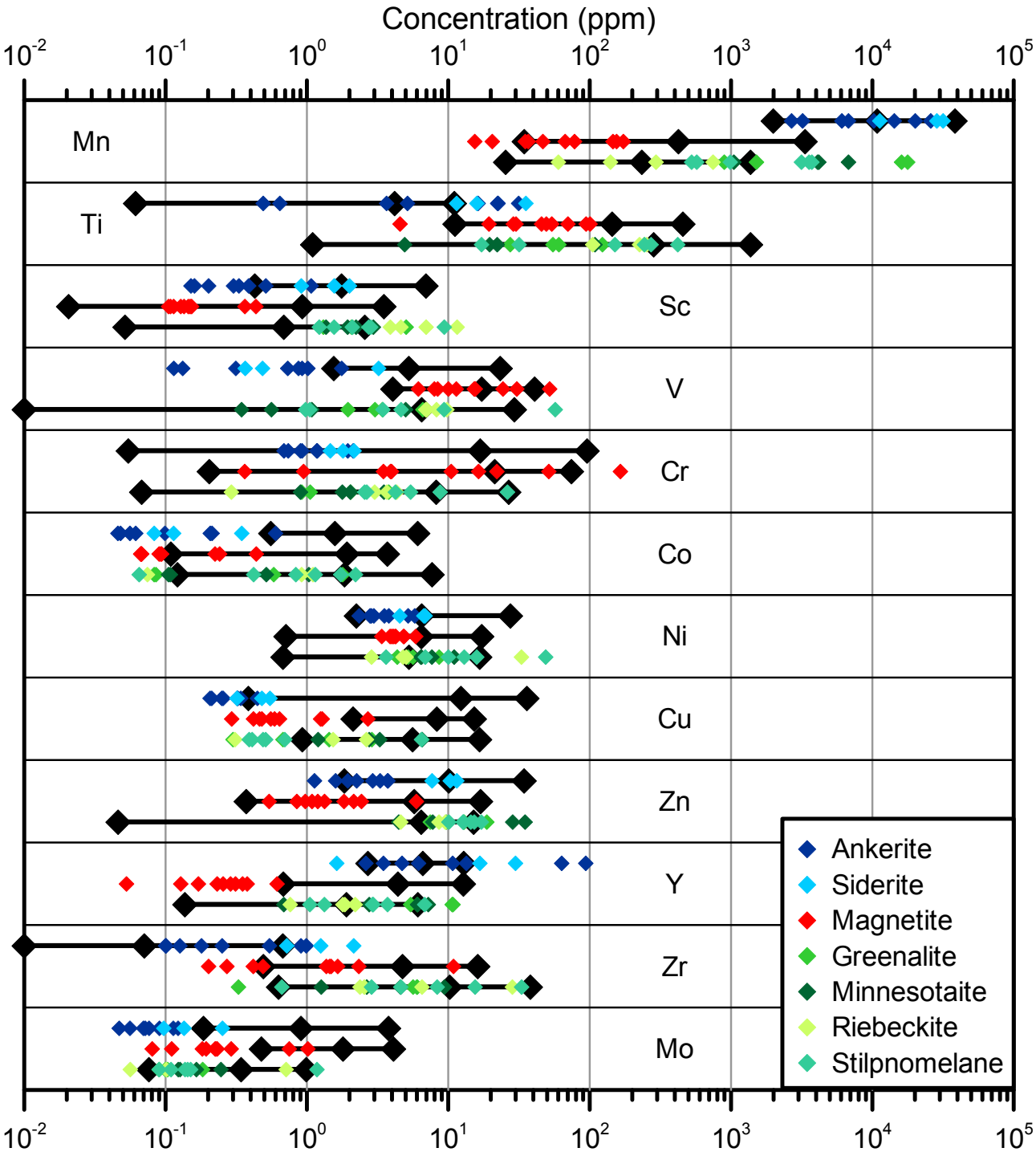

Figure 3.5: Sequentially extracted and LA-ICP-MS mineral specific trance element concentration ranges. Black lines are the sequentially extracted ranges per element for acetate, oxalate and HF from top to bottom, respectively. The three filled black diamonds are, from left to right, the 5th percentile, the median and the 95th percentile of the range in the data. Overlain are the individual grain-specific analyses for the carbonates (blue), magnetite (red) and the Fe-silicate (green) minerals.

3.4. Discussion

3.4.1. Data quality and comparisons

Normalizing sequentially extracted data per fraction has the advantage of enabling direct comparisons with independent microanalytical techniques. The fractions are generally a mixture of different minerals whereas the EMP and LA-ICP-MS techniques focus on specific grains. If the end-member compositions can be determined for the specific minerals the mineral-mixtures in the fractions should fall in-between the extremes.

3.4.1.1. Carbonate fraction

The different carbonate minerals were analysed by EMP in multiple samples from the ERI core. The average major element composition of these individual minerals brackets the acetate-extracted values as would be expected (Figure 3.4). The near-purity of the carbonate extraction is confirmed by the low abundances of Si, K and Al, with averages at 1.5, 0.5 and <0.1 wt% respectively, which indicate only very minor contamination by silicate minerals. The samples with relative high Al and K concentrations include the stilpnomelane lutite sample, indicating that minor stilpnomelane digestion occurred in these cases. The high Si numbers (up to 5 wt%) are unrelated to the lutites or to other elements and seem to occur randomly, implying the digestion of SiO_2. Since microcrystalline quartz Si was not dissolved by the acetate extraction (Tessier, et al., 1979) a possible explanation for the silica-presence are chert inclusions in the rhomobohedral carbonates. EMP data of these carbonates have an average of 1.2 wt% SiO_2 (Rafuza, 2015) and the LA-ICP-MS concentrations in this study are even higher. Furthermore, literature EMP data show averages of 2.5 and 3.3 wt% SiO_2 in siderite and ankerite respectively (Pecoits, et al., 2009), which also shows that silicate inclusions can be present.

The LA-ICP-MS data of some transition metals are at the lower end of the extracted range (Figure 3.5). There are three potential explanations for this; 1) erroneous laser-ablation data for example due to callibration errors or an incorrectly estimated internal standard, 2) the ablated grains were not completely representative or 3) the extraction data were inaccurate. The internal standards

used in LA-ICP-MS were FeO for siderite (49.53 wt%) and CaO for ankerite (27.55 wt%). Based on this the other major elements (except Si) fit within the expected mineralogical ranges. The relative high Si concentration indicates the presence of the quartz matrix, since other typical elements present in the Fe-silicate minerals (Al_2O_3 and K_2O) were well below 0.1 wt%. If the internal standards were inaccurate, a systematic offset would be expected for all elements of that specific analysis. This is not the case, and in fact for most elements, the correlation between the techniques is good.

The carbonate extraction was designed to digest all carbonate minerals, including the very fine grained siderite matrix portion, whereas the laser ablation analyses could only be performed on large grains (>80 µm). These larger diagenetic grains potentially differ geochemically from the finer, potentially primary precipitate, due to a different crystallization history. Siderite LA-ICP-MS data from the Dales Gorge IF has transition element ranges of 6-27 ppm Cr, 0.4-18 ppm Cu and 6-59 ppm Zn (Pecoits, et al., 2009), which are higher than our ranges but do match the extracted values in this study.

The average process blank correction carried out for the ICP-MS measurements affected the transition metals most significantly. Process blank values for Cr, Zn and Cu were up to 30 % of the average measured values in the BIF samples, making the uncertainties for these elements significant. These elements are already amongst the most difficult to measure by ICP-MS due to spectroscopic and non-spectroscopic interferences (Jarvis, et al., 1992). For these transition metals the exact concentration in the carbonate fraction might thus be erroneous due to the ICP-MS measurements. However, if no blank correction was applied, the fraction normalized values would deviate even more from the *in situ* ones. The discrepancies between the microanalytical and sequential extraction techniques for the acetate fraction are therefore most likely related to inaccuracy during ICP-MS analysis.

3.4.1.2. Oxide fraction

Since all Fe is treated as magnetite, a clean leach consists of virtually only Fe (72.4 wt% Fe). EMP analyses of magnetite in BIF shows generally pure Fe end-member compositions, with less than 0.1 wt% of other oxides present (Klein, 1974; Gole, 1980; Pecoits, et al., 2009). The highest measured oxide after FeO and SiO_2 in the LA-ICP-MS results is MgO with values up to 0.5 wt%.

The majority of the oxalate normalized samples have Fe values above 70 wt% (median 70.4). The most common contamination can be seen in Si and Mg with median values of 0.8 and 0.4 wt% respectively. This indicates that the oxalate extraction was quite specific, but still dissolved a small quantity of silicates. Median Ca and Mn values were <0.05 wt%, suggesting that virtually no cross-contamination between oxides and carbonates took place.

Most microanalytical mineral trace element data follow the range indicated by the extracted ones, although lower ablation values were recorded for Cu, Y and Mo. Transition metal LA-ICP-MS data from the Hamersley BIF (Pecoits, et al., 2009) shows values for these elements which are in the same range as our extracted data.

The very low concentrations of all minor and trace elements in unaltered BIF magnetite has been described before (Nadoll, et al., 2014; Chung, et al., 2015). This is also holds for the Kuruman

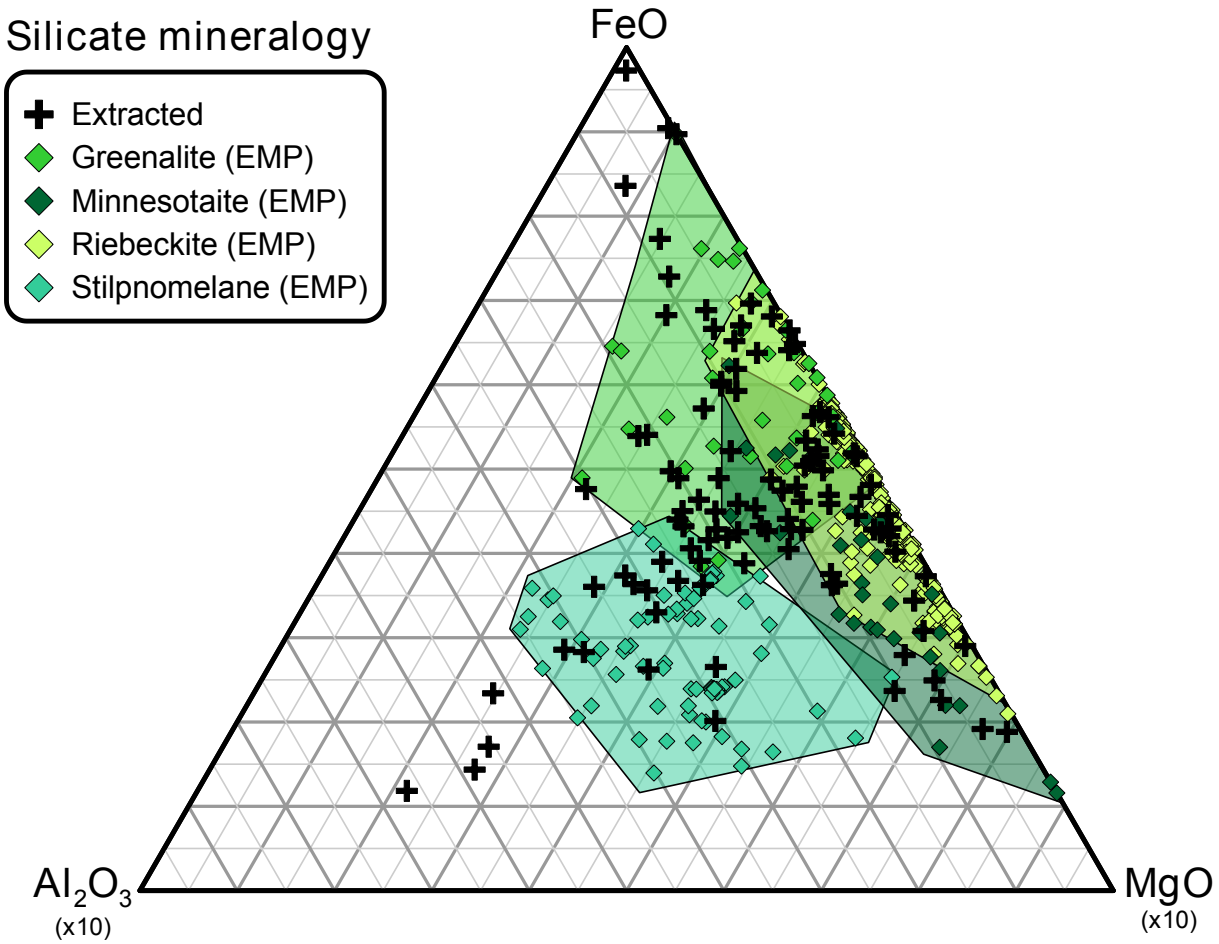

Figure 3.6: AFM diagram of the silicate fraction. The four different fields are created by literature EMP data (Beukes and Klein, 1990; Dymek and Klein, 1988; Floran and Papike, 1975; 1978; Klein, 1974; Klein and Gole, 1981; Gole, 1980). Additional unpublished riebeckite and stilpnomelane data from Van den Brug (in prep.). See text for discussion

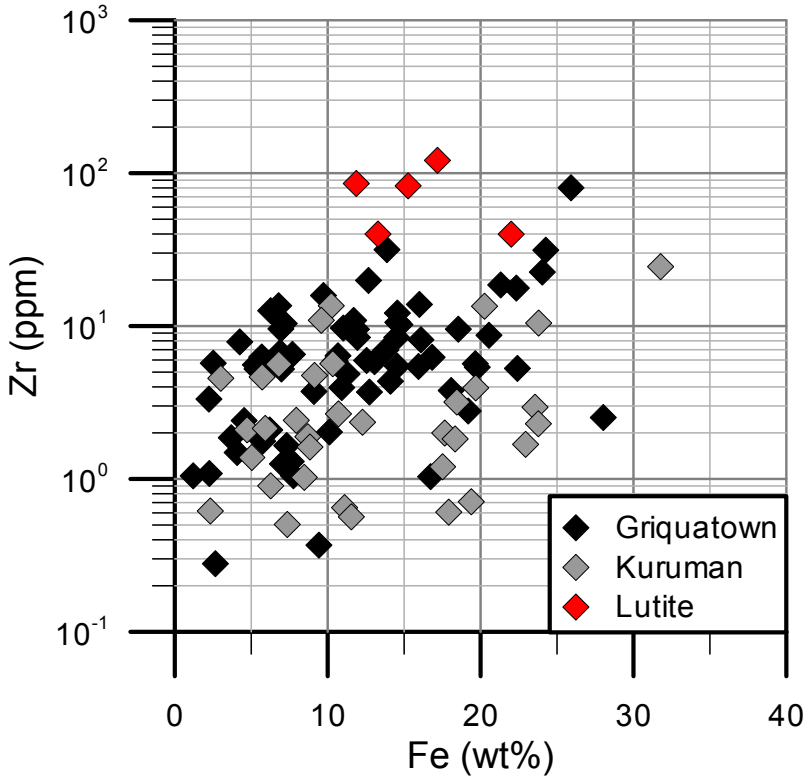

Figure 3.7: Silicate fraction extracted Zr (ppm) vs. Fe (wt%) showing no relationship

and Griquatown BIFs (Figure 3.3). The oxide fraction and the microanalyses of magnetite yield concentrations that are low compared to the other fractions. An exception to this trend is V (and to a lesser extent Cr), which is most enriched in the oxide-fraction. This inter-fraction relationship is similar in the Dales Gorge BIF (Pecoits, et al., 2009) and the V ranges found here are similar to other BIF magnetites (Nadoll, et al., 2014; Chung, et al., 2015).

3.4.1.3. Silicate fraction

Direct comparison of different silicate fractions with each other is difficult since variable amounts of chert are responsible for the range in Fe/Si ratios. Literature EMP values of the four main Fe-bearing silicate minerals; greenalite, minnesotaite, riebeckite and stilpnomelane, create the distinguishing fields on an AFM diagram (Figure 3.6). The extracted data scatter all over the different fields. Two groups of samples plot outside the fields outer limits. Samples closer to the Al corner are the stilpnomelane lutites, which could potentially contain some biotite (Beukes and Klein, 1990). End-member greenalite does not contain any Mg, so the Fe-rich samples can be included as almost pure Fe-greenalite. For these samples the other major elements, Al, Mn and K are also absent. For most of the trace elements, the ablated data is at the higher end of the range. Dilution of the

extracted samples due to chert presence is the most obvious explanation.

Zirconium is, as expected, only present in the silicate fraction (Figure 3.3). Zirconium can be used as an indicator for clastic contamination. When Zr is plotted against the silicate extracted Fe (Figure 3.7) there is no trend visible. This indicates that the majority of iron bound to the silicates is not of detrital origin.

To summarize it appears that the majority of the extracted data fit with the mineral data. Some trace metals of the carbonate fraction deviate slightly from the expected values based on LA-ICP-MS. The silicate fraction is the most difficult to interpret since multiple Fe-silicates minerals are generally present and cation substitution can alter the mineral chemistry quite extensively, making potential modal mineralogy calculations based on the major elements a first order estimate at best.

3.4.2. Elemental behaviour

The major elements behave as expected, with Si and Al plotting in the silicate corner, Ca is bound to the carbonate minerals and Mg is divided between the silicate and carbonate fractions (Figure 3.3). Iron varies significantly from samples dominated by a single fraction to evenly mixed samples. For a discussion on Fe see the Fe-isotope section (Chapter 5).

Only a few trace elements are predominately present in a single fraction, such as Mn in the carbonate one and Ti, Zr and U in the silicate fraction, so most are distributed over multiple phases (Figure 3.3). Amongst these elements is Sc, which can be used as a proxy for detrital input (e.g. Bau, 1993), and was therefore expected to plot in the silicate corner. The high recovery for Sc (1.22; Figure 3.2) and the unexpected presence in the carbonate fraction (Figure 3.3) is most likely related to a spectroscopic-interference of the carbonate-ions ($^{13}C^{16}O_2^+$; Jochum, et al., 2012) on ^{45}Sc, for which no correction can be applied since the carbonate content varies per sample. This interference also explains the high Sc concentrations in the microanalytical carbonate data (Figure 3.5).

Iron isotope ratios vary extensively between co-existing Fe-carbonates and Fe-oxides (Chapter 5, Johnson, et al., 2008b), which means that any bulk-rock Fe-isotope signature is, at least partially, related to the sample mineralogy. Therefore bulk-rock Fe-isotope ratios in BIF should be interpreted carefully when discussing oxidation states of the surface environment. Next to Fe, other non-traditional stable isotopic systems have also been used to infer the relative oxygenation of the Earth include Cr

(Frei, et al., 2009; Konhauser, et al., 2011; Crowe, et al., 2013) and Mo (e.g. Czaja, et al., 2012). Also the bulk-rock abundance of U (Partin, et al., 2013) has been used to infer oxygenic weathering. With the available speciation data, first-order suggestions can be made about the applicability of these proxies in BIF systems and whether some basic assumptions need to be revisited.

3.4.2.1. Molybdenum

Molybdenum abundance and isotope ratios have been used to infer paleo-oxidation states (Anbar and Rouxel, 2007 and references therein). In the contemporaneous oceans Mo is the most abundant transition element, due to the highly conservative behaviour of the molybdate ion (MoO_4^{2-}) under oxic conditions (e.g. Farquhar, et al., 2011). The long oceanic residence time homogenises the Mo abundance and its isotopic composition (Siebert, et al., 2003). Conservative behaviour has also been inferred in anoxic ferrous waters (Kurzweil, et al., 2015).

Under euxinic conditions Mo is sequestrated from seawater due to its reaction with H_2S to form particle-reactive thiomolybdates (e.g. Algeo and Lyons, 2006; Anbar and Rouxel, 2007). In sulfur-poor settings the adsorption of Mo onto Mn-oxide crusts represents the most important Mo sink (e.g. Bertine and Turekian, 1973; Arnold, et al., 2004). This latter mechanism preferentially adsorbs lighter Mo isotopes (Siebert, et al., 2003). Molybdenum isotopes can thus be used to argue for anoxic versus euxinic conditions in ancient marine settings (Arnold, et al., 2004).

The presence of a light Mo isotopic signal in pre-GOE rocks would then potentially indicate

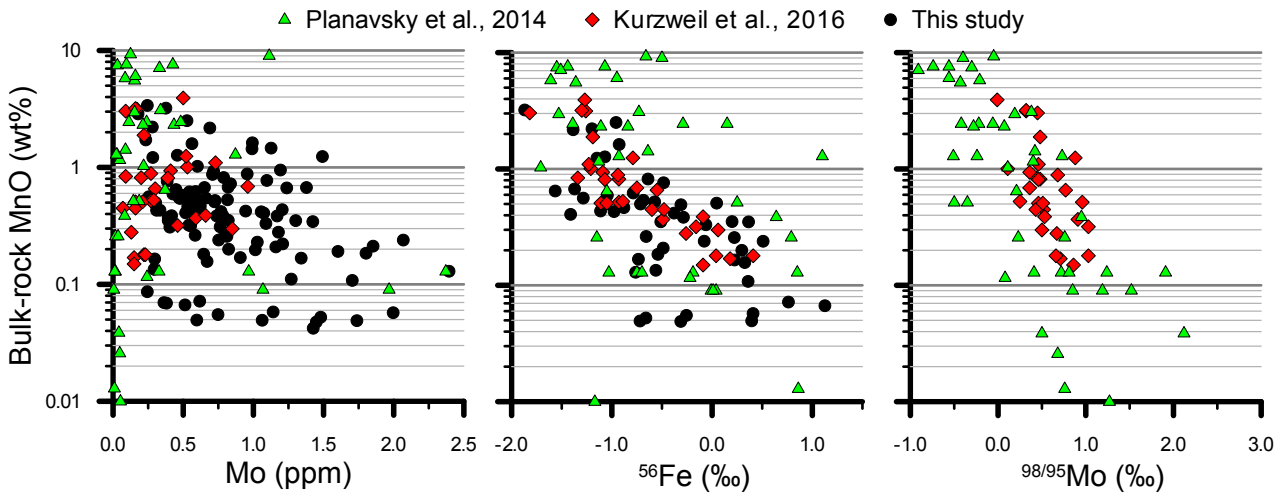

Figure 3.8: Bulk-rock MnO (wt%) versus Mo, δ^{56}Fe and $\delta^{98/95}$Mo in BIF samples. Data from Planavsky, et al. (2014), Kurzweil, et al. (2016) and this study. Note the logarithmic MnO scale. See text for discussion.

the presence of oxidized Mn-species in the original sediment (Planavsky, et al., 2014; Kurzweil, et al., 2016). The presence of free O_2 in pre-GOE sedimentary environments has also been made using coupled Fe-Mo isotopes (Czaja, et al., 2012), Re-Mo geochemistry (Anbar, et al., 2007; Wille, et al., 2007; Kendall, et al., 2010), varying $\delta^{98/95}$Mo in microbial carbonates (Voegelin, et al., 2010) and combined Mo-C-O isotopes (Kurzweil, et al., 2015). As sulfide can quantitatively scavenge Mo, thereby reducing the residence time dramatically, varying $\delta^{98/95}$Mo in sulfur-rich shales can indicate changing inputs, which is potentially related to oxidative weathering of sulfide-minerals (Duan, et al., 2010). The combined result of the aforementioned studies gives a robust indication for pre-GOE oxygenic photosynthesis and the occasional atmospheric whiffs of O_2 (Anbar, et al., 2007).

Due to the low, sub-ppm concentrations of Mo in BIFs (Pecoits, et al., 2009; Kurzweil, et al., 2016), most studies around the GOE have focussed to date on (black) shales and/or carbonates which have higher Mo concentrations (e.g. Duan, et al., 2010; Czaja, et al., 2012). The Mo concentrations in the bulk-rock BIF samples here follow this trend with ranges from 0.2 to 2.4 ppm and an average of 0.8 ppm (Table 3.1). The Mo and Mn abundances and speciation are not related in any way. Molybdenum is distributed over the three fractions (Figure 3.3) and does not show any stratigraphic relationship with the carbonates. In the studies by Planavsky, et al. (2014) and Kurzweil, et al. (2016) concentration relationships between Mn and Mo in BIFs were also absent, but a negative relationship was found between MnO content and $\delta^{98/95}$Mo (Figure 3.8) as noted by Kurzweil, et al. (2016). Similar to the Koegas Subgroup (Johnson, et al., 2013), Mn in the Asbestos Hills BIFs is primarily bound to the carbonates, which means that the presence of Mn in the carbonate fraction strongly influences the $\delta^{98/95}$Mo values. This hints to the presence of Mn-oxyhydroxides onto which the ^{95}Mo is preferentially adsorbed compared to ^{98}Mo (Siebert, et al., 2003), which get then reduced by DIR to form Mn-bearing carbonates in the Koegas Subgroup.

Kurzweil, et al. (2016) noted that in their samples Fe-oxides are subordinate to Fe-carbonates and Fe-silicates. In our extracted data Fe-oxides can host similar amounts of Mo to the Fe-carbonates. The Mo concentration in the silicate fraction is minor, and no relationship is seen between Zr and Mo suggesting no detrital control (Figure 3.9). Preliminary data show that there might be a mineralogical dependence on Mo isotopes as various extracted fractions of the same stromatolite samples show different isotope ratios (Thoby, et al., 2016). For Fe isotopes such a dependence has

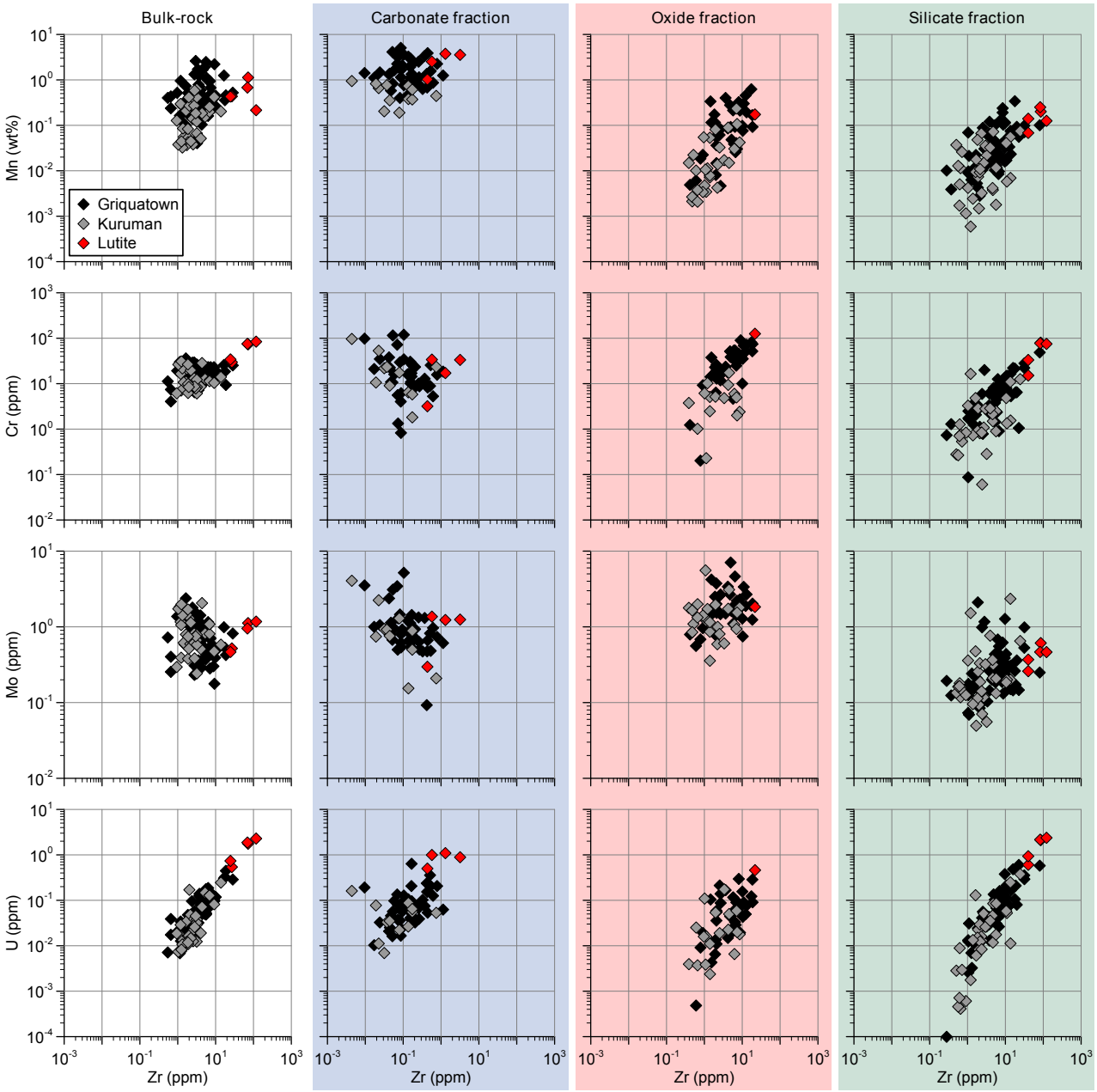

Figure 3.9: Various transition metals (Mn, Cr, Mo, U) vs Zr for the bulk-rock and the three different fractions. Only accepted samples included. Where present, a positive linear trend indicates a correlation between the transition metal abundance and the presence of a detrital component. Note; 1) the higher abundances in the Griquatown of Mn in the carbonate extracted and Cr in the oxide fraction compared to the Kuruman Formation and 2) the low Zr abundance in the carbonate fraction (<1 ppm), indicating no detrital component in this fraction. See text for discussion.

been well established (e.g. Johnson, et al., 2003; 2008a; 2008b). As the samples of Kurzweil, et al. (2016) are carbonate and silicate dominated and if the silicate fraction does not contain significant Mo, like in our samples, then the MnO/$\delta^{98/95}$Mo relationship might be a function of oxide versus carbonate abundance instead of the presence of Mn-oxyhydroxides. In that case increased carbonate

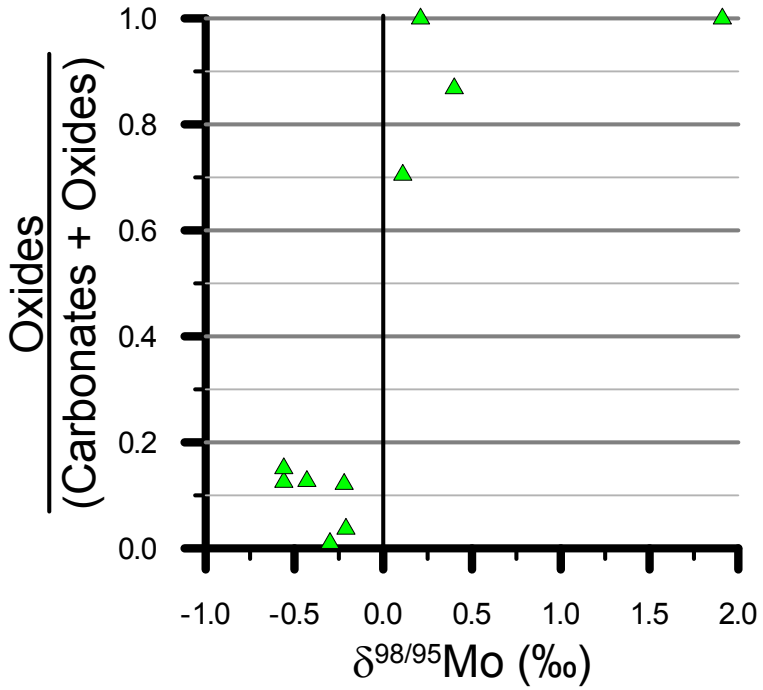

Figure 3.10: Relative portion of oxides versus $\delta^{98/95}$Mo. Data from Planavsky, et al. (2014). See text for discussion.

concentrations (MnO abundant) would have a low $\delta^{98/95}$Mo and oxide-rich samples a high $\delta^{98/95}$Mo.

The study by Planavsky, et al. (2014) contains quantitative XRD data for a number of samples. The relative percentage of oxide minerals (hematite + magnetite) can be normalized to the sum of the oxides and carbonates (ankerite + siderite). When this percentage is plotted against the measured $\delta^{98/95}$Mo of the same samples two clear groups emerge. Carbonate dominated samples with $\delta^{98/95}$Mo < 0 and positive $\delta^{98/95}$Mo for the oxide-rich samples (Figure 3.10). This alternative hypothesis might have some consequences for Mo isotope interpretation in BIF, and by extension shale, samples. A quick way to test this would be to either measure bulk-rock Mo isotopes from the same sample set in this study, or to do Mo speciation on the samples by Kurzweil, et al. (2016). Fraction specific Mo isotopes will also improve our understanding, but this would be challenging to achieve.

3.4.2.2. Chromium

Chromium is a redox proxy that can be affected by a strong detrital influence (Tribovillard, et al., 2006) and its supply to the modern oceans is therefore dominated by terrestrial processes (Konhauser, et al., 2011). Chromium isotope fractionation has been used to infer the onset of oxidative weathering (Frei, et al., 2009; Crowe, et al., 2013), as conversion of insoluble trivalent to

mobile hexavalent Cr preferentially releases the heavier ^{53}Cr isotope. The product chromate ions can be readily reduced to Cr(III) in the presence of ferrous ions, of which the majority will hydrolyze to form insoluble $Cr(OH)_3$ (Reinhard, et al., 2014) and co-precipitate with the ferric oxides. Because reduction of Cr(VI) by Fe^{2+} is efficient, the Cr residence time in the ferrous, anoxic Paleoproterozoic oceans would be very short, and the isotopic signature would be captured quantitatively (Frei, et al., 2009).

Cr isotopes have been used to argue for a very early (3.0 Ga) onset of oxygenic photosynthesis based upon fractionated values observed in a paleosol and a slightly younger iron formation (Crowe, et al., 2013). Recent data from the Eoarchean BIFs in Greenland indicate oxidative Cr cycling by 3.8 Ga (Frei, et al., 2016), without necessarily needing the presence of cyanobacteria. The largest Cr isotope fractionations occur at the end of the Neoproterozoic coinciding with the diversification of eukaryotes and the rise of animals (Cole, et al., 2016). This was preceded by minimal Cr oxidation throughout the mid-Proterozoic.

Cr abundances are dominated by detrital fluxes. By dividing Cr by Ti and then normalizing to the restoration model for the upper continental crust (values from Condie, 1993), authigenic Cr enrichement can be calculated for bulk-rock samples (Konhauser, et al., 2011). This eliminates the variability in detrital input. The largest crustal normalized Cr/Ti ratios are observed in BIFs coinciding with the GOE. This was explained by oxidative weathering of sulfides, causing acidity which would have enhanced *in situ* dissolution of Cr-bearing minerals (Konhauser, et al., 2011). Such a model would also explain why the bulk-rock BIF $\delta^{53}Cr$ record does not vary extensively until the Neoproterozoic. The *in situ* dissolution does not include a Cr-fractionation step as Cr(III) does not necessarily need to be oxidized to Cr(VI). The minor fractionations seen before the GOE (Frei, et al., 2009; 2016; Crowe, et al., 2013) might also be related to such processes.

The lutite samples in the Asbestos Hills have a median Cr/Ti ratio of 0.033 which is nearly

Figure 3.11: Transition element versus stratigraphy. Crosses are bulk-rock samples, diamonds represent a fraction normalized vlaue (blue = carbonate, red = oxide, green = silicate). Molybdenum shows no variation with stratigraphy for bulk and carbonate fraction, indicating also no relation with the carbonate-bound Mn. For Cr no significant increase in the bulk and carbonate fraction, but the oxide and silicate-bound Cr increase stratigraphically, which relates to the increase in Zr in these fractions (see Figure 3.9). Uranium concentration and bulk U/Ti ratio remain constant over the stratigraphy. The high U values (>1 ppm) are the lutite samples.

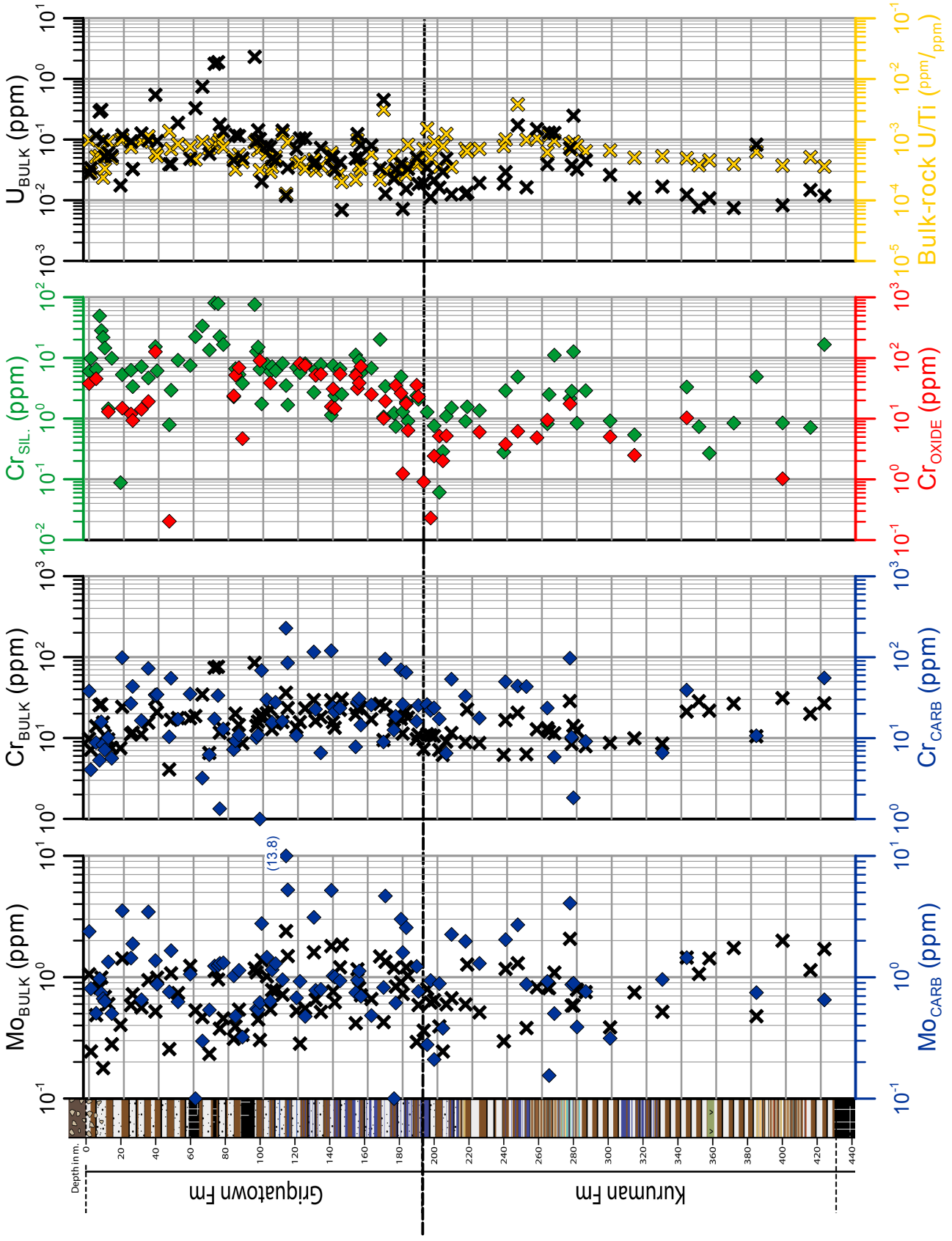
U_BULK (ppm)
Bulk-rock U/Ti (ppm/ppm)
Cr_SIL. (ppm)
Cr_OXIDE (ppm)
Cr_BULK (ppm)
Cr_CARB (ppm)
Mo_BULK (ppm)
Mo_CARB (ppm)
(13.8)
Depth in m.
Griquatown Fm
Kuruman Fm

Table 3.3: Cr and Ti behaviour through the sample set. Left side: median Cr and Ti concentrations of all samples. Right side median taken after ratios were calculated per sample, whereby n= gives the amount of Cr-Ti pairs used, so dividing the median Cr and Ti value does not neccesarily result in the median Cr/Ti ratio. Abbreviations: BR = bulk-rock values, Ac. = Acetate fraction, Ox. = oxalate fraction, HF = HF fraction.

		Median concentration (ppm)					Median Cr/Ti ratio			
	Fraction:	BR.	Ac.	Ox.	HF		BR.	Ac.	Ox.	HF
Lutite	Cr	73.8	25.4	126.4	75.5	Cr/Ti	0.033	1.433	0.192	0.028
	Ti	2120.9	15.1	656.9	2514.1	n=	5	4	1	5
Griquatown	Cr	16.3	17.1	25.6	6.1	Cr/Ti	0.119	3.105	0.162	0.033
	Ti	124.5	5.0	125.0	169.4	n=	67	48	38	65
Kuruman	Cr	11.5	23.6	5.0	1.2	Cr/Ti	0.332	5.429	0.087	0.041
	Ti	32.1	4.9	34.2	26.6	n=	34	17	15	27
All samples	Cr	15.7	19.9	16.7	4.9	Cr/Ti	0.149	3.168	0.158	0.034
	Ti	93.7	5.2	83.6	124.7	n=	106	69	54	97

identical to the upper continental crustal ratio of 0.035 (Condie, 1993), which additionally supports their origin as volcanic ash layers (Table 3.3). The median bulk-rock Cr content of all 106 samples is 16 ppm, which is in range for superior-type BIFs (Konhauser, et al., 2011). The median Cr/Ti ratio is about three and nine times the crustal value for the Griquatown and Kuruman BIFs respectively. The median Cr abundance increases from 11.5 to 16.3 ppm from the Kuruman to the Griquatown, the main factor in the changing ratio is the Ti concentration which increases from 32.1 to 124.5 ppm (Table 3.3). When looking at fraction specific level Cr and Ti behave opposite, the median Cr concentration tends to decrease from the acetate to the oxalate and HF leaches, whereas Ti increases. The HF Cr/Ti ratios are in good agreement with the upper continental crustal ratios (Table 3.3), indicating authigenic behaviour for the silicate bounded trace elements.

Although the uncertainties are significant, the fraction specific Cr concentration data for the carbonate fraction remain apparently homogeneous through the Asbestos Hills stratigraphy (Figure 3.11). For the oxide fraction there is a clear increase in Cr concentration from a 5 ppm median in the Kuruman Formation to 26 ppm in the Griquatown, which can be related to increased detrital input (as indicated by a correlation with Zr; Figure 3.9). This is also the case for the silicate fraction, although with slightly more scatter (Figure 3.11). This fits with the changing depositional environment as the Griquatown IF was deposited in shallower water, i.e. more proximal to land, than the Kuruman Formation.

The potential primary formation pathway of the carbonate minerals (section 3.4.2.4; Tsikos,

et al., in prep.) and the lack of concentration changes in the carbonate fraction suggest that the seawater Cr concentration remained fairly constant. Instead of bulk-rock $\delta^{53}Cr$, carbonate-bound $\delta^{53}Cr$ might be a more sensitive tracer for redox processes (Frei, et al., 2011). Carbonate-specific stable Cr isotopes could help to further construct the local redox conditions. However, the virtually constant Cr_{CARB} concentration and the positive correlation between that and $\delta^{53}Cr$ (Frei, et al., 2011), might already indicate little $\delta^{53}Cr$ variability throughout the Asbestos Hills. The stratigraphically increasing Cr and Zr content in the oxide and silicate fraction indicate enhanced detrital input. This increase might potentially reflect increasing acid-weathering as suggested by Konhauser, et al. (2011).

3.4.2.3. Uranium

Uranium has been used to infer the presence of oxidative weathering (Partin, et al., 2013; Satkoski, et al., 2015). Sharing similarities with Cr, rock-hosted immobile U(IV) is oxidized to mobile U(VI). The seawater U budget is mainly controlled by riverine input, so increasing seawater U concentrations could indicate oxidative weathering (Partin, et al., 2013). Once it reaches the Precambrian oceans U(VI) would be quantitatively trapped, either due to sorption onto on ferric oxyhydroxides (Waite, et al., 1994) and/or rapid reduction at an Fe-oxyhydroxide surface by Fe(II) and precipitation as a U(IV)-Fe(III) complex (Liger, et al., 1999). However, U can also be brought in as a detrital uraninite grains (Johnson, et al., 2014) under anoxic atmospheres.

The average measured U concentrations in the Kuruman and Griquatown BIFs are low with 0.05 and 0.08 ppm, respectively. The 5 lutite samples have average at 1.45 ppm. When corrected for radioactive decay ($U_{corr.} = U_{measured} \times e^{0.155125 \cdot \text{Age (Ga)}}$) in similar fashion as in Partin, et al. (2013), these abundances become 0.07, 0.12 and 2.13 ppm, respectively. These values are more or less in line with the average, corrected U concentration in the Kuruman samples of 0.16 ppm (Klein and Beukes, 1989; Beukes and Klein, 1990; Bau and Dulski, 1996; Partin, et al., 2013). The Asbestos Hills samples analysed by Horstmann and Hälbich (1995) and Pickard (2003) have a corrected average U concentration of 4.67 ppm, which is significantly higher than any sample measured in this study. The low U concentrations do not indicate an input through oxidative weathering in the Kuruman and Griquatown Formation BIFs.

This is confirmed by the strong relationships between bulk U content and Sc and Ti with a R^2

of 0.92 and 0.97, respectively (Table 3.1). Furthermore, the majority of U is silicate hosted (ca. 70%; Figure 3.3), the U/Ti ratio remains constant throughout the stratigraphy (Figure 3.11) and the strong relationship with Zr (Figure 3.9) indicate a detrital or volcanic-ash origin for most of the U present. Next to that uraninite grains have not been found in the Asbestos Hills Subgroup, but the presence of them in the Koegas Subgroup (Johnson, et al., 2014) supports this interpretation.

3.4.2.4. Manganese

The role of Mn in banded iron formations has largely been ignored because the majority of BIFs have low bulk MnO concentrations of <0.5 wt% (Klein, 2005) and Mn is monoisotopic, precluding stable isotope analysis. However, Mn has multiple oxidation states which behave differently in aqueous media. Like Fe, the divalent form of Mn is highly soluble in oxygen deficient aqueous media whereas oxidation of Mn(II) to metastable Mn(III) or Mn(IV) will form insoluble oxyhydroxide complexes (Calvert and Pedersen, 1996). These complexes are a good substrate to adsorb various transition metals (Ni, Cu, Zn, Co, Pb, Mo, V and Cr; Tribovillard, et al., 2006), whose abundances and stable isotopes can be used to indicate Mn(II)-oxidation (e.g. Kurzweil, et al., 2016). However, in reducing sediments Mn is highly mobile and therefore less suitable as a redox proxy (Tribovillard, et al., 2006).

The two key aspects of Mn in the Asbestos Hills BIFs are a bulk-rock concentration increase with stratigraphy and the speciation-data showing that the carbonates predominantly host the Mn. The average Fe/Mn ratio (ca. 230) in the Kuruman IF is significantly higher than that of the Griquatown Formation (ca. 60). The stratigraphic increase in bulk-rock Mn content is not completely mineralogically controlled, since the acetate fraction becomes more manganiferous in the Griquatown Formation (Figure 3.12). At the base of the Kuruman Formation less than 0.5 wt% Mn is present in the carbonates, which increases to more than 5.0 wt% at the top of the Griquatown IF. EMP data

Figure 3.12 Manganese plots with stratigraphy. Bulk-rock concentrations/ratios are black crosses, whereas the fraction normalized values are the diamonds. The stratigraphical Mn increase is present in the bulk-rock, but better indicated in the fractions. The carbonate fraction (blue) and the bulk-rock Mn/C show both an Mn increase. For the oxide fraction (red) this increase is also present but much more scattered. The Mn/Fe ratio is not indicative of the amount of Mn bound to oxides. The silicate fraction also shows the increase and again the bulk-rock ratio (Mn/Al) is not indicative of silicate bound Mn. Note the changes on the horizontal scales, especially for the extracted fractions. Carbonate is clearly the dominant Mn host.

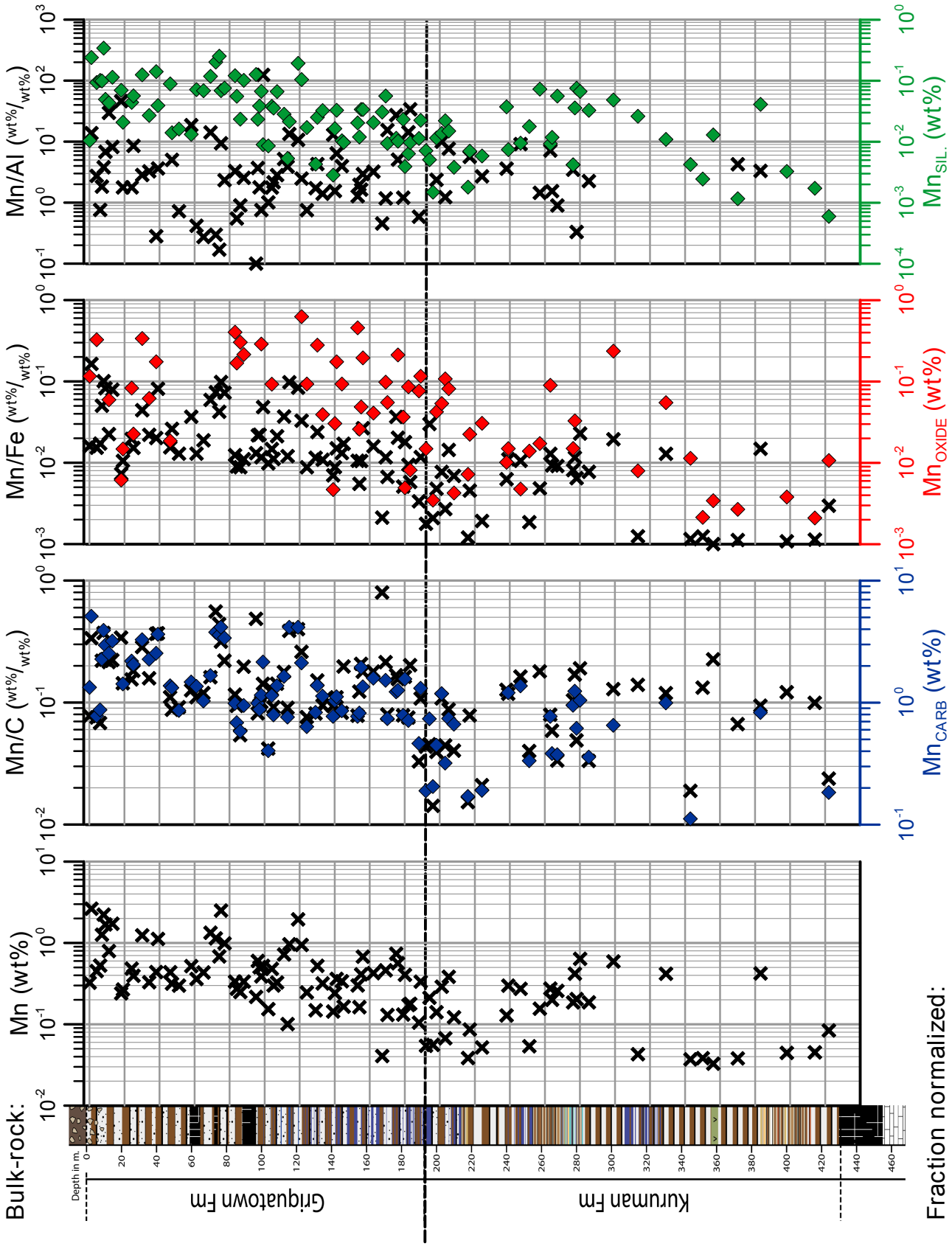
Bulk-rock:
Mn (wt%)
Mn/C (wt%/wt%)
Mn/Fe (wt%/wt%)
Mn/Al (wt%/wt%)
Mn_CARB (wt%)
Mn_OXIDE (wt%)
Mn_SIL. (wt%)
Fraction normalized:
Depth in m.
Grigualtown Fm
Kurruman Fm

confirmed this, and show that both ankerite and siderite host the Mn (Rafuza, 2015).

The Koegas Subgroup developed only in the southern part of the Griqualand West basin, off the Campbellrand carbonate platform (Figure 1.9). Here Mn is also predominantly hosted in carbonates and has bulk-rock concentrations peaking at 9.0 wt% Mn in a carbonate-rich sample (Johnson, et al., 2013). This Mn spike might not be that dissimilar from the top of the Griquatown Formation studied here. In fact, the Koegas BIFs could be a lateral correlative to the top of the Griquatown Formation on the carbonate platform. This claim is supported by the continuous transition from the Griquatown in the Makganyene diamictite for the cores studied here and the new age for the Ongeluk lavas at ca. 2.426 Ga (Gumsley, et al., 2017).

The increase in Mn continues further up in the stratigraphy, where it culminates in the Hotazel Formation, which is an alternation between hematitic BIF, Mn-ore and hematite lutites. The bulk-rock Mn content of the Hotazel BIFs is again comparable to the top of the Griquatown Formation (Tsikos and Moore, 1997; Tsikos, et al., 2003). However, the bulk of the Mn is concentrated in distinct Mn-ore layers, which consist of a mixed valence silicate (braunite; $Mn(II)Mn(III)_6O_8SiO_4$) and divalent, Fe-free Mn-carbonates (kutnahorite and rhodochrosite) with bulk-rock Mn-contents of over 40 wt% (Tsikos, et al., 2003; Johnson, et al., 2016). In the Hotazel Formation Mn is thus present in a higher oxidation state and a different mineralogy than in the underlying Asbestos Hills and Koegas BIFs.

The increase in Mn, from the Kuruman through to the Hotazel Formation, can be explained by an increase in Mn input, i.e. enhanced hydrothermal activity, or by accumulation in the water column. Increasing and varying hydrothermal Mn input can only be speculated, as there is no geological data to support this. Additionally no other element shows such a strong concentration increase as Mn, arguing against enhanced hydrothermal input. Furthermore, contemporaneous hydrothermal vent fluids have Fe/Mn ratios which are an order of magnitude lower than the Griquatown values (German and Von Damm, 2006), indicating preferential sequestration of Fe over Mn in BIF (Tsikos, et al., 2010), thereby passively enriching the seawater Mn^{2+} concentration. In anoxic to sub-oxic aqueous environments Mn^{2+} ions can build up significantly, such as in the present-day Orca Basin where Mn^{2+} concentrations reach >400 µM (Van Cappellen, et al., 1998). In anoxic environments, the deficiency of high-potential oxidants, coupled with the lack of reactivity with sulfide, has the result that the primary Mn(II) sink would be into carbonates as a trace constituent (Johnson, et al., 2013).

Manganese enrichment in sediments is generally associated with oxidizing conditions, as the standard model to explain Mn behaviour and its present day redox states in BIF starts with the oxidation of soluble Mn(II) to insoluble Mn(IV)-(oxy)hydroxides (hereafter Mn-oxyhydroxides). These Mn-oxyhydroxides then adsorb various trace elements during settling and precipitation. The oxyhydroxides can be diagenetically reduced by dissimilatory Mn-reduction (DMR) (Lovley, 1991). DMR oxidizes organic carbon, thereby creating alkalinity, which enhances carbonate precipitation and incorporates the reduced Mn. Part of the reduced, mobile Mn can be cycled back into seawater (Tribovillard, et al., 2006) creating an active Mn redox cycle.

Manganese oxidation can be mediated by UV-photolysis (Anbar and Holland, 1992), through Mn-phototrophy (Johnson, et al., 2013; Fischer, et al., 2015) or through reaction with photosynthetically produced O_2 (Kurzweil, et al., 2016). UV-photolysis can oxidize Mn, but in the presence of ferrous Fe these rates are significantly decreased and the product oxyhydroxide Fe/Mn ratio would be similar to BIF and therefore is unable to explain the stratigraphic increase towards the Hotazel Formation (Anbar and Holland, 1992). Mn-phototrophs have been inferred to be the major oxidizer in pre-GOE basins (Fischer, et al., 2015). However, modern Mn-phototrophic organisms have not yet been identified. If they were present, this would indicate that the Mn enrichment was not related to photosynthetically produced O_2, and thus, by extension Mn would not be capturing a seawater redox-change. Therefore the increase in Mn is most likely related to basin wide redox-changes by photosynthetically produced O_2. The 2.426 Ga Ongeluk age (Gumsley, et al., 2017) puts the deposition of the Hotazel Formation right at the GOE, which fits this model. When free O_2 became present in the surface waters, a Mn concentration gradient would be expected to form similar to present-day stratified anoxic lakes (e.g. Busigny, et al., 2014) or basins (Van Cappellen, et al., 1998), where the oxic zone was Mn impoverished and the highest concentrations were present at the redox-cline.

Virtually all the Mn oxidation pathways discussed in the recent literature involve the oxidation of Mn(II) to Mn(IV). Pathways considering the intermediate Mn(III) species are generally ignored (Madison, et al., 2013). The Mn-speciation in the Hotazel Formation is dominated by mixed valent braunite and divalent, Fe-free Mn-carbonates, and only a few, very small Mn(IV)-oxide inclusions have been found (Johnson, et al., 2016). This in itself might already question a Mn(IV) pathway,

since sufficient reducing capacity should have been available to quantitatively reduce all Mn(IV) to form only di- and trivalent minerals. So, whereas the oxidation pathway only considers direct oxidation from Mn(II) to Mn(IV), the reduction pathway needs to quantitatively reduce Mn(IV) to Mn(III), as there are no Mn(IV) species around, and only when the reducing capacity is high enough continue reduction to Mn(II). Furthermore, the absence of a Mn-enrichment in the sediments does not directly mean that Mn was not oxidized. Both Mn(III) and Mn(IV) are capable of oxidizing ferrous iron (Van Cappellen, et al., 1998; Tsikos, et al., 2010), due to their higher standard oxidation potentials. The exact reaction kinetics are poorly understood, but oxidation of Fe(II) by Mn-oxides in anoxic and slightly acidic conditions (pH 6) proceeds on a time scale of hours (Postma, 1985; Postma and Appelo, 2000). So, for any oxidized Mn species in a ferruginous, anoxic water column it is highly doubtful whether the product Mn-oxyhydroxides would reach the sediment interface before being cycled back as Mn(II).

The majority of the Kuruman and Griquatown samples are not enriched in Mn compared to other BIFs (Klein, 2005). The stratigraphic increase seen in all four drill cores studied here seems to argue against a diagenetic formation pathway for Mn-incorporation. Even if the Mn-redox cycle started to operate as discussed above, major fluctuations in Mn-abundance between the cores would be expected if the carbonates were diagenetically formed. In the vast majority of samples measured here, Ce anomalies are absent (Chapter 4; Figure 4.1) indicating reducing conditions with respect to Mn (Bau and Dulski, 1996). The appearance of minor but negative, PAAS-normalized Ce anomalies in the Mn-rich samples from the Koegas Subgroup (Nel, 2013; data shown in Figure 4.1), followed by larger Ce anomalies in the Hotazel Formation (Bau and Alexander, 2006) partially supports the onset of an active Mn-redox cycle after the deposition of the Asbestos Hills BIFs.

The exponential relationship between bulk-rock $\delta^{56}Fe$ and MnO (wt%) described for the Koegas samples (Kurzweil, et al., 2016) is also present for the Asbestos Hills samples (Figure 3.8), which further strengthens a claim that the Koegas and the top of the Griquatown are potential laterally correlative. This relationship was interpreted to represent an association between Mn-oxide formation and Fe-isotope fractionation within the water column (Kurzweil, et al., 2016). However, a continuous drawdown of more positive $\delta^{56}Fe$ in Fe-oxyhydroxides needed to form the Asbestos Hills BIFs would already leave the seawater depleted in ^{56}Fe compared to ^{54}Fe. This combined with the

passive increase in Mn, as detailed above, also could explain such a relationship, without the need for forming Mn-oxides in the Asbestos Hills BIFs. A more comprehensive discussion will follow below when the data are combined with Fe isotope variations (see Section 5.4.5).

Incorporation of Mn(II) into primary carbonates is a much better explanation for Mn abundances in the Griqualand West basin than a diagenetic model. The stratigraphically correlatable bulk-rock $\delta^{13}C$ values, of the same samples, also favour a primary origin for the carbonate (Figure 1.11; Tsikos, et al., in prep.). In a modern anoxic analogue, the Orca Basin, virtually all Mn in the sediments is hosted in the carbonates. Carbonate formation takes place in the water column, where it scavenges Mn(II) (Van Cappellen, et al., 1998). Direct incorporation of Mn(II) in carbonates implies that Mn behaved passively as a redox-player during the deposition of the Kuruman and Griquatown IFs. Although there might have been some Mn-cycling mediated by biological processes, the oxidation state of the basin and the presence of ferrous Fe prevented the preservation of Mn-oxyhydroxides. It also fits with the stratigraphic increase in Mn, as it could have built up over time relative to Fe. This implies that the Mn-concentration in carbonates is potentially a good proxy for seawater Mn^{2+} under Mn reducing conditions. Such a model could potentially form a manganiferous basin if time and redox conditions permitted. An increase in oxidation state of the surface environment would then eventually change the Mn behaviour from a passive to an active redox player, potentially starting in the Koegas Subgroup (Kurzweil, et al., 2016).

3.5. Conclusions

The most widespread approach to investigate banded iron formations (BIF) is by working with bulk-rock samples. In these very fine grained heterogeneous rocks bulk-rock sampling means varying compositions in modal mineralogy, which significantly influences the sample geochemistry. A previously tested sequential extraction method was applied to the ca. 2.4 Ga BIFs of the Kuruman and Griquatown Formations in the Griqualand West basin of the Transvaal Supergroup. Their deposition right before the Great Oxidation Event (GOE) means that these BIFs potentially capture the redox-changes in the surface environment when going from an anoxic to a sub-oxic atmosphere.

The elemental concentrations in the various extracted fractions generally match the ranges found by microanalytical techniques on the individual minerals making up these fractions. Exceptions

to this are some transition metals in the acetate fraction, such as Cr and Zn, which tend to be challenging to measure by ICP-MS. The distribution of most elements was found to be as anticipated, i.e. Al, Ti, Zr and U are mainly present in the silicate fraction, Mn and Ca are predominantly in the carbonate fraction, Mg is distributed among the silicates and carbonates and a few elements have a significant component bound to the Fe-oxides (Fe, Mo and V).

The distribution of Mo and Cr over multiple phases indicates that bulk-rock concentration values might be influenced by modal mineralogy. As suggested before for Fe, variable mineralogies with variable isotope ratios could compromise bulk-rock studies. Bulk-rock concentration values for Cr and U do not hint to oxidative weathering at the time of BIF deposition, which is consistent with their deposition in a practically detritus-free environments.

After Fe, mono-isotopic Mn is the most abundant redox element in BIF samples. In order to oxidize divalent Mn the oxidation state of the basin needs to be significantly higher than for Fe-oxidation. Manganese is only present in the carbonate fraction in its divalent form where its concentration increases stratigraphically. Combined with bulk-rock carbon isotopes from a precursor study (Tsikos, et al., in prep.), the easiest explanation is the formation of primary carbonates from seawater. Aqueous divalent Mn would be incorporated in the crystal structure, potentially aided by microbial Mn-cycling. The oxidation state of the ocean during deposition of the Kuruman and Griquatown Formations remained reducing with respect to Mn. This decreased the Fe/Mn ratio over time, since Fe was removed from the system as ferric particulates precipitated. Manganese became an active redox-player only during the deposition of the overlying Hotazel Formation.

“It strikes me that all our knowledge about the structure of our Earth is very much like what an old hen would know of the hundred-acre field in a corner of which she is scratching.“

Charles Darwin to his friend John Maurice Rodwell (1831)

4

RARE EARTH ELEMENTS

Abstract

Rare earth element + yttrium (REY) abundances in banded iron formations have been widely used to track the chemistry of seawater and changes in the redox state of the near-surface environment. Banded iron formations (BIFs) are mineralogically heterogeneous with varying amounts of carbonate (ankerite + siderite), oxide (predominantly magnetite) and silicate (chert and Fe-silicates). To date, little is known about their respective contributions to the bulk-rock REY signal and the reason for the seawater-like REY patterns. This information is critical for interpreting the role of primary water column versus diagenetic processes in their formation.

This study focusses on the ca. 2.46 Ga Kuruman and Griquatown BIFs from the Griqualand West Basin in South Africa, which were deposited immediately before the Great Oxidation Event. Trace elements were sequentially extracted using acetate, oxalate and total digestion methods that were developed in previous chapters of this thesis. The extraction techniques were verified using REY recoveries, reproducibilities and *in situ* mineral specific abundances. This is the first study to successfully apply such a technique for REY on BIFs.

The Kuruman to the Griquatown Formation show distinctive REY patterns with strongly variable $(Yb/Ce)_{SN}$ observed in both bulk-rock and fraction specific patterns. This is most pronounced in the carbonate fraction, which in combination with other geochemical indicators suggests primary carbonate precipitation in a stratified ocean which became more shallow over time. The silicate fraction is influenced by various allochthonous (detrital and volcanic ash) sources. The oxide fraction is the most REY-depleted and therefore susceptible for allochthonous influences, but it shows a clear MREE enrichment. Such enrichment has not been described in BIFs before, but has been seen in sub-oxic, ferrous environments. Compared to the Griquatown, the Kuruman samples tend to be more oxide-rich, which potentially relates to an increase in dissimilatory iron reduction from the deeper Kuruman to the shallower Griquatown Formation.

4.1. Introduction

Shale-normalized rare earth element (REE) and REE + Yttrium (REY) patterns of bulk-rock banded iron formations (BIFs) show characteristic similarities with modern day seawater signatures (e.g. Derry and Jacobsen, 1990; Bau, 1993; Bau and Dulski, 1996; Bolhar, et al., 2004; Frei, et al., 2008; Planavsky, et al., 2010; Delvigne, et al., 2012). This has been one of the key arguments for direct chemical precipitation of the BIF minerals from seawater and that post-depositional modification of REE distribution is almost negligible (Bau and Dulski, 1996).

Based on the gradual decrease in ionic radii from La (1.16 Å) to Lu (0.977 Å), a result of progressive filling of the 4f electron orbital, the trends in lanthanide series element abundances tend to be smooth and predictable in many geochemical systems. Anomalous behaviour from this trend can be quantified by dividing the measured abundance of an element by one extrapolated from the neighbouring REEs: $[REE_n/REE_n^*] = REE_n/(½REE_{n-1}+½REE_{n+1})$, where REE_n as the normalized elemental abundance and n=1, 2, 3, is the REE in the order of the lanthanide series (Bolhar, et al., 2004). Some deviations from this method are necessary when an element has only one neighbour or if a neighbouring element potentially behaves anomalously as well. Both La and Ce can be anomalous and since La has no other neighbour, La and Ce anomalies are expressed graphically by plotting Ce/Ce* vs. Pr/Pr* (Bau and Dulski, 1996). Since both Eu and Gd can be anomalous in BIF, their anomalies are calculated by extrapolating between Sm and Tb: [Eu/Eu*] = Eu/(⅔Sm + ⅓Tb) and [Gd/Gd*] = Eu/(⅓Sm + ⅔Tb).

Ce and Eu are the only redox-sensitive REEs, due to the presence of an additional oxidation state next to the standard trivalent one. The microbial oxidation pathways of Ce and Mn are closely linked and are not simple functions of pH, oxygen concentration or other physical parameters (Moffett, 1994). So although the standard electron potentials for Ce oxidation are higher than for Mn (Table 4.1; Vanysek, 2017) under most Eh-pH conditions Mn can still be in its divalent form when is Ce already oxidized (e.g. Nakada, et al., 2016). The modern negative Ce anomaly in seawater is linked to scavenging of Ce(IV) onto Mn-nodules/particulates (e.g. Elderfield, et al., 1981). Therefore the absence of a negative Ce anomaly in seawater-like patterns captured by many Archean and Paleoproterozoic BIFs (e.g. Bau and Dulski, 1996; Alexander, et al., 2008; Frei, et al., 2008; Planavsky, et al., 2010) indicates that the seawater was still reducing enough to prevent the formation of Mn-

Table 4.1: Standard reduction potentials (E°) (Vanysek, 2017)

Half-reaction	E° (V) at 25 °C
$Ce^{3+} \leftrightarrow Ce^{4+} + e^-$	+1.72
$Mn^{2+} \leftrightarrow Mn^{3+} + e^-$	+1.5415
$Mn^{2+} + 2H_2O \leftrightarrow MnO_2\ (s) + 4H^+ + 2e^-$	+1.224
$Fe^{2+} \leftrightarrow Fe^{3+} + e^-$	+0.771

oxides.

Positive Eu anomalies in chemical sediments indicate a strong influence of hydrothermal fluids on the seawater Eu concentration (Bau and Dulski, 1996; Bolhar, et al., 2004). Under high-temperature (>250 °C) and low Eh, hydrothermal extraction of divalent Eu is more efficient than for other trivalent REEs (Bau and Möller, 1993). The hydrothermal fluid will therefore contain a positive Eu anomaly, which under anoxic conditions will influence the seawater budget (Bau and Möller, 1993; Bau and Dulski, 1996). Positive Eu anomalies are present in most BIFs (e.g. Planavsky, et al., 2010), however they are absent in IFs deposited in association with "Snowball Earth" conditions (e.g. Tsikos and Moore, 1997; Halverson, et al., 2011).

The usefulness of inserting Y between Dy and Ho, based on its ionic radius, has been shown before in BIFs (e.g. Bau and Dulski, 1996; Delvigne, et al., 2012). In present day seawater, Y behaves anomalously compared to Ho, which is its geochemical twin based on charge and radius (Bau, 1996). This behaviour has been attributed to surface complexation effects, whereby differences in type of chemical bonding (covalent vs electrostatic) signify that Y binds less strongly as surface-complexes compared to REEs, and is therefore less prone to removal from seawater, creating superchondritic Y/Ho ratios in the contemporary oceans (Bau, 1996). Superchondritic Y/Ho ratios in BIF have therefore been interpreted as a primary seawater signature (Bolhar, et al., 2004).

Although the majority of REE data on BIFs to date is for bulk-rock samples, some studies have measured distribution in individual minerals using techniques such as Laser Ablation ICP-MS. The study by Lepland, et al. (2002) investigated REE in apatite to determine its origin in the Eoarchean Isua BIFs. LA-ICP-MS analysis of various minerals (incl. magnetite) in the metamorphosed IFs of the Nuvvuagittuq Supracrustal Belt helped to constrain IF paragenesis and its suitability as a 3.8 Ga seawater proxy (Mloszewska, et al., 2012). Alibert (2016) produced the first mineral specific REE patterns in the Dales Gorge BIFs representative for typical, unmetamorphosed BIFs, in an attempt

to constrain diagenetic pathways for mineral formation. She concluded that many minerals do not show seawater-like REE patterns but display features better explained by equilibration with pore-waters, and hence formed during early diagenesis (Alibert, 2016). No attempt has yet been made to measure sequentially extracted REE patterns for BIF samples, but the technique has been shown to work for soils (Land, et al., 1999).

In this chapter I measure REE abundances in carbonate, oxide and silicate fractions using the sequential extraction technique developed in Chapter 2. Results for individual fractions are compared to bulk-rock and mineral specific REE data and demonstrate that a full concentration mass balance can be achieved. This is the first attempt to quantitatively compare REY patterns in BIF carbonates with co-existing oxides and silicates.

4.2. Methods

A total of 106 quarter-core bulk-rock BIF samples (~15 cm) capture the lithological variety of the Kuruman and Griquatown BIFs (Section 1.3.3; Appendix I). These samples were crushed and powdered in an agate mill. After pulverization major elements were measured by XRF, following the method of Norrish and Hutton (1969), at Rhodes University.

Chemical separation of the samples was carried out using a recently-developed sequential extraction procedure, described in Chapter 2. In summary, 30-50 mg of powdered sample was transferred into a 15 ml Greiner© tube. Each extractions used 10 ml of reagent, and after each step the sample was centrifuged and the supernatant filtered (0.2 µm). The extraction was started with 1M Na-acetate (pH adjusted with acetic acid to 4.5) under an inert N_2-atmosphere and allowed to react for 48 h at 50°C in a shaking incubator. The acetate step targeted the carbonates, with a duration and temperature optimized to extract crystalline siderite (Chapter 2; Poulton and Canfield, 2005). Subsequently a digestion step in 0.2 M NH_4-oxalate/0.17 M oxalic acid was applied for for 24 h, to extract the magnetite and any minor amounts of hematite present. The final residue was transferred to PFA-vials (Savillex, USA) for digestion using HF-HNO_3-$HClO_4$, targeting the silicate minerals.

The REE and trace element distributions, of both bulk-rock and fractions, were determined by ICP-MS (Themo Finnigan X-series) at Utrecht University. Calibration standards were matrix-matched to avoid suppression/enhancement effects and calibration curves were weighted (weighing factors

of 1/concentration) to take account of the concentration range that covered several orders of magnitude. A 10 ppb In-spike was used for internal standardization to correct for intra-run drift. Data are reported only above the element specific limit of quantification (LOQ), calculated as 10x the standard deviation of 10 blank, matrix-matched samples. Blank subtraction was calculated independently within each run.

Mineral specific REE patterns were determined *in situ* using a 193 nm wavelength COMPex 102 ArF excimer laser ablation system (Lambda Physik, Göttingen, Germany) connected to an Element 2 sector field ICP-MS (Thermo Scientific, Bremen, Germany) at Utrecht University. The mass spectrometer was operated in low resolution mode, with an energy density of 10 J/cm^2 and a pulse repetition rate of 10 Hz. The spot size (80 µm) was optimized to provide low detection limits for the REE but prevented measurement on small grains. ^{56}Fe was used as an internal standard for all minerals, except ankerite with ^{43}Ca. Data reduction of laser ablation data was performed using the GLITTER software. Calibration was performed against NIST SRM 612 and BCR-2G was used as a secondary reference standard, with results typically within 20% of published reference values in the GeoReM database (Jochum, et al., 2005).

At least four individual grains of the target minerals were analysed in every thin section (n=13). The purity of each grain was evaluated offline, by comparing the major element abundances to pure mineral data. The Si concentration could not be used to evaluate purity, because very fine grained chert was present in all samples. The filtered results (n=1 to 6) mineral were then averaged for each sample. REE (and REY) patterns were normalized to Post-Archean Australian Shale (PAAS) using the values of McLennan (1989).

4.3. Results and discussion

For the full data tables the reader is referred to Appendix IV: bulk-rock and sequentially extracted data and Appendix V: LA-ICP-MS data.

4.3.1. Bulk-data

PAAS-normalized bulk-rock REY data show a clear distinction between the lutite and BIF samples (Figure 4.1a). The lutites have generally unfractionated LREE/HREE, i.e. shale like patterns,

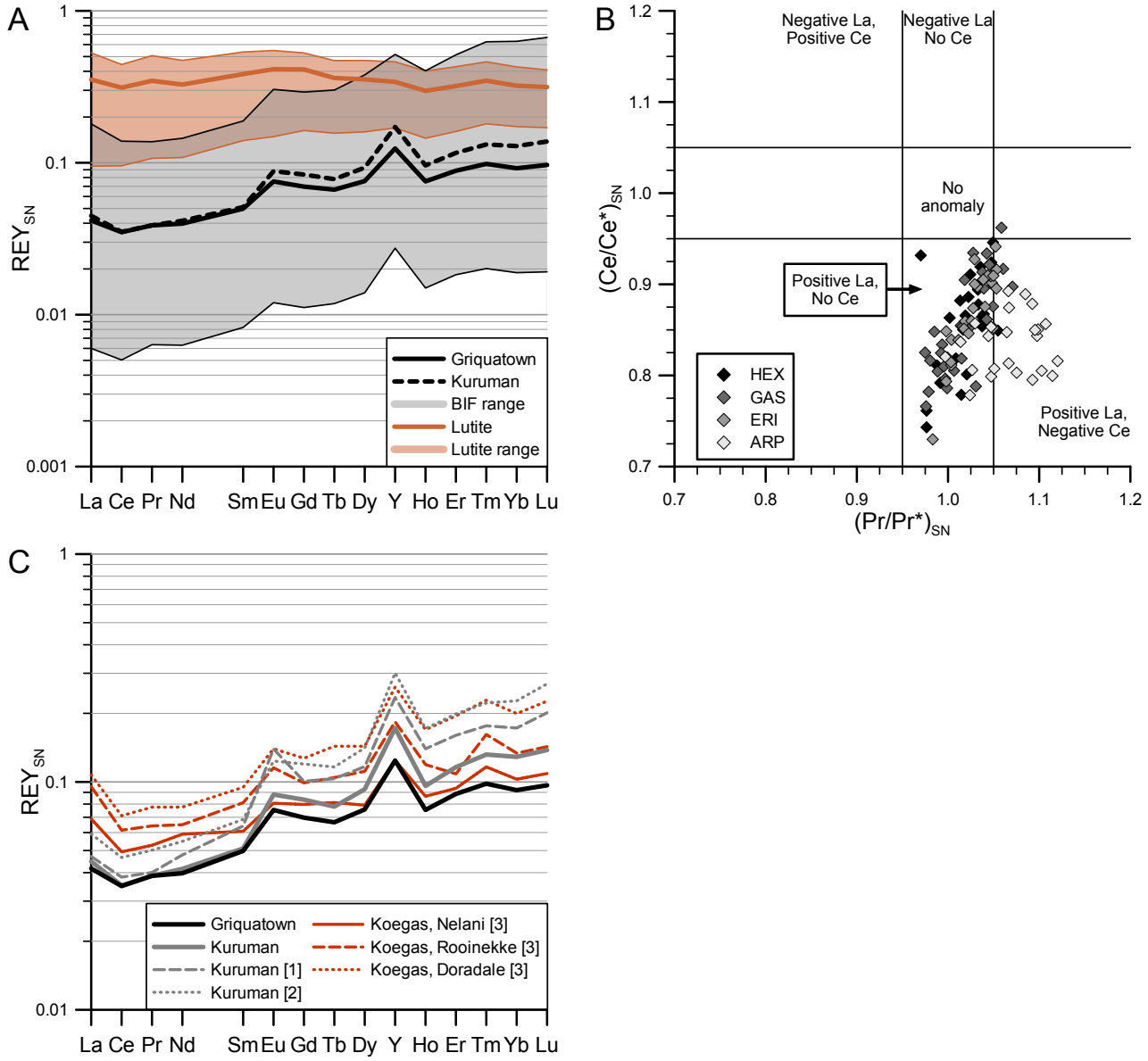

Figure 4.1 Bulk-rock REY data. A: Bulk-rock REY_{SN} ranges and averages for BIF (grey) and lutite (brown; n=5) samples. The BIF averages are for the Kuruman (n=34) and Griquatown (n=67) formations. B: $(Ce/Ce^*)_{SN}$ vs $(Pr/Pr^*)_{SN}$ showing the true La and Ce anomalies as described in Bau and Dulski (1996). C: Average Griquatown and Kuruman data of panel A compared to averaged literature REY_{SN} data of the Transvaal BIFs. Kuruman data are from [1] Bau and Dulski (1996; n= 14) and [2] Planavsky, et al. (2010; n= 3; note that here are Gd data absent). Koegas data from [3] Nel (2013), where flat lutite patterns were excluded for averaging. Koegas data include Nelani IF (n=20), Rooinekke IF (n= 10) and Doradale IF (n= 7).

whereas the BIF tend to be HREE enriched. These trends match those found previously for the Kuruman BIFs (Bau and Dulski, 1996; Planavsky, et al., 2010), the Koegas BIFs (Nel, 2013) and bulk-rock samples from the Dales Gorge BIF in the Hamersley basin (Pecoits, et al., 2009; not shown).

The bulk-rock samples of Bau and Dulski (1996) came only from the lower half of the Kuruman BIF (Groenwater member). The stratigrapic location of the three samples from Planavsky, et al.

(2010) is not disclosed and Gd data missing. The strong Eu anomaly present in the Kuruman data of Bau and Dulski, (1996) is less obvious in the other averaged patterns (Figure 4.1c).

The average Y/Ho ratio is super-chondritic for the BIF samples (45.2 ± 6.1), but near the chondrite ratio for the 5 lutite samples (29.5 ± 2.0). Bulk-rock Ce anomalies are absent whilst La shows predominantly positive anomalies (Figure 4.1b), confirming previous work on Paleoproterozoic BIFs (Bau and Dulski, 1996; Bolhar, et al., 2004; Planavsky, et al., 2010). The absence of Ce anomalies indicates that the seawater was still reducing with respect to Mn (Bau and Dulski, 1996).

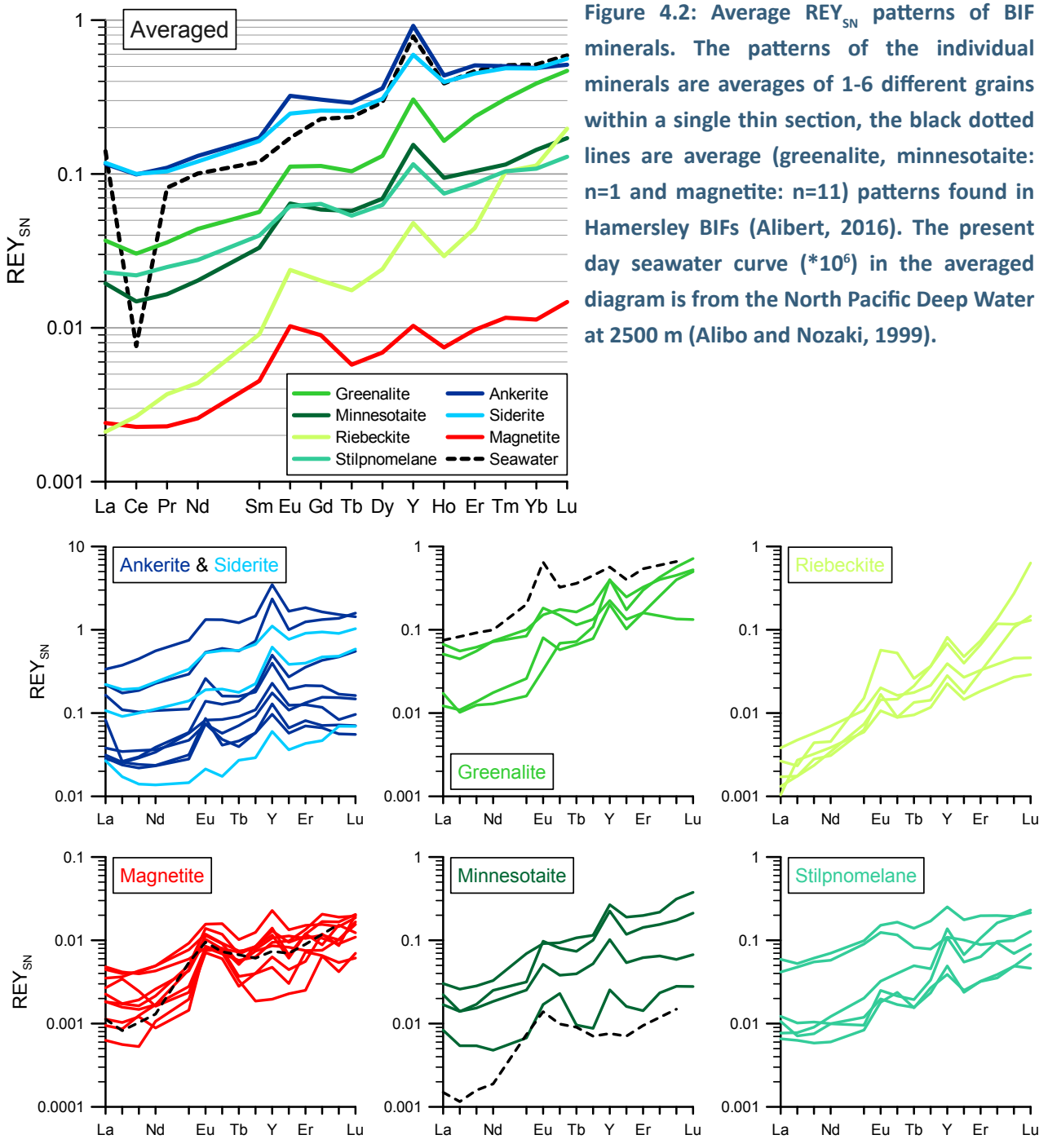

Figure 4.2: Average REY_{SN} patterns of BIF minerals. The patterns of the individual minerals are averages of 1-6 different grains within a single thin section, the black dotted lines are average (greenalite, minnesotaite: n=1 and magnetite: n=11) patterns found in Hamersley BIFs (Alibert, 2016). The present day seawater curve (*10^6) in the averaged diagram is from the North Pacific Deep Water at 2500 m (Alibo and Nozaki, 1999).

4.3.2. Mineral specific analyses

Grain-specific REY patterns of the different BIF minerals are plotted in Figure 4.2. All averaged trends show positive Eu and Y anomalies and positive La anomalies are present in all minerals except magnetite and riebeckite.

The positive slope in carbonate minerals matches those found in Dales Gorge BIF carbonate minerals (Alibert, 2016) and is similar to present day seawater (Alibo and Nozaki, 1999). Although there is some scatter in the silicate data, most of the patterns are HREE enriched. Some of the REY-enriched stilpnomelane patterns tend to be more flat. The steepest slopes are present of the amphibole-mineral riebeckite. Although the Eu anomaly in the data from Alibert (2016) tends to be more pronounced, the general trends for magnetite, greenalite and minnesotaite are quite similar. However, the Dales Gorge magnetite and minnesotaite are more depleted in LREE (La-Nd). See section 4.3.5.1 for a more detailed discussion.

4.3.3. Extracted data: Recoveries, distribution and reproducibility

Iron and other major elements show excellent recoveries, summed fractional data versus bulk-rock data which are presented elsewhere in this thesis (Chapters 3, 5). For the REE the recoveries are equally good (Figure 4.3a). For most of the samples the REE-recovery lies between 75 and 120 %,

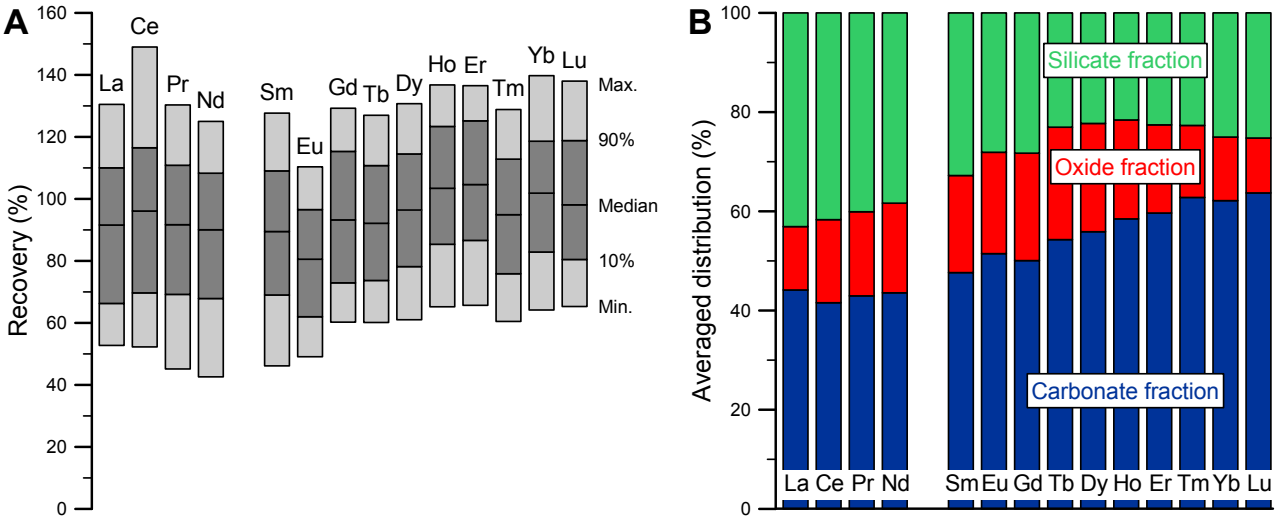

Figure 4.3: Extracted data. A: Recovery values of the REEs, summed extracted compared to bulk-rock. The median and the range for all samples are shown. B: The average sample-specific REE distribution over the three extracted fractions (i.e. determine distribution per sample, than average over all samples).

which is within the standard error of sub-ppb measurements on the ICP-MS. The median recovery for Eu is slightly poorer at 80 %. Based on QC and reference standard values, bulk-rock measurements overestimate Eu by ca. 10 %, whereas the species-specific QC values show an underestimation of ca. 20 %, which combined account for the low Eu-recovery. The Eu anomalies described previously for the Kuruman BIF (Bau and Dulski, 1996; Planavksy, et al., 2010) are higher than the ones found here, whereas the average Koegas IF patterns are similar (Figure 4.1c).

The measured ^{153}Eu values could be influenced by Ba-oxide interferences (Jarvis, et al., 1989), but no systematic offset was found when comparing Ba concentrations and corresponding Eu value. The average Ba/Eu ratio (ca. 236) in the measured samples is close to those of the calibration standards (110). Furthermore this is too small to induce significant uncertainties on the Eu data. Even when 5 % of the measured Ba is BaO^+, which is far higher than the expected percentage (ca. 0.1%, Jarvis, et al., 1989), the effect on the QC recovery rate of Eu is only minor (3 % increase). Thus slightly the poorer quality of the Eu-data is not related to Ba-interferences, but should still be treated with caution.

The averaged distribution of the specific REEs per sample are shown in Figure 4.3b. The acetate and HF fractions show an antithetic relationship, where the silicates are enriched in LREE and the carbonates in HREE. Although generally REE-poor, the oxalate fraction is relative enriched in MREE.

Two samples, HEX836 and GAS722 have been repeated in 8-fold. Their REE patterns (Figure 4.4) show in general an excellent reproducibility. The reproducibilities of Gd and Tb are slighly poorer

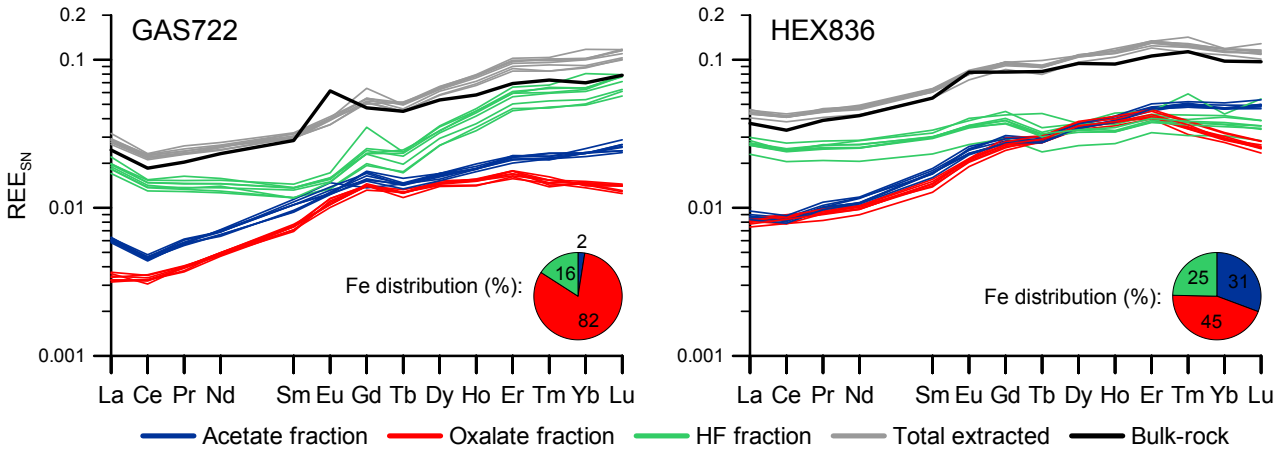

Figure 4.4: Species specific REE_{SN} patterns of GAS722 and HEX836 in 8-fold. The reproducibility is good and the total extracted matches the bulk-rock values. The pie-graph shows the Fe-distribution of the respective samples.

in the silicate fraction. For the other duplicate samples, the reproducibility lies generally within the typical uncertainty at the tens of percent level of the ICP-MS measurements. From here on duplicate values are averaged per sample.

4.3.4. Species-specific REY patterns

To directly compare species-specific REY patterns with each other and mineral data, they have

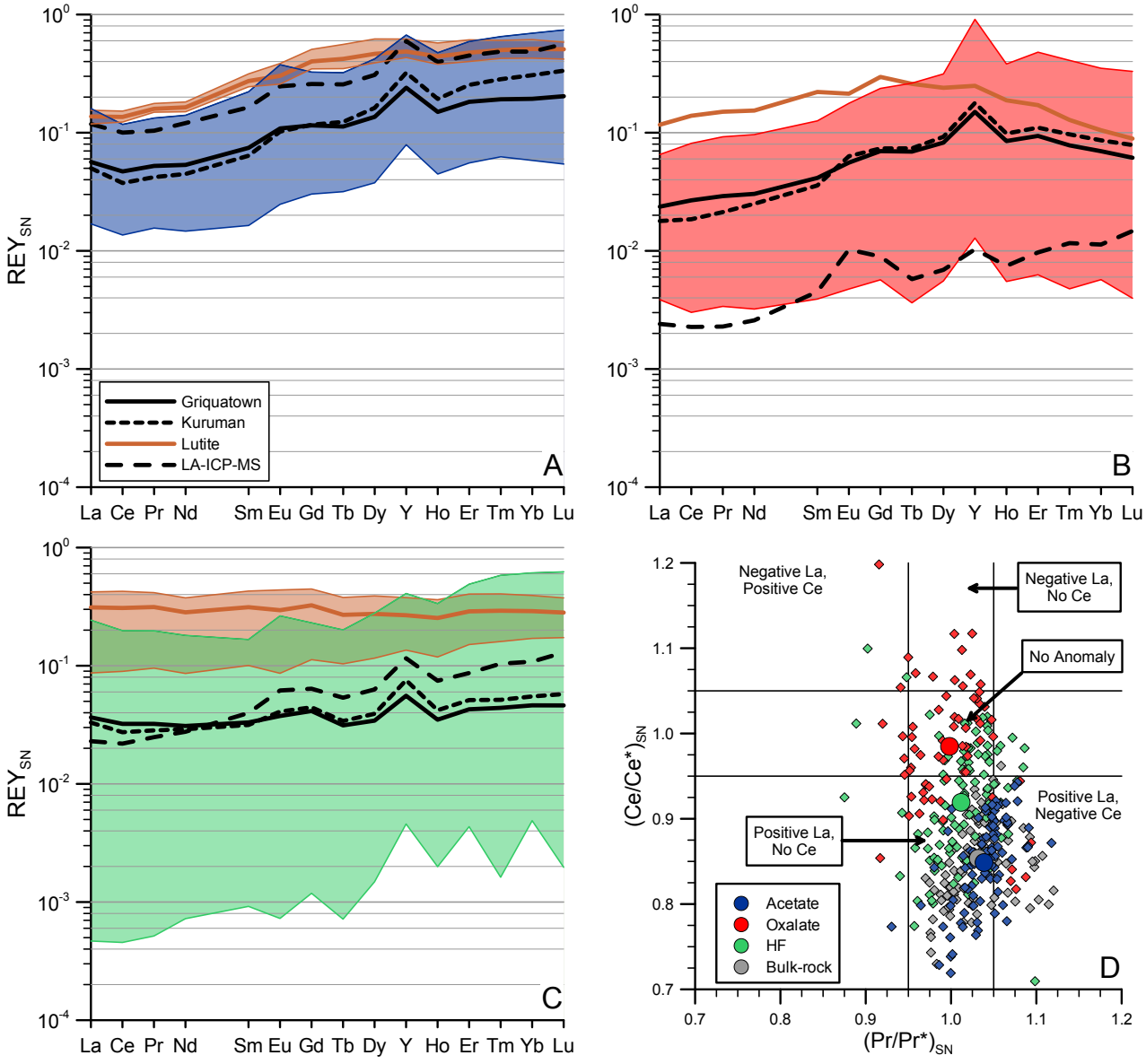

Figure 4.5: Fraction specific REY_{SN}-ranges for the (A) acetate, (B) oxalate and (C) HF extractions. Black and dotted lines are the means for the Griquatown and Kuruman samples respectively. Brown line and ranges are for the lutite sample(s). The dashed LA-ICP-MS line is the mean siderite, magnetite and stilpnomelane data for A, B and C respectively. D: $(Ce/Ce^*)_{SN}$ vs $(Pr/Pr^*)_{SN}$ showing fraction specific La and Ce anomalies as described in Bau and Dulski (1996). The round symbols are the means of the fractions, the colored diamonds represent individual analyses.

to be normalized to the percentage that fraction constituted of the bulk-rock. Each normalization factor was calculated based on the amount of major oxides extracted (plus bulk-rock CO_2 for the acetate). Fractions consisting of less than 10 wt% were omitted because of their large uncertainties due to the low REY-abundances in combination with high normalization factors.

Next to the five lutite samples, the remaining 101 BIF samples are distributed over the Kuruman (n= 34) and Griquatown (n= 67) Formation. After filtering the dataset for LOQ (section 4.2) and the 10 wt% cut-offs, 92 acetate, 67 oxalate and 100 HF samples were accepted and have complete REY patterns. The 92 acetate samples constitute 25 Kuruman samples, 63 Griquatown BIF samples and 4 Griquatown lutites; for the 67 oxalate samples these numbers are 27, 39 and 1 respectively and the 100 HF-samples are split as 32, 63 and 5 respectively. These cut-off criteria reflect the fact that the Kuruman samples are relatively magnetite-rich (27 accepted of the 34 samples) and the Griquatown samples are magnetite-poor (39 of the 67).

The REY_{SN}-ranges of the BIF and lutite samples are plotted in Figure 4.5a-c together with the averages for the Kuruman and Griquatown samples. The acetate fraction shows a relatively narrow range (Figure 4.5a) and all samples have a positive slope. The oxalate-extracted REY_{SN} patterns show a relative MREE enrichment to the Pr-Yb line from Eu to Er (Figure 4.5b). The largest REE-range is found in the silicate fraction (Figure 4.5c) which varies over 3 orders of magnitude. This variation can be explained by the sample specific silicate mineralogy and includes the variable dilution with chert.

The Y/Ho ratios seen in the bulk BIF and lutite samples are also recorded in the different fractions, i.e. super-chondritic ratios for BIF and near chondrite values for the lutites. The positive La anomaly present in the bulk-rock samples is only absent in the oxalate fraction (Figure 4.5d). The La anomaly is most pronounced in the carbonate fraction, which averages around the bulk-rock mean. The silicate fraction plots in-between the end-members. These anomalies are consistent in the LA-ICP-MS data, as magnetite and riebeckite are the only minerals without a positive La anomaly (Figure 4.2). Riebeckite is generally considered to be of secondary origin related to external Na input (e.g. Trendall and Blockey, 1970), and the large magnetite crystals analysed by LA-ICP-MS are also non-primary, so the absence of a distinct La anomaly might be related to early diagenesis.

The Griquatown samples are enriched in LREE and depleted in HREE compared to the Kuruman samples, in both the bulk-rock and all three fractions. In other words, the Kuruman REY patterns are

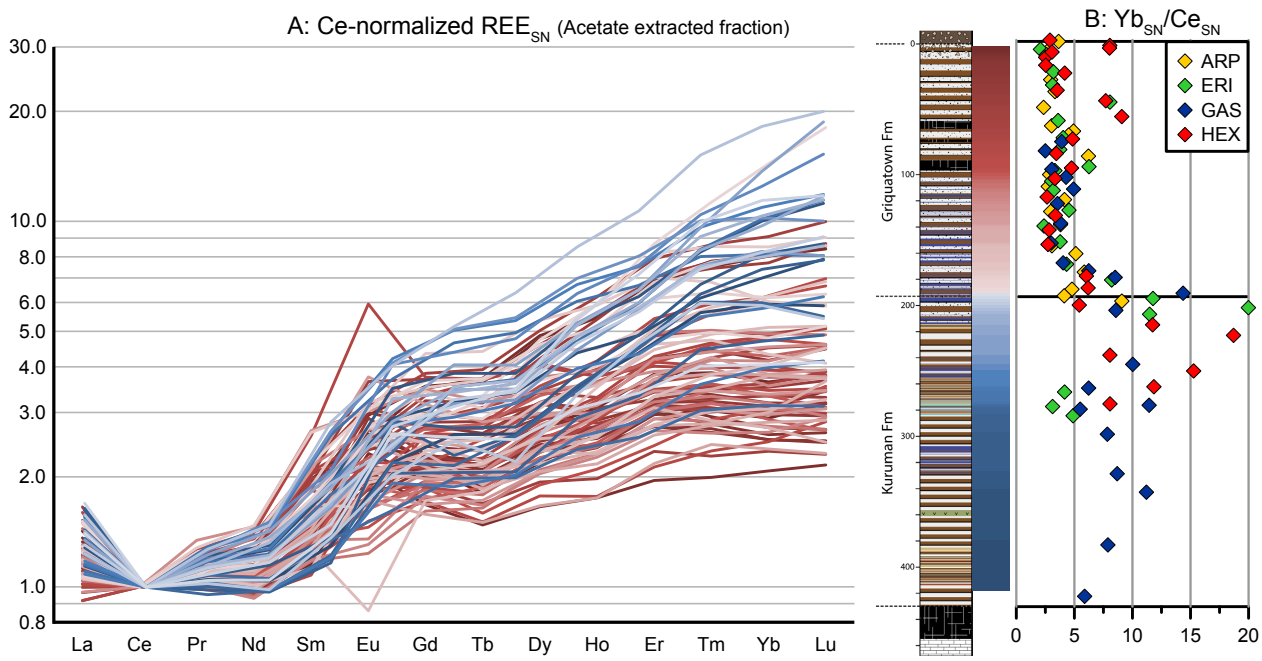

Figure 4.6: REE$_{SN}$-slope changes in the acetate extracted fraction. A: By normalizing to Ce the change from the Kuruman (blue) to the Griquatown (Red) becomes apparent. Color codes are plotted next to the log. B: The (Yb/Ce)$_{SN}$ plot for the samples by drill-core shows the slope change between the Kuruman and Griquatown Formations.

steeper than the Griquatown ones. This can be constrained by the (Yb/Ce)$_{SN}$ ratios, which in case of the acetate fraction, decrease with stratigraphy from a mean value of 9.2 in the Kuruman Formation to 4.4 in the Griquatown IF (Figure 4.6). This decrease is less pronounced in both the oxalate (4.3 to 2.7) and HF (2.7 to 2.1) fractions. An explanation for this flattening could be contamination by detrital input. Going from the deeper water Kuruman IF to the shallower Griquatown indicates deposition potentially more proximal to land, and hence might yield a higher detrital input. Widely used indicators for clastic contamination are elements regarded as immobile in aqueous solutions such as Zr, Ti, Hf, Th and Sc (Bau, 1993).

When Zr is plotted against Nd (Viehmann, et al., 2015) a clear trend is visible for the bulk-rock samples (Figure 4.7). The five lutite bulk-rock samples, representing volcanic ash input, contain the highest concentrations of both elements. When the most enriched lutite sample is taken as the detrital dominated end-member a mixing line between near-pure BIF and allochthonous influence can be constructed. Most of the bulk-rock BIF samples contain less than 10% detrital or volcanic ash material, but the Griquatown samples are more enriched in Zr than the Kuruman ones. So, for the bulk-rock patterns (Figure 4.1) the variation might be due to a slight increase in a detrital or volcanic ash component. This is also confirmed by the plot of the steepness (Yb/Ce vs. Zr), which follow a

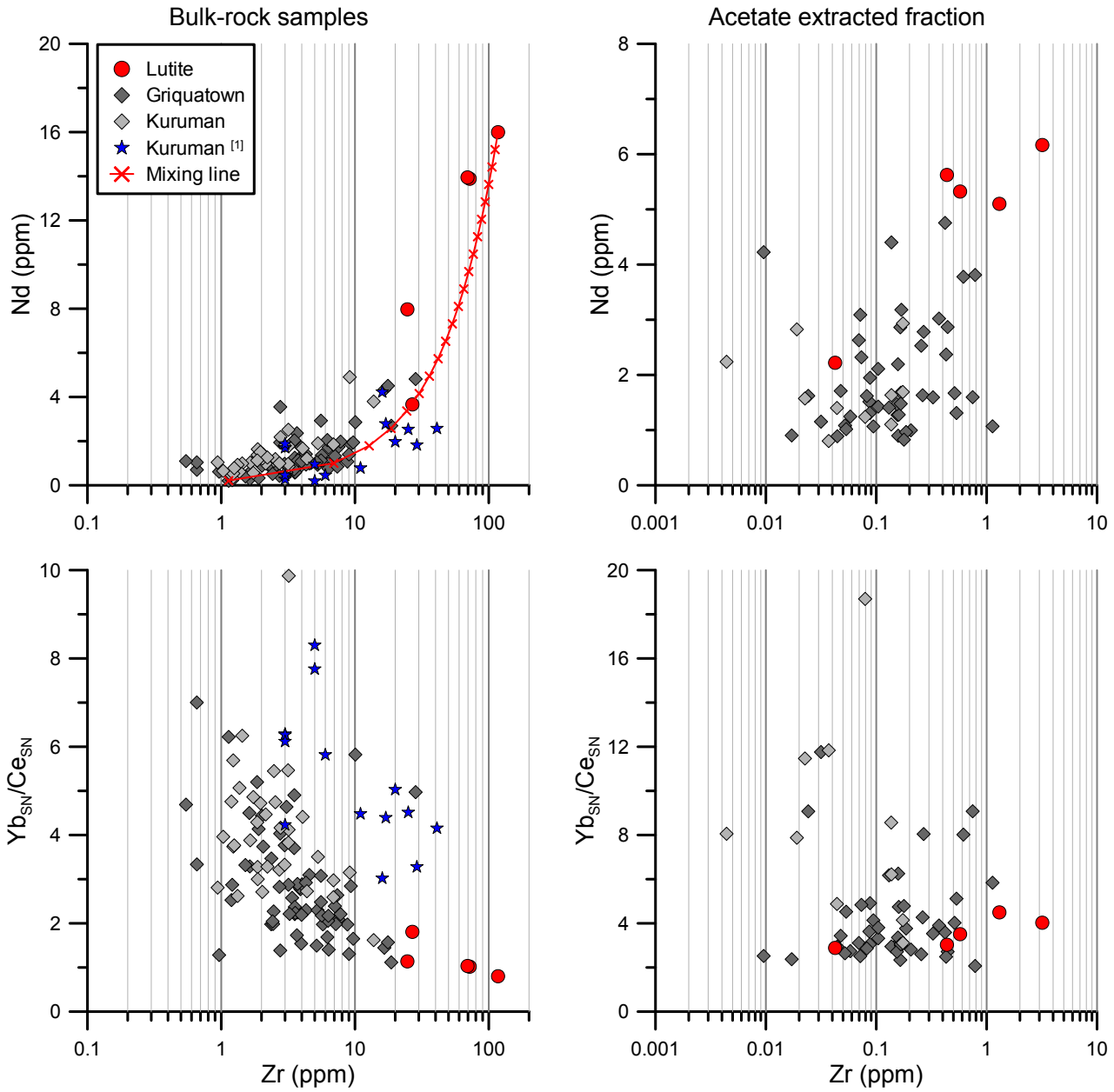

Figure 4.7: Nd-concentration (top) and $(Yb/Ce)_{SN}$ ratio (bottom) versus Zr (concentration) of the bulk-rock (left panels) and acetate extracted (right panels) samples. The lutite sample (red dots) with the highest Zr and Nd concentration was taken as detrital component and the lowest concentration as pure BIF. The crosses on the mixing line represent a 5% increase in detrital contaminant, suggesting that most BIF samples contain less than 10% detrital material. The Kuruman [1] bulk-rock values published in Bau and Dulski (1996), for Zr <5 ppm an arbitrary concentration of 3 ppm was assigned to allow plotting. Note the scale changes between the left and right panels.

distinct trend. This is also the case for the bulk-rock samples from the lower half of the Kuruman IF as published in Bau and Dulski, (1996), where higher Zr-contents are generally associated with flatter REE slopes (Figure 4.7).

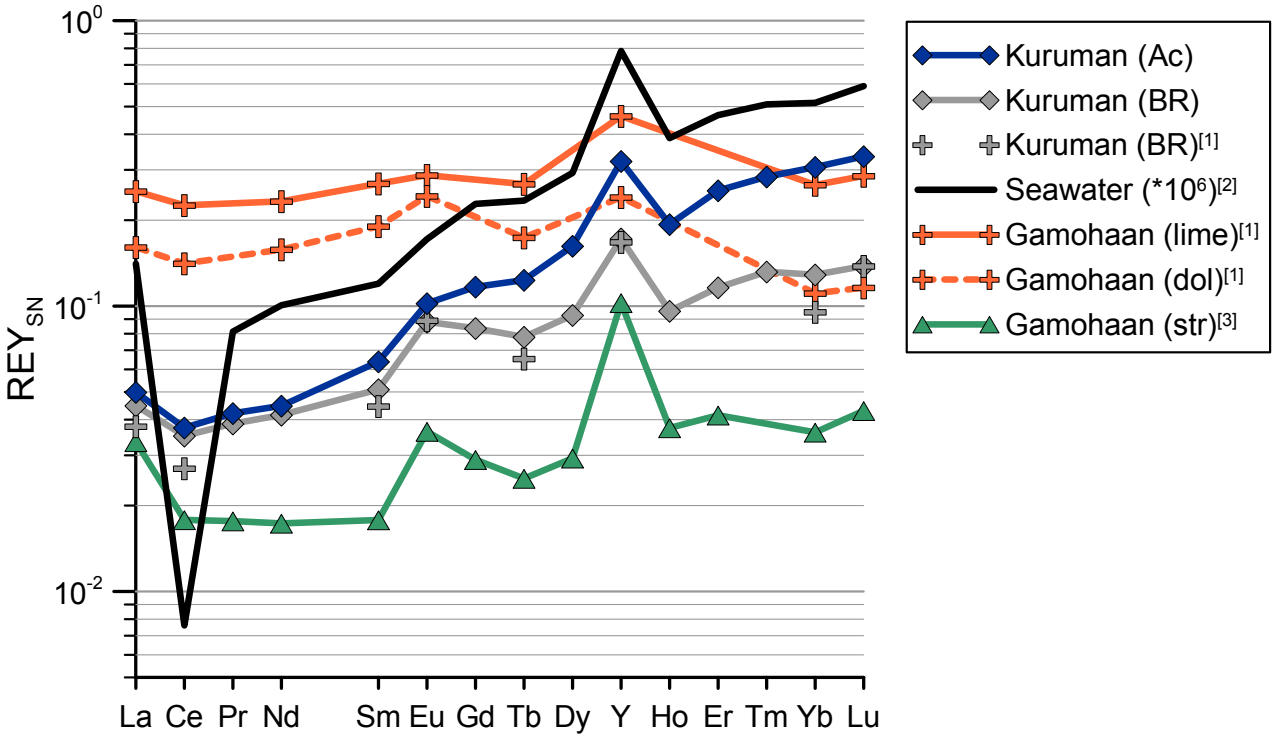

Figure 4.8: REY$_{SN}$ patterns of the Kuruman and Gamohaan Formations. Showing the averages of the acetate-extracted fraction (Ac), the bulk-rock (BR) of the Kuruman (this study and [1]), the modern seawater composition (*10⁶) [2] and the Gamohaan carbonates (limestone and dolomite [1] and microbial carbonates [3]) Data from: [1] Klein and Beukes, 1989; [2] Alibo and Nozaki, 1999; [3] Kamber and Webb, 2001.

4.3.4.1. Carbonate fraction

Whilst changes in the REE slope in the bulk-rock samples can be explained by detrital/volcanic ash input, this is not the case for in the carbonate fraction. The Zr concentration in the carbonate fraction is generally well below 1 ppm, indicating near-zero detrital contamination and no trend is present in the (Yb/Ce)$_{SN}$ vs. Zr plot (Figure 4.7). The carbonate mineralogy can be constrained by the Ca concentration in the fraction since siderite is Ca-free, calcite only exists as a trace mineral and the Ca/Fe ratio in ankerite is fixed. Because no relationship exists between Ca and the Yb/Ce ratio, the slope change is also independent of mineralogy. The foregoing arguments indicate that the stratigraphical variation in the Yb/Ce ratio of the carbonate fraction is authigenic. In contemporanous oxidized seawater such a slope change is also observed, showing an increased (Yb/Pr)$_{SN}$ ratio with depth (e.g. Piepgras and Jacobsen, 1992; Alibo and Nozaki, 1999).

The carbonate fraction in the Kuruman BIFs can be compared with the underlying Gamohaan carbonates of the Campbellrand Subgroup (Figure 4.8). The steep trend described earlier is not

visible in the microdrilled microbialites of Kamber and Webb (2001), which actually show a much flatter pattern ($(Yb/Ce)_{SN}$ = 1.8). Bulk-rock microbialite samples from the slightly older Upper Nauga Formation within the Campbellrand Subgroup show similar patterns, although slightly more REE enriched (Voegelin, et al., 2010). Incomplete REY patterns of the Gamohaan Formation published previously by Klein and Beukes (1989) show a flat or even HREE depleted trend. However, their bulk-rock analyses shows high abundances of Al_2O_3 and SiO_2, indicating that the samples analysed were not pure carbonates. Minor amounts of REE-rich shales (< 1 wt%) for example can influence the slope of the carbonate pattern dramatically (Bau, 1993; Webb and Kamber, 2000; Van Kranendonk, et al., 2003).

Bulk-rock BIF REY patterns and their similarities to contemporary seawater patterns have been described before (e.g. Derry and Jacobsen, 1990). The fact that both the carbonate-fraction and the *in situ* carbonate analyses show an even better correlation could indicate direct derivation of the REE from seawater and a possible primary origin for the carbonate. Present-day microbialitic carbonates capture the seawater signature without strong fractionations (Webb and Kamber, 2000).

The distinct carbonate patterns between the three continuous formations, Gamohaan, Kuruman and Griquatown can be explained by varying water depths, whereby the subtidal Gamohaan Formation (Sumner, 1997) shows the flattest REY pattern. The transition from a stromatolite platform to siderite-rich and then oxide-rich BIF is consistent with continued deepening of the basin (Klein and Beukes, 1989; Sumner, 1997). The Kuruman samples in this study are mainly from the oxide-rich section, indicating the deepest setting and they display the steepest REY patterns. The transition to the granular Griquatown Formation indicates a shallowing towards storm-wave base (Beukes and Klein, 1990) and their respective REY patterns are intermediate in slope between the formations mentioned above. Contemperanous seawater shows similar variations in seawater REE_{SN} patterns with depth (e.g. Piepgras and Jacobsen, 1992; Alibo and Nozaki, 1999).

Another way to explain the differences between the two iron-formations might be that the basin became relative HREE depleted (or LREE enriched) by reservoir effects over time due to preferential HREE incorporation into the crystal lattice of $FeCO_3$ (e.g. Bau, 1993). However, to accommodate the jump from the Campbellrand to the Kuruman samples, the basin would need to be completely refreshed in REY. Sustained Rayleigh fractionation over the Asbestos Hills deposition time-scales (10^7

years; Pickard, 2003) is unlikely.

A conceptual model of >2.4 Ga ocean redox structure based on REE in BIF and carbonates (*Figure 6c in* Planavsky, et al., 2010) indicates a water column depth-gradient in REE (Kamber and Webb, 2001; Planavsky, et al., 2010). Based on this, in combination with other evidence indicating seawater gradients during the Asbestos Hills deposition, such as $\delta^{56}Fe$ (Chapter 5) and $\delta^{13}C$ (Figure 1.11; Tsikos, et al., in prep.), a water column gradient in REE is the favoured interpretation.

4.3.4.2. Oxide fraction

In the sequentially extracted oxide fraction most MREE (especially from Eu to Er) are enriched. This MREE enrichment is quantified here by calculating the deviation of Tb from the Pr-Yb line. These elements were chosen since no anomalies have been described previously for them and Tb lies centrally between Pr and Yb in the lanthanide series. Since Tb lies 6 places from Pr, including Pm and 5 from Yb excluding Y, the reference value should be: $Tb^* = (^5/_{11})Pr + (^6/_{11})Yb$. The range of Tb/Tb* for the BIF samples in the oxide fraction is 0.78 - 2.50 with an average of 1.49 ± 0.37.

An enrichment of MREE and its relationship with Fe has been shown before, amongst others, on oxide-coatings on fossil foraminfera (Palmer and Elderfield, 1986), particulates from a hydrothermal vent (Sherrell, et al., 1999) and in anoxic, Fe-rich porefluids (Haley, et al., 2004). In the latter study the enrichment was explained by dissolution of a surficial solid Fe-phase which inherited this pattern from seawater (Haley, et al., 2004). An explanation for the oxide fraction Eu-Er enrichment might thus be related to preferential MREE adsorption onto ferric-iron particles during settling through the water column (Sherrell, et al., 1999).

An MREE-enriched pattern, however, has not been described in any detail for bulk-BIF samples. This can be attributed to the low abundance of REE in magnetite (Figure 4.2), especially compared to the other mineralogical fractions (Figure 4.3), which means that there are few reliable literature data available for comparison.

Two different techniques have been used to determine magnetite-specific REE patterns; LA-ICP-MS (Mloszewska, et al., 2012; Alibert, 2016) and microdrilling or mineral separation (Barrett, et al., 1988; Bau and Alexander, 2009). The average patterns of the mineral separation techniques are flatter and have a higher REE concentration compared to the LA-ICP-MS or the sequentially extracted

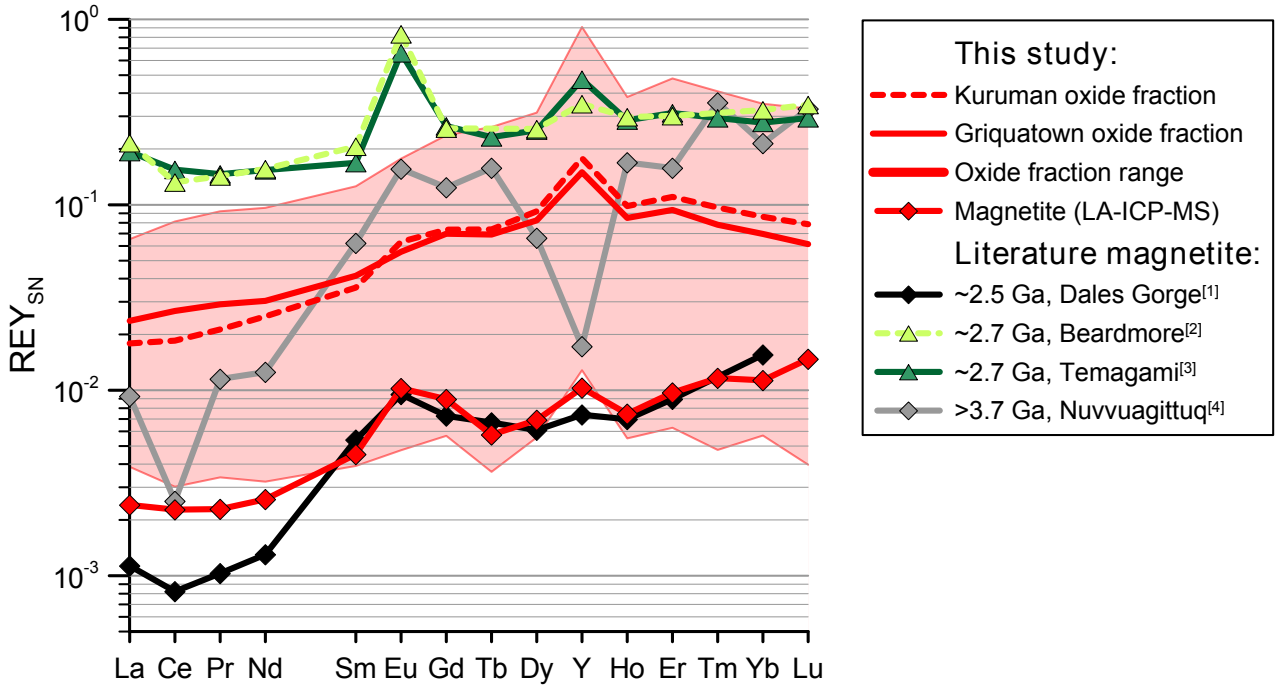

Figure 4.9: REY_{SN} patterns of oxide fractions and magnetite in BIF. The different techniques used to determine the magnetite REY patterns are LA-ICP-MS (diamonds) and mineral separation/microdilling (triangles). [1] Average of 11 magnetite samples of the Hamersley BIF (Alibert, 2016). [2] Average of 2 mineral seperates of the Beardmore-Geraldton BIFs (CD-2 and VL-1, Barrett, et al., 1988). [3] Average of 12 microdrilled magnetite bands of the Temagami IF (Bau and Alexander, 2009). [4] Average of the silicate- poor and rich BIFs in the Nuvvuagittuq Supracrustal Belt (Mloszewska, et al., 2012).

(this study) ones (Figure 4.9). Possible detrital contamination in the microdrilled samples could explain the difference. With such low ΣREE concentrations only minor amounts or REY-rich shale can strongly influence magnetite data (e.g. Van Kranendonk, et al., 2003). Contamination is supported by the realively high Al (0.4 to 1.2 wt%) and Zr (6-17 ppm) concentration-ranges in the study by Bau and Alexander (2009), above the averages in the sequentially extracted fractions reported here (0.2 wt% and 5 ppm, respectively).

Two studies have published REE patterns of magnetite in BIF using LA-ICP-MS; the ca. 2.5 Ga Dales Gorge BIF in Australia (Alibert, 2016) and the ≥3.75 Ga metamorphosed Nuvvuagittuq BIFs (Mloszewska, et al., 2012). The REE patterns of the latter study are not comparable to the unmetamorphosed BIFs of the Transvaal Basin. With the exception of La-Nd the magnetite data for the Dales Gorge and the Kuruman/Griquatown BIFs compare really well (Figure 4.9). The low LREE values in the Dales Gorge magnetite (Alibert, 2016) result in a strong MREE enrichment based on the Pr-Yb line. As the Transvaal magnetites have higher LREE values, the MREE enrichment here is virtually absent.

The oxide fraction patterns are much more enriched in REE when compared to the LA-ICP-MS magnetite ones. An explanation could be that the micro-analysed magnetites represent only the larger aggregates in the sample and not the significant portion of smaller oxide-crystals. The larger magnetites are clearly secondary and could have incorporated signals from other precursor minerals and/or pore-fluids during diagenesis, whereas the fraction data covers the entire oxide mineral budget.

4.3.4.3. Silicate bound REE

The wide range in overall REE abundances for the silicate fraction is attributed to dilution by chert. The individual REY-data of the acetate and oxalate fractions follow the average trends shown in Figure 4.5 whereas the individual silicate patterns show considerable variation. This variation can be grouped into 5 distinct trends (Figure 4.10). The largest of which consist of 42 samples showing a positive slope. The 5 lutite samples are among the 28 samples with a horizontal pattern. Less frequent patterns are those that are MREE depleted (n= 17) and show negative slopes (n= 6). The 7 patterns showing MREE enrichment are identical to each other and only vary in overall REY abundance.

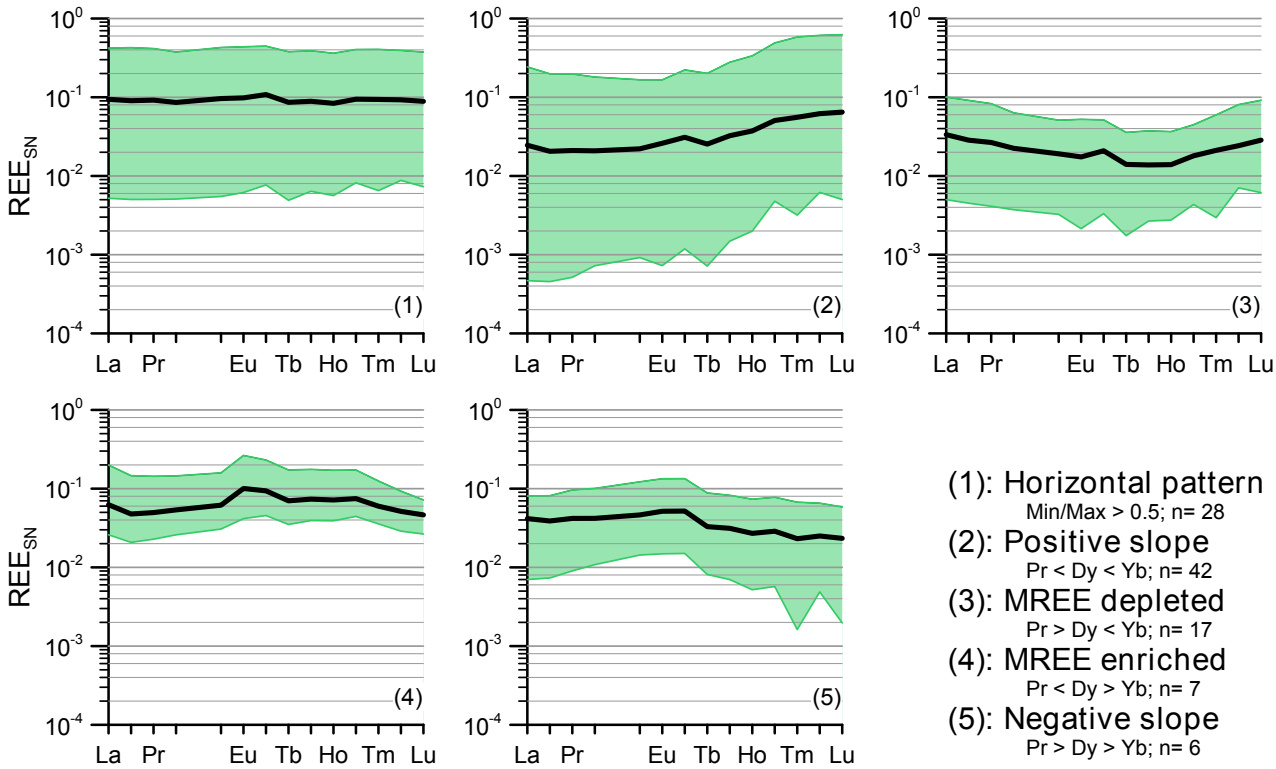

Figure 4.10: The five distinct type of patterns are shown and include both the range and the mean value. See text for discussion.

The average LA-ICP-MS data of all the measured silicate minerals have a positive REE_{SN} slope (Figure 4.2), thus mixing of these minerals should retain this positive slope. However, the stilpnomelanes in Figure 4.2 with the most abundant REEs tend to be flatter than the other ones. The fact that the lutites are present in the horizontal group and that their main Fe-silicate mineral is stilpnomelane indicates that these patterns can, at least partially, explained by abundant stilpnomelane. Any other correlation between mineralogy and REE pattern is not clear.

Very small grains or inclusions of REE-rich minerals such as xenotime, monazite and apatite, which have been described in the Dales Gorge BIF, could potentially have a major influence on bulk-rock or even mineral specific REY-data. These minerals can be either detrital or authigenic in origin (Alibert, 2016). The complex and challenging REE patterns in the silicate fraction can thus related to differences formation processes and origins of the silicate minerals. A complete explanation for all different patterns is beyond the scope of this study.

4.3.5. Depositional model based on REY

4.3.5.1. Existing model based on mineral specific analyses

The mineral specific REE patterns shown here (Figure 4.2), match generally well with those published by Alibert (2016) for magnetite, greenalite, minnesotaite and, although not shown, the carbonate minerals. The magnetite and minnesotaite from the Dales Gorge BIF are slightly more depleted in LREE (La-Nd) than the ones from the Transvaal Supergroup.

The focus of the study by Alibert (2016) is on apatite, which, although a good REE host, is only a minor constituent in the Dales Gorge BIFs (P_2O_5 ≈ 0.2 wt%). Based on similar patterns between the whole-rock and the apatite REEs and high REE concentrations in apatite, Alibert (2016) concluded that the iron oxides and carbonates carry only a small fraction of the whole-rock REE budget. In the Kuruman and Griquatown samples studied here the average P_2O_5 content is only 0.06 wt% as determined by XRF, making this less plausible for these samples. The vast majority of bulk-rock Asbestos Hills samples analysed (Klein and Beukes; 1989, Beukes and Klein, 1990) have similar (<0.10 wt%) concentrations of P_2O_5 and the average value of all samples analysed by Horstmann and Hälbich (1995) is 0.10 wt%. None of these studies mentioned any apatite, and to my knowledge

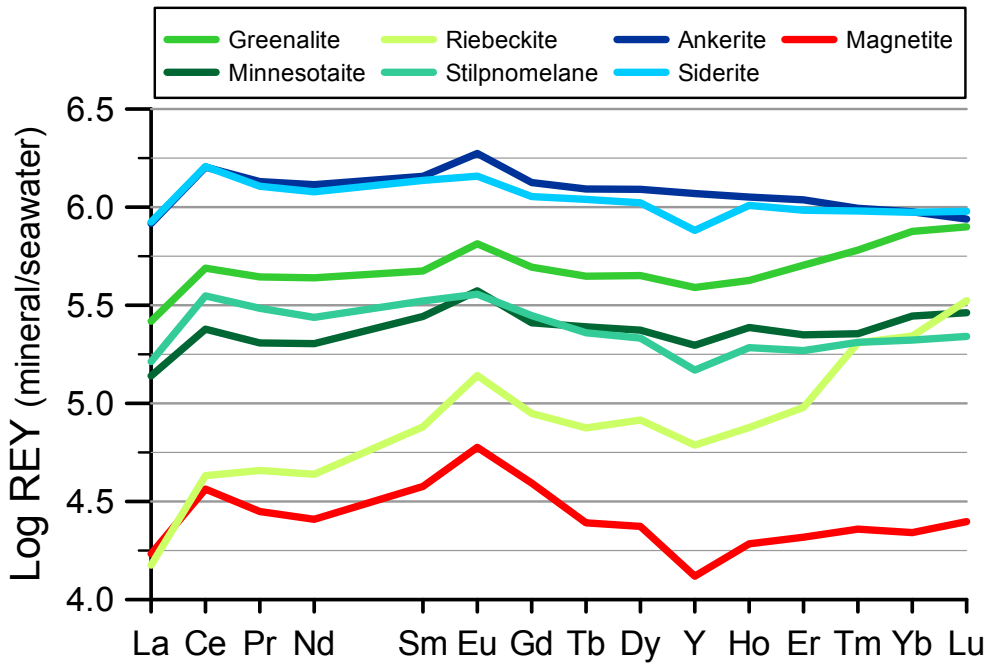

Figure 4.11: Average REY mineral composition normalized to NPDW seawater at 2500 m depth (Alibo and Nozaki, 1999). The contemporaneous seawater Ce anomaly was removed by extrapolating the Pr-Nd line to Ce. The flatter the lines, the more they resemble present day seawater.

apatite has not been described in the Asbestos Hills BIFs. Although not explicitly searched for, was not found during thin section petrography in this study.

In the Alibert (2016) model, apatite was considered to be the main REE host. Si-ferrihydrite quantitatively captured seawater REE signals due to the high partition coefficients (K_d) for REEs sorbed on Fe-(hydr)oxides (Quinn, et al., 2006) and high Fe/REE ratios. This precipitating Si-ferrihydrite then released its Fe^{2+}, P and REEs into the porewaters of the sediment during dissimilatory iron reduction (DIR). REEs were then sequestered into authigenic apatite and to a lesser extent the iron oxides and carbonates. These apatites thus inherited a seawater-like REE signature from the Si-ferrihydrite, whereas the REE patterns of hematite, greenalite, siderite or ankerite, show features typical of equilibration with pore-water. The similarities between contemporaneous seawater and the apatite REE patters is shown by a relatively flat line in the log-plot for mineral REE abundance normalized to seawater concentrations (*Figure 5 in* Alibert, 2016). When this is done for the average Asbestos Hills mineral-specific REE data (Figure 4.11) similar arguments can be made for the carbonate minerals, which show REY slopes almost unfractionated from seawater.

The recent discovery of apatite nanoparticles intergrown in magnetite in the Dales Gorge

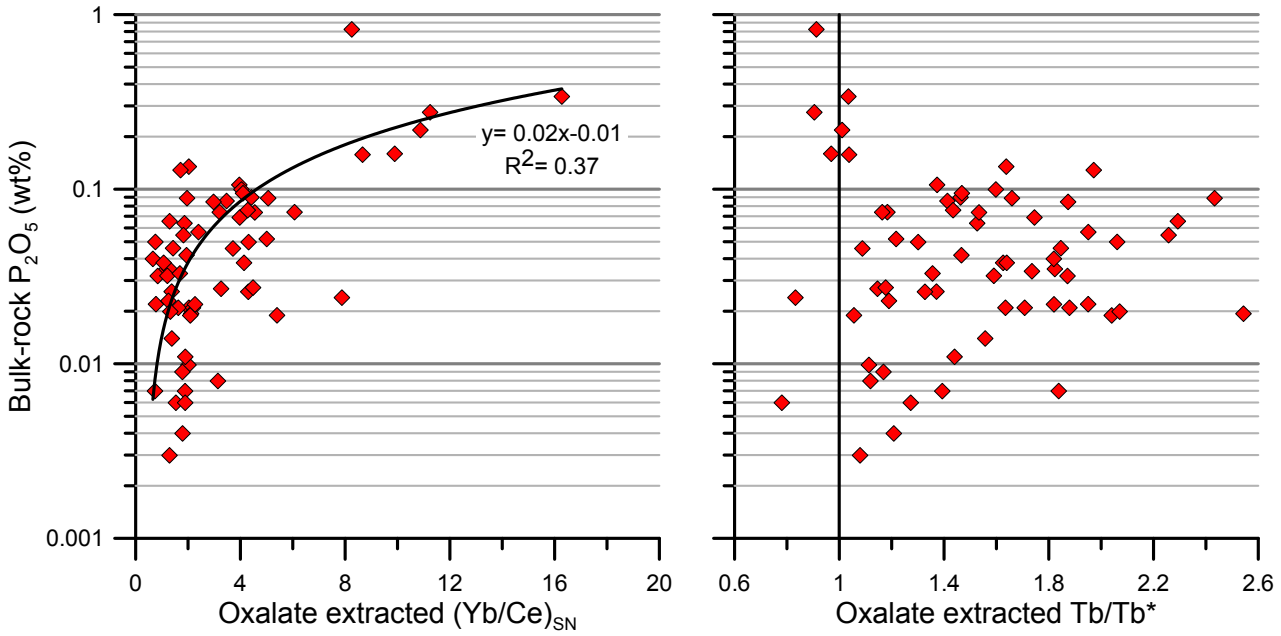

Figure 4.12: Bulk-rock P_2O_5 versus the oxalate extracted $(Yb/Ce)_{SN}$ and Tb/Tb*. See text for discussion

Member of the Brockman IF (Li, et al., 2011) can potentially be an explanation as to where the P is present in the Asbestos Hills BIFs. Phosporus was generally below detection limit for the extracted samples. However, there is a relationship visible for the relative P-rich bulk-rock samples and the $(Yb/Ce)_{SN}$ ratio in the oxalate extracted fraction (Figure 4.12). The P-rich samples coincide with steeper REE patterns, which potentially could be related to the presence of LREE depleted, HREE enriched phosphate minerals such as apatite or xenotime (Alibert, 2016). Nanoparticulate apatite could be readily digested during the oxalate-step. However, there seems to be no relationship between bulk-rock P_2O_5 and MREE enrichment (as Tb/Tb*), indicating that the distinctive REY slope is related to preferential MREE adsorption onto ferric-iron particles (Sherrell, et al., 1999).

For the greenalite pattern, Alibert (2016) argues that it resembles the experimental distribution patterns between clays and saline solutions. This was interpreted in her study to reflect direct precipitation from pore-water enriched in silica, Fe^{2+} and REEs, similar to the Fe-oxides and Fe-carbonates. The possibility that, instead of releasing these constituents by DIR into porewaters, these were released in the "open" benthic zone was not considered by Alibert (2016), but this would fit the data. In this case the greenalite formation pathway could be relative similar to the Fe-carbonates. An alternative model, based on the fraction specific data and *in situ* mineral data is given below.

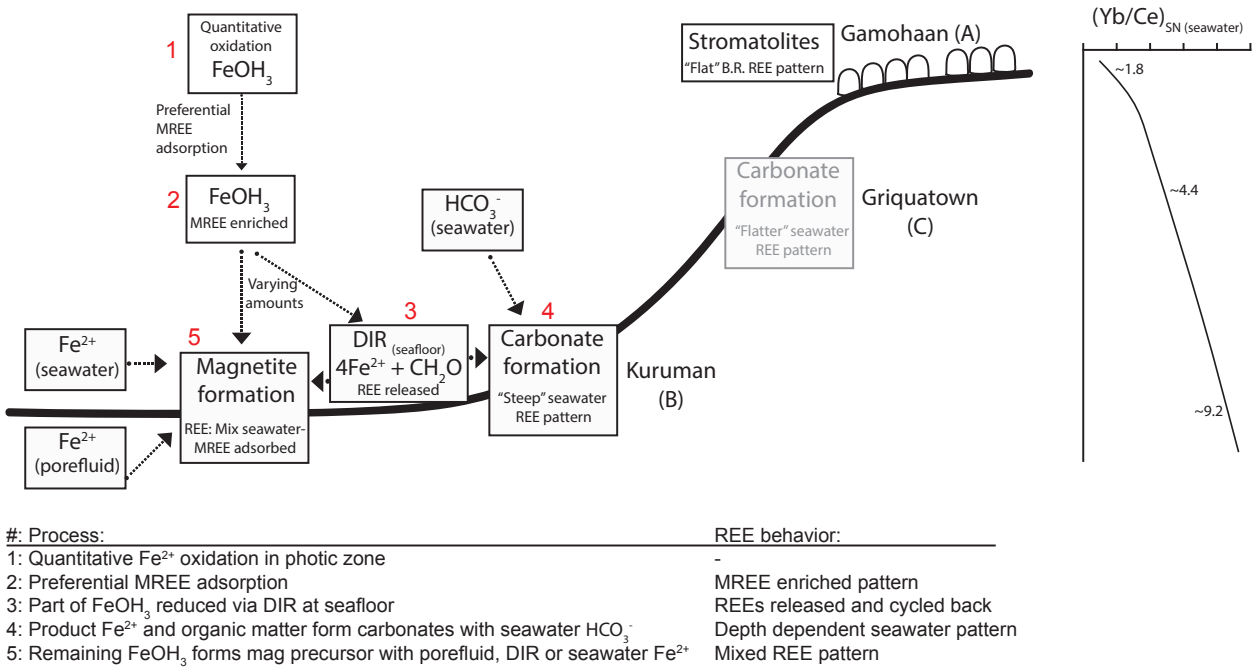

#: Process:	REE behavior:
1: Quantitative Fe^{2+} oxidation in photic zone	-
2: Preferential MREE adsorption	MREE enriched pattern
3: Part of $FeOH_3$ reduced via DIR at seafloor	REEs released and cycled back
4: Product Fe^{2+} and organic matter form carbonates with seawater HCO_3^-	Depth dependent seawater pattern
5: Remaining $FeOH_3$ forms mag precursor with porefluid, DIR or seawater Fe^{2+}	Mixed REE pattern

Figure 4.13: Conceptual depositional model based on REE behaviour of the Kuruman and Griquatown BIFs. Average $(Yb/Ce)_{SN}$ data for Gamohaan from Kamber and Webb (2001).

4.3.5.2. Model based on sequential extracted, bulk-rock and mineral REY data

Based on the arguments made above, a generalized model can be constructed for the depositional environment of the Asbestos Hills BIF (Figure 4.13). Ferrous Fe was quantitatively oxidized to insoluble ferric iron in the photic zone, either directly by oxygen produced by photosynthesis or via ferroautotrophy (Chapter 1). During sinking through the water column, the ferric Fe-(oxy)hydroxide preferentially adsorbed MREE. Upon settling at the sediment-water interface, part of this ferric Fe was reduced by DIR. During DIR the sorbed REE elements were released back into the porefluid or overlying watere column. The organic matter combined with seawater HCO_3^- and ferrous Fe from seawater or porefluids (the latter could be the reaction product of DIR) forming the Fe-carbonates and preserving the seawater-like REE pattern with a positive slope. In a REE-stratified basin with an increasing Yb/Ce_{SN} ratio, the depth of deposition controlled the steepness of the carbonate REE_{SN}-slope. Any Fe-(oxy)hydroxides not consumed by DIR could, with the ferrous Fe-sources mentioned before, produce (precursors to) magnetite. This assemblage would have the MREE enrichment mixed with the seawater REE pattern because the Yb/Ce_{SN} ratio remained high i.e. higher than desribed for the hydrothermal vent particulates of ca. 2 (Sherrell, et al., 1999) and decreased from the Kuruman

to Griquatown IF.

A relative time sequence of events can be envisaged as follows. The stromatolitic platform deposited in the Campbellrand stratigraphy became drowned and the relative deepwater Kuruman IF was deposited conformably on top. The transition from the Kuruman to the Griquatown occured over a few meters based on chemostratigraphy (including Yb/Ce_{SN} ratios, C-isotopes and Fe-isotopes). The decrease in magnetite abundance in the Griquatown compared to the Kuruman Formation (section 4.3.4) could be explained by an increase in DIR. So due to partial DIR during the Kuruman deposition a significant portion of the ferric iron could be used to form magnetite, whereas near complete DIR in the Griquatown resulted in carbonate domination.

Near quantitative oxidation of Fe in the surface waters might have led to very low Fe^{2+} concentrations and might therefore partially explain the lack of Fe-carbonates in the Campbellrand Formation. The oxidation state of this water however was still too low to oxidize Ce and produce Ce anomalies. Even if some Ce would oxidize in the presence of photosynthetic O_2 this would be cycled back using Fe^{2+} as an electron acceptor.

4.4. Conclusions

The bulk-rock REY_{SN} patterns of 101 Asbestos Hills Subgroup BIF samples follow the typical patterns generally observed in Archean and Paleoproterozoic BIFs. PAAS-normalized patterns are LREE depleted and HREE enriched, have positive La and Eu anomalies and superchondritic Y/Ho ratios. The absence of Ce anomalies indicate that conditions were reducing with respect to Ce and by extension to Mn. The five lutite samples show shale-like patterns, which can be used as allochthonous end-members. Based on this, a general limit of <10 % allochthonous input could be determined for bulk-BIF samples.

The three-step sequential extraction procedure was succesfully applied to all samples and mineral fraction specific REY_{SN} patterns were obtained. Sequentially extracted patterns could be compared against the mineral-specific LA-ICP-MS patterns. The REY_{SN} patterns of both the bulk-rock and the individual fractions decrease in slope from the Kuruman to the Griquatown Formation. Although for the bulk-rock pattern this can be related to the Zr-content (proxy for detritial input), it does not hold for the carbonate fraction. This can either be due to the shallowing of the basin in an

REE stratified ocean or a Rayleigh fractionation effect in which the ocean became relatively depleted in HREE. The latter seems unlikely based upon the time scales (10^7 years) in which the Asbestos Hills BIF was deposited.

The oxide fraction is the most REY-depleted fraction and therefore susceptible for allochthonous influences. The fraction specific slight MREE enrichment above the Pr-Yb line has not been described before in BIF, but seen in other oxygen limited ferrous environments. Furthermore, is this the only fraction without a clear La anomaly. The samples from the Kuruman Formation generally contain more oxide-minerals than the Griquatown samples, which could potentially be related to an increase in DIR activity from the deeper Kuruman to the shallower Griquatown Formation.

The silicate fraction shows varying trends which are the result of various allochthonous sources and a highly variable silicate-mineralogy. Small amounts of REY-rich trace elements might also skew this signal. A conceptual deposition model was proposed based upon the carbonate and oxide fraction REY patterns, which includes Yb/Ce stratification in the depositional basin in order to explain the varying slopes of the different patterns.

“You can’t always get what you want *(3x)*
But if you try sometimes well you might find
You get what you need“

The Rolling Stones (1969) Chorus of “You can’t always get what you want”

5

IRON ISOTOPES

Abstract

Banded iron formations (BIF), deposited prior to and concurrent with the Great Oxidation Event (GOE) at ca. 2.4 Ga, record changes in the oceanic and atmospheric chemistry during this critical time interval. Three previously unstudied drill-cores from the Griqualand West Basin, South Africa that capture the rhythmically mesobanded Kuruman BIF and the overlying granular Griquatown BIF, were sampled every ca. 20 m along core depth. These samples were analysed for their mineralogy, geochemistry and bulk Fe and C-isotopes. Bulk Fe-isotopic values of 50 samples show an apparent relationship with mineralogy. The most negative $\delta^{56}Fe$ values (< -1.3 ‰) correlate with carbonate-rich samples, whereas more positive $\delta^{56}Fe$ values (> 0.0 ‰) correspond to samples rich in magnetite. To further investigate this relationship, a three-step sequential extraction protocol was developed to separate the three main Fe-hosting fractions (Fe-carbonates, Fe-oxides and Fe-silicates). Using the leachate destruction protocol of Henkel, et al. (2016), I was able to measure for the first time fraction specific Fe-isotopes of bulk-BIF samples.

Fraction specific Fe-isotopes are probably a better proxy for the Palaeoproterozoic ocean than bulk-rock values, since the latter are strongly influenced by the modal mineralogy of each sample. I used bulk-rock C-isotope data combined with species-specific REE and $\delta^{56}Fe$ to argue that the Fe-carbonates (and possibly Fe-silicates) in the Transvaal BIFs record primary chemical signatures. The difference between the carbonate and oxide fraction isotope ratios can be constrained by the $\Delta\delta^{56}Fe_{OX\text{-}CAR}$ value. The ferrous-Fe dominated samples tend to have a low $\Delta\delta^{56}Fe_{OX\text{-}CAR}$, in contrast to the high value for the oxide-rich samples. This indicates near-quantitative dissimilatory iron reduction (DIR) in the benthic zone where predominantly Fe-carbonates form, and partial DIR during magnetite-rich BIF formation. Such a model can also be used to explain the bulk-rock $\delta^{13}C$ and $\delta^{56}Fe$ co-variation in the lowermost part of the Griquatown Formation.

5.1. Introduction

With extensive deposition around the Great Oxidation Event (GOE) at circa 2.4 Ga, banded iron formations (BIFs) have been widely studied to constrain the oxidation state of the Archean and Paleoproterozoic ocean and atmosphere (Rouxel, et al., 2005; Pecoits, et al., 2009; Bekker, et al., 2010). Among the BIFs deposited around the GOE is the Asbestos Hills Subgroup of the Ghaap Group in the Griqualand West sequence of the Transvaal basin. This Subgroup consists of two iron formations, the microbanded, oxide-rich Kuruman IF and the more granular Griquatown IF (Beukes and Klein, 1990; Pickard, 2003; see also section 1.3). These pristine looking BIFs are virtually unmetamorphosed (Miyano and Beukes, 1984), making them a suitable target for resolving the oxidation state of near-surface environments just prior to the GOE (Johnson, et al., 2003).

Iron is the most abundant redox-sensitive element in Precambrian BIFs (Klein, 2005) and its concentration, speciation and isotope composition have been well-studied. However key issues, such as the role of primary mineral formation versus diagenetic overprinting in determining the Fe-isotope ratios in BIF remain unresolved. Redox reactions lead to the largest amounts of Fe-isotope fractionation (Anbar, 2004; Johnson, et al., 2008b) giving Fe-isotope systematics potentially a key role for constraining redox changes in the Precambrian ocean. Archean and Paleoproterozoic BIFs show large ranges in δ^{56}Fe (Anbar, 2004; Planavksy, et al., 2012). The complex and heterogeneous mineralogy of typical BIFs yield significant challenges with respect to sampling and interpretation. Most iron-isotope studies to date have focussed on bulk-rock samples (e.g. Dauphas, et al., 2004; Yamaguchi, et al., 2005; Tsikos, et al., 2010; Planavsky, et al., 2012; Haugaard, et al., 2016; Mendes, et al., 2016) but also micro-drilled mono-mineralogic samples (Johnson, et al., 2003; 2008a) and hand-separated mineral powders (Craddock and Dauphas, 2011) have been analysed. Grain specific analyses by *in situ* femtosecond laser-ablation ICP-MS (Steinhoefel, et al., 2009; 2010; Li, et al., 2013) have helped to further investigate isotopic-distribution on very small scales.

All of these techniques have specific draw-backs. Modal mineralogical variation in bulk-rock samples could potentially skew their isotope ratios as Fe-carbonates and Fe-oxides have different δ^{56}Fe values (e.g. Dauphas, et al., 2004; Johnson, et al., 2008b). Most bands in BIFs studied here are not completely mono-mineralogical and in fact a majority of the bands contain multiple Fe-bearing minerals. Thus sampling pure mono-mineralogical bands is challenging and arguably they are not

completely representative of BIF. Femto-second LA-ICP-MS data has revealed micro-scale isotopic variation for adjacent grains (Steinhoefel, et al., 2009). These variations are generally related to localized diagenesis and thereby unsuitable for tracking large scale stratigraphical variations.

Chapter 2 outlines an optimized sequential extraction procedure (Poulton and Canfield, 2005) for typical magnetite-BIF samples. The technique accommodates, through a leachate-destruction protocol (Henkel, et al., 2016), fraction specific Fe-isotope measurements on bulk-rock BIF samples. The procedure dissolves the carbonate, oxide and silicate fractions separately giving insight into iron speciation and its isotopes over the different fractions. Limitations to the procedure include the quality of the extraction (i.e. selectivity and potential contaminations) and the assumption that the microscale isotope variability within the fractions of a bulk-rock sample is limited (e.g. no significant δ^{56}Fe changes from one carbonate-band to the next). Bulk-rock sampling and sequential leaching will average out the micro-scale isotopic variation, which eventually might represent the original seawater signature from which the BIF chemically precipitated.

A combination of a sequential extraction procedure and Fe-isotope measurements has been employed before on 1.9 Ga Biwabik BIF (Frost, et al., 2007) and the Neoproterozoic (0.7 Ga) Rapitan IF (Halverson, et al., 2011). These studies used acetic acid, HCl and HF to dissolve the carbonates, oxides and silicates respectively. The study of Frost, et al. (2007) focussed on the preservation of isotopic signals during diagenesis and metamorphism. Only the least metamorphosed samples here fall in range with the lower greenschist facies described for the Asbestos Hills Subgroup (Miyano and Beukes, 1984). Halverson, et al. (2011) worked with carbonate-poor hematite jaspilites, which are also not directly comparable to the samples investigated here.

In this chapter, I show Fe-speciation data for 106 samples from the Kuruman and Griquatown Iron Formations (Section 1.3) combined with 50 bulk-rock Fe-isotope ratios to interpret these δ^{56}Fe values with regard to modal mineralogy and potential stratigraphic variation. A subgroup of 12 samples were processed for fraction specific Fe-isotope measurements, in order to show relations between Fe-carbonates, Fe-oxides and Fe-silicates. In the discussion these signals are discussed with respect to primary versus diagenetic formation models with an emphasis on the role of dissimilatory iron reduction (DIR). Microbially mediated DIR uses organic carbon [CH_2O] to reduce ferric Fe and produces alkalinity. This reaction can be written as:

$4Fe(OH)_3 + [CH_2O] + 7H^+ \rightarrow 4Fe^{2+} + HCO_3^- + 10H_2O$ (Reaction 5.1)

In addition to DIR, the potential to reconstruct the seawater oxidation state just prior to the GOE is assessed.

5.2. Methodology

Major and trace elements were determined in bulk-rock powders by XRF using the Norrish-Hutton method (1969) at Rhodes University. Bulk-rock Fe-isotopes were measured following HF-HNO_3-$HClO_4$ digestion and standard purification procedures (Williams, et al., 2004). Sequential extraction of all 106 samples followed the protocol described in Chapter 2, which was based on the method of Poulton and Canfield (2005). In short, a pH 4.5 buffered, 48 hour 1 M Na-acetate leach at 50 °C under an inert atmosphere was used to dissolve the carbonates quantitatively. The Fe-oxides (dominated by magnetite) were digested in a 24 hour NH_4-oxalate leach and the final silicate residue was dissolved with a standard HF-HNO_3-$HClO_4$ protocol. All solutions were analysed by ICP-OES to determine the recoveries and elemental distributions.

To avoid matrix-induced bias on isotope ratio measurements, the leachates were broken down via multiple cycles of acid addition and evaporation and a Fe-precipitation step (Chapter 2; Henkel, et al., 2016). Iron was purified using anion exchange column chromatography (Williams, et al., 2004). Iron concentrations were measured colorimetrically before purification and using ICP-OES for a final purity and concentration check.

Iron-isotope ratios were measured on a ThermoFinnigan Neptune MultiCollector Inductively Coupled Plasma Mass Spectrometer (MC-ICP-MS) at Durham University, UK. Prior to any Fe-isotope measurement, the samples were concentration matched to the lab-specific IRMM-014 standard, which was used for sample-standard bracketing. The reported $\delta^{56}Fe$ values ($\delta^{56}Fe = [(^{56}Fe/^{54}Fe)_{sample}/(^{56}Fe/^{54}Fe)_{IRMM\text{-}014} - 1]\cdot 10^3$) were calculated as the mean of replicates (n= 2 - 4) during the same measurement sequence. All measurements followed established analytical procedures. Samples (ca. 8 ppm Fe) were introduced under wet plasma conditions (ESI Cinnabar spray chamber) using an ESI 50 µl/min PFA concentric nebulizer, with a 0.1 M HNO_3 matrix (Williams, et al., 2004; 2012).

Accuracy was monitored using international reference standards (BHVO-1 and IF-G) and an in-house FeCl salt standard ($\delta^{56}Fe$ = -0.71 ± 0.06 ‰; Williams and Bizimis, (2014)). Where necessary, published $\delta^{57}Fe$ data were recalculated to $\delta^{56}Fe$ and everything was standardized to IRMM-014.

5.3. Results

The bulk-rock iron concentration was found to vary significantly, ranging between 7.1 and 41.1 wt% Fe. The iron distribution over the three fractions varied extensively, although Fe-silicate dominated samples are the least abundant (Table 5.1; Figure 5.1). Larger bulk-rock samples averaged out the heterogeneous modal mineralogy, compared to smaller samples. This explained the large group of samples plotting around the centre of the ternary diagram.

The Fe-recovery was good (99.8 ± 3.0 % 1 sd) based on the sum of the extracted fractions (ICP-MS) compared to the bulk-rock XRF measurement. Incomplete dissolution or digestion of minerals other than the targeted fraction was insignificant based on the absence or low concentrations of tracer elements such as Ca, Mn, Ti, Al and Si (Chapter 3).

Bulk-rock $\delta^{56}Fe$ values were determined for a subset of 50 samples from three cores with values ranging from -1.87 to +1.13 ‰ (Table 5.1), covering nearly the whole existing range of Fe-

Table 5.1: Fe distribution (wt%) and bulk-rock $\delta^{56}Fe$ values (‰) per sample, which are averaged in the case of replicate analyses. The Fe distribution is shown over the acetate (A), oxalate (B) and HF (C) fractions and can be compared to the bulk-rock value (D). The average discrepancy between duplicate samples was <0.5 wt% per fraction and typical external repoducibilities for isotope ratios were smaller than 0.10 ‰ (2sd). In case no bulk-rock $\delta^{56}Fe$ was measured the cell remains blank.

Sample	A	B	C	D	$\delta^{56}Fe$
HEX648	8.3	9.4	2.4	20.2	-0.38
HEX651	14.6	10.1	5.0	29.5	
HEX653	16.5	6.2	8.1	30.6	
HEX656	15.9	1.5	2.7	20.5	-1.39
HEX661	14.6	3.1	3.4	21.7	-1.20
HEX667	3.0	18.4	3.9	25.4	
HEX672	2.9	16.1	7.4	25.9	0.05
HEX685	4.2	9.6	9.2	21.8	
HEX694	5.4	10.0	14.4	28.2	-1.29
HEX706	10.7	1.5	1.6	14.1	
HEX722	17.7	5.2	2.7	25.4	-1.87

Sample	A	B	C	D	$\delta^{56}Fe$
GAS142	8.0	1.3	4.1	13.6	-1.07
GAS150	10.4	12.4	7.3	30.4	-0.51
GAS174	13.1	9.7	10.6	33.2	-0.71
GAS192	8.2	17.5	6.3	32.6	
GAS201	2.8	0.5	5.0	8.3	-0.76
GAS212	10.5	9.6	7.8	28.0	
GAS229	2.6	13.5	4.2	20.5	-0.54
GAS244	4.4	16.6	8.2	29.5	-0.49
GAS259	7.6	20.2	11.9	39.5	-1.05
GAS266	12.5	4.5	2.2	20.2	
GAS271	3.1	13.7	5.6	22.6	-0.57

Table 5.1: *continued*

Sample	A	B	C	D	δ^{56}Fe
HEX733	13.8	6.8	8.0	28.3	
HEX744	13.7	2.4	6.2	22.7	-1.57
HEX753	12.5	6.2	8.1	26.9	
HEX767	11.6	4.8	7.5	23.3	-0.96
HEX780	6.5	17.2	5.5	29.2	
HEX792	12.0	11.3	2.5	25.7	-1.11
HEX802	6.5	23.2	8.0	39.1	
HEX814	1.0	2.2	17.9	19.2	-0.66
HEX827	4.7	14.5	6.7	25.8	
HEX836	8.7	14.2	6.4	31.2	-0.56
HEX849	10.5	23.1	3.0	37.6	
HEX864	7.3	21.3	3.2	32.0	0.39
HEX872	8.7	11.9	5.7	27.0	1.13
HEX887	5.3	17.9	4.6	27.0	-0.29
HEX899	3.1	11.6	16.2	28.9	
HEX920	8.2	9.5	2.7	21.3	0.20
HEX934	3.9	16.3	1.8	22.9	0.51
ERI373	14.6	5.3	5.9	25.1	-0.93
ERI377	7.7	20.4	7.8	35.3	
ERI387	5.1	10.8	9.3	24.6	-0.79
ERI395	3.4	7.7	3.7	14.9	
ERI405	8.8	1.2	1.5	12.1	-1.41
ERI415	7.6	5.3	15.9	27.9	
ERI427	3.0	1.3	12.7	16.2	
ERI436	9.2	7.7	11.1	27.0	-0.98
ERI450	19.5	5.7	1.9	27.7	
ERI459	8.6	1.0	0.8	10.8	-1.37
ERI470	5.7	2.6	7.0	15.4	
ERI476	6.9	0.8	1.7	9.9	-1.15
ERI489	5.5	4.0	2.8	12.9	
ERI499	7.5	9.9	6.5	24.0	-0.88
ERI510	9.2	11.5	8.1	28.4	
ERI524	4.2	9.0	5.6	19.4	-0.74
ERI535	4.8	8.3	4.9	18.3	
ERI550	5.4	12.6	8.9	26.7	0.76
ERI562	5.5	6.8	13.6	25.0	
ERI572	3.5	10.0	3.5	17.7	0.33
ERI584	2.4	7.8	8.1	19.0	
ERI603	0.3	14.7	5.2	20.4	0.22
ERI618	0.7	25.6	5.0	32.1	0.30
ERI628	18.1	3.4	7.0	28.3	-0.06
ERI637	9.5	4.0	19.8	31.6	-0.66
ERI646	11.1	3.3	10.0	24.0	-0.08

Sample	A	B	C	D	δ^{56}Fe
GAS283	4.8	19.9	5.8	30.6	
GAS296	9.4	12.0	5.1	26.6	-0.31
GAS336	2.0	18.7	5.2	25.9	0.36
GAS354	10.6	4.1	6.5	21.6	0.22
GAS367	7.5	15.8	13.0	36.1	
GAS371	7.9	5.6	15.3	27.9	-0.64
GAS390	15.5	6.7	8.4	30.4	-0.48
GAS404	1.6	20.9	12.4	34.4	-0.26
GAS420	8.3	20.7	2.4	32.5	-0.69
GAS434	7.0	19.9	4.4	32.1	
GAS441	0.9	27.0	2.9	30.9	-0.72
GAS447	1.3	25.2	7.0	33.2	
GAS461	1.0	27.9	3.5	33.9	-0.31
GAS474	13.0	2.9	13.4	28.4	
GAS488	0.8	32.5	6.1	41.1	0.41
GAS505	1.0	28.7	9.8	39.8	
GAS513	8.9	10.0	9.9	28.3	0.36
ARP484	9.4	2.6	4.0	16.1	
ARP490	9.4	3.2	10.1	22.2	
ARP499	0.9	20.8	10.8	32.8	
ARP509	8.0	14.0	6.2	28.0	
ARP516	6.5	3.8	2.9	13.8	
ARP527	6.7	4.3	12.2	23.2	
ARP538	6.8	4.1	13.5	23.0	
ARP542	17.1	3.2	2.1	22.6	
ARP547	4.9	1.2	9.4	15.5	
ARP560	7.1	10.0	14.6	30.3	
ARP571	1.2	0.9	15.6	16.6	
ARP578	6.8	3.3	4.9	15.6	
ARP586	9.8	2.7	6.9	19.5	
ARP596	9.5	7.7	11.6	28.8	
ARP605	8.0	8.3	6.0	22.0	
ARP614	3.7	11.9	12.4	27.4	
ARP619	2.4	0.2	7.0	9.6	
ARP629	11.3	11.1	3.0	25.5	
ARP635	3.9	15.0	8.2	26.7	
ARP649	10.5	15.0	1.3	27.7	
ARP656	1.6	25.5	3.9	30.8	
ARP661	8.4	15.9	3.7	28.5	
ARP666	3.8	1.2	1.4	7.1	
ARP670	9.8	13.5	5.6	29.4	

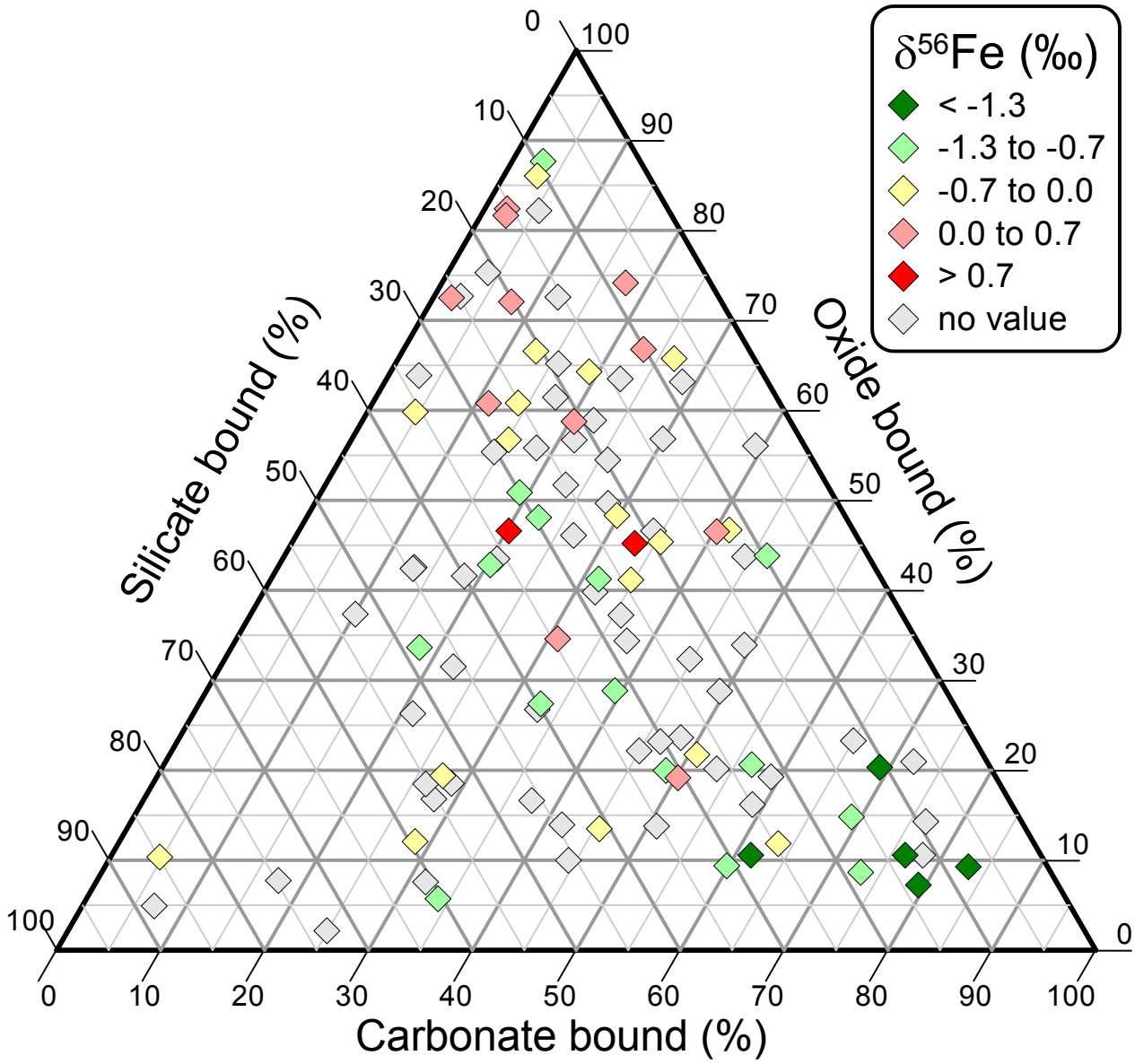

Figure 5.1: Fe distribution for all samples (n=106) with color-coded bulk-rock δ^{56}Fe ranges for the measured samples (n=50)

isotope variability in BIF (Anbar, 2004; Planavsky, et al., 2012). A link between the dominant Fe-hosting fraction and bulk-rock isotopic ratio was apparent (Figure 5.1). The lower δ^{56}Fe values tended to correspond with carbonate-dominated samples, whereas the positive values contained more oxide-bound Fe. Next to the Fe-hosting fraction, there was also a stratigraphic relationship, showing co-varying bulk-rock δ^{56}Fe between the three different cores (Figure 5.2a). The average bulk-rock δ^{56}Fe value of the Kuruman IF was significantly higher than that of the Griquatown IF with 0.03 ‰ (n=23) and -0.92 ‰ (n=27), respectively. The corresponding bulk-rock C-isotopes from Tsikos, et al. (in prep.) show an antithetic relationship with the Fe-isotopes in the lower part of the Griquatown Formation (Figure 5.2b,c). Note here that the δ^{13}C values are fluctuating independent

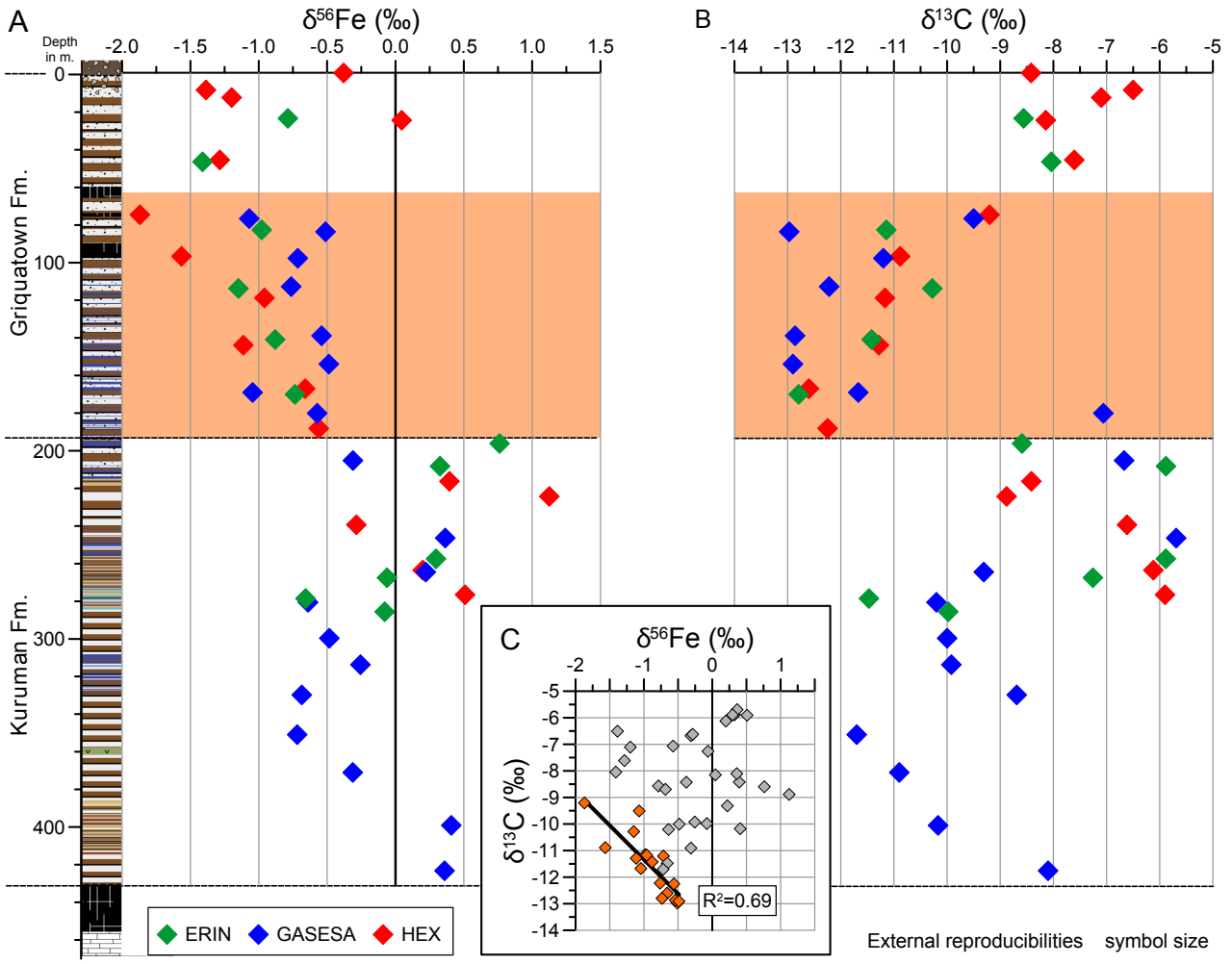

Figure 5.2: Stratigraphical distribution of bulk-rock (A) $\delta^{56}Fe$ and (B) $\delta^{13}C$. Note, due to missing $\delta^{13}C$ three $\delta^{56}Fe$-points from the ERIN core are not plotted here. The $\delta^{13}C$ values are from Tsikos, et al. (in prep.). The inset (C) shows the $\delta^{56}Fe$ and $\delta^{13}C$ relationship for all samples. The negative correlation given by the orange diamonds here, are all the samples from the shaded area in A and B.

of the carbonate mineralogy, as the $\delta^{13}C$ values for ankerite and siderite generally agree within 1 ‰ (Rafuza, 2015).

In this study, I present fraction-specific Fe-isotope data for 9 new samples in addition to the 3 published in the protocol-development chapter (Chapter 2). The calculated bulk-rock isotopic value, based on Fe-distribution and fraction specific isotope ratios, matched the measured bulk-rock value within uncertainty in all cases (Table 5.2). In the eleven samples from the HEX core the ferrous fractions (carbonates and silicates) were generally found to be isotopically lighter than the bulk-rock whereas the mixed-valence oxide fraction was generally heavier (Figure 5.3).

The difference in $\delta^{56}Fe$ between the carbonate and oxide fraction ($\Delta\delta^{56}Fe_{OX\text{-}CAR} = \delta^{56}Fe_{OX} - \delta^{56}Fe_{CAR}$) was calculated to further examine trends with respect to stratigraphy or mineralogy. The

Table 5.2: Fe distribution and fraction specific $\delta^{56}Fe$ values. The fraction specific Fe concentration were analysed by ICP-OES, the bulk-rock (Bulk) values by XRF. Typical external reproduciblities for the $\delta^{56}Fe$ values are 0.10‰ (2 sd).

	Fe distribution (wt%)					$\delta^{56}Fe$ (‰)				
Sample	Acetate	Oxalate	HF	Σ Ext.[1]	Bulk	Acetate	Oxalate	HF	Calc.[2]	Bulk
HEX656	15.9	1.5	2.5	19.9	20.5	-1.34	-1.23	-1.28	-1.33	-1.39
HEX672	3.0	16.1	7.2	26.3	25.9	-0.59	0.78	-1.64	-0.04	0.05
HEX694	5.4	10.1	14.2	29.7	28.2	-1.70	-0.54	-1.63	-1.29	-1.29
HEX722[3]	17.5	5.2	2.5	25.2	25.4	-1.76	-2.03	-1.70	-1.81	-1.77
HEX744	13.7	2.4	6.0	22.1	22.7	-1.57	-1.50	-1.51	-1.54	-1.57
HEX767	11.6	4.8	7.3	23.7	23.3	-1.17	-0.26	-1.22	-1.00	-0.96
HEX814	1.0	2.2	17.8	21.0	19.2	-0.74	-0.52	-0.75	-0.72	-0.66
HEX836[3]	10.0	16.1	6.0	32.1	31.2	-1.23	-0.11	-0.99	-0.62	-0.60
(repeat)[3]	*9.8*	*14.2*	*6.3*	*30.3*		*-1.25*	*0.15*	*-1.69*	*-0.74*	
HEX872	8.7	11.9	5.5	26.1	27	0.70	1.63	0.40	1.06	1.13
HEX887	5.3	17.9	4.5	27.7	27	-0.99	0.26	-1.82	-0.32	-0.29
HEX934	3.9	16.3	1.6	21.8	22.9	-0.17	0.62	0.07	0.44	0.51
GAS488[3]	0.9	32.8	5.4	39.1	41.1	-0.39	0.51	-0.56	0.34	0.42
(repeat)[3]	*0.9*	*32.3*	*6.3*	*39.5*		*-0.47*	*0.38*	*0.48*	*0.38*	

[1] Σ Ext.: Total wt% Fe extracted
[2] Calc.: Calculated bulk-rock value, fraction specific $\delta^{56}Fe$ times the relative extracted abundance
[3] Values from Chapter 2

$\Delta\delta^{56}Fe_{OX\text{-}CAR}$ was generally large for the thinner bedded (micro/mesobanded), oxide-dominated samples of the Kuruman IF and the top and bottom of the Griquatown IF. In contrast to this, the thickly banded, ferric-poor and carbonate-rich samples of central part of the Griquatown IF show a small $\Delta\delta^{56}Fe_{OX\text{-}CAR}$ value.

5.4. Discussion

5.4.1. Bulk-rock stratigraphic relationships

The similarity in bulk-rock $\delta^{56}Fe$ between the different cores, independent of the sample mineralogy, indicate that a regional mechanism, at least partially, controlled the isotopic distribution (Figure 5.1). Localized microbial Fe reduction in the soft-sediment/pore-fluids has been shown previously shown to create erratic $\delta^{56}Fe$ patterns, with variable isotopic ratios across a mm-scale due to differences in productivity and ferric Fe supply (Steinhoefel, et al., 2009; 2010). Although bulk-rock sampling averages out this variation, isotopic co-variation over tens of km would not be possible

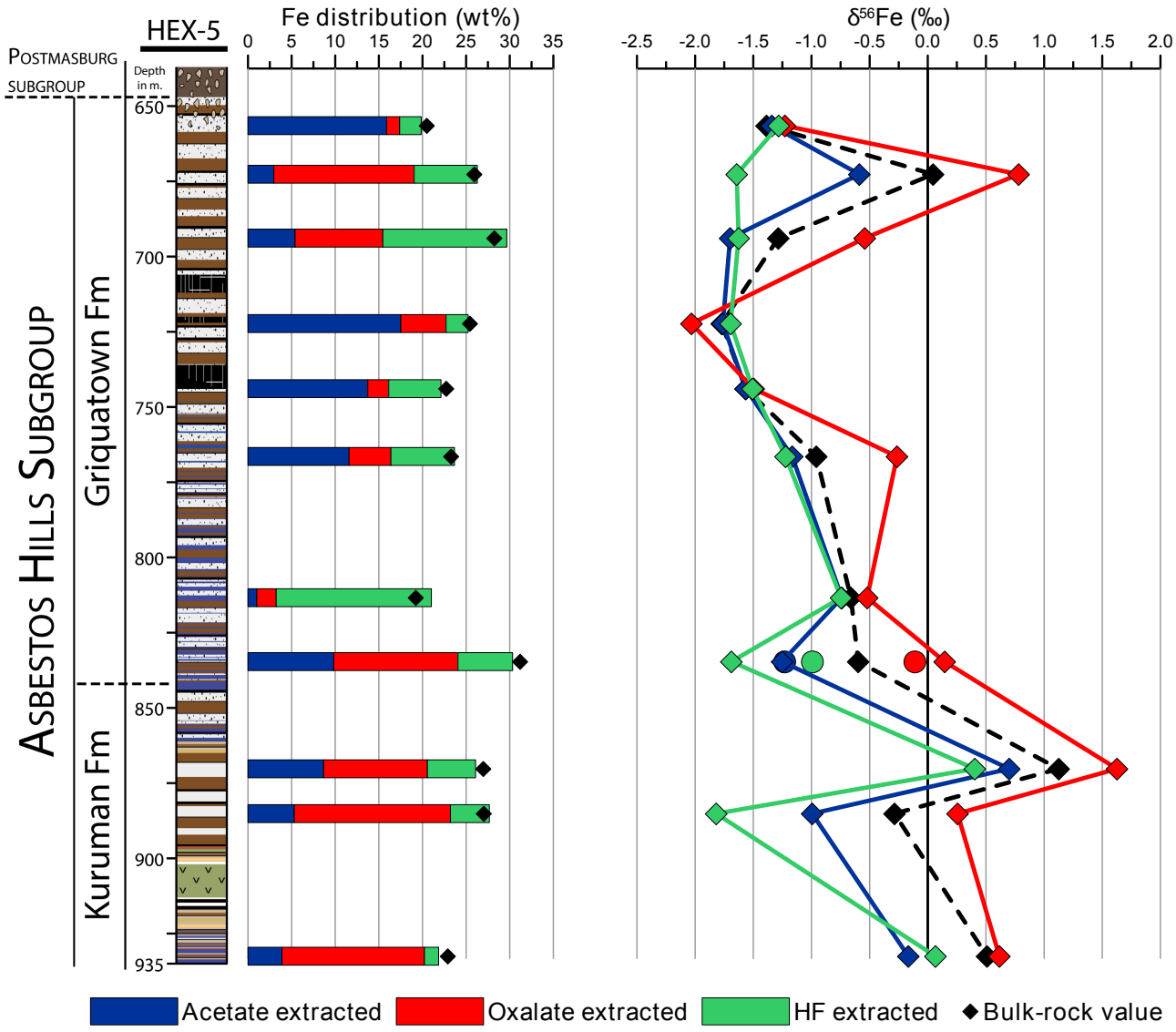

Figure 5.3: Sequentially extracted Fe-distribution and their isotopic values for the HEX-core.

if diagenesis was responsible for controlling δ^{56}Fe variability. Furthermore, the amount of organic matter would vary and thus create areas with varying Fe-oxidizing capacities. The extensive lateral continuity of "*major and minor banding*" in BIF (Trendall and Blockey, 1970; Ewers and Morris, 1981) also argues against locally-controlled mechanisms. Regional mechanisms that could have controlled δ^{56}Fe include primary mineral precipitation from a redox-stratified basin (Halverson, et al., 2011), basin-wide Rayleigh fractionation effects (Tsikos, et al., 2010) or a combination of the two.

A water column gradient with respect to Fe-isotopes as envisaged by Halverson, et al. (2011) has been reported for two modern, anoxic, non-sulfidic lake systems; Lake Nyos (Teutsch, et al., 2009) and Lac Pavin (Busigny, et al., 2014). In both systems, the upper oxic layer has a near-zero Fe concentration, which is also implied in to be the case for seawater around the GOE (e.g. Sumner,

1997; Planavsky, et al., 2012). The lowest $\delta^{56}Fe^{2+}_{(aq)}$ values are present near the redoxcline where, after an initial sharp increase, the ratios increase with depth.

In modern sub-oxic fjords, dissolved inorganic carbon concentrations increase below the chemocline, while their $\delta^{13}C_{DIC}$ decreases sharply from slightly negative values to as low as -19 ‰ (Van Breugel, et al., 2005). Both these changes are attributed to respiration of particulate organic matter. A similar trend is seen (with different $\delta^{13}C_{DIC}$) in the waters of Lac Pavin, although below the mesolimnion the $\delta^{13}C_{DIC}$ increases again (Assayag, et al., 2008), potentially due to a hydrothermal influx. A combination of these two opposing gradients, with a decreasing waterdepth, could be an explanation for the antithetic behaviour seen in the lower parts of the Griquatown Formation (Figure 5.2).

Regional bulk-rock $\delta^{56}Fe$ variation can be explained by long-term Rayleigh effects. However, the significant Fe and C isotope relationship is harder to explain this way. The lower $\delta^{56}Fe$ values (average $\delta^{56}Fe$ of -1.2 ‰) in the hematite of the younger Hotazel Mn-BIF was a major reason to argue for temporal evolution of the seawater $\delta^{56}Fe(II)$ (Tsikos, et al., 2010). It should be noted though, that the difference in bulk-rock Fe isotopic ratio between the Griquatown and Kuruman samples also supports such a long-term evolution, independent of the percentage of oxide-bound Fe (Figure 5.4a).

Based on micro-drilled powders from samples within three meters of each other, Johnson, et al. (2008a) concluded that the large ranges in $\delta^{56}Fe$ cannot reflect changes in the Fe isotope compositions of Late Archean or Early Proterozoic seawater. Indeed heterogeneities on a sub-mm scale (Steinhoefel, et al., 2009; 2010) are not interpretable as Archean seawater variability due to the large residence time of Fe in this seawater (on the order of 10^6 years; Johnson, et al., 2003). However, even with the highest compacted sedimentation rates of 22 m/Myr (Pickard, 2003) the 440 m thick section would have been deposited in 20 Myr, which is still significantly larger than the predicted Fe-residence times and therefore might reflect seawater changes. In bulk-rock samples the micro-scale $\delta^{56}Fe$ variability would be averaged out and therefore bulk-samples are potentially more representative of the $\delta^{56}Fe$ in the Fe-source.

Another mechanism which could be of regional extent is a seafloor benthic Fe-shuttle (Lyons and Severmann, 2006; Severmann, et al., 2008; Li, et al., 2015). Nonetheless, the first-order change

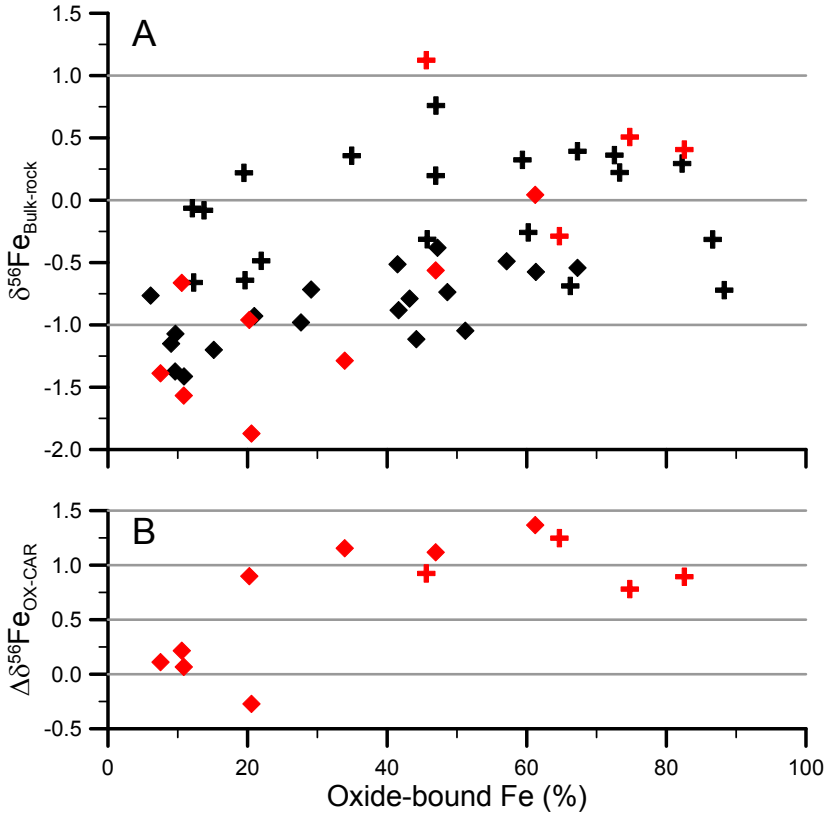

Figure 5.4: Percentage of Fe bound to oxides versus the (A) bulk-rock isotopic composition and (B) the $\Delta\delta^{56}Fe_{OX\text{-}CAR}$. The red symbols in A correspond to the samples in B. The typical external reproducibility of $\delta^{56}Fe$ is 0.1 ‰ (2 sd). Crosses are samples from the Kuruman Formation, diamonds are from the Griquatown.

in Fe-isotopic composition from the Kuruman to the Griquatown is hard to explain this way without a water column gradient. A benthic Fe-shuttle could explain second-order deviations from the main trend. Combined C, O and Fe isotopes on micro-drilled carbonate-laminations have been used to argue against primary carbonate-precipitation (Heimann, et al., 2010). However, these small-scale samples might represent a second-order microbial processes.

5.4.2. Iron silicates

Little work has been done to date on the Fe-silicates in BIF since most researchers argue that this fraction is detrital in origin (e.g. Beukes, 1984). However, greenalite micro-particles have been suggested to be one of the precursor phases in BIF based on petrographic examination (Rasmussen, et al., 2013; 2015b; Tosca, et al., 2016). The only published iron-silicate $\delta^{56}Fe$ (Table 5.3) are from the post-GOE Biwabik IF (Frost, et al., 2007; Valaas Hyslop, et al., 2008) and a single bulk value for a stilpnomelane mudrock of the Joffre BIF (Haugaard, et al., 2016). The Bibabik IF iron-isotopic ratios of silicate-minerals have been determined by basic sequential extraction techniques. To date no

Table 5.3: Literature δ^{56}Fe of BIF-hosted Fe-silicates and co-occurring minerals in the 1.8 Ga Biwabik IF. Data obtained by sequential extraction after magnetic separation of magnetite ([1], Frost, et al., 2007), magnetite extraction followed by bulk-digestion ([2], Valaas Hyslop, et al., 2008) and a bulk-rock value of a stilpnomelane mudrock of the 2.5 Ga Joffre BIF ([3], Haugaard, et al., 2016). n.a. is not assessed

Sample name	δ^{56}Fe (‰)			Silicate mineralogy	Ref.
	Carbonate	Magnetite	Silicate		
A1.1, A2.1, A1.2	-0.61 ± 0.04	-0.15 ± 0.04	-0.33 ± 0.04	Greenalite ±magnetite	[1]
A3.1, A3.2	-0.74 ± 0.04	n.a.	-0.79 ± 0.04	Greenalite	[1]
A4.1, A5.1	n.a.	0.67 ± 0.04	-0.12 ± 0.04	Greenalite	[1]
35B-1	n.a.	0.73 ± 0.07	0.16 ± 0.07	Minnesotaite ± greenalite	[2]
DD98-28	n.a.	n.a.	-0.74 ± 0.08	Stilpnomelane mudrock	[3]

femto-second LA-ICP-MS data is available for δ^{56}Fe in Fe-silicates.

In all cases silicate δ^{56}Fe is lower than for accompanying magnetite, whereas the only published pure greenalite-carbonate couple have practically the same value (Table 5.3; Frost, et al., 2007; Valaas Hyslop, et al., 2008). The stilpnomelane mudrock bulk value is lower than all the BIF-samples, which in that study (Haugaard, et al., 2016) tend to be oxide-rich.

Our data show that the silicate fraction tracks the carbonate fraction within 0.3 ‰. Two exceptions are the samples HEX672 and HEX887, where the silicate fraction is >0.8 ‰ lower (Table 5.2). Both samples differ in modal mineralogy, with minnesotaite as the major Fe-silicate for HEX672 and riebeckite for HEX877 based on petrography and XRD. Furthermore, ankerite is the main carbonate mineral in HEX672 whereas in HEX877 siderite and ankerite are equal in abundance, based on XRD and Ca/Fe ratios in the carbonate fraction. To better understand the relationship of the carbonate and silicate δ^{56}Fe, more complementary data is needed either through micro-drilling or from *in situ* measurement techniques.

In general, ferrous minerals have lower isotopic values then mixed-valence or ferric-minerals (Polyakov and Mineev, 2000), partially explaining the similar behaviour between ferrous-dominated Fe-silicates and the Fe-carbonates. Based on this, Frost, et al. (2007) predicted a relationship between these two mineral groups, but their data was insufficient to make valid conclusions. The Asbestos Hills Subgroup data presented endorses this prediction with similar δ^{56}Fe for the carbonate and silicate fractions. Because of the limited literature data available for the BIF silicates, the following sections primarily focus on the oxide versus carbonate fractions. But, due to the similarities with the ferrous carbonate fraction, the arguments presented below could also apply to the silicate fraction.

5.4.3. Coupling of ferrous and mixed-valence fractions

The advantage of a sequential extraction method is the possibility of comparing $\delta^{56}Fe$ in bulk-rock samples to individual fractions. Bulk-rock samples average out all $\delta^{56}Fe$ variability, whereas fraction specific samples only average out the variability within a fraction. This implictly assumes that the isotopic heterogeneity of a targeted fraction is limited on the sample scale. For bulk-rock samples containing for example multiple carbonate bands it assumes that the average band-to-band $\delta^{56}Fe$ variability is minor.

Figures 5.1 and 5.4a show an apparent relationship where oxide-dominated samples tend to have higher bulk-rock $\delta^{56}Fe$ then carbonate-rich samples, which was confirmed by the fraction specific isotopes.

5.4.3.1. Equilibrium fractionation

Thermodynamics predict that when both ferrous and ferric minerals precipitate in equilibrium with each other, the ferric minerals should have higher $\delta^{56}Fe$ than the ferrous ones (e.g. Polyakov and Mineev, 2000; Johnson, et al., 2008b). The equilibrium isotopic fractionation factors determined experimentally and calculated based on β-factors do not always align, discrepancies exist especially in fluid-mineral systems.

The $\Delta^{56}Fe_{Fe(II)\text{-}siderite}$ value determined for abiotic precipitated siderite is +0.5 ‰ (Wiesli, et al., 2004), which is ca. 1.5 ‰ lower than calculated by vibrational spectroscopic data (+2.1 ‰ at 20 °C, Polyakov and Mineev, 2000; Schauble, et al., 2001). Biological siderite precipitation (Johnson, et al., 2005) and the range determined for natural samples (-1.7 to +0.3 ‰, Johnson, et al., 2003) show agreement with the abiotic value. For $\Delta^{56}Fe_{Fe(II)\text{-}magnetite}$ similar inconsistencies exist, with biotic and abiotic factors at -1.3 ‰ (Johnson, et al., 2005) and -1.6 ‰ (Frierdich, et al., 2014) respectively, whereas the calculated values lie around -4.2 ‰ at 25 °C (Polyakov and Mineev, 2000; Schauble, et al., 2001). The average preferred value defined by natural minerals (-2.5 ‰, Johnson, et al., 2003) lies in-between them. This strengthens a basic assumption regarding BIF deposition, namely that the oxidation of Fe(II) leads to a ferric particulate with a higher $\delta^{56}Fe$ than the dissolved pool. The magnitude of this value still varies depending on the extent of oxidation.

When using the experimentally determined factors a siderite-magnetite pair precipitated from

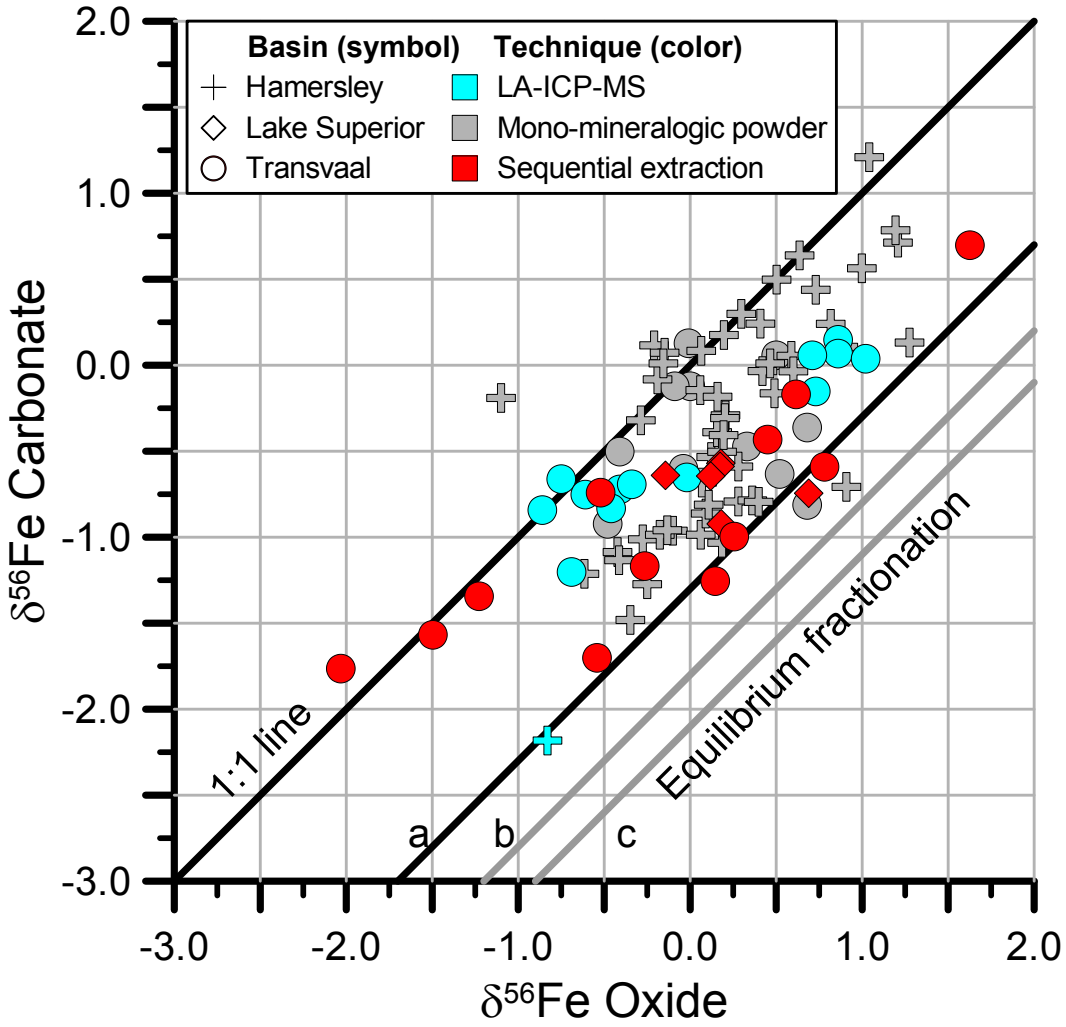

Figure 5.5: Literature comparison of δ^{56}Fe oxide (magnetite) vs carbonate (siderite where possible) fraction for multiple basins and techniques. Data for mono-mineralogic powders from Johnson, et al. (2003; 2008a) and Craddock and Dauphas (2011), for femtosecond-LA-ICP-MS from Steinhoefel, et al. (2009; 2010, data from the Old Wanderer BIF plotted as Transvaal), and for sequential extraction from Frost, et al. (2007) and this study. The values used for the calculated equilibrium fractionation lines are for magnetite and siderite respectively from a) both from Johnson, et al. (2005), b) Johnson, et al. (2005) and Wiesli, et al. (2004), c) Frierdich, et al. (2014) and Wiesli, et al. (2004). See text for discussion.

the same fluid in equilibrium (with excess $Fe^{2+}_{(aq)}$) should, therefore have a difference in δ^{56}Fe of at least 1.3 ‰ (Johnson, et al., 2005) and even up to 2.1 ‰ (Wiesli, et al., 2004; Frierdich, et al., 2014). Since the equilibrium fractionation factor for Ca-bearing carbonates is higher than for siderite, the equilibrium fractionation between magnetite and ankerite is even larger than for siderite (Johnson, et al., 2005).

Only a few carbonate-oxide pairs plot on the lowermost fractionation line (Figure 5.5), indicating that most of the samples did not form in equilibrium with each other. Although kinetic

effects might play a role, microbially mediated DIR during early diagenesis has been put forward as the main mechanism to explain a non-equilibrium fractionation relationship (Johnson, et al., 2003; 2008a; Steinhoefel, et al., 2009; 2010; Craddock and Dauphas, 2011).

5.4.3.2. Dissimilatory iron reduction

Microbially mediated DIR preferentially selects the lighter isotopes of Fe (e.g. Staubwasser, et al., 2006; Johnson, et al., 2008b), producing low δ^{56}Fe ferrous iron and leaving an isotopically heavy ferric pool behind. The diagenetic DIR-model has traditionally been used to explain small scale δ^{56}Fe variations generally within single samples (Johnson, et al., 2003; 2008a; 2008b; Heimann, et al., 2010). In a closed system this light, DIR-produced ferrous pool can react with HCO_3^- produced by C_{org} oxidation during DIR to produce low δ^{56}Fe siderite, and any remnant ferrous Fe can react with residual ferric particulates to form magnetite with higher δ^{56}Fe. Although systems undergoing DIR may not be completely closed, it is implicitly assumed that they are on the sample scale. If treated as an open system, the full range of δ^{56}Fe values can be produced.

Based on the extent of DIR and the ratio of alkalinity versus organic carbon (Reaction 5.1), various reaction pathways can be designed to reach isotopic mass-balance for individual micro-drilled carbonate samples (e.g. *Table 1 in* Heimann, et al., 2010). The formation of siderite with varying δ^{56}Fe but similar δ^{13}C in mm-scale samples has been explained by a conceptual model (Figure 5.6) showing the degree of DIR-completeness within the sediment (Heimann, et al., 2010). Although maximum micro-scale δ^{56}Fe variation within a microband or a cm-scale sample for a certain mineral can be over 1 ‰ (e.g. magnetite in sample 3/59, Steinhoefel, et al., 2010), the average variation is much smaller (Johnson, et al., 2003; 2008a; Steinhoefel, et al., 2009; 2010; Heimann, et al., 2010; Li, et al., 2013; 2015). Diagenetic δ^{56}Fe re-distribution on sub-sample scales, either via DIR or another mechanism, is of obvious importance and this is corroborated by other isotopic systems, including C, O and Nd (Heimann, et al., 2010; Li, et al., 2013; 2015).

However, as stated in Li, et al. (2015): "*…local recycling of Fe by DIR cannot well explain the changes in δ^{56}Fe values of BIFs on stratigraphic scales, unless a mechanism is found to transport large quantities of DIR-generated Fe on a basin-wide scale.*" The sequential extraction technique averages out these small-scale variations to a bulk-rock level, but still has the advantage of determining

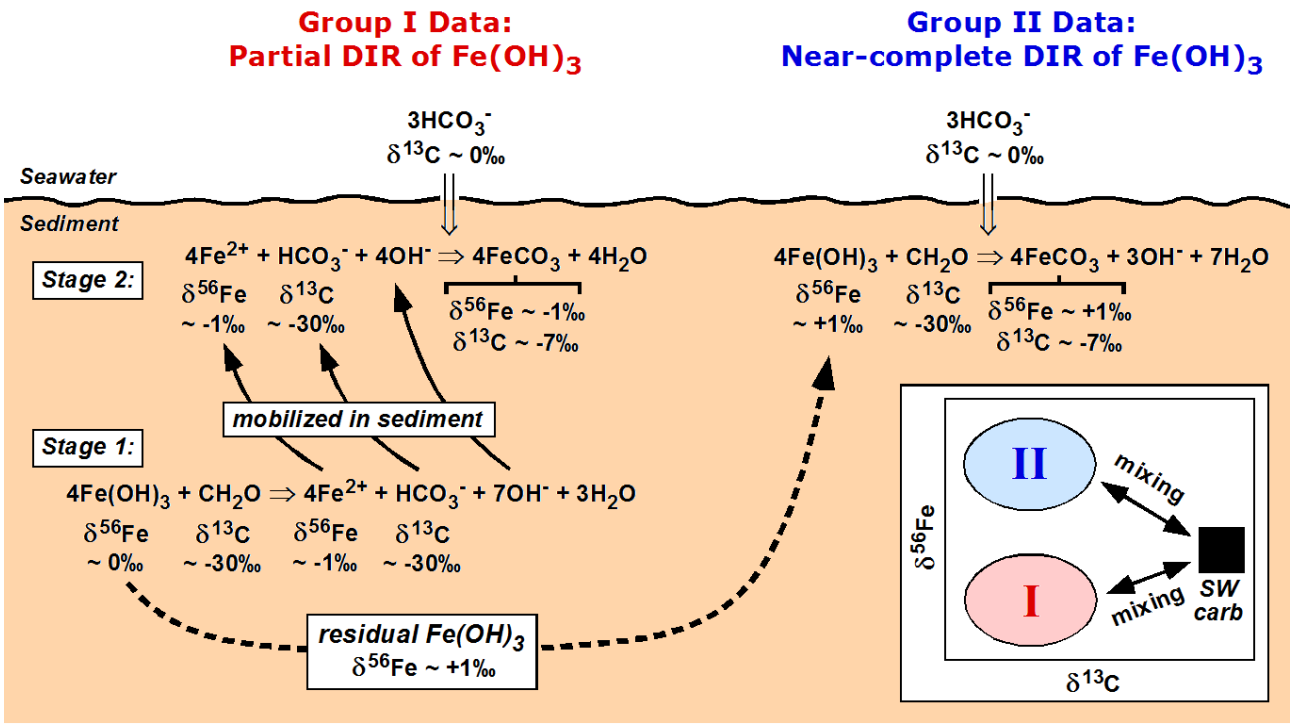

Figure 5.6: Conceptual diagram that shows a conceptual model for the diagenetic origin of BIF Fe carbonates based on mineralogical, chemical, and C, O, and Fe isotope data. Two main groups of carbonates that have low-$\delta^{13}C$ values (~–7.5 ‰) are defined by low $\delta^{56}Fe$ values (~–1 ‰; Group I) and high $\delta^{56}Fe$ values (~+1 ‰; Group II), which originate through a multi-step process. For Group I data, in "stage 1," partial microbial reduction of $Fe(OH)_3$ with $\delta^{56}Fe$ of ~0‰ and oxidation of CH_2O with $\delta^{13}C$ ~–30 ‰ results in generation of Fe_{aq}^{2+} with $\delta^{56}Fe$ ~–1 ‰ and HCO_3^- with $\delta^{13}C$ ~–30 ‰. In "stage 2," low–$\delta^{56}Fe$ Fe_{aq}^{2+} is mobilized and reacts elsewhere in the sediment column with (i) HCO_3^- derived from stage 1, and (ii) seawater HCO_3^- to form siderite with $\delta^{56}Fe$ ~–1 ‰ and $\delta^{13}C$ ~–7.5 ‰. Because Fe_{aq}^{2+} and HCO_3^- have been mobilized prior to carbonate precipitation, Fe carbonates in this group do not contain Fe-oxide inclusions. Group II data are interpreted to reflect Fe_{aq}^{2+} produced by near-complete reduction of high-$\delta^{56}Fe$ residual $Fe(OH)_3$ from stage 1, which will produce siderite with $\delta^{56}Fe$ ~+1 ‰ and $\delta^{13}C$ ~–7.5 ‰. In this case, DIR and siderite formation are envisioned to occur "in place," and a small amount of un-reacted $Fe(OH)_3$ is later converted (by dehydration and recrystallization) to ferric oxide, forming hematite inclusions. This process is represented by carbonates that contain ferric oxide inclusions and fall in Group II of isotope compositions. *Reproduced including caption from Heimann, et al. (2010).*

fraction specific signals over stratigraphic intervals. If diagenetic DIR acted as a closed system on a sub-sample scale levels, then the bulk-rock values are still representative of the initially sourced Fe, however the fraction specific isotope ratios do not necessarily reflect these similar values.

As shown above, the $\Delta\delta^{56}Fe_{OX\text{-}CAR}$ value is dependent on the amount of oxide-bound Fe present (Figure 5.4b). If the ferrous iron fraction reflects closed-system diagenetic processes such as DIR, then the products were fractionated with respect to the initial reactants. Regardless of the exact

fractionation process, either equilibrium or kinetically driven, both ferric (oxide) and ferrous fractions (carbonates, silicates) in a closed-system are then coupled, and linked to the initial precursor $\delta^{56}Fe$.

Oxidation of ferrous Fe in the upper layers of the basin could have occured via photosynthetically produced O_2, photoferrotrophs or an abiotic pathway to produce insoluble ferric-(oxy)hydroxides. Depending on the extent of oxidation these particulates could have had a positive to near-seawater isotopic signature. During settling these particles would have equilibrated with the surrounding seawater within weeks, based on experimental studies wherein isotopic equilibrium is reached between aqueous Fe(II) and ferric oxides due to adsorption and atomic exchange (Pedersen, et al., 2005; Handler, et al., 2009; Mikutta, et al., 2009). So, depending on the extent of initial oxidation, seawater $\delta^{56}Fe$ and settling speed, the ferric-oxyhydroxide reaching the seafloor could have a $\delta^{56}Fe$ value ranging from seawater to more positive values linked to the equilibrium fractionation value.

When only a small portion of these ferric particulates is reduced, the isotopic difference between the products and reactants would be large (Johnson, et al., 2005). If this was transferred into the diagenetic minerals, the ferrous minerals would be relatively low in abundance and significantly lighter isotopically than the mixed-valence oxides, i.e. large $\Delta\delta^{56}Fe_{OX\text{-}CAR}$. In this case the modal sample mineralogy would have a considerable influence on the bulk-rock value.

Near-complete DIR with respect to Fe would produce a ferrous fraction with an iron isotope ratio closer to the initial ferric precipitate (Percak-Dennet, et al., 2013). Provided that enough bi-carbonate or silica was present to form abundant ferrous minerals, the modal mineralogy would not then play such an important role since the end-member iron isotope values of individual fractions are closer to one other. Bulk-rock and extracted data would track the initial seawater $\delta^{56}Fe$ more closely as long as magnetite was low in abundance.

Based on this argument, the lower, carbonate-rich part of the Griquatown IF could be argued to more closely record a primary seawater signal. However, this would mean that the seawater values varied and were negative (<-1.0 ‰). These negative values deviating from more normal seawater of 0 ‰ could be explained by an isotopic gradient in the water column or a Rayleigh-mechanism as discussed above (section 5.4.1). Rouxel, et al. (2005) suggested similar negative seawater signatures for pre 2.3 Ga oceans, due to the continous drawdown of iron oxides with positive $\delta^{56}Fe$.

5.4.3.3. Magnetite-rich samples

The magnetite-rich bulk-rock samples, possibly linked to partial DIR, tend to be relatively thinly banded in the Asbestos Hills BIFs, with an absence of more massive magnetite-mesobands. In these samples magnetite exists essentially as monomineralic microbands or as crystal aggregates up to a cm in thickness. In thicker banded samples magnetite is generally present as individual crystals or as fine laminae in between ferrous mineral or chert bands, making it only a minor constituent.

In microbanded BIF, magnetite laminae are intercalated with various oxide-poor chert/carbonate/silicate bands. This textural evidence suggests decoupling of the magnetite and oxide-poor bands, or possibly even diverse sources for each. However, they could still be coupled as surplus Fe(II), produced by DIR, could have moved upward through the sediment column and reacted with precipitating ferric particulates to form magnetite at a suitable redox-front.

As discussed above, oxide-rich samples tend to have larger $\Delta\delta^{56}Fe_{OX\text{-}CAR}$ values (Figure 5.4b), which bracket the bulk-rock isotope ratios. These bulk-rock ratios might be dependent on modal mineralogy rather than initial seawater composition. However, the range bracketed by the various fractions and the fact that the oxide sample with the highest $\delta^{56}Fe$ (HEX872) does not have the largest $\Delta\delta^{56}Fe_{OX\text{-}CAR}$ variation, indicates that the variability across stratigraphy carries a primary seawater signal.

5.4.4. Decoupled formation pathways

One of the key assumptions generally made in the interpretation of $\delta^{56}Fe$ in BIFs is that ferrous minerals were produced through a single formation pathway from primary ferric precipitate during diagenesis (e.g. Johnson, et al., 2008a). Arguments, based on petrology (e.g. Ayres, 1972) and geochemistry (e.g. Kaufman, et al., 1990; Bau and Dulski, 1996) however, indicate that primary carbonate precipitation can occur. By transferring DIR into the water column (Tsikos, et al., in prep.) or involvement of a benthic shuttle (Lyons and Severmann, 2006; Severmann, et al., 2008; Li, et al., 2015) a new decoupled interpretation for the ferric versus ferrous fraction in BIF can be considered.

The Fe source for the ferrous fraction could remain as the initial ferric precipitate which was formed in the surface waters. Water column DIR would produce ferrous Fe and deliver the carbon to be included in the carbonate fraction. Depending on the availability of organic carbon versus ferric

particulate, various isotopic ratios could be produced consistent with observations in BIF carbonate (Heimann, et al., 2010). The rhombohedral carbonates present in BIF were remineralized from very fine grained primary carbonates and could retain their original geochemical signature (Frost, et al., 2007).

The ferric fraction in BIF is in this instance would be related to periods when there was low organic carbon supply relative to the amounts of ferric-particulate. In this instance a significant portion of the ferric precursor would not have been reduced and could thus react with ferrous Fe to form magnetite. This magnetite would have a higher $\delta^{56}Fe$ than the surrounding seawater.

Such a model has advantages over a completely localized DIR model. First of all, by transferring the formation process into the water column, the regional consistency seen in bulk-rock C and Fe isotopes (Figure 5.2) can be explained. Instead of very local diagenesis, this model will create a more regional mechanism, which averages out any erratic patterns on the bulk-rock sample scale.

Secondly it can explain the fraction specific trends seen in Figure 5.3. The carbonate-rich samples in the Griquatown Formation are the result of dominant water column DIR over ferric particulate accumulation. Since the majority of the ferric particulate was reduced, no large $\Delta\delta^{56}Fe_{OX\text{-}CAR}$ values would be expected, as the reduction was near quantitative giving the ferrous fraction near-zero $\delta^{56}Fe$ values (Percak-Dennet, et al., 2013). As it would have been a dynamic open process in the water column, the ferric-particulate which would eventually form would also more or less retain its original isotopic signature.

The magnetite-dominated samples, which have larger $\Delta\delta^{56}Fe_{OX\text{-}CAR}$ values, would have formed during periods when ferrous oxidation in surface waters prevailed over water column DIR either at the chemocline or in the benthic zone. Since the ferric particulate would have been in surplus, partial DIR would have preferentially selected the lighter isotopes. The isotopic ratios in the minor ferrous fraction would therefore deviate strongly from the dominant oxide fraction. The bulk-rock $\delta^{56}Fe$ signatures are, as discussed above, still dependent on mineralogy and, at best, reflect the degree of oxidation that was present in the surface waters.

This model does not exclude localized diagenesis. The precursor minerals recrystallized to form the rhombohedral carbonate grains and larger magnetite aggregates. Microbially-driven processes might have played a role here, causing the isotope variations seen on mm-scales in other studies

(e.g. Johnson, et al., 2003). These small-scale secondary processes and related isotope variations are however averaged out by the bulk-rock character of the sequential extractions.

5.4.5. δ^{56}Fe and Mn

The correlations between bulk MnO or Fe/Mn with δ^{56}Fe in BIF samples (Figure 5.7) are intriguing and span nearly half a billion of years during Superior-type BIF deposition prior to and including the GOE. The correlation is exponential with respect to MnO and Fe/Mn and the trends are not visible on a linear scale. The behaviour of Mn is described elsewhere in this thesis in detail (Section 3.4.2.4). This resulted in a model for the Asbestos Hills in which Mn was passively incorporated into the primary precipitating Fe-carbonates as Mn(II). The model was supported by inter-core correlatable bulk-rock δ^{13}C values (Figure 1.10; Tsikos et al., in prep.) and the absence of negative Ce anomalies (Chapter 4; Figure 4.1). Ce anomalies are also absent in the contemporaneous Brockman IF (Haugaard, et al., 2016).

The onset of an active Mn redox cycle, and hence redox stratification, might be indicated for the Koegas Subgroup and has been well established in the Hotazel Formations based on the presence of negative Ce anomalies (Bau and Alexander, 2006; Nel, 2013). The MnO and δ^{56}Fe trend was previously reported for the Koegas Subgroup BIF, and explained in a model where partial oxidation of Fe and isotope fractionation was associated with Mn-oxide formation (Kurzweil, et al., 2016). However, this model does not work for the Asbestos Hills BIFs. Therefore an explanation is favoured based upon a continuous drawdown of more positive δ^{56}Fe in Fe-oxyhydroxides needed to form the Asbestos Hills BIFs that depleted the seawater in ^{56}Fe compared to ^{54}Fe, in combination with the passive increase in Mn (Section 3.4.2.4).

A compilation of literature bulk-rock δ^{56}Fe and Fe/Mn data, combined with the data from this thesis, shows a clear general trend (Figure 5.7). Over a time period of 0.4 Ga the average bulk-rock δ^{56}Fe and Fe/Mn ratio decreased and bulk-rock MnO increased. This suggests two underlying processes, assuming a constant influx of Fe, Mn and δ^{56}Fe. First of all, the seawater δ^{56}Fe would not have been constant over time, but in fact became more negative due to preferential precipitation of ferric oxy-hydroxides with positive δ^{56}Fe. Secondly, and in tandem, the global oceans would have become more manganiferous over time due to passive enrichment, culminating in the deposition of

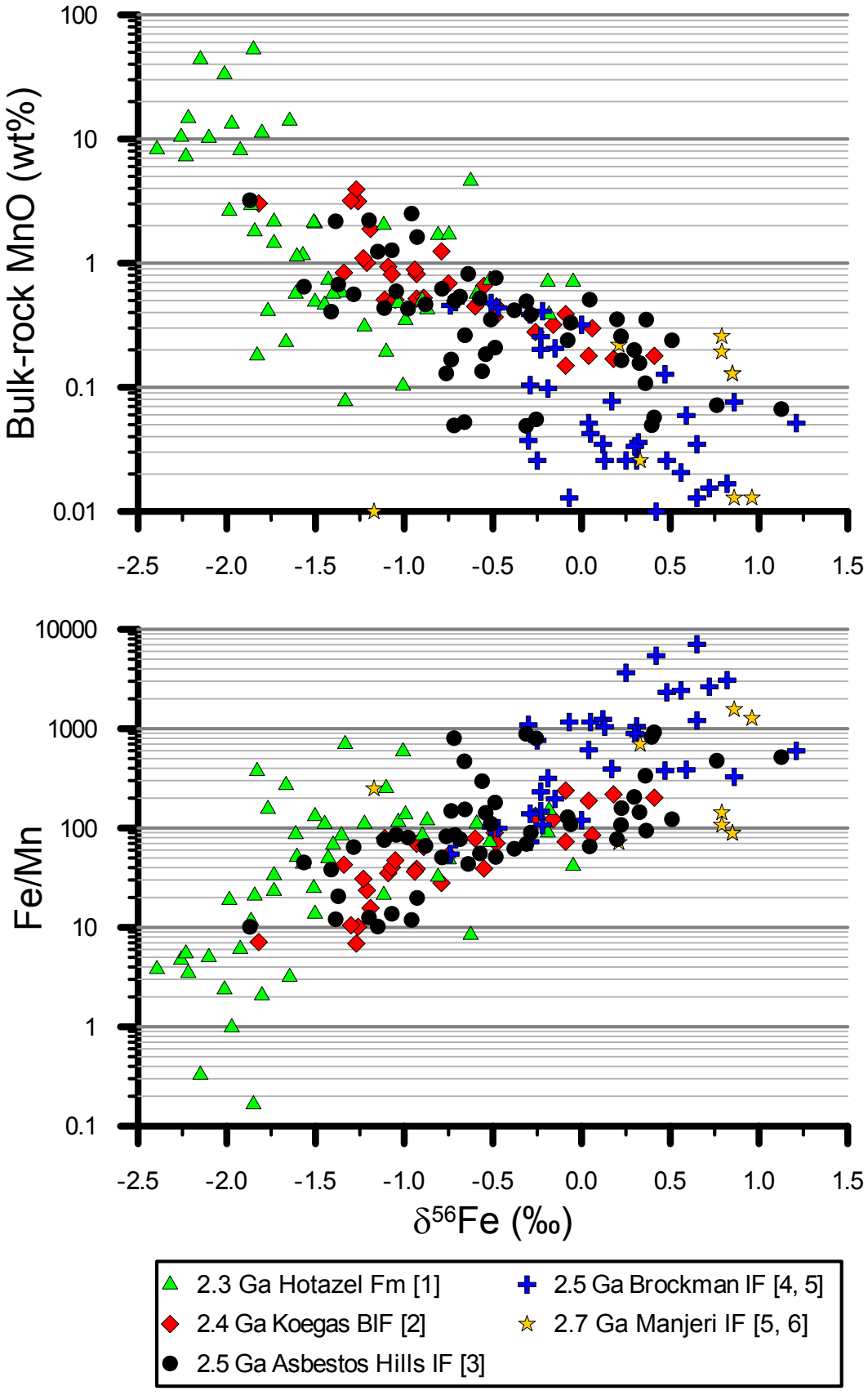

Figure 5.7: Correlation between bulk-rock $\delta^{56}Fe$ and bulk-rock MnO and Mn/Fe ratio of multiple iron formations. Note vertical axes are logarithmic scaled so trends are exponential functions. See text for discussion. Data sources: [1] Tsikos, et al. (2010), [2] Kurzweil, et al. (2016), [3] this study, [4] Haugaard, et al. (2016), [5, 6] Planavsky, et al. (2012, 2014).

the Hotazel Formation. The apparent trend in this compilation supports a global reservoir effect (e.g. Tsikos, et al., 2010). However, a globally-evolving, but opposite, trend of $\delta^{56}Fe$ in pyrite was observed by Rouxel, et al. (2005), with highly negative $\delta^{56}Fe$ trending towards more positive over time.

These large global trends suggest a changing background against which individual iron formations should be assessed. Variations seen between samples from the same IF could be heavily influenced by local conditions such as modal mineralogy, depth of deposition, diagenetic overprints and the local oxidation state. These conditions will affect the Mn, Fe and $\delta^{56}Fe$ of each sample and shift individual values away from the background trend. The existence of the general trend however indicates that the bulk-rock samples quantitatively capture a changing seawater signature.

5.5. Conclusions

The 50 bulk-rock iron isotope ratios of the Kuruman and Griquatown IF nearly span the previously identified range for BIF across the entire geological record. The bulk-rock $\delta^{56}Fe$ of the samples from three separate drill-cores, with more than 20 km in between them, show a regional, stratigraphic co-variation independent of sample mineralogy. Nonetheless, modal mineralogy still influences the bulk-rock values, as Fe-carbonate dominated samples have lower $\delta^{56}Fe$ values then magnetite ones. Determining the fraction specific isotopic values helped to interpret these initially paradoxical relationships. The expected trends of lower $\delta^{56}Fe$ for ferrous fractions and a higher one for the mixed-valence oxide were found. The co-variation between the Fe-silicates and Fe-carbonates are striking and hint to a similar Fe-source. The disparity in $\delta^{56}Fe$ between the oxide and carbonate fraction ($\Delta\delta^{56}Fe_{OX\text{-}CAR}$) seems to relate the mineralogy to the stratigraphy. Generally the thinner banded sections of BIF are more oxide-rich than the thicker banded parts, because magnetite does not occur in thick discrete bands whereas the other fractions do. In other words, in the thicker bedded sections most Fe is ferrous dominated, whereas the microbanded parts contain have more mixed-valence Fe.

When translated to the original deposition models the variation cannot be explained by equilibrium fractionation. A coupled diagentic conceptual model, linking the oxide and carbonate formation, might be possible, although this model does not necessary explain the regional co-variation in bulk-rock $\delta^{56}Fe$. Therefore we prefer a decoupled model with primary precipitation of the

carbonate and oxide precursor minerals. In the thicker bands, with near-zero $\Delta\delta^{56}Fe_{OX\text{-}CAR}$, precipitation occured in a setting with near quantitative water column DIR. In the magnetite dominated parts of the stratigraphy, partial DIR fractionated the ferrous and ferric isotope ratios. When this occurs in a basin with gradients in $\delta^{13}C_{DIC}$ and $\delta^{56}Fe$, such a model could also explain their bulk-rock co-variation in the near-quantitative DIR part of the stratigraphy.

The presence of a global trend in bulk-rock $\delta^{56}Fe$ and Fe/Mn can be explained by changing seawater chemistry. Due to precipitation of ferric oxy-hydroxides with positive $\delta^{56}Fe$ and redox passive behaviour of Mn, the overall seawater becomes more negative in $\delta^{56}Fe$ and enriched in Mn over time. The second-order deviation from this trend can be related to the varying conditions such as modal mineralogy, depth of deposition, diagenetic overprints and the local oxidation state.

“Nelson Mandela reminds us that it always seems impossible until it is done.“

Barack Obama, *Eulogy for Nelson Mandela* (2013)

6

SYNTHESIS

6.1. Primary signals in BIF

Bulk-rock BIF samples potentially have contrasting mineralogies, which could significantly affect their geochemistry. To interpret bulk-rock signals it is therefore important to constrain the modal mineralogy. Based on species-specific rare earth element patterns (Chapter 4) and iron-isotope ratios (Chapter 5) there are various formation pathways for the different mineral fractions in BIF. This indicates that bulk-rock signals do not necessarily depict original ocean chemistry, but could instead represent the ratio of the various minerals controlled by depositional or diagenetic processes.

In contrast, bulk-rock PAAS-normalized REE patterns have often been interpreted to reflect primary seawater signals (e.g. Derry and Jacobsen, 1990; Planavsky, et al., 2010). The samples analysed in those studies tend to be Fe-silicate-poor, making the carbonate fraction the dominant REE host as the oxides are REE depleted (e.g. Alibert, 2016). Based on the work presented in this thesis, there are multiple lines of evidence which indeed argue in favour of primary geochemical signals being recorded in the carbonate fraction in BIF.

Among the strongest indicators for primary carbonates are the REE. First of all, the PAAS-normalized carbonate fraction and the *in situ* ankerite and siderite data are similar to contemporaneous seawater (Chapter 4). Secondly, the stratigraphically dependent $(Yb/Ce)_{SN}$ ratios cannot be readily explained diagenetically, and indicate a relationship with primary carbonate. Another key indicator is the regional stratigraphical co-variation in bulk-rock $\delta^{13}C$ between the four different cores (Figure 1.11; Tsikos, et al., in prep.). This co-variation is independent of the ankerite/siderite ratio, bulk-rock carbon content or TOC-concentration. The reproducible signal also indicates a regional formation mechanism, which is arguably easiest explained by primary carbonate precipitation from seawater.

Another clear trend observed in the carbonate fraction is the stratigraphic increase in Mn (Chapter 3), which eventually culminated in the deposition of the high-grade Mn-ore in the Hotazel

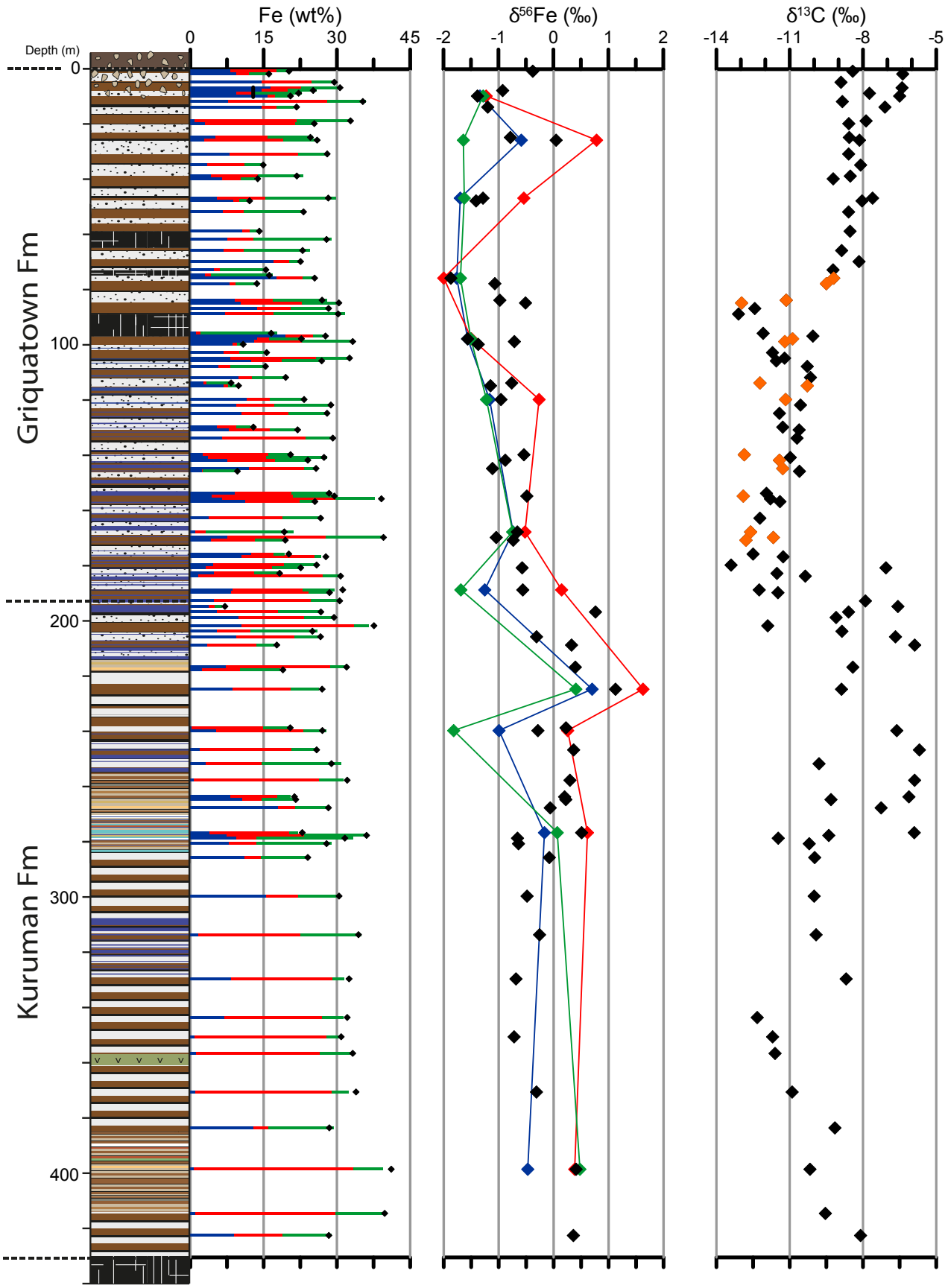

Figure 6.1: Fe-distribution, $\delta^{56}Fe$ and $\delta^{13}C$ versus stratigraphy. Blue colors are acetate extracted, red oxalate extracted, green silicate residue. Black symbols are bulk-rock values. The orange symbols in the $d^{13}C$-plot are the samples which correlate to the bulk-rock $d^{56}Fe$ isotopes (Chapter 5).

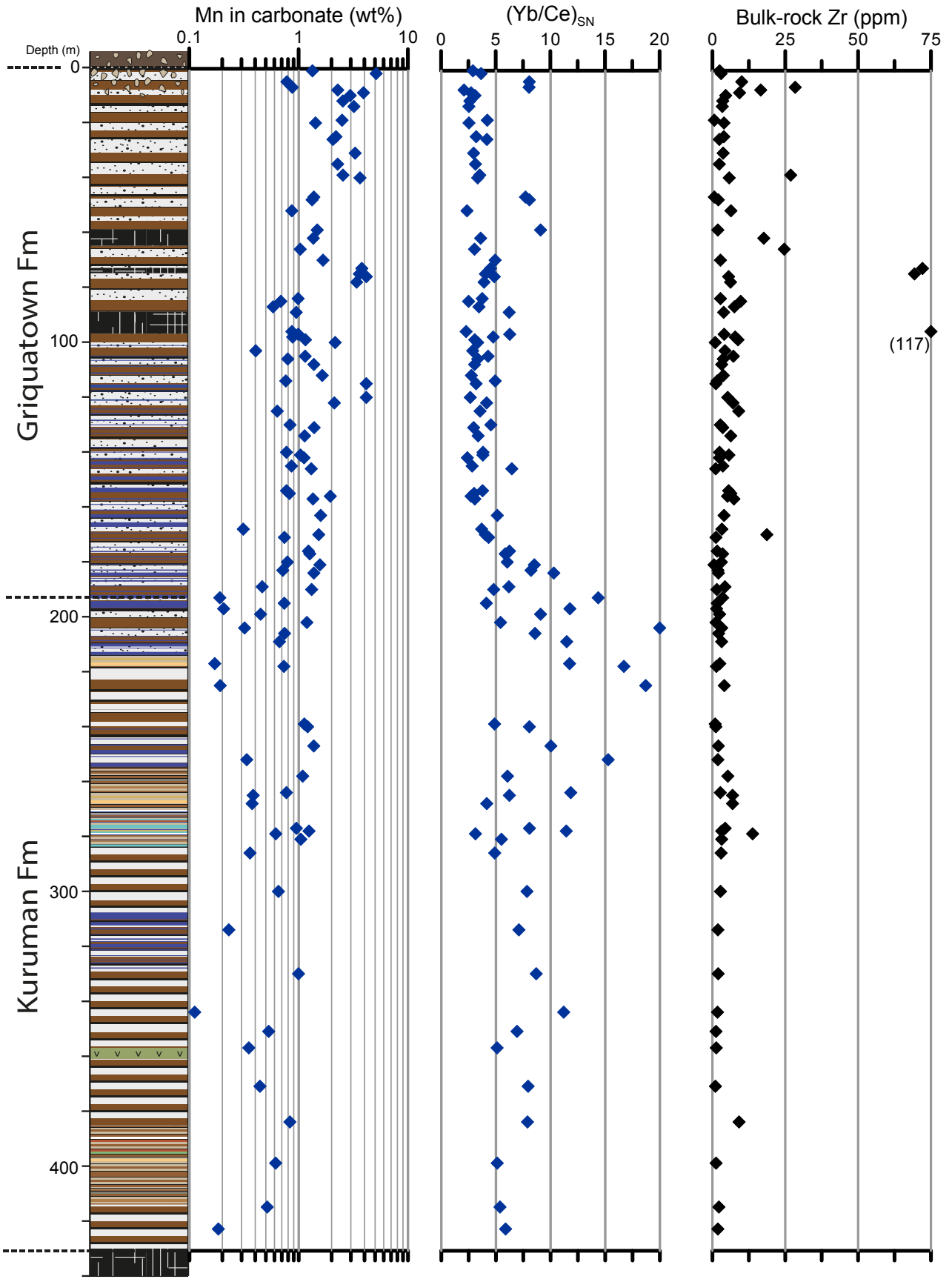

Figure 6.1 *continued*: **Mn and $(Yb/Ce)_{SN}$ of the carbonate fraction and bulk-rock Zr versus stratigraphy. Blue colors are acetate extracted samples. Most samples contain very little detrital input as seen by the Zr content.**

Formation (Tsikos, et al., 2003). The Mn-increase can be observed in all cores and is independent of carbonate mineralogy (Figure 6.1), as both ankerite and siderite can host more than 5 wt% MnO (Table 1.1; Rafuza, 2015). Combined with the absence of Ce anomalies (Chapter 4) in the bulk-rock, the fraction specific and the *in situ* LA-ICP-MS data, this indicates that at the time of deposition of the Asbestos Hills BIF, the ocean was reducing with respect to Mn (Bau and Dulski, 1996). Mn-hosted in carbonates is in the divalent state (e.g. Johnson, et al., 2016); therefore passive Mn-incorporation in the crystal structure of the primary carbonates could explain this trend. Diagenetic pathways, such as Mn-oxidation by photosynthetically produced O_2 and subsequent dissimilatory Mn reduction are a less parsimonious explanation for the increase of Mn in carbonates (Chapter 4).

There are however other arguments against a primary origin of the carbonate fraction. The most obvious one is based on petrology. The larger rhombohedral, predominantly ankeritic carbonate crystals are recrystallized. The assumption that this recrystallization did not significantly alter the carbonate geochemistry in the samples studied here is viable, and has been shown before, including arguments for a minor influence of diagenesis on REE patterns (e.g. Bau, 1993) and the preservation of $\delta^{56}Fe$ heterogeneities during metamorphism (Frost, et al., 2007).

Nonetheless, Heimann, et al. (2010) and Johnson, et al. (2013) argue based on Fe, C, O and Rb-Sr isotope systematics in micro-drilled carbonates of the Kuruman IF that they record extensive microbial Fe-cycling in the soft-sediment. Alibert (2016) also argues that the carbonate-REE patterns were equilibrated with pore-waters instead of seawater. However, these studies were performed on specific Fe-carbonate bands or large carbonate grains, and are therefore prone to sample selection bias. Although the heterogeneities on these scales possibly represent diagenetic processes, the overall bulk-carbonate signal still has the ability to track chemical seawater changes.

The two other fractions extracted in this study, the Fe-oxides and Fe-silicates, are less accurate tracers of seawater chemistry. The Fe-oxides are depleted in almost all trace elements and their $\delta^{56}Fe$ values rather reflect the extent of dissimilatory iron reduction (DIR; Section 6.3). However, the extracted MREE-enriched signals might reveal a primary REE component in precipitating ferric-particulates. The proxies for the iron-silicate fraction give contrasting signals. Co-variation in the $\delta^{56}Fe_{silicate}$ with the $\delta^{56}Fe_{carbonate}$ hints to a similar (primary) origin (Chapter 5), whereas the variable REE patterns indicate various influences from detrital material or volcanic ash (Chapter 4). This paradox

can be explained by decoupling the sources of REE and iron in the silicates.

The deposition of the Asbestos Hills BIF took place in a detritus poor setting with water depths up to 100s of meters (e.g. Beukes, 1984). In these settings only the most resistant detrital minerals (e.g. zircon, monazite) would still be present to form the detrital fraction. These resistant minerals are generally good REE hosts and might have a significantly impacted the fraction specific REE data. This can also explain why all the silicate-minerals analysed *in situ* by LA-ICP-MS show a PAAS-normalized LREE depleted, HREE enriched pattern, whereas the extracted REE_{SN} patterns vary significantly. The *in situ* analysed minerals could potentially capture a seawater-like pattern, similar to the carbonate fraction, whereas the extracted fraction represents a mixture between these patterns and a significant detrital component.

As described by Rasmussen, et al. (2013; 2015b) the Fe-silicate mineral greenalite can potentially be a primary mineral. Although the crystal structure accommodates ferrous Fe, generally it tends to be ferric dominated (Klein, 1974; 2005; Beukes and Gutzmer, 2008). If this Fe has a source similar to the Fe-carbonates, e.g. ferric Fe reduced by DIR, it could explain the $\delta^{56}Fe$ values. Silica adsorption to hydrous surfaces on ferric-Fe particulates has been proposed as the major mechanism incorporating Si in Fe-silicate minerals in BIF (Fischer and Knoll, 2009). Furthermore, this indicates that the silica-source was also seawater-like instead of detrital material (Delvigne, et al., 2012).

The Na present in the riebeckite was most likely derived from pore-fluids during diagenesis or from alkali-rich hydrothermal fluids. In the Asbestos Hills BIF, riebeckite exists in distinct bands (e.g. Horstmann and Hälbich, 1995). Localized riebeckite occurrence in only part of the stratigraphy argues, in my opinion, against the formation from pore-fluids, as there is no reason for it not to be present in other parts of the stratigraphy. Alkali-enrichment from hydrothermal fluids, potentially derived from the sills cross-cutting the stratigraphy, better explain the localized presence of riebeckite. The relationship with stratigraphy could be explained by various pulses of hydrothermal fluid flow. Still the lack of clear indicators for these fluids makes this explanation also speculative at best.

6.2. Oxidation mechanism

Various oxidative mechanisms have been proposed to explain the formation of ferric particulates (Chapter 1). Although there are abiotic pathways possible (UV photo-oxidation), recent focus has

shifted to biological pathways. Photoferrotrophic bacteria use ferrous Fe as an electron donor and can oxidize it directly to ferric Fe. A less direct way is through the activity of cyanobacteria, which use H_2O as the electron donor and produce O_2, which as a strong oxidiser can oxidize all the reduced species. The presence of stromatolites on the Campbellrand carbonate platform (e.g. Sumner, 1997) indicates the presence of phototrophic microbial communities before the deposition of the Asbestos Hills BIF. There is no direct way to discriminate between the biological pathways, i.e. both can explain the variation in $\delta^{56}Fe$ and $\delta^{13}C$. A key difference between the two mechanisms is the production of O_2. Whereas photoferrotrophs specifically target ferrous Fe, O_2 can oxidize any reduced redox-species.

As shown before, Mn is a passive redox-player throughout the deposition of the Kuruman and Griquatown IFs, because of its incorporation in the carbonate fraction, the stratigraphic increase and the lack of Ce anomalies (Chapter 3). However, the latter might be absent because of the complex relationship between Mn and Ce oxidation (Moffett, 1994; Nakada, et al., 2016). Passive Mn redox behaviour does not necessarily mean the absence of O_2. Even if some Mn was oxidized, it could be cycled back by oxidizing ferrous Fe, and in this case Mn would not be sequestered out of the basin. The strongest evidence that might help to discriminate between these mechanisms is a shift in N-isotopes in kerogen extracted from shales across the Campbellrand platform, which requires the presence of O_2 and thus indicates the presence of oxygen-producing cyanobacteria (Godfrey and Falkowski, 2009). Furthermore, the coupled Fe and Mo stable isotope data in the Campbellrand carbonates are also better explained by oxygenic instead of anoxygenic photosynthesis (Czaja, et al., 2012).

No clear conclusions can be drawn about the oxidative mechanism based upon the Kuruman and Griquatown BIF. Increasing literature-data indicating that oxygenic photosynthesis evolved before the GOE (e.g. Buick, 1992; Crowe, et al., 2013). Any oxidized Mn would be cycled back directly, or be completely reduced during early diagenesis. A detailed study into the valence state of Mn associated with the Fe-oxides might find grains with higher Mn-valences providing another pathway to argue in favour of oxygenic photosynthesis.

6.3. Depositional model

Figure 6.1 shows some of the stratigraphic relationships found and described in the previous

chapters. In this section, I create a conceptual model for the deposition of the Asbestos Hills BIFs. The main results that support this model are summarized in Table 6.1. Oxygen-producing cyanobacteria could have formed the stromatolites present in Campbellrand platform (Section 6.3). Sea level rise would have drowned the platform resulting in deposition of the banded iron formations (Klein and Beukes, 1989). The seawater would have been enriched in hydrothermally-sourced Fe and Si and/or a component from continental run-off (e.g. Isley, 1995; Fischer and Knoll, 2009; Bekker, et al., 2014; Li, et al., 2015). Hydrothermal fluids would have also introduced REE and other trace elements (e.g. Bau and Dulski, 1996; Bolhar, et al., 2004). Detrital or volcanic ash input was very small with little effect on most bulk-rock trace elements and would have consisted mainly of weathering-resistant minerals (e.g. zircon, monazite), bringing in additional elements such as Al, Ti, Zr and REE.

Microbial oxidation of Fe occuring in the surface layers of the ocean, produced insoluble ferric Fe-(oxy)hydroxide particles. These particles would have had more positive δ^{56}Fe than seawater, due to partial oxidation in surface waters with possible modification during re-equilibration on settling through the water column. Furthermore, they would have sorbed Si and preferentially incorporated MREE over the other REE during transport to the sediment layer. The reduction of these particulates took place via DIR. This could have happened at 1) the redox-cline, between the surface and deeper waters, 2) at the sediment-water interface as large benthic mats or 3) in the sediment itself (diagenetic). For the latter option regional coherent bulk-rock isotope patterns are hard to explain and therefore only played a minor role, as seen in the small-scale variations revealed by micro-analytical techniques (e.g. Johnson, et al., 2008b; Heimann, et al., 2010; Steinhoefel, et al., 2010).

To explain the chemical changes in the BIF bands there are three different end-member scenarios. These three scenarios involve variations in microbial activity, which can potentially be linked to variations in orbital cycles for the larger bands whereby climate/annual variations could be responsible for the smaller-scale banding. In the first scenario, both oxidizing (photosynthetic) and reducing (DIR) microbial communities were dormant or absent and Fe cycling was minimal. In other words, little or no ferric particulates were produced and very little Fe reduction was going on. In these periods the Fe-poor chert bands were deposited, potentially due to basin-wide (Siever, 1992), local (Beukes and Gutzmer, 2008) or pore-fluid (Delvigne, et al., 2012) oversaturation of silica. Background chert precipitation continued throughout the entire deposition of the Kuruman and Griquatown IFs.

Table 6.1: Summary of the key findings of this project and their effect on the interpretation of the Griquatown and Kuruman IFs. The section column refers to the specific section in the thesis where the findings are discussed.

Findings	Interpretation	Section
Only trace amounts of hematite present	Lack of fully oxic conditions and minimal recent alteration	1.2.2.2
Stromatolitic fossils on the Campbellrand Platform	Presence of microbiology in the area and potential for biological Fe oxidation	1.3.1
Continuous transition from Griquatown IF to Makganyene diamictite in sections studied	Glaciation (possible Snowball Earth) directly followed BIF deposition	1.3.2
Regionally co-varying bulk-rock $\delta^{13}C$ independent of mineralogy or carbonate abundance [1]	The $\delta^{13}C$ values are a primary signal indicating carbonate formation by a regional mechanism	1.3.4
Swings in the bulk $\delta^{13}C$ with stratigraphy [1,2]	Variation in organic carbon abundance or water-column gradients in DIC and $\delta^{13}C_{DIC}$	1.3.4, 5.4.1
Presence of minor MIF-S variations in the lutites [3]	Deposition before the GOE ($pO_2 < 10^{-5}$ PAL)	1.3.4
Mn only present in carbonate fraction as Mn(II)	Primary incorporation of aqueous Mn(II)	3.4.2.4
Stratigraphical increase of Mn in the carbonates	Basin becomes more manganiferous, indicating passive enrichment	3.4.2.4
No correlation between Fe and Zr in the silicate fraction	Very limited detrital Fe-component. Potentially primary origin for (some) Fe-silicates	3.4.1.3
Lack of Ce anomalies in the REY patterns	Oxidation state of the water still reducing with respect to Ce and Mn	4.1, 4.3.4
Positive Eu anomalies and super-chondritic Y/Ho ratios	Hydrothermal source for the REY elements and by extension for Fe (and Si)	4.3.1
Changing slopes of carbonate fraction REY_{SN} patterns with stratigraphy	The presence of a water column gradient or change in input sources (riverine/ hydrothermal) or long term Rayleigh fractionation*	4.3.4.1
MREE enrichment in oxide fraction REY_{SN} patterns	Preferential MREE sorption on ferric particulates *en route* to the sediment.	4.3.4.2
Completely varying silicate fraction REY_{SN} patterns	Indicates multiple sources of detrital material or volcanic ash	4.3.4.3
Regionally correlatable bulk-rock $\delta^{56}Fe$ independent of modal mineralogy	Regional scale processes involved, hinting to a water column gradient in $\delta^{56}Fe$ and potential Rayleigh fractionation with respect to Fe	5.4.1
Positive correlation between $\delta^{13}C$ and bulk $\delta^{56}Fe$ in the lower part of the Griquatown Formation	Similar gradients in isotopic ratios at the depth of carbonate formation. Near complete DIR reduces seawater equilibrated $\delta^{56}Fe$	5.4.1
Decrease in bulk-rock $\delta^{56}Fe$ from Kuruman via Griquatown to Hotazel Formation.	Long term basin-wide Rayleigh fractionation with respect to Fe, which has residence times in the order of 10^7 years.	5.4.1
Similar $\delta^{56}Fe$ for the carbonate and silicate fractions	Similar source of ferrous Fe	5.4.2
Varying $\Delta\delta^{56}Fe_{OX\text{-}CAR}$ values linked to amount of ferric vs ferrous Fe	Changing degrees of DIR in the water column, with near-complete DIR yielding small $\Delta\delta^{56}Fe_{OX\text{-}CAR}$ values and partial DIR bigger ones. Oxide-rich samples formed in the partial DIR domain.	5.4.4
Global correlation between bulk-rock Fe/Mn and $\delta^{56}Fe$	Long term changes in seawater conditions due to reservoir effects.	5.4.5

* Unlikely due to flat patterns for the Gamohaan Fm. and the relative short residence times expected for REE in Archean seawater compared to the deposition time of the stratigraphy.

[1] Tsikos, et al., in prep., [2] Rafuza, 2015, [3] Van der Waal, 2016

In the second scenario, both microbial mechanisms were present and in balance with one other. The majority of the iron oxidized in the surface waters was reduced by water column DIR, which formed the ferrous carbonate and silicate minerals. This near-quantitative reduction also yielded small $\Delta\delta^{56}Fe_{OX\text{-}CAR}$ values with only minor Fe-oxides present. In these cases the bulk-rock $\delta^{56}Fe$ were representative of the seawater and can be coupled to the $\delta^{13}C$.

The third scenario involves a cyanobacteria bloom, thereby creating an oxygen-rich surface layer and oxidizing large quantities of Fe. The DIR-bacteria were overwhelmed and only reduced a portion of the ferric iron. As ferric Fe was omnipresent the microbes could select isotopically light iron, thereby creating isotopically light ferrous and a relative heavy ferric Fe-pools. Transformation to the various minerals then resulted in large $\Delta\delta^{56}Fe_{OX\text{-}CAR}$ values.

The presence of a sub-oxic surface-layer in the Paleoproterozoic ocean could have produced depth gradients for various proxies. Contemporaneous Fe-rich, anoxic lakes show $\delta^{56}Fe$ gradients (Teutsch, et al., 2009; Busigny, et al., 2014) and $\delta^{13}C_{DIC}$ variations are present in sub-oxic fjords (Van Breugel, et al., 2005) and anoxic lakes (Assayag, et al., 2008). In modern seawater the REE_{SN} slope tends to get steeper in deeper water, i.e. increasing Yb/Pr ratios with depth (e.g. Piepgras and Jacobsen, 1992; Alibo and Nozaki, 1999). The presence of these gradients could explain the regional consistency in the various proxies used in this study. The average Kuruman and Griquatown values for $\delta^{56}Fe$, $\delta^{13}C$, carbonate $(Yb/Ce)_{SN}$ ratio might be (partially) related to the depth of formation.

If these proxies are indeed related to the depth of formation then the location of the DIR-colony becomes important again. If DIR occurred at the base of the redox-cline, i.e. the transition from sub-oxic to anoxic conditions, then the depth of carbonate formation should not fluctuate that much between the Kuruman and Griquatown Formation. This makes it more difficult to explain the stratigraphic depth variations in the proxies. Dissimilatory Fe reduction in the benthic zone would be better suitable to capture a depth gradient, since depending on the water depth it would incorporate the various proxies differently. If surface-oxidation was only very local around shallow- water stromatolites then a benthic Fe-shuttle (Lyons and Severmann, 2006; Severmann, et al., 2008) could transfer the ferric-Fe to the deeper parts of the basin. If surface-oxidation was more widespread, then the ferric-particulates could have also “rained” down.

As stated in the previous sections, Mn remained passive throughout the Asbestos Hills

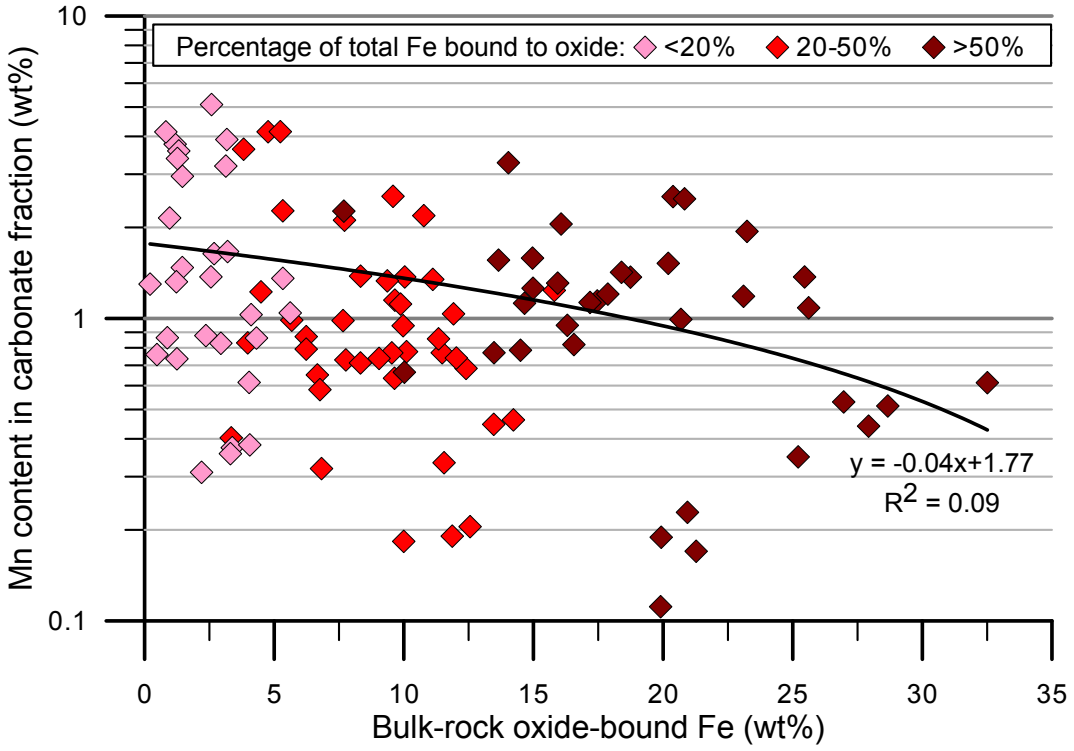

Figure 6.2: Mn content in carbonate fraction (wt%) versus the total bulk-rock oxide-bound Fe (wt%). Color code is fraction of the total Fe bound as Fe-oxides, which correlates strongly with the total bulk-rock oxide content (R^2 = 0.88).

deposition. With oxygenic photosynthesis present, some Mn would inevitably be oxidized and sink through the water column. If conditions were oxidizing enough (e.g. cyanobacterial blooms) relatively large Mn fluxes would be expected which should oxidize ferrous Fe at/below the redoxcline. If carbonate formation took place here, it would potentially have captured these enhanced Mn fluxes in the oxide-rich samples. This is not observed in the data and actually the opposite seems to be the case (Figure 6.2). The more oxide-bound Fe present, the lower the relative content of Mn in the carbonate fraction. This also argues for carbonate formation, and hence Mn incorporation, in the benthic zone instead of at the redoxcline.

This generalized conceptual model is summarized in Figure 6.3. The deposition of the Gamohaan Formation would have taken place in a shallow setting, as indicated by the stromatolites. The more oxide-rich Kuruman IF deposition took place in the deeper parts whereas the waters were shallower during Griquatown sedimentation. The basin was stratified with respect to Fe^{2+}, $(Yb/Ce)_{SN}$, $\delta^{56}Fe$, $\delta^{13}C$ and O_2, whereas Mn was more or less constant throughout the water column but became more enriched with time. The formation of carbonate (ferrous) versus oxide (mixed-valence) BIF facies with respect to depth as present before (e.g. Klein, 2005) might have been related to more intensive

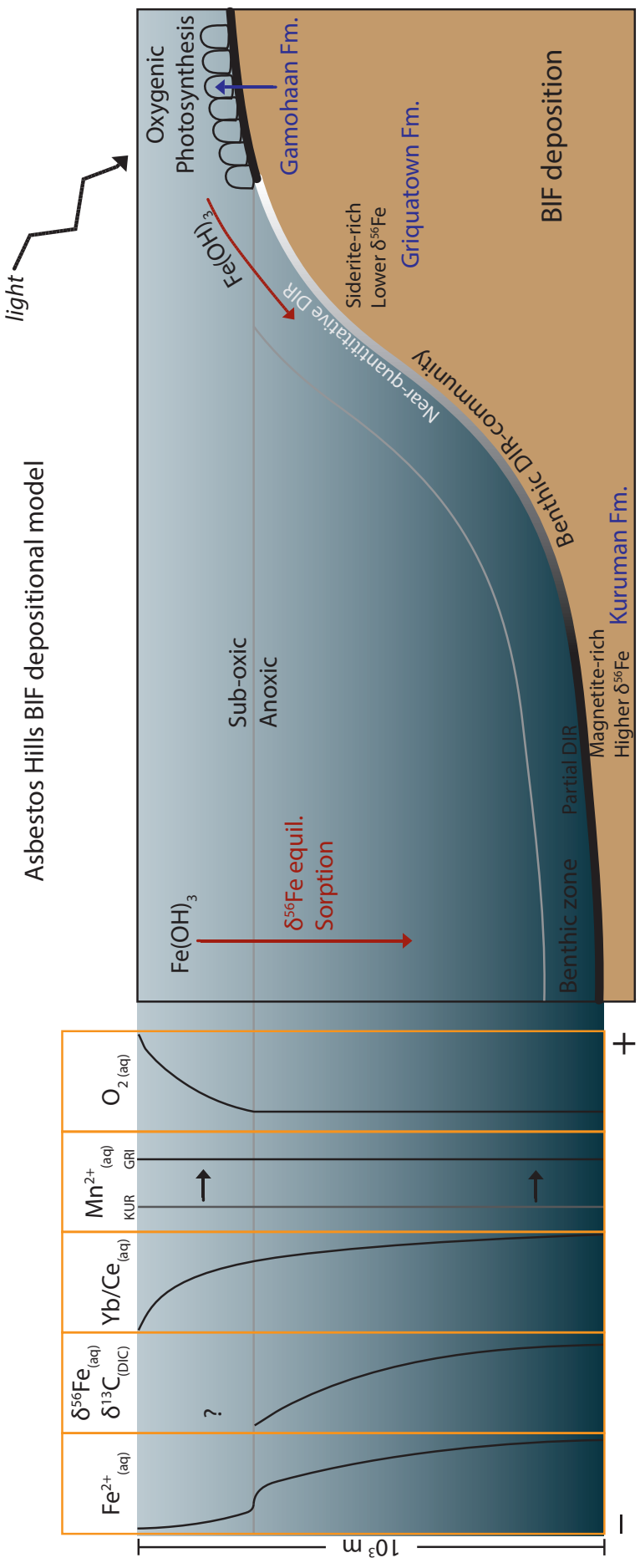

Figure 6.3: General conceptual model of BIF deposition of the Kuruman and Griquatown Formations. The seawater contains gradients in Fe^{2+}, $\delta^{56}Fe$ and $\delta^{13}C$, $(Yb/Ce)_{SN}$. Iron oxidation occurs in the sub-oxid surface waters. Ferric particulates are shuttled down wards in the benthic zone or rain down. Sorption of REE (preferential MREE) and Si onto the particulates occurs during transport. A benthic DIR community (partially) reduces the iron and forms the precursor minerals therby trapping the surrounding seawater signals. The magnetite-rich Kuruman banded iron formation is formed in deeper water than the more carbonate-rich Griquatown granular IF. Manganese is passively incorporated in the primary carbonates, which record an increasing $Mn^{2+}_{(aq)}$ concentration with time

or more quantitative DIR in the shallower water compared to deeper parts of the shelf.

6.4. Future directions

This study combined with the ongoing work of the PRIMOR-group on the Hotazel Formation complements our understanding of the BIFs in Griqualand West Basin of the Transvaal Supergroup. The focus of this project was on the geochemistry of the BIFs and the petrography and sedimentology of the samples was given less attention. That would be my first recommendation; strengthen the correlation of the geochemical signals with sedimentology and/or detailed petrography. Work like this could provide more details within the formations with regard to transgressive cycles for example.

Other work should focus on the regional stratigraphy and relationships with overlying strata. The possible lateral correlation with of the top of the Asbestos Hills Subgroup on the carbonate platform with the Koegas Subgroup (Section 3.4.2.4) in the basin needs to be investigated. A potential way to do this would be to measure bulk-rock $\delta^{13}C$ in the Koegas and try to correlate this to the existing chemo-stratigraphy (Tsikos, et al. in prep.). Furthermore, a high-resolution (geochemical) study of the transition from the Griquatown BIF into the Makganyene diamictite could provide important insights in the changing global environment immediately before the GOE. If the "Snowball Earth" was caused by enhanced weathering which acted as a major CO_2 sink, this should be reflected in the chemo-stratigraphy. This work should also include Mn, because if the correlation with the Koegas is present, then the onset of an active Mn redox-cycle might be captured here as well. The new Ongeluk age of 2.426 ± 3 Ga (Gumsley, et al., 2017) brackets the Asbestos Hills deposition quite rigorously. Attempting to correlate these BIFs with their counterparts in the Hamersley basin, Australia based upon chemo-stratigraphy would be a very useful exercise. This could utilize bulk-rock $\delta^{13}C$, Mn concentrations and potentially $\Delta\delta^{56}Fe_{OX\text{-}CAR}$.

The presence of distinct blue riebeckite (crocidolite) bands, after which the Asbestos Hills are named, is also intriguing. Riebeckite occurs only as a trace mineral in other parts of the stratigraphy. Questions regarding the formation processes of riebeckite regarding potential alkali-rich fluids or a hydrothermal component might be answered by detailed REE analysis and petrography. As the prime alkali-bearing mineral, riebeckite might hold some answers regarding post-depositional fluid flow and low-grade metamorphism.

One of the key problems for BIFs in general is the lack of datable minerals and hence accurate deposition rates of various parts of the stratigraphy. The influence of Milankovitch cycles on BIF deposition has been suggested numerous times. Such processes might also be responsible for the changes of partial-DIR to near-quantitative DIR as seen by the $\Delta\delta^{56}Fe_{OX\text{-}CAR}$. This change could be due to varying ferric input (e.g. varying conditions at the surface layer) or varying sizes of the microbial DIR community (e.g. nutrient limited) which can respond to astronomical forcing.

The depositional model proposed here could further be tested in an experimental setup. Experiments could include an investigation of Mn incorporation into Fe-carbonates under controlled laboratory conditions with varying degrees of oxidation potential. This could simulate the changing conditions needed to form Mn in Fe-carbonates in the Griquatown and pure Fe-free, Mn carbonates in the Hotazel Formation. Dissimilatory iron reduction experiments with varying amounts of ferric input could also simulate the proposed cyanobacterial blooms and/or declines.

The Transvaal Supergroup BIFs capture the period immediately prior to and including the GOE. Increased atmospheric oxygen should be reflected in the isotope-geochemistry. Detailed stable isotope stratigraphy of transition metals such as Mo, Cr, Ce, Ni and Cu and might help to constrain this change, either on bulk-rock or on the specific fractions. Acetate leached Cr-isotopes on marine carbonates (Frei, et al., 2009) might be suitable to apply in BIFs as well, considering the primary geochemical signals they carry. Whereas some work has been done on MIF-S in the Transvaal Supergroup, a more detailed study might further constrain the increase in atmospheric oxygen, especially across stratigraphy including or equivalent to the Hotazel Formation. Other isotope systems like Si, Se and Ge could also help unravelling the deposition and post-deposition processes.

Finally, the sequential extraction procedure and subsequent Fe-isotope analysis developed here could be applied, with relative ease, on other BIFs of different ages and locations. The conclusions from this thesis are potentially valid for other BIFs as well. The Rapitan-like IFs, deposited during the second oxidation pulse at the late Neoproterozoic, might be interesting to analyse with this technique, as the relationship between the oxygenation and the rise of animals remains convoluted. However, these IFs contain hematite and further development of the extraction techniques would be required.

REFERENCES

Abbott D. H. and Isley A. E. (2002) The intensity, occurrence, and duration of superplume events and eras over geological time. *Journal of Geodynamics* **34,** 265-307.

Alexander B. W., Bau M., Andersson P. and Dulski P. (2008) Continentally-derived solutes in shallow Archean seawater: rare earth element and Nd isotope evidence in iron formation from the 2.9 Ga Pongola Supergroup, South Africa. *Geochim. Cosmochim. Acta* **72,** 378-394.

Algeo T. J. and Lyons T. W. (2006) Mo–total organic carbon covariation in modern anoxic marine environments: Implications for analysis of paleoredox and paleohydrographic conditions. *Paleoceanography* **21,**

Alibert C. (2016) Rare earth elements in Hamersley BIF minerals. *Geochim. Cosmochim. Acta* **184,** 311-328.

Alibo D. S. and Nozaki Y. (1999) Rare earth elements in seawater: particle association, shale-normalization, and Ce oxidation. *Geochim. Cosmochim. Acta* **63,** 363-372.

Anbar A. D. (2004) Iron stable isotopes: beyond biosignatures. *Earth Planet. Sci. Lett.* **217,** 223-236.

Anbar A. D. and Holland H. (1992) The photochemistry of manganese and the origin of banded iron formations. *Geochim. Cosmochim. Acta* **56,** 2595-2603.

Anbar A. D. and Rouxel O. (2007) Metal Stable Isotopes in Paleoceanography. *Annu. Rev. Earth Planet. Sci.* **35,** 717-746.

Anbar A. D., Duan Y., Lyons T. W., Arnold G. L., Kendall B., Creaser R. A., Kaufman A. J., Gordon G. W., Scott C., Garvin J. and Buick R. (2007) A whiff of oxygen before the great oxidation event? *Science* **317,** 1903-1906.

APHA (2005) *Standard methods for the examination of water and wastewater.* American Public Health Association (APHA) - Water Environmental Federation, Washington, DC, USA.

Arnold G. L., Anbar A. D., Barling J. and Lyons T. W. (2004) Molybdenum isotope evidence for widespread anoxia in mid-Proterozoic oceans. *Science* **304,** 87-90.

Assayag N., Jézéquel D., Ader M., Viollier E., Michard G., Prévot F. and Agrinier P. (2008) Hydrological budget, carbon sources and biogeochemical processes in Lac Pavin (France): constraints from $\delta^{18}O$ of water and $\delta^{13}C$ of dissolved inorganic carbon. *Appl. Geochem.* **23,** 2800-2816.

Ayres D. (1972) Genesis of Iron-bearing Minerals in Banded Iron Formation Mesobands in The Dales Gorge Member, Hamersley. *Economic Geology* **67,** 1214-1233.

Barrett T., Fralick P. and Jarvis I. (1988) Rare-earth-element geochemistry of some Archean iron formations north of Lake Superior, Ontario. *Canadian Journal of Earth Sciences* **25,** 570-580.

Bau M. (1993) Effects of syn-and post-depositional processes on the rare-earth element distribution in Precambrian iron-formations. *European Journal of Mineralogy* **5,** 257-267.

Bau M. (1996) Controls on the fractionation of isovalent trace elements in magmatic and aqueous systems: evidence from Y/Ho, Zr/Hf, and lanthanide tetrad effect. *Contributions to Mineralogy and Petrology* **123,** 323-333.

Bau M. and Alexander B. W. (2006) Preservation of primary REE patterns without Ce anomaly during dolomitization of Mid-Paleoproterozoic limestone and the potential re-establishment of marine anoxia immediately after the "Great Oxidation Event". *South African Journal of Geology* **109,** 81-86.

Bau M. and Alexander B. W. (2009) Distribution of high field strength elements (Y, Zr, REE, Hf, Ta, Th, U) in adjacent magnetite and chert bands and in reference standards FeR-3 and FeR-4 from the Temagami iron-formation, Canada, and the redox level of the Neoarchean ocean. *Precambrian Res.* **174,** 337-346.

Bau M. and Dulski P. (1996) Distribution of yttrium and rare-earth elements in the Penge and Kuruman iron-formations, Transvaal Supergroup, South Africa. *Precambrian Res.* **79,** 37-55.

Bau M. and Möller P. (1993) Rare earth element systematics of the chemically precipitated component in Early Precambrian iron formations and the evolution of the terrestrial atmosphere-hydrosphere-lithosphere system. *Geochim. Cosmochim. Acta* **57,** 2239-2249.

Bau M., Höhndorf A., Dulski P. and Beukes N. J. (1997) Sources of rare-earth elements and iron in Paleoproterozoic iron-formations from the Transvaal Supergroup, South Africa: evidence from neodymium isotopes. *J. Geol.* **105,** 121-129.

Bau M., Romer R. L., Lüders V. and Beukes N. J. (1999) Pb, O, and C isotopes in silicified Mooidraai dolomite (Transvaal Supergroup, South Africa): implications for the composition of Paleoproterozoic seawater and 'dating'the increase of oxygen in the Precambrian atmosphere. *Earth Planet. Sci. Lett.* **174,** 43-57.

Bekker A., Holland H., Wang P., Rumble D., Stein H., Hannah J., Coetzee L. and Beukes N. (2004) Dating the rise of atmospheric oxygen. *Nature* **427,** 117-120.

Bekker A., Planavsky N. J., Rasmussen B., Krapez B., Hofmann A., Slack J., Rouxel O. and Konhauser K. (2014) Iron formations: Their origins and implications for ancient seawater chemistry. In: Holland, H. and Turekian, K. (Eds.), *Treatise on Geochemistry* **9,** Elsevier, 561-628.

Bekker A., Slack J. F., Planavsky N. J., Krapež B., Hofmann A., Konhauser K. O. and Rouxel O. J. (2010) Iron formation: the sedimentary product of a complex interplay among mantle, tectonic, oceanic, and biospheric processes. *Economic Geology* **105,** 467-508.

Bertine K. K. and Turekian K. K. (1973) Molybdenum in marine deposits. *Geochim. Cosmochim. Acta* **37,** 1415-1434.

Beukes N. J. (1983) Palaeoenvironmental setting of iron-formations in the depositional basin of the Transvaal Supergroup, South Africa. *Developments in Precambrian Geology* **6,** 131-198.

Beukes N. J. (1984) Sedimentology of the Kuruman and Griquatown iron-formations, Transvaal supergroup, Griqualand West, South Africa. *Precambrian Res.* **24,** 47-84.

Beukes N. J. and Gutzmer J. (2008) Origin and paleoenvironmental significance of major iron formations at the Archean-Paleoproterozoic boundary. *Reviews in Economic Geology* **15,** 5-47.

Beukes N. J. and Klein C. (1990) Geochemistry and sedimentology of a facies transition—from microbanded to granular iron-formation—in the early Proterozoic Transvaal Supergroup, South Africa. *Precambrian Res.* **47,** 99-139.

Beukes N. J., Klein C., Kaufman A. J. and Hayes J. M. (1990) Carbonate petrography, kerogen distribution, and carbon and oxygen isotope variations in an early Proterozoic transition from limestone to iron-formation deposition, Transvaal Supergroup, South Africa. *Econ. Geol.* **85,** 663-690.

Bjerrum C. J. and Canfield D. E. (2002) Ocean productivity before about 1.9 Gyr ago limited by phosphorus adsorption onto iron oxides. *Nature* **417,** 159-162.

Bolhar R., Kamber B. S., Moorbath S., Fedo C. M. and Whitehouse M. J. (2004) Characterisation of early Archaean chemical sediments by trace element signatures. *Earth Planet. Sci. Lett.* **222,** 43-60.

Braterman P. S., Cairns-Smith A. G. and Sloper R. W. (1983) Photo-oxidation of hydrated Fe2 -significance for banded iron formations. *Nature* **303,** 163-164.

Brocks J. J. (2011) Millimeter-scale concentration gradients of hydrocarbons in Archean shales: Live-oil escape or fingerprint of contamination? *Geochim. Cosmochim. Acta* **75,** 3196-3213.

Brocks J. J., Logan G. A., Buick R. and Summons R. E. (1999) Archean molecular fossils and the early rise of eukaryotes. *Science* **285,** 1033-1036.

Buick R. (1992) The antiquity of oxygenic photosynthesis: evidence from stromatolites in sulphate-deficient Archaean lakes. *Science* **255,** 74-77.

Buick R. (2008) When did oxygenic photosynthesis evolve? *Philos. Trans. R. Soc. Lond. B. Biol. Sci.* **363,** 2731-2743.

Bullen T. D., White A. F., Childs C. W., Vivit D. V. and Schulz M. S. (2001) Demonstration of significant abiotic iron isotope fractionation in nature. *Geology* **29,** 699-702.

Busigny V., Planavsky N. J., Jézéquel D., Crowe S. A., Louvat P., Moureau J., Viollier E. and Lyons T. W. (2014) Iron isotopes in an Archean ocean analogue. *Geochim. Cosmochim. Acta* **133,** 443-462.

Cairns-Smith A. (1978) Precambrian solution photochemistry, inverse segregation, and banded iron formations. *Nature* **276,** 807-808.

Calvert S. and Pedersen T. (1996) Sedimentary geochemistry of manganese; implications for the environment of formation of manganiferous black shales. *Economic Geology* **91,** 36-47.

Canfield D. E. (2005) The early history of atmospheric oxygen: homage to Robert M. Garrels. *Annu. Rev. Earth Planet. Sci.* **33,** 1-36.

Chan C., Emerson D. and Luther G. (2016) The role of microaerophilic Fe-oxidizing micro-organisms in producing banded iron formations. *Geobiology* **14,** 509-528.

Chi Fru E., Rodriguez N. P., Partin C. A., Lalonde S. V., Andersson P., Weiss D. J., El Albani A., Rodushkin I. and Konhauser K. O. (2016) Cu isotopes in marine black shales record the Great Oxidation Event. *Proc. Natl. Acad. Sci. U.S.A.* **113,** 4941-4946.

Chung D., Zhou M., Gao J. and Chen W. T. (2015) In-situ LA–ICP-MS trace elemental analyses of magnetite: The late Palaeoproterozoic Sokoman Iron Formation in the Labrador Trough, Canada. *Ore Geology Reviews* **65,** 917-928.

Cloud P. E.,Jr (1965) Significance of the Gunflint (Precambrian) Microflora: Photosynthetic oxygen may have had important local effects before becoming a major atmospheric gas. *Science* **148,** 27-35.

Cole D. B., Reinhard C. T., Wang X., Gueguen B., Halverson G. P., Gibson T., Hodgskiss M. S., McKenzie N. R., Lyons T. W. and Planavsky N. J. (2016) A shale-hosted Cr isotope record of low atmospheric oxygen during the Proterozoic. *Geology,* **44,** 555-558, .

Condie K. C. (1993) Chemical composition and evolution of the upper continental crust: contrasting results from surface samples and shales. *Chem. Geol.* **104,** 1-37.

Cornell D., Schütte S. and Eglington B. (1996) The Ongeluk basaltic andesite formation in Griqualand West, South Africa: submarine alteration in a 2222 Ma Proterozoic sea. *Precambrian Res.* **79,** 101-123.

Craddock P. R. and Dauphas N. (2011) Iron and carbon isotope evidence for microbial iron respiration throughout the Archean. *Earth Planet. Sci. Lett.* **303,** 121-132.

Croal L. R., Johnson C. M., Beard B. L. and Newman D. K. (2004) Iron isotope fractionation by Fe (II)-oxidizing photoautotrophic bacteria. *Geochim. Cosmochim. Acta* **68,** 1227-1242.

Crowe S. A., Døssing L. N., Beukes N. J., Bau M., Kruger S. J., Frei R. and Canfield D. E. (2013) Atmospheric oxygenation three billion years ago. *Nature* **501,** 535-538.

Crowe S. A., Jones C., Katsev S., Magen C., O'Neill A. H., Sturm A., Canfield D. E., Haffner G. D., Mucci A., Sundby B. and Fowle D. A. (2008) Photoferrotrophs thrive in an Archean Ocean analogue. *Proc. Natl. Acad. Sci. U.S.A.* **105,** 15938-15943.

Czaja A. D., Johnson C. M., Roden E. E., Beard B. L., Voegelin A. R., Nägler T. F., Beukes N. J. and Wille M. (2012) Evidence for free oxygen in the Neoarchean ocean based on coupled iron–molybdenum isotope fractionation. *Geochim. Cosmochim. Acta* **86,** 118-137.

Dauphas N., van Zuilen M., Wadhwa M., Davis A. M., Marty B. and Janney P. E. (2004) Clues from Fe isotope variations on the origin of early Archean BIFs from Greenland. *Science* **306,** 2077-2080.

Delvigne C., Cardinal D., Hofmann A. and André L. (2012) Stratigraphic changes of Ge/Si, REE Y and silicon isotopes as insights into the deposition of a Mesoarchaean banded iron formation. *Earth Planet. Sci. Lett.* **355,** 109-118.

Derry L. A. and Jacobsen S. B. (1990) The chemical evolution of Precambrian seawater: evidence from REEs in banded iron formations. *Geochim. Cosmochim. Acta* **54,** 2965-2977.

Duan Y., Anbar A. D., Arnold G. L., Lyons T. W., Gordon G. W. and Kendall B. (2010) Molybdenum isotope evidence for mild environmental oxygenation before the Great Oxidation Event. *Geochim. Cosmochim. Acta* **74,** 6655-6668.

Eigenbrode J. L. and Freeman K. H. (2006) Late Archean rise of aerobic microbial ecosystems. *Proc. Natl. Acad. Sci. U. S. A.* **103,** 15759-15764.

Elderfield H., Hawkesworth C., Greaves M. and Calvert S. (1981) Rare earth element geochemistry of oceanic ferromanganese nodules and associated sediments. *Geochim. Cosmochim. Acta* **45,** 513-528.

Eriksson P., Altermann W. and Hartzer F. (2006) The Transvaal Supergroup and its precursors. In Johnson, M. R. et al. (Eds.) *The Geology of South Africa: Geological Society of South Africa,* Johannesburg/Council for Geoscience, Pretoria, 237-260.

Ewers W. and Morris R. (1981) Studies of the Dales Gorge member of the Brockman iron formation, Western Australia. *Economic Geology* **76,** 1929-1953.

Farquhar J. and Wing B. A. (2003) Multiple sulfur isotopes and the evolution of the atmosphere. *Earth Planet. Sci. Lett.* **213,** 1-13.

Farquhar J., Zerkle A. L. and Bekker A. (2011) Geological constraints on the origin of oxygenic photosynthesis. *Photosynthesis Res.* **107,** 11-36.

Fischer W. W. and Knoll A. H. (2009) An iron shuttle for deepwater silica in Late Archean and early Paleoproterozoic iron formation. *Geological Society of America Bulletin* **121,** 222-235.

Fischer W. W., Hemp J. and Johnson J. E. (2015) Manganese and the Evolution of Photosynthesis. *Origins of Life and Evolution of Biospheres* **45,** 351-357.

Floran R. and Papike J. (1975) Petrology of the low-grade rocks of the Gunflint Iron-Formation, Ontario-Minnesota. *Geological Society of America Bulletin* **86,** 1169-1190.

Frei R., Crowe S. A., Bau M., Polat A., Fowle D. A. and Dossing L. N. (2016) Oxidative elemental cycling under the low O2 Eoarchean atmosphere. *Sci. Rep.* **6,** 21058.

Frei R., Dahl P. S., Duke E. F., Frei K. M., Hansen T. R., Frandsson M. M. and Jensen L. A. (2008) Trace element and isotopic characterization of Neoarchean and Paleoproterozoic iron formations in the Black Hills (South Dakota, USA): assessment of chemical change during 2.9–1.9 Ga deposition bracketing the 2.4–2.2 Ga first rise of atmospheric oxygen. *Precambrian Res.* **162,** 441-474.

Frei R., Gaucher C., Døssing L. N. and Sial A. N. (2011) Chromium isotopes in carbonates—a tracer for climate change and for reconstructing the redox state of ancient seawater. *Earth Planet. Sci. Lett.* **312,** 114-125.

Frei R., Gaucher C., Poulton S. W. and Canfield D. E. (2009) Fluctuations in Precambrian atmospheric oxygenation recorded by chromium isotopes. *Nature* **461,** 250-253.

French K. L., Hallmann C., Hope J. M., Schoon P. L., Zumberge J. A., Hoshino Y., Peters C. A., George S. C., Love G. D., Brocks J. J., Buick R. and Summons R. E. (2015) Reappraisal of hydrocarbon biomarkers in Archean rocks. *Proc. Natl. Acad. Sci. U. S. A.* **112,** 5915-5920.

Frierdich A. J., Beard B. L., Scherer M. M. and Johnson C. M. (2014) Determination of the Fe (II) aq–magnetite equilibrium iron isotope fractionation factor using the three-isotope method and a multi-direction approach to equilibrium. *Earth Planet. Sci. Lett.* **391,** 77-86.

Frost C., Von Blanckenburg F., Schoenberg R., Frost B. and Swapp S. (2007) Preservation of Fe isotope heterogeneities during diagenesis and metamorphism of banded iron formation. *Contributions to Mineralogy and Petrology* **153,** 211-235.

Fryer L. (2015) Controls on the distribution of Manganese in Banded Iron-Formations (BIF) of the Palaeoproterozoic Transvaal Supergroup, South Africa, *MSc-thesis, Rhodes University,* 155p.

Garrels R., Perry E. and Mackenzie F. (1973) Genesis of Precambrian iron-formations and the development of atmospheric oxygen. *Economic Geology* **68,** 1173-1179.

German C. and Von Damm K. (2006) Hydrothermal processes. *Treatise on geochemistry* **6,** 181-222.

Gole M. (1980) Mineralogy and petrology of very-low-metamorphic grade Archaean banded iron-formations, Weld Range, Western Australia. *Am. Mineral.* **65,** 8-25.

Gross G. A. (1983) Tectonic systems and the deposition of iron-formation. *Precambrian Res.* **20,** 171-187.

Guelke M., von Blanckenburg F., Schoenberg R., Staubwasser M. and Stuetzel H. (2010) Determining the stable Fe isotope signature of plant-available iron in soils. *Chem. Geol.* **277,** 269-280.

Gumsley A. P., Chamberlain K. R., Bleeker W., Soderlund U., de Kock M. O., Larsson E. R. and Bekker A. (2017) Timing and tempo of the Great Oxidation Event. *Proc. Natl. Acad. Sci. U. S. A.* **114,** 1811-1816.

Haley B. A., Klinkhammer G. P. and McManus J. (2004) Rare earth elements in pore waters of marine sediments. *Geochim. Cosmochim. Acta* **68,** 1265-1279.

Halverson G. P., Poitrasson F., Hoffman P. F., Nédélec A., Montel J. and Kirby J. (2011) Fe isotope and trace element geochemistry of the Neoproterozoic syn-glacial Rapitan iron formation. *Earth Planet. Sci. Lett.* **309,** 100-112.

Handler R. M., Beard B. L., Johnson C. M. and Scherer M. M. (2009) Atom exchange between aqueous Fe (II) and goethite: an Fe isotope tracer study. *Environ. Sci. Technol.* **43,** 1102-1107.

Haugaard R., Pecoits E., Lalonde S. V., Rouxel O. and Konhauser K. (2016) The Joffre banded iron formation, Hamersley Group, Western Australia: Assessing the palaeoenvironment through detailed petrology and chemostratigraphy. *Precambrian Res.* **273,** 12-37.

Heimann A., Johnson C. M., Beard B. L., Valley J. W., Roden E. E., Spicuzza M. J. and Beukes N. J. (2010) Fe, C, and O isotope compositions of banded iron formation carbonates demonstrate a major role for dissimilatory iron reduction in~ 2.5 Ga marine environments. *Earth Planet. Sci. Lett.* **294,** 8-18.

Henkel S., Kasten S., Poulton S. W. and Staubwasser M. (2016) Determination of the stable iron isotopic composition of sequentially leached iron phases in marine sediments. *Chem. Geol.* **421,** 93-102.

Hoffman P. F., Kaufman A. J., Halverson G. P. and Schrag D. P. (1998) A neoproterozoic snowball earth. *Science* **281,** 1342-1346.

Holland H. D. (2002) Volcanic gases, black smokers, and the Great Oxidation Event. *Geochim. Cosmochim. Acta* **66,** 3811-3826.

Horstmann U. E. and Hälbich I. W. (1995) Chemical composition of banded iron-formations of the Griqualand West Sequence, Northern Cape Province, South Africa, in comparison with other Precambrian iron formations. *Precambrian Res.* **72,** 109-145.

Isley A. E. (1995) Hydrothermal plumes and the delivery of iron to banded iron formation. *J. Geol.* **103,** 169-185.

Isley A. E. and Abbott D. H. (1999) Plume-related mafic volcanism and the deposition of banded iron formation. *Journal of Geophysical Research: Solid Earth* **104,** 15461-15477.

James H. L. (1954) Sedimentary facies of iron-formation. *Economic Geology* **49,** 235-293.

Jarvis K. E., Gray A. L. and Houk R. S. (1992) *Handbook of inductively coupled plasma mass spectrometry.* Blackie; Chapman and Hall, 256p.

Jarvis K. E., Gray A. L. and McCurdy E. (1989) Avoidance of spectral interference on europium in inductively coupled plasma mass spectrometry by sensitive measurement of the doubly charged ion. *J. Anal. At. Spectrom.* **4,** 743-747.

Jochum K. P., Nohl U., Herwig K., Lammel E., Stoll B. and Hofmann A. W. (2005) GeoReM: a new geochemical database for reference materials and isotopic standards. *Geostandards and Geoanalytical Research* **29,** 333-338.

Jochum K. P., Scholz D., Stoll B., Weis U., Wilson S. A., Yang Q., Schwalb A., Börner N., Jacob D. E. and Andreae M. O. (2012) Accurate trace element analysis of speleothems and biogenic calcium carbonates by LA-ICP-MS. *Chem. Geol.* **318,** 31-44.

Johnson C. M., Beard B. L. and Roden E. E. (2008b) The iron isotope fingerprints of redox and biogeochemical cycling in modern and ancient Earth. *Annu. Rev. Earth Planet. Sci.* **36,** 457-493.

Johnson C. M., Beard B. L., Beukes N. J., Klein C. and O'Leary J. M. (2003) Ancient geochemical cycling in the Earth as inferred from Fe isotope studies of banded iron formations from the Transvaal Craton. *Contributions to Mineralogy and Petrology* **144,** 523-547.

Johnson C. M., Beard B. L., Klein C., Beukes N. J. and Roden E. E. (2008a) Iron isotopes constrain biologic and abiologic processes in banded iron formation genesis. *Geochim. Cosmochim. Acta* **72,** 151-169.

Johnson C. M., Ludois J. M., Beard B. L., Beukes N. J. and Heimann A. (2013) Iron formation carbonates: Paleoceanographic proxy or recorder of microbial diagenesis? *Geology* **41,** 1147-1150.

Johnson C. M., Roden E. E., Welch S. A. and Beard B. L. (2005) Experimental constraints on Fe isotope fractionation during magnetite and Fe carbonate formation coupled to dissimilatory hydrous ferric oxide reduction. *Geochim. Cosmochim. Acta* **69,** 963-993.

Johnson J. E., Gerpheide A., Lamb M. P. and Fischer W. W. (2014) O2 constraints from Paleoproterozoic detrital pyrite and uraninite. *Geological Society of America Bulletin* **126,** 813-830.

Johnson J. E., Webb S. M., Ma C. and Fischer W. W. (2016) Manganese mineralogy and diagenesis in the sedimentary rock record. *Geochim. Cosmochim. Acta* **173,** 210-231.

Johnson J. E., Webb S. M., Thomas K., Ono S., Kirschvink J. L. and Fischer W. W. (2013) Manganese-oxidizing photosynthesis before the rise of cyanobacteria. *Proc. Natl. Acad. Sci. U. S. A.* **110,** 11238-11243.

Kamber B. S. and Webb G. E. (2001) The geochemistry of late Archaean microbial carbonate: implications for ocean chemistry and continental erosion history. *Geochim. Cosmochim. Acta* **65,** 2509-2525.

Kampmann T. C., Gumsley A. P., de Kock M. O. and Söderlund U. (2015) U–Pb geochronology and paleomagnetism of the Westerberg Sill Suite, Kaapvaal Craton–Support for a coherent Kaapvaal–Pilbara Block (Vaalbara) into the Paleoproterozoic? *Precambrian Res.* **269,** 58-72.

Kappler A., Pasquero C., Konhauser K. O. and Newman D. K. (2005) Deposition of banded iron formations by anoxygenic phototrophic Fe (II)-oxidizing bacteria. *Geology* **33,** 865-868.

Kaufman A. J., Hayes J. and Klein C. (1990) Primary and diagenetic controls of isotopic compositions of iron-formation carbonates. *Geochim. Cosmochim. Acta* **54,** 3461-3473.

Kendall B., Reinhard C. T., Lyons T. W., Kaufman A. J., Poulton S. W. and Anbar A. D. (2010) Pervasive oxygenation along late Archaean ocean margins. *Nature Geoscience* **3,** 647-652.

Klein C. (1974) Greenalite, stilpnomelane, minnesotaite, crocidolite and carbonates in a very low-grade metamorphic Precambrian iron formation. *The Canadian Mineralogist* **12,** 475-498.

Klein C. (2005) Some Precambrian banded iron-formations (BIFs) from around the world: Their age, geologic setting, mineralogy, metamorphism, geochemistry, and origins. *Am. Mineral.* **90,** 1473-1499.

Klein C. and Beukes N. J. (1989) Geochemistry and sedimentology of a facies transition from limestone to iron-formation deposition in the early Proterozoic Transvaal Supergroup, South Africa. *Economic Geology* **84,** 1733-1774.

Klein C. and Beukes N. J. (1992) Time distribution, stratigraphy, and sedimentologic setting, and geochemistry of Precambrian iron-formations. In: J.W. Schopf, C. Klein (Eds.), *The Proterozoic Biosphere: A Multidisciplinary Study,* Cambridge Univ. Press, New York, 139–146.

Klein C. and Gole M. J. (1981) Mineralogy and petrology of parts of the Marra Mamba iron formation, Hamersley Basin, Western Australia. *Am. Mineral.* **66,** 507-525.

Konhauser K. O., Amskold L., Lalonde S. V., Posth N. R., Kappler A. and Anbar A. (2007) Decoupling photochemical Fe (II) oxidation from shallow-water BIF deposition. *Earth Planet. Sci. Lett.* **258,** 87-100.

Konhauser K. O., Hamade T., Raiswell R., Morris R. C., Ferris F. G., Southam G. and Canfield D. E. (2002) Could bacteria have formed the Precambrian banded iron formations? *Geology* **30,** 1079-1082.

Konhauser K. O., Lalonde S. V., Planavsky N. J., Pecoits E., Lyons T. W., Mojzsis S. J., Rouxel O. J., Barley M. E., Rosìere C. and Fralick P. W. (2011) Aerobic bacterial pyrite oxidation and acid rock drainage during the Great Oxidation Event. *Nature* **478,** 369-373.

Konhauser K. O., Pecoits E., Lalonde S. V., Papineau D., Nisbet E. G., Barley M. E., Arndt N. T., Zahnle K. and Kamber B. S. (2009) Oceanic nickel depletion and a methanogen famine before the Great Oxidation Event. *Nature* **458,** 750-753.

Kopp R. E., Kirschvink J. L., Hilburn I. A. and Nash C. Z. (2005) The Paleoproterozoic snowball Earth: a climate disaster triggered by the evolution of oxygenic photosynthesis. *Proc. Natl. Acad. Sci. U. S. A.* **102,** 11131-11136.

Krapež B., Barley M. E. and Pickard A. L. (2003) Hydrothermal and resedimented origins of the precursor sediments to banded iron formation: sedimentological evidence from the Early Palaeoproterozoic Brockman Supersequence of Western Australia. *Sedimentology* **50,** 979-1011.

Kump L. R. and Barley M. E. (2007) Increased subaerial volcanism and the rise of atmospheric oxygen 2.5 billion years ago. *Nature* **448,** 1033-1036.

Kurzweil F., Wille M., Gantert N., Beukes N. J. and Schoenberg R. (2016) Manganese oxide shuttling in pre-GOE oceans–evidence from molybdenum and iron isotopes. *Earth Planet. Sci. Lett.* **452,** 69-78.

Kurzweil F., Wille M., Schoenberg R., Taubald H. and Van Kranendonk M. J. (2015) Continuously increasing δ 98 Mo values in Neoarchean black shales and iron formations from the Hamersley Basin. *Geochim. Cosmochim. Acta* **164,** 523-542.

Land M., Öhlander B., Ingri J. and Thunberg J. (1999) Solid speciation and fractionation of rare earth elements in a spodosol profile from northern Sweden as revealed by sequential extraction. *Chem. Geol.* **160,** 121-138.

Lantink M. L. (2016) Fe isotopes of a ca 2.4 Ga hematite-rich IF confirm oxygenation of the Transvaal basin in relation to the GOE, *MSc-thesis, Utrecht University*, 62p.

Lascelles D. F. (2007) Black smokers and density currents: a uniformitarian model for the genesis of banded iron-formations. *Ore Geology Reviews* **32,** 381-411.

Lepland A., Arrhenius G. and Cornell D. (2002) Apatite in early Archean Isua supracrustal rocks, southern West Greenland: its origin, association with graphite and potential as a biomarker. *Precambrian Res.* **118,** 221-241.

Li W., Beard B. L. and Johnson C. M. (2015) Biologically recycled continental iron is a major component in banded iron formations. *Proc. Natl. Acad. Sci. U. S. A.* **112,** 8193-8198.

Li W., Huberty J. M., Beard B. L., Kita N. T., Valley J. W. and Johnson C. M. (2013) Contrasting behavior of oxygen and iron isotopes in banded iron formations revealed by in situ isotopic analysis. *Earth Planet. Sci. Lett.* **384,** 132-143.

Li Y., Konhauser K. O., Cole D. R. and Phelps T. J. (2011) Mineral ecophysiological data provide growing evidence for microbial activity in banded-iron formations. *Geology* **39,** 707-710.

Liger E., Charlet L. and Van Cappellen P. (1999) Surface catalysis of uranium (VI) reduction by iron (II). *Geochim. Cosmochim. Acta* **63,** 2939-2955.

Liu X., Kah L., Knoll A., Cui H., Kaufman A., Shahar A. and Hazen R. (2016) Tracing Earth's O2 evolution using Zn/Fe ratios in marine carbonates. *Geochemical Perspectives Letters* **2,** 24-34.

Lovley D. R. (1991) Dissimilatory Fe(III) and Mn(IV) reduction. *Microbiol. Rev.* **55,** 259-287.

Lovley D. R., Phillips E. J. and Lonergan D. J. (1991) Enzymic versus nonenzymic mechanisms for iron (III) reduction in aquatic sediments. *Environ. Sci. Technol.* **25,** 1062-1067.

Lyons T. W. and Severmann S. (2006) A critical look at iron paleoredox proxies: new insights from modern euxinic marine basins. *Geochim. Cosmochim. Acta* **70**, 5698-5722.

Lyons T. W., Reinhard C. T. and Planavsky N. J. (2014) The rise of oxygen in Earth/'s early ocean and atmosphere. *Nature* **506,** 307-315.

Madison A. S., Tebo B. M., Mucci A., Sundby B. and Luther G. W.,3rd (2013) Abundant porewater Mn(III) is a major component of the sedimentary redox system. *Science* **341,** 875-878.

März C., Poulton S. W., Beckmann B., Küster K., Wagner T. and Kasten S. (2008) Redox sensitivity of P cycling during marine black shale formation: dynamics of sulfidic and anoxic, non-sulfidic bottom waters. *Geochim. Cosmochim. Acta* **72,** 3703-3717.

März C., Poulton S. W., Brumsack H. and Wagner T. (2012) Climate-controlled variability of iron deposition in the Central Arctic Ocean (southern Mendeleev Ridge) over the last 130,000 years. *Chem. Geol.* **330,** 116-126.

McLennan S. M. (1989) Rare earth elements in sedimentary rocks; influence of provenance and sedimentary processes. *Reviews in Mineralogy and Geochemistry* **21,** 169-200.

Mendes M., Lobato L. M., Kunzmann M., Halverson G. P. and Rosière C. A. (2016) Iron isotope and REE Y composition of the Cauê banded iron formation and related iron ores of the Quadrilátero Ferrífero, Brazil. *Miner. Deposita* (2016) 22p.

Mhlanga, X. R. (in prep.) Unravelling the diagenetic and primary depositional history of the Hotazel Fe-Mn Formation, through the application of mineral chemistry, stable isotopes and speciation geochemistry, *PhD-thesis, Rhodes University.*

Mikutta C., Wiederhold J. G., Cirpka O. A., Hofstetter T. B., Bourdon B. and Von Gunten U. (2009) Iron isotope fractionation and atom exchange during sorption of ferrous iron to mineral surfaces. *Geochim. Cosmochim. Acta* **73,** 1795-1812.

Miyano T. and Beukes N. (1984) Phase relations of stilpnomelane, ferri-annite, and riebeckite in very low-grade metamorphosed iron-formations. *South African Journal of Geology* **87,** 111-124.

Mloszewska A. M., Pecoits E., Cates N. L., Mojzsis S. J., O'Neil J., Robbins L. J. and Konhauser K. O. (2012) The composition of Earth's oldest iron formations: the Nuvvuagittuq Supracrustal Belt (Québec, Canada). *Earth Planet. Sci. Lett.* **317,** 331-342.

Moffett J. W. (1994) The relationship between cerium and manganese oxidation in the marine environment. *Limnol. Oceanogr.* **39,** 1309-1318.

Molendijk S. M. (2016) Nature and implications of igneous rock in the Kuruman Formation from Griqualand West Basin, South Africa, *BSc-thesis, Utrecht University,* 36p.

Moore J. M., Polteau S., Armstrong R., Corfu F. and Tsikos H. (2012) The age and correlation of the Postmasburg Group, southern Africa: Constraints from detrital zircon grains. *J. Afr. Earth Sci.* **64,** 9-19.

Moore J. M., Tsikos H. and Polteau S. (2001) Deconstructing the Transvaal Supergroup, south Africa: implications for Palaeoproterozoic palaeoclimate models. *J. Afr. Earth Sci.* **33,** 437-444.

Nadoll P., Angerer T., Mauk J. L., French D. and Walshe J. (2014) The chemistry of hydrothermal magnetite: a review. *Ore Geology Reviews* **61,** 1-32.

Nakada R., Takahashi Y. and Tanimizu M. (2016) Cerium stable isotope ratios in ferromanganese deposits and their potential as a paleo-redox proxy. *Geochim. Cosmochim. Acta* **181,** 89-100.

Nel B. P. (2013) Petrography and geochemistry of iron formations of the Paleoproterozoic Koegas Subgroup, Transvaal Supergroup, Griqualand West, South Africa, *MSc-thesis, University of Johannesburg,* 134p.

Nie N. X., Dauphas N. and Greenwood R. C. (2017) Iron and oxygen isotope fractionation during iron UV photo-oxidation: Implications for early Earth and Mars. *Earth Planet. Sci. Lett.* **458,** 179-191.

Norrish K. and Hutton J. T. (1969) An accurate X-ray spectrographic method for the analysis of a wide range of geological samples. *Geochim. Cosmochim. Acta* **33,** 431-453.

Ohmoto H., Watanabe Y., Ikemi H., Poulson S. R. and Taylor B. E. (2006b) Sulphur isotope evidence for an oxic Archaean atmosphere. *Nature* **442,** 908-911.

Ohmoto H., Watanabe Y., Lasaga A. C., Naraoka H., Johnson I., Brainard J. and Chorney A. (2014) Oxygen, iron, and sulfur geochemical cycles on early Earth: Paradigms and contradictions. *Geological Society of America Special Papers* **504,** 55-95.

Ohmoto H., Watanabe Y., Yamaguchi K. E., Naraoka H., Haruna M., Kakegawa T., Hayashi K. and Kato Y. (2006a) Chemical and biological evolution of early Earth: constraints from banded iron formations. *Geological Society of America Memoirs* **198,** 291-331.

Olson S. L., Kump L. R. and Kasting J. F. (2013) Quantifying the areal extent and dissolved oxygen concentrations of Archean oxygen oases. *Chem. Geol.* **362,** 35-43.

Palmer M. and Elderfield H. (1986) Rare earth elements and neodymium isotopes in ferromanganese oxide coatings of Cenozoic foraminifera from the Atlantic Ocean. *Geochim. Cosmochim. Acta* **50,** 409-417.

Panias D., Taxiarchou M., Paspaliaris I. and Kontopoulos A. (1996) Mechanisms of dissolution of iron oxides in aqueous oxalic acid solutions. *Hydrometallurgy* **42,** 257-265.

Parkhurst D. L. and Appelo C. A. J. (1999) User's guide to PHREEQC (Version 2): A computer program for speciation, batch-reaction, one-dimensional transport, and inverse geochemical calculations. *US Geological Survey, Water-Resources Investigations Report* **99-4259,** 312p,

Partin C., Lalonde S. V., Planavsky N. J., Bekker A., Rouxel O., Lyons T. and Konhauser K. (2013) Uranium in iron formations and the rise of atmospheric oxygen. *Chem. Geol.* **362,** 82-90.

Pavlov A. A., Kasting J. F., Brown L. L., Rages K. A. and Freedman R. (2000) Greenhouse warming by CH4 in the atmosphere of early Earth. *Journal of Geophysical Research* **105,** 981-911.

Pecoits E., Gingras M., Barley M., Kappler A., Posth N. and Konhauser K. (2009) Petrography and geochemistry of the Dales Gorge banded iron formation: Paragenetic sequence, source and implications for palaeo-ocean chemistry. *Precambrian Res.* **172,** 163-187.

Pedersen H. D., Postma D., Jakobsen R. and Larsen O. (2005) Fast transformation of iron oxyhydroxides by the catalytic action of aqueous Fe (II). *Geochim. Cosmochim. Acta* **69,** 3967-3977.

Percak-Dennett E. M., Beard B. L., Xu H., Konishi H., Johnson C. M. and Roden E. E. (2011) Iron isotope fractionation during microbial dissimilatory iron oxide reduction in simulated Archaean seawater. *Geobiology* **9,** 205-220.

Percak-Dennett E. M., Loizeau J., Beard B. L., Johnson C. M. and Roden E. E. (2013) Iron isotope geochemistry of biogenic magnetite-bearing sediments from the Bay of Vidy, Lake Geneva. *Chem. Geol.* **360,** 32-40.

Pickard A. (2003) SHRIMP U–Pb zircon ages for the Palaeoproterozoic Kuruman Iron Formation, Northern Cape Province, South Africa: evidence for simultaneous BIF deposition on Kaapvaal and Pilbara Cratons. *Precambrian Res.* **125,** 275-315.

Piepgras D. J. and Jacobsen S. B. (1992) The behavior of rare earth elements in seawater: Precise determination of variations in the North Pacific water column. *Geochim. Cosmochim. Acta* **56,** 1851-1862.

Planavsky N. J., Asael D., Hofman A., Reinhard C. T., Lalonde S. V., Knudsen A., Wang X., Ossa F. O., Pecoits E. and Smith A. J. (2014) Evidence for oxygenic photosynthesis half a billion years before the Great Oxidation Event. *Nature Geoscience* **7,** 283-286.

Planavsky N. J., Bekker A., Rouxel O. J., Kamber B., Hofmann A., Knudsen A. and Lyons T. W. (2010) Rare earth element and yttrium compositions of Archean and Paleoproterozoic Fe formations revisited: new perspectives on the significance and mechanisms of deposition. *Geochim. Cosmochim. Acta* **74,** 6387-6405.

Planavsky N. J., Rouxel O. J., Bekker A., Hofmann A., Little C. T. and Lyons T. W. (2012) Iron isotope composition of some Archean and Proterozoic iron formations. *Geochim. Cosmochim. Acta* **80,** 158-169.

Polteau S., Moore J. M. and Tsikos H. (2006) The geology and geochemistry of the Palaeoproterozoic Makganyene diamictite. *Precambrian Res.* **148,** 257-274.

Polyakov V. B. and Mineev S. D. (2000) The use of Mössbauer spectroscopy in stable isotope geochemistry. *Geochim. Cosmochim. Acta* **64,** 849-865.

Posth N. R., Hegler F., Konhauser K. O. and Kappler A. (2008) Alternating Si and Fe deposition caused by temperature fluctuations in Precambrian oceans. *Nature Geoscience* **1,** 703-708.

Posth N. R., Konhauser K. O. and Kappler A. (2013) Microbiological processes in banded iron formation deposition. *Sedimentology* **60,** 1733-1754.

Postma D. (1985) Concentration of Mn and separation from Fe in sediments—I. Kinetics and stoichiometry of the reaction between birnessite and dissolved Fe (II) at 10 C. *Geochim. Cosmochim. Acta* **49,** 1023-1033.

Postma D. and Appelo C. (2000) Reduction of Mn-oxides by ferrous iron in a flow system: Column experiment and reactive transport modeling. *Geochim. Cosmochim. Acta* **64,** 1237-1247.

Poulton S. W. and Canfield D. E. (2005) Development of a sequential extraction procedure for iron: implications for iron partitioning in continentally derived particulates. *Chem. Geol.* **214,** 209-221.

Poulton S. W., Fralick P. W. and Canfield D. E. (2004) The transition to a sulphidic ocean ~1.84 billion years ago. Nature **431,** 173-177.

Quinn K. A., Byrne R. H. and Schijf J. (2006) Sorption of yttrium and rare earth elements by amorphous ferric hydroxide: influence of solution complexation with carbonate. *Geochim. Cosmochim. Acta* **70,** 4151-4165.

Rafuza S. (2015) Carbonate Petrography and Geochemistry of BIF of the Transvaal Supergroup: evaluating the potential of Iron Carbonates as proxies for Palaeoproterozoic Ocean Chemistry. *MSc thesis, Rhodes University,* 105p

Raiswell R., Canfield D. and Berner R. (1994) A comparison of iron extraction methods for the determination of degree of pyritisation and the recognition of iron-limited pyrite formation. *Chem. Geol.* **111,** 101-110.

Raiswell R., Reinhard C. T., Derkowski A., Owens J., Bottrell S. H., Anbar A. D. and Lyons T. W. (2011) Formation of syngenetic and early diagenetic iron minerals in the late Archean Mt. McRae Shale, Hamersley Basin, Australia: new insights on the patterns, controls and paleoenvironmental implications of authigenic mineral formation. *Geochim. Cosmochim. Acta* **75,** 1072-1087.

Rasmussen B., Fletcher I. R., Brocks J. J. and Kilburn M. R. (2008) Reassessing the first appearance of eukaryotes and cyanobacteria. *Nature* **455,** 1101-1104.

Rasmussen B., Krapež B. and Muhling J. R. (2015a) Seafloor silicification and hardground development during deposition of 2.5 Ga banded iron formations. *Geology* **43,** 235-238.

Rasmussen B., Krapež B., Muhling J. R. and Suvorova A. (2015b) Precipitation of iron silicate nanoparticles in early Precambrian oceans marks Earth's first iron age. *Geology* **43,** 303-306.

Rasmussen B., Meier D. B., Krapež B. and Muhling J. R. (2013) Iron silicate microgranules as precursor sediments to 2.5-billion-year-old banded iron formations. *Geology* **41,** 435-438.

Reinhard C. T., Planavsky N. J., Wang X., Fischer W. W., Johnson T. M. and Lyons T. W. (2014) The isotopic composition of authigenic chromium in anoxic marine sediments: A case study from the Cariaco Basin. *Earth Planet. Sci. Lett.* **407,** 9-18.

Reinhard C. T., Raiswell R., Scott C., Anbar A. D. and Lyons T. W. (2009) A late Archean sulfidic sea stimulated by early oxidative weathering of the continents. *Science* **326,** 713-716.

Ring E. J. (1993) The Preparation and Certification of Fourteen South African Silicate Rocks for Use as Referecen Materials*. *Geostandards Newsletter* **17,** 137-158.

Rouxel O. J., Bekker A. and Edwards K. J. (2005) Iron isotope constraints on the Archean and Paleoproterozoic ocean redox state. *Science* **307,** 1088-1091.

Satkoski A. M., Beukes N. J., Li W., Beard B. L. and Johnson C. M. (2015) A redox-stratified ocean 3.2 billion years ago. *Earth Planet. Sci. Lett.* **430,** 43-53.

Schauble E., Rossman G. and Taylor H. (2001) Theoretical estimates of equilibrium Fe-isotope fractionations from vibrational spectroscopy. *Geochim. Cosmochim. Acta* **65,** 2487-2497.

Schilling K., Johnson T. M. and Mason P. R. D. (2014) A sequential extraction technique for mass-balanced stable selenium isotope analysis of soil samples. *Chem. Geol.* **381,** 125-130.

Schoenberg R. and von Blanckenburg F. (2005) An assessment of the accuracy of stable Fe isotope ratio measurements on samples with organic and inorganic matrices by high-resolution multicollector ICP-MS. *International Journal of Mass Spectrometry* **242,** 257-272.

Severmann S., Lyons T. W., Anbar A., McManus J. and Gordon G. (2008) Modern iron isotope perspective on the benthic iron shuttle and the redox evolution of ancient oceans. *Geology* **36,** 487-490.

Sherrell R. M., Field M. P. and Ravizza G. (1999) Uptake and fractionation of rare earth elements on hydrothermal plume particles at 9 45′ N, East Pacific Rise. *Geochim. Cosmochim. Acta* **63,** 1709-1722.

Siebert C., Nägler T. F., von Blanckenburg F. and Kramers J. D. (2003) Molybdenum isotope records as a potential new proxy for paleoceanography. *Earth Planet. Sci. Lett.* **211,** 159-171.

Siebert C., Pett-Ridge J., Opfergelt S., Guicharnaud R., Halliday A. and Burton K. (2015) Molybdenum isotope fractionation in soils: Influence of redox conditions, organic matter, and atmospheric inputs. *Geochim. Cosmochim. Acta* **162,** 1-24.

Siever R. (1992) The silica cycle in the Precambrian. *Geochim. Cosmochim. Acta* **56,** 3265-3272.

Simonson B. M. (2003) Origin and evolution of large Precambrian iron formations. *Special Papers-Geological society of America* **370,** 231-244.

Smith A. J. and Beukes N. J. (2016) Palaeoproterozoic Banded Iron formationhosted High-Grade Hematite Iron Ore Deposits of the Transvaal Supergroup, South Africa. *Episodes* **39,** 269-284.

Staubwasser M., Von Blanckenburg F. and Schoenberg R. (2006) Iron isotopes in the early marine diagenetic iron cycle. *Geology* **34,** 629-632.

Steinhoefel G., Horn I. and von Blanckenburg F. (2009) Micro-scale tracing of Fe and Si isotope signatures in banded iron formation using femtosecond laser ablation. *Geochim. Cosmochim. Acta* **73,** 5343-5360.

Steinhoefel G., von Blanckenburg F., Horn I., Konhauser K. O., Beukes N. J. and Gutzmer J. (2010) Deciphering formation processes of banded iron formations from the Transvaal and the Hamersley successions by combined Si and Fe isotope analysis using UV femtosecond laser ablation. *Geochim. Cosmochim. Acta* **74,** 2677-2696.

Sumner D. Y. (1997) Carbonate precipitation and oxygen stratification in late Archean seawater as deduced from facies and stratigraphy of the Gamohaan and Frisco formations, Transvaal Supergroup, South Africa. *Am. J. Sci.* **297,** 455-487.

Suter D., Siffert C., Sulzberger B. and Stumm W. (1988) Catalytic dissoluion of iron (III)(hydr) oxides by oxalic acid in the presence of Fe (II). *Naturwissenschaften* **75,** 571-573.

Swanner E. D., Planavsky N. J., Lalonde S. V., Robbins L. J., Bekker A., Rouxel O. J., Saito M. A., Kappler A., Mojzsis S. J. and Konhauser K. O. (2014) Cobalt and marine redox evolution. *Earth Planet. Sci. Lett.* **390,** 253-263.

Taxiarchou M., Panias D., Douni I., Paspaliaris I. and Kontopoulos A. (1997) Dissolution of hematite in acidic oxalate solutions. *Hydrometallurgy* **44,** 287-299.

Taxiarchou M., Panias D., Douni I., Paspaliaris I. and Kontopoulos A. (1998) Dissolution of magnetite in acidic oxalate solutions. *Transactions of the Institution of Mining and Metallurgy-Section C-Mineral Processing* **107,** 37-41.

Tessier A., Campbell P. G. and Bisson M. (1979) Sequential extraction procedure for the speciation of particulate trace metals. *Anal. Chem.* **51,** 844-851.

Teutsch N., Schmid M., Müller B., Halliday A. N., Bürgmann H. and Wehrli B. (2009) Large iron isotope fractionation at the oxic–anoxic boundary in Lake Nyos. *Earth Planet. Sci. Lett.* **285,** 52-60.

Thoby M. A., Lalonde S. V., Sumner D. Y. and Konhauser K. (2016) The molybdenum isotope composition of modern and ancient stromatolites. *Abstract 5252, 35th International Geological Congress, Cape Town, South Africa.*

Tosca N. J., Guggenheim S. and Pufahl P. K. (2016) An authigenic origin for Precambrian greenalite: Implications for iron formation and the chemistry of ancient seawater. G*eological Society of America Bulletin* **128,** 511-530.

Trendall A. F. (1983) Introduction. In Trendall, A.F. and Morris R. (Eds.) *Iron-formation: Facts and problems,* Elsevier Science, Inc., 558 p.

Trendall A. F. and Blockey J. (1970) *The iron formations of the Precambrian Hamersley Group, Western Australia with special reference to the associated crocidolite.* Geological Survey of Western Australia, 366p.

Trendall A. F., Compston W., Nelson D., De Laeter J. and Bennett V. (2004) SHRIMP zircon ages constraining the depositional chronology of the Hamersley Group, Western Australia. *Aust. J. Earth Sci.* **51,** 621-644.

Trendall A. F., Nelson D., Thorne A., Compston W., Williams I. and Armstrong R. (1990) Precise zircon U-Pb chronological comparison of the volcano-sedimentary sequences of the Kaapvaal and Pilbara cratons between about 3.1 and 2.4 Ga. In: Glover, J.E., Ho, S.E. (Eds.), *Proceedings of the Third International Archaean Symposium, Perth, 1990, Extended Abstracts*, pp. 81–83. Geoconferences (W.A.) Inc., Perth

Tribovillard N., Algeo T. J., Lyons T. and Riboulleau A. (2006) Trace metals as paleoredox and paleoproductivity proxies: an update. *Chem. Geol.* **232,** 12-32.

Tsikos H. and Moore J. M. (1997) Petrography and geochemistry of the Paleoproterozoic Hotazel Iron-Formation, Kalahari manganese field, South Africa; implications for Precambrian manganese metallogenesis. *Economic Geology* **92,** 87-97.

Tsikos H., Beukes N. J., Moore J. M. and Harris C. (2003) Deposition, diagenesis, and secondary enrichment of metals in the Paleoproterozoic Hotazel iron formation, Kalahari Manganese Field, South Africa. *Economic Geology* **98,** 1449-1462.

Tsikos H., Matthews A., Erel Y. and Moore J. M. (2010) Iron isotopes constrain biogeochemical redox cycling of iron and manganese in a Palaeoproterozoic stratified basin. *Earth Planet. Sci. Lett.* **298,** 125-134.

Tsikos H., Rafuza S., Oonk P. B. H., Mhlanga X. R., Mason P. R. D., Boyce A. C., Grocke D.R., and Lyons T. W. (in prep.)Banded iron-formation carbonates record water-column organic carbon cycling in the Palaeoproterozoic ocean.

Valaas Hyslop E., Valley J. W., Johnson C. M. and Beard B. L. (2008) The effects of metamorphism on O and Fe isotope compositions in the Biwabik Iron Formation, northern Minnesota. *Contributions to Mineralogy and Petrology* **155,** 313-328.

Van Breugel Y., Schouten S., Paetzel M., Nordeide R. and Damsté J. S. (2005) The impact of recycling of organic carbon on the stable carbon isotopic composition of dissolved inorganic carbon in a stratified marine system (Kyllaren fjord, Norway). *Org. Geochem.* **36,** 1163-1173.

Van Cappellen P., Viollier E., Roychoudhury A., Clark L., Ingall E., Lowe K. and Dichristina T. (1998) Biogeochemical cycles of manganese and iron at the oxic-anoxic transition of a stratified marine basin (Orca Basin, Gulf of Mexico). *Environ. Sci. Technol.* **32,** 2931-2939.

Van de Brug J. J. (in prep.) The origin of riebeckite in the Iron Formations of the Transvaal Supergroup, South Africa, *MSc-thesis, Utrecht University.*

Van der Waal A. R. W. (2016) The origin of stilpnomelane lutite layers in Banded Iron Formations from the West Transvaal Basin, South Africa, *MSc-thesis, Utrecht University,* 106p.

Van Kranendonk M. J., Webb G. E. and Kamber B. S. (2003) Geological and trace element evidence for a marine sedimentary environment of deposition and biogenicity of 3.45 Ga stromatolitic carbonates in the Pilbara Craton, and support for a reducing Archaean ocean. *Geobiology* **1,** 91-108.

Vanysek P. (2017) Electrochemical series. In: Haynes, W. M. (Ed) *CRC Handbook of Chemistry and Physics* CRC Press/Taylor & Francis, Boca Raton, FL, Internet Version

Vargas M., Kashefi K., Blunt-Harris E. L. and Lovley D. R. (1998) Microbiological evidence for Fe (III) reduction on early Earth. *Nature* **395,** 65-67.

Viehmann S., Bau M., Hoffmann J. E. and Münker C. (2015) Geochemistry of the Krivoy Rog Banded Iron Formation, Ukraine, and the impact of peak episodes of increased global magmatic activity on the trace element composition of Precambrian seawater. *Precambrian Res.* **270,** 165-180.

Voegelin A. R., Nägler T. F., Beukes N. J. and Lacassie J. P. (2010) Molybdenum isotopes in late Archean carbonate rocks: implications for early Earth oxygenation. *Precambrian Res.* **182,** 70-82.

von Blanckenburg F., Oelze M., Schmid D. G., van Zuilen K., Gschwind H., Slade A. J., Stitah S., Kaufmann D. and Swart P. (2014) An iron stable isotope comparison between human erythrocytes and plasma. *Metallomics* **6,** 2052-2061.

Waite T., Davis J., Payne T., Waychunas G. and Xu N. (1994) Uranium (VI) adsorption to ferrihydrite: Application of a surface complexation model. *Geochim. Cosmochim. Acta* **58,** 5465-5478.

Webb G. E. and Kamber B. S. (2000) Rare earth elements in Holocene reefal microbialites: a new shallow seawater proxy. *Geochim. Cosmochim. Acta* **64,** 1557-1565.

Widdel F., Schnell S., Heising S., Ehrenreich A., Assmus B. and Schink B. (1993) Ferrous iron oxidation by anoxygenic phototrophic bacteria. *Nature* **362,** 834-836.

Wiederhold J. G., Kraemer S. M., Teutsch N., Borer P. M., Halliday A. N. and Kretzschmar R. (2006) Iron isotope fractionation during proton-promoted, ligand-controlled, and reductive dissolution of goethite. *Environ. Sci. Technol.* **40,** 3787-3793.

Wiederhold J. G., Teutsch N., Kraemer S. M., Halliday A. N. and Kretzschmar R. (2007) Iron isotope fractionation in oxic soils by mineral weathering and podzolization. *Geochim. Cosmochim. Acta* **71,** 5821-5833.

Wiesli R. A., Beard B. L. and Johnson C. M. (2004) Experimental determination of Fe isotope fractionation between aqueous Fe (II), siderite and "green rust" in abiotic systems. *Chem. Geol.* **211,** 343-362.

Wille M., Kramers J., Nägler T. F., Beukes N. J., Schröder S., Meisel T., Lacassie J. and Voegelin A. (2007) Evidence for a gradual rise of oxygen between 2.6 and 2.5 Ga from Mo isotopes and Re-PGE signatures in shales. *Geochim. Cosmochim. Acta* **71,** 2417-2435.

Williams H. M. and Bizimis M. (2014) Iron isotope tracing of mantle heterogeneity within the source regions of oceanic basalts. *Earth Planet. Sci. Lett.* **404,** 396-407.

Williams H. M., McCammon C. A., Peslier A. H., Halliday A. N., Teutsch N., Levasseur S. and Burg J. P. (2004) Iron isotope fractionation and the oxygen fugacity of the mantle. *Science* **304,** 1656-1659.

Williams H. M., Wood B. J., Wade J., Frost D. J. and Tuff J. (2012) Isotopic evidence for internal oxidation of the Earth's mantle during accretion. *Earth Planet. Sci. Lett.* **321,** 54-63.

Yamaguchi K. E., Johnson C. M., Beard B. L. and Ohmoto H. (2005) Biogeochemical cycling of iron in the Archean–Paleoproterozoic Earth: constraints from iron isotope variations in sedimentary rocks from the Kaapvaal and Pilbara Cratons. *Chem. Geol.* **218,** 135-169.

APPENDICES

To access the data in spread-sheets please contact the author.

Appendix I: Sample descriptions and mineralogy

The following tables contain sample discriptions and mineralogy. The mineralogy is primarily based upon XRD analysis (Appendix II), supported by optical microscopy. Mineral abbreviations in *italic* indicate presence as a minor or trace mineral. Chert/quartz is present in all samples and therefore not included in the list. Mineral abbreviations: ank=ankerite, cal=calcite, gre=greenalite, hem=hematite, mag=magnetite, min=minnesotaite, rie=riebeckite, sid=siderite, stp=stilpnomelane

Core: AARPAN-5	Sample	Mineralogy	Description
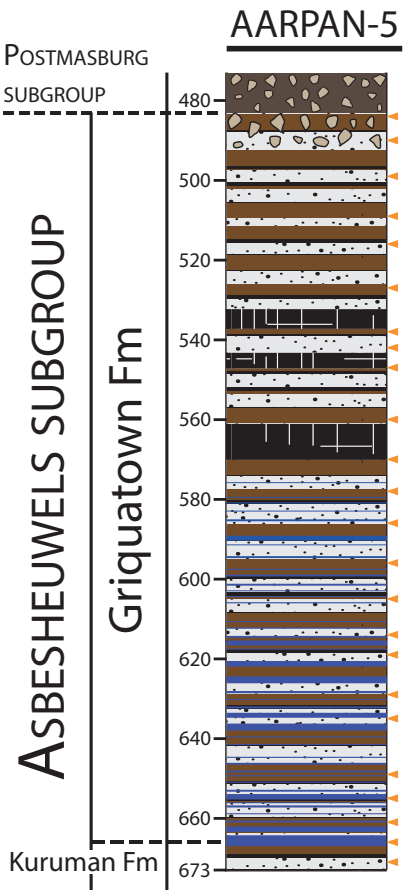	ARP484	Ank, sid, min, stp, *cal, mag*	Dark macrobanded BIF
	ARP490	Stp, ank, sid, gre, cal, mag	Grey mesobanded GIF
	ARP499	Min, mag, ank, *hem*	Grey mesobanded GIF, milky patches and mag. bands
	ARP509	Stp, ank, sid, mag, *cal*	Whitish GIF, some darker bands present
	ARP516	Sid, ank, stp, mag, *cal*	White-Greenish GIF, chert clasts
	ARP527	Sid, stp, ank, hem, mag, *cal*	Mesobanded GIF, dark-light-dark
	ARP538	Stp, ank, sid, mag, *hem, gre, cal*	Dark lutite sample
	ARP542	Sid, ank, stp, *mag*	Light grey mesobanded GIF containing pelloids
	ARP547	Stp, sid, mag, ank, *hem*	Lighter lutite sample
	ARP560	Gre, sid, mag, min, *ank*	Dark microbanded IF
	ARP571	Stp, min, ank, rie, *mag*	Blueish lutite sample, no distinct layering
	ARP578	Ank, sid, rie, min, *mag, cal*	Mesobanded grey GIF with one white-blue patched mesoband
	ARP586	Sid, ank, min, rie, *mag*	Blue-light grey alternating mesobands
	ARP596	Sid, min, ank, mag, *hem*	Meso/microbanded BIF in various greys
	ARP605	Ank, sid, mag, min, *hem*	Well-developed light-dark mesobands. Including some chert patches
	ARP614	Rie, ank, mag, *sid, stp*	Greyish meso/microbanded BIF, with blue layers
	ARP619	Rie, ank, mag, *sid*	Blue macroband which contains spheroids.
	ARP629	Sid, ank, mag, min	Greyish GIF, clear oxide-rich patches
	ARP635	Ank, mag, rie, *sid*	Brown-blue-greyish alternating GIF
	ARP649	Sid, mag, ank, *hem*	Blue-orange mesobanded GIF, clear magnetite crystals visible
	ARP656	Mag, ank, *gre, stp*	Black-white (mikly) BIF, soft-sediment deformation features
	ARP661	Sid, mag, ank, gre, *min, hem*	Greyish mesobanded GIF
	ARP666	Cal, sid, rie, *ank, hem*	Orange-blue GIF, patched
	ARP670	Sid, mag, ank, gre	Grey-blueish GIF, with light grey nodules present

Core: ERIN-3	Sample	Mineralogy	Description
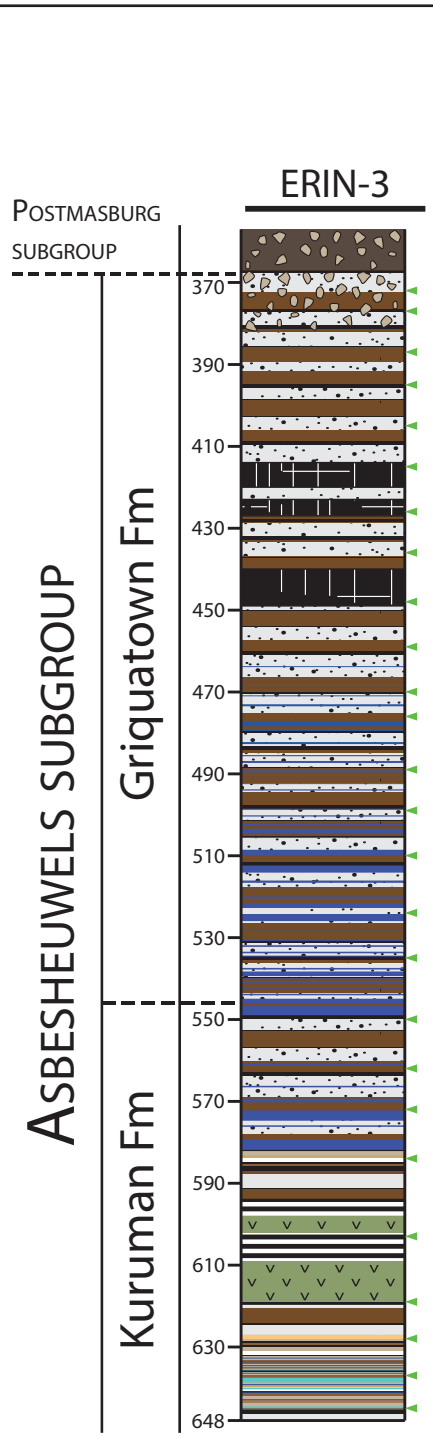	ERI373	Sid, *gre, min, mag*	Dark grey BIF with light grey dropstones
	ERI377	Stp, ank, mag, sid, *gre, cal*	Greenish microbanded BIF, wavy banding
	ERI387	Ank, mag, sid, *stp*	Dark macrobanded GIF, some blueish and lighter bands present
	ERI395	Ank, mag, sid, *gre*	Blue-whitish very granular macrobanded IF
	ERI405	Sid, ank, *mag, stp*	Grey mesobanded GIF, with a reddish patch
	ERI415	Sid, hem, mag, *ank*	Dark macrobanded BIF
	ERI427	Ank, sid, stp, *mag*	Dark mudstone, no clear banding. Stilpnomelane lutite
	ERI436	Sid, gre, min, *ank*	Dark grey mesobanded BIF, sometimes milky texture
	ERI450	Sid, ank, *min, mag, rie*	Blue-ish dominated microbanded GIF
	ERI459	*Sid, ank, mag, stp*	Light (grey, white, brown) macrobanded BIF
	ERI470	Sid, ank, *mag, stp, rie*	Dark macrobanded BIF
	ERI476	Sid, *ank, stp, mag*	Dark black and milky white macrobanded BIF, some blue, red and brown colors present
	ERI489	Sid, ank, mag, *gre, rie*	Macrobanded blue-white-grey GIF
	ERI499	Sid, ank, *mag, rie, hem, stp*	Gey mesobanded BIF, distinctive red line present
	ERI510	Sid, min, ank, *mag, hem, rie*	Grey microbanded fine grained IF
	ERI524	Sid, ank, mag, hem, *rie*	Blue-dark gray alternating macrobanded GIF, lateral band-thickness variations
	ERI535	Sid, ank, mag, *rie, cal*	Dark-white alternating mesobanded BIF with a blue-ish teint
	ERI550	Ank, mag, hem, *stp*	Light colored grey GIF, with blue, red, white and black clasts
	ERI562	Gre, min, sid, mag, *stp*	Grey mesobanded BIF, with blueish-brownish alternating teints
	ERI572	Mag, sid, *rie, stp*	Wavy microbanded BIF, generally black-white alternating with blueish and reddish patches
	ERI584	Mag, hem, *ank*	Rhytmically banded BIF, black bands alternating wiht white and red ones. Lighter bands are granular
	ERI603	Mag, cal, *gre, min*	Dark mesobanded BIF
	ERI618	Mag, *stp, min, cal*	Light macrobanded GIF alternating with black mesobanded BIF
	ERI628	Sid, ank, *mag, gre, min*	Grey to blueish alternating mesobanded BIF
	ERI637	Sid, *mag, ank, gre, rie*	Grey BIF with varying thickness in bands (macro-micro scale)
	ERI646	Sid, cal, *min, mag*	Rhytmically grey mesobanded BIF

Core: GASESA-1	Sample	Mineralogy	Description
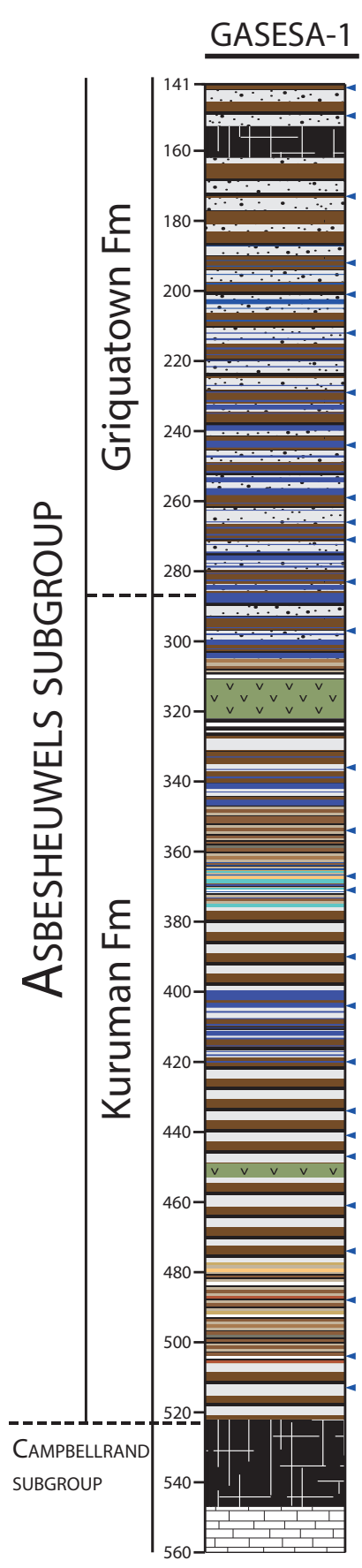	GAS142	Ank, stp, sid, *mag, cal*	Grey-brown and blue mesobanded GIF, blue band consists of pelloids
	GAS150	Sid, gre, mag, *min*	Dark grey/black macrobanded BIF
	GAS174	Sid, min, *gre, mag*	Light to dark grey alternating mesobanded GIF
	GAS192	Mag, ank, sid	Brown/white/blue mesobanded GIF
	GAS201	Ank, rie, sid, *mag*	Grey/blue mesobanded GIF
	GAS212	Sid, mag, *ank, min*	Homogeneous dark-grey marobanded GIF
	GAS229	Ank, mag	Greyish meso/microbanded GIF with 3 dark magnetite bands
	GAS244	Mag, sid, *ank, rie*	Blue-grey mesobanded BIF with thin white layers. Band thickness varies laterally
	GAS259	Mag, sid, *min*	Greyish microbanded GIF
	GAS266	Sid, ank, *mag*	Greyish mesobanded BIF, with blueish lenses
	GAS271	Rie, mag, ank	Lighly colored macrobanded GIF, some sub-mm magnetite bands waver
	GAS283	Sid, mag, gre, min	Grey/blue/white meso-microbanded BIF
	GAS296	Ank, sid, mag, *stp*	Light colored microbanded GIF
	GAS336	Ank, mag, rie, stp, *min*	Grey/black/blue mesobanded BIF with white chert patches
	GAS354	*Ank, sid, mag, gre*	Grey microbanded BIF. Wavering bands present
	GAS367	Min, mag, sid, *ank*	Blue-grey and black alternating microbanded GIF
	GAS371	Rie, sid, min, *ank, cal, mag, gre*	Blue dominated microbanded GIF
	GAS390	Sid, gre, min, *cal*	Dark grey microbanded BIF
	GAS404	Min, mag	Light grey mesobands alternated with black microbands
	GAS420	Mag, sid, *ank*	Multicolored (grey, blue, black, white, pink, orange) microbanded BIF
	GAS434	Mag, sid, *ank*	Light/dark grey alternating microbanded GIF
	GAS441	Mag	Black/white alternating mesobanded GIF
	GAS447	Mag, min	Light colored granular mesobands with wavering, thin, black microbands
	GAS461	Mag, *hem*	Black/white alternating microbanded BIF with the presence of a distinctive pinkish-chert band
	GAS474	Min, sid, *mag, ank*	Grey-colored microbands with variyng granularity
	GAS488	Mag, *hem, gre*	Black microbands with thick granular white chert-lenses
	GAS505	Mag, *hem, gre*	Light-dark gray microband alternating BIF with distinct reddish parts
	GAS513	Mag, sid, *ank, gre, hem*	Reddish mesobanded GIF with thin dark bands

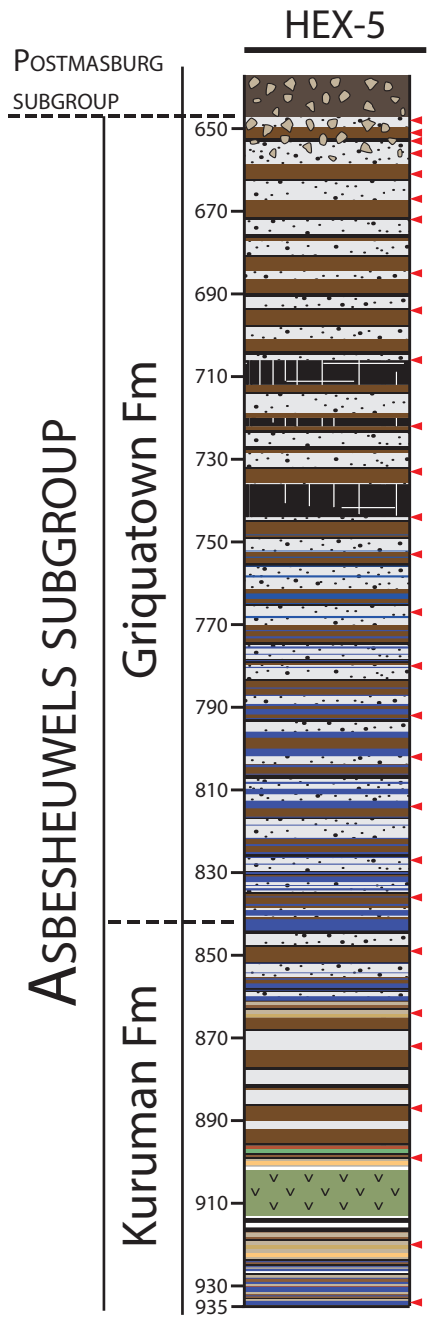

Core: HEX-5	Sample	Mineralogy	Description
	HEX648	Sid, mag, *ank, cal*	Grey mesobanded GIF, crinkly laminated magnetite, sample has a pinkish teint
	HEX651	Sid, ank, mag, *gre*	Grey macrobanded GIF
	HEX653	Sid, ank, stp, *mag*	Grey-browninsh GIF, pelloids present
	HEX656	Sid, *ank, stp, mag*	Dark grey meso/microbanded BIF
	HEX661	Sid, ank, *gre*	Grey macrobanded GIF
	HEX667	Mag, ank, *stp*	Dark grey macrobanded GIF
	HEX672	Ank, min, mag, *stp, cal*	Dark and light grey alternating mesobanded GIF
	HEX685	Mag, stp, sid	Dark (grey/black) macrobanded BIF, with 2 distinct bright-red bands
	HEX694	Min, ank, mag	Grey macrobanded very granular IF, with lens-shaped bands present
	HEX706	Sid, ank, *mag, stp*	Mesobanded grey GIF
	HEX722	Sid, ank, *stp, min*	Thick grey bands (~4cm) alternated with thin black microbands
	HEX733	Sid, min, *mag, hem, stp*	Dark macrobanded BIF with discontinous bands/clasts of blue-grey material
	HEX744	Sid, ank, *rie, stp*	Grey macrobanded BIF with black microbands
	HEX753	Sid, mag, *ank, gre, min, rie*	Alternating dark/light mesobanded BIF
	HEX767	Sid, ank, mag, min, *hem*	Alternating dark and light grey macrobanded BIF
	HEX780	Mag, ank, sid, *stp*	Macro and mesobanded, dark BIF
	HEX792	Sid, mag, *ank, rie*	Grey BIF with varying thicknesses and 3 distinct blue bands
	HEX802	Mag, sid, *rie, stp*	Thick blue macrobanded GIF alternated with thinner grey bands
	HEX814	Rie, mag, *sid, stp*	Blue-ish to grey alternating macrobanded GIF
	HEX827	Mag, sid, *min, ank, rie*	Multicolored (Black, blue, grey, white) macrobanded GIF
	HEX836	Sid, mag, *min, rie*	Grey microbanded, fine grained IF, with a single blue macroband
	HEX849	Sid, mag, *cal, stp*	Heterogeneous looking IF, generally grey with different types of bands
	HEX864	Mag, sid, *ank, min*	Grey microbanded GIF, with lateral band-thickness variations
	HEX872	Sid, mag, *gre, ank, hem*	Dark/light grey alternating GIF, some distinct, thin white veins and patchess
	HEX887	Mag, sid, ank, *rie*	Grey mesobanded BIF, some blue, reddish and black bands present
	HEX899	Mag, min, ank, *sid, rie*	Light/dark alternating microbanded BIF, with diagonally cross-cutting veins
	HEX920	Sid, ank, mag, *min*	Light grey rhytmic microbanded BIF
	HEX934	Mag, ank, sid, *rie, stp*	Grey/black/blue rhytmic mesobanded BIF

APPENDIX II: XRD SPECTRA

The diagrams in this appendix show the individual XRD spectra (2Θ = 5 - 40 °) after background corrections and quartz peak outlining of all samples. The peaks for the various silicate minerals are barely visible for some samples and needed to be confirmed by petrography. XRD analysis was performed at the Chemistry Department, Rhodes University.

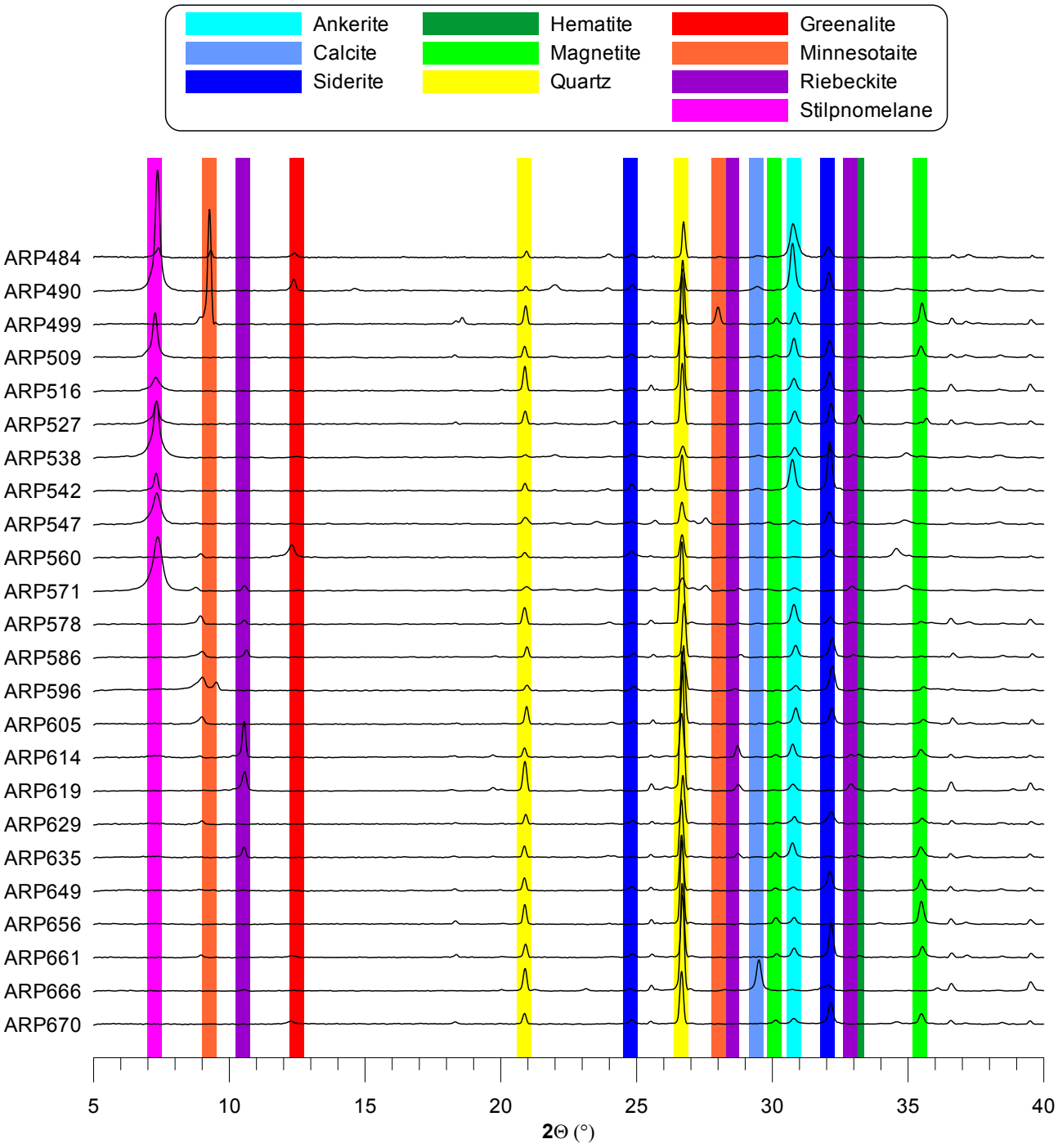

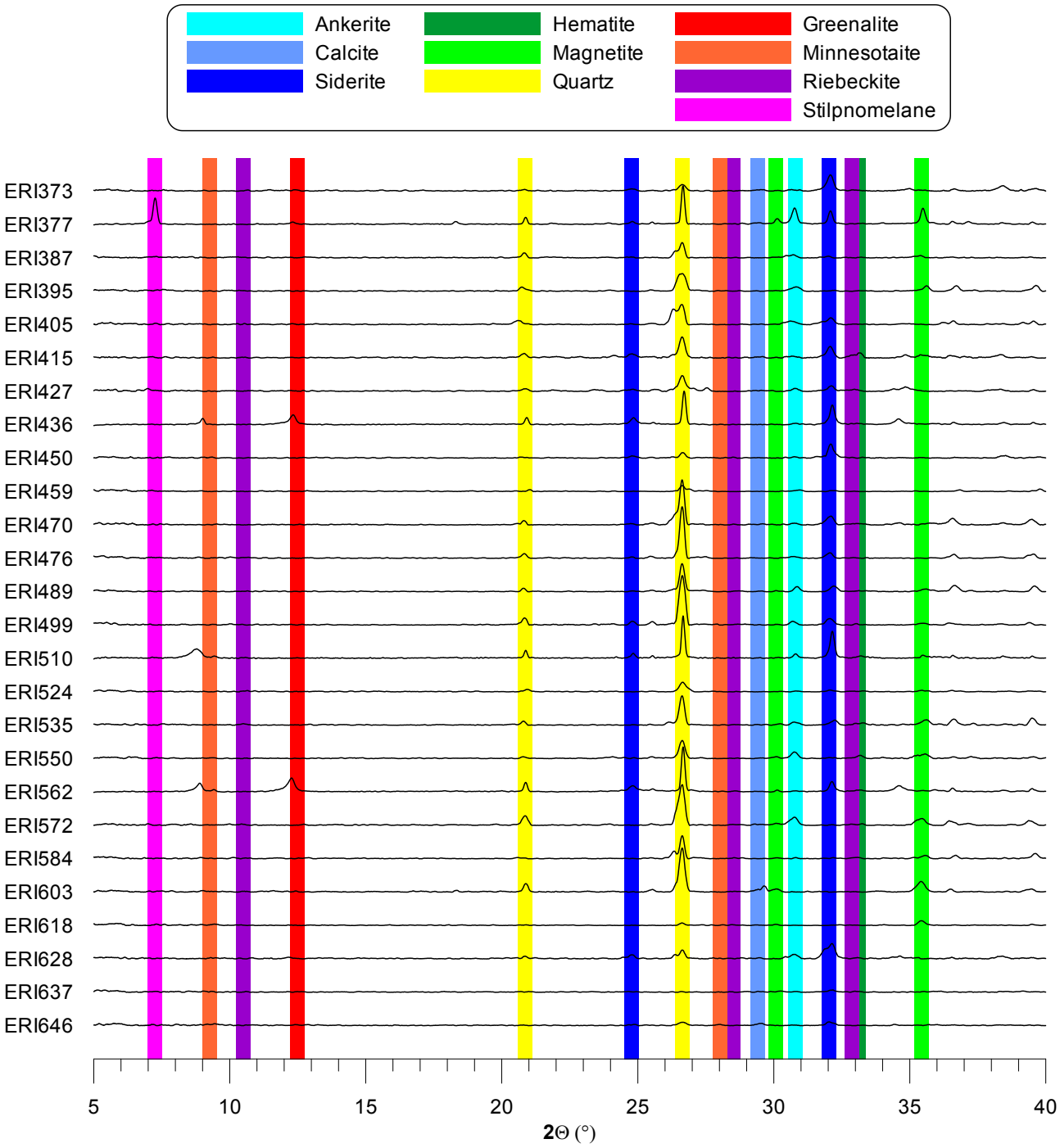
Ankerite
Calcite
Siderite
Hematite
Magnetite
Quartz
Greenalite
Minnesotaite
Riebeckite
Stilpnomelane
ERI373
ERI377
ERI387
ERI395
ERI405
ERI415
ERI427
ERI436
ERI450
ERI459
ERI470
ERI476
ERI489
ERI499
ERI510
ERI524
ERI535
ERI550
ERI562
ERI572
ERI584
ERI603
ERI618
ERI628
ERI637
ERI646
5
10
15
20
25
30
35
40
2Θ (°)

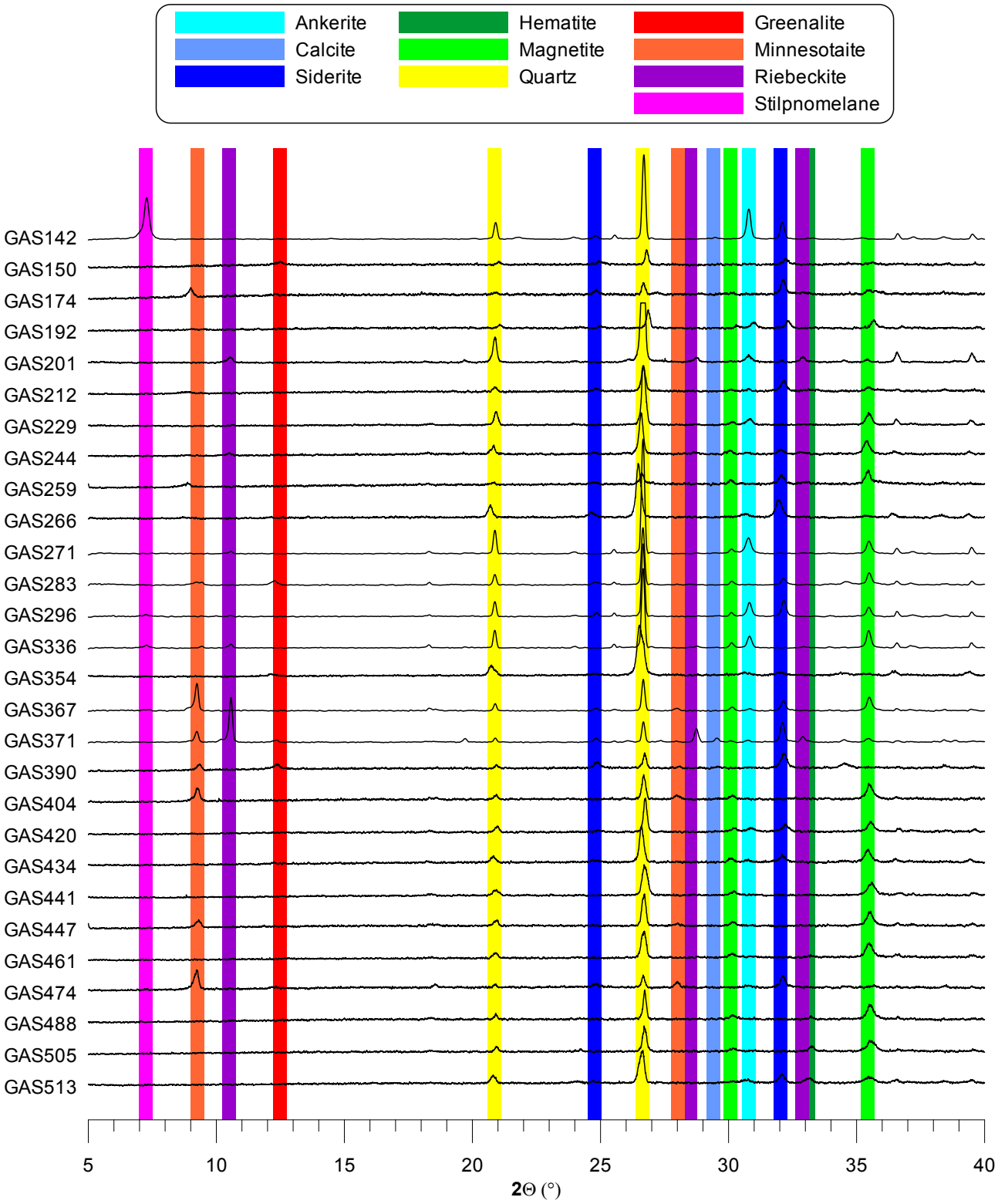
Ankerite
Calcite
Siderite
Hematite
Magnetite
Quartz
Greenalite
Minnesotaite
Riebeckite
Stilpnomelane
GAS142
GAS150
GAS174
GAS192
GAS201
GAS212
GAS229
GAS244
GAS259
GAS266
GAS271
GAS283
GAS296
GAS336
GAS354
GAS367
GAS371
GAS390
GAS404
GAS420
GAS434
GAS441
GAS447
GAS461
GAS474
GAS488
GAS505
GAS513
5
10
15
20
25
30
35
40
2Θ (°)

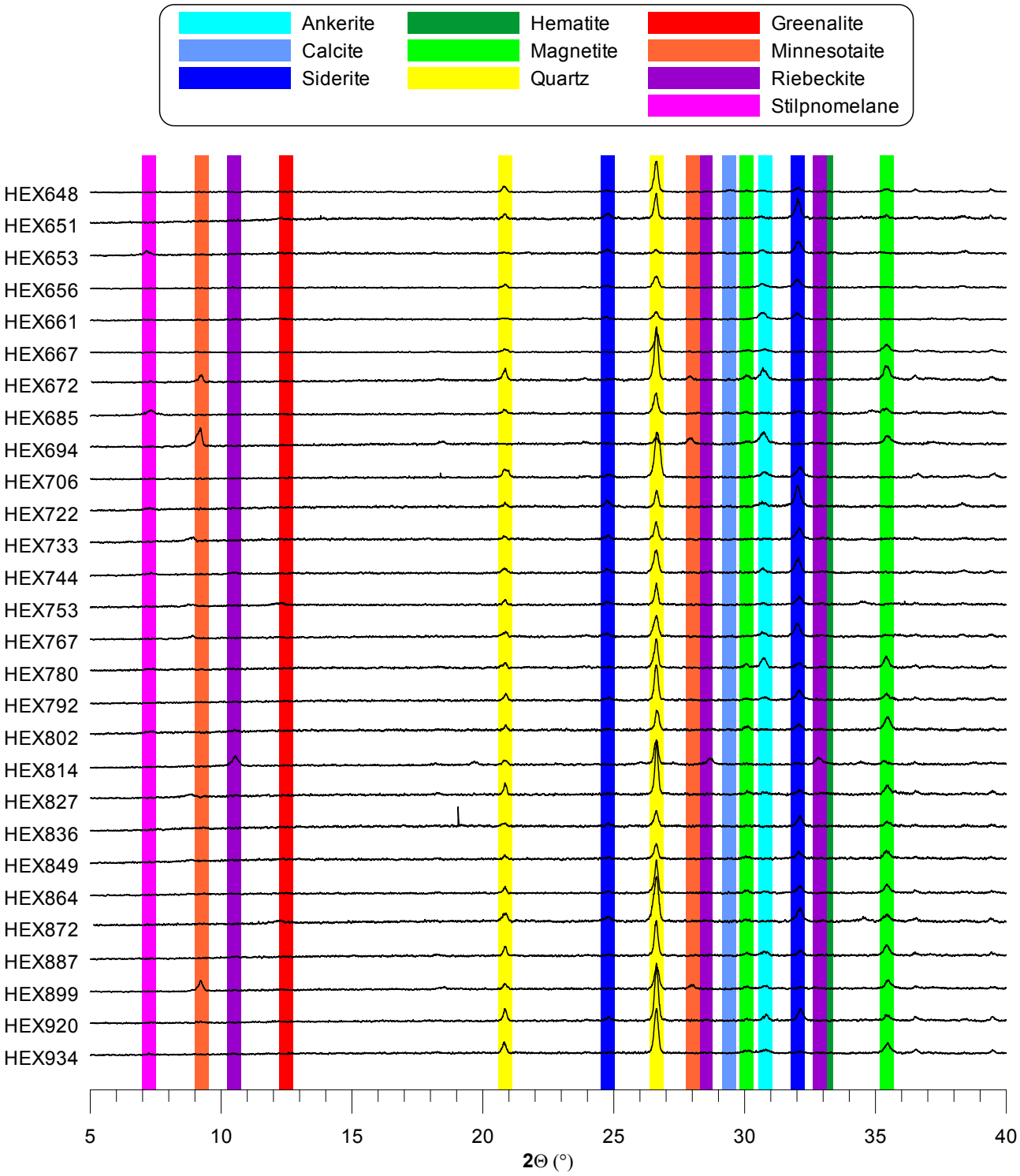
Ankerite
Calcite
Siderite
Hematite
Magnetite
Quartz
Greenalite
Minnesotaite
Riebeckite
Stilpnomelane
HEX648
HEX651
HEX653
HEX656
HEX661
HEX667
HEX672
HEX685
HEX694
HEX706
HEX722
HEX733
HEX744
HEX753
HEX767
HEX780
HEX792
HEX802
HEX814
HEX827
HEX836
HEX849
HEX864
HEX872
HEX887
HEX899
HEX920
HEX934
5
10
15
20
25
30
35
40
2Θ (°)

Appendix III: Sequential extraction protocol optimization data

The following tables contain the test results of the sequential extraction optimization. After the test and sample columns follow the elemental concentrations (Fe, Mn, Ca, Mg and Si) followed by the distribution over the fractions. The first line contains the bulk-rock data in wt% (XRF determined). The lines below are for each of the extracted samples. In these cases the concentrations are the sum of the individual fractions (ICP-OES determined). Recoveries were calculated using the bulk-rock values above. The elemental distributions (% of total extracted) follow. For the setup of the different sequential extraction schemes (SE1-7, SE-Ac, SE-Ox) the reader is referred to Chapter 2.

Notes/abbreviations:

Ac: Acetate extraction

Hy: Hydroxylamine-HCl extraction

Di: Dithionite extraction

Ox: Ammonium Oxalate extraction

HF: Extraction of final residue by HF

n.d.: Not determined due to lack of suitable standard solutions for SE1

Si-distribution*: Si evaporated during HF extraction, so HF was calculated as bulk-rock minus sum of the previous leaches. The Si (wt%) is the sum of the Si dissolved in the Ac, Hy, Di and Ox extractions.

		Fe	Mn	Ca	Mg	Si	Fe - distribution (%)					Mn - distribution (%)					Ca - distribution (%)					Mg - distribution (%)					Si - distribution* (%)					
Extraction	Sample	wt%	wt%	wt%	wt%	wt%	Ac	Hy	Di	Ox	HF	Ac	Hy	Di	Ox	HF	Ac	Hy	Di	Ox	HF	Ac	Hy	Di	Ox	HF	Ac	Hy	Di	Ox	HF	Notes
Bulk-rock	**GAS488**	**41.12**	**0.04**	**0.59**	**1.26**	**17.37**																									
SE1	GAS488-I	38.06	n.d.	n.d.	n.d.	n.d.	2	2	21	41	34																				ICP-OES in Cologne
SE1	GAS488-II	36.55	n.d.	n.d.	n.d.	n.d.	2	2	19	40	35																				ICP-OES in Cologne
SE1	GAS488-III	40.82	n.d.	n.d.	n.d.	n.d.	2	3	27	32	35																				ICP-OES in Cologne
SE2	GAS488-I	38.87	0.03	0.61	1.15	0.31	2	2	17	50	28	98	0	0	0	2	88	8	1	1	2	38	7	0	0	55	1	0	0	1	98	
SE2	GAS488-II	39.11	0.03	0.61	1.12	0.31	2	2	19	51	25	99	0	0	0	1	89	9	1	1	1	39	7	0	0	54	1	0	0	1	98	
SE2	GAS488-III	38.89	0.03	0.62	1.11	0.31	2	2	18	52	25	98	0	0	0	2	88	8	1	1	3	39	7	0	0	53	1	0	0	1	98	
SE3	GAS488-I	38.99	0.03	0.70	1.17	0.30	2	2		66	29	99	0		0	1	84	9		6	1	37	7		1	55	1	0		1	98	
SE3	GAS488-II	39.31	0.03	0.64	1.17	0.30	2	2		70	25	99	0		0	1	89	9		1	1	37	7		1	55	1	0		1	98	
SE3	GAS488-III	40.01	0.03	0.74	1.18	0.35	2	2		76	20	100	0		0	0	88	9		1	2	37	7		1	55	1	0		1	98	
SE4	GAS488-I	38.66	0.03	0.62	1.13	0.65	3	2	18	48	29	99	0	0	0	1	90	8	1	1	1	45	2	0	0	52	3	0	0	1	96	
SE4	GAS488-II	39.94	0.03	0.64	1.14	0.67	2	2	18	41	36	98	0	0	0	2	90	7	1	0	1	45	2	0	0	52	3	0	0	1	96	
SE4	GAS488-III	40.15	0.03	0.63	1.10	0.64	2	3	18	40	36	98	0	0	0	2	90	8	1	1	1	46	3	0	0	51	3	0	0	1	96	
SE5	GAS488-I	39.49	0.03	0.53	1.17	0.53	2			82	16	99			1	0	94			1	5	43			3	54	2			1	97	
SE5	GAS488-II	38.79	0.04	0.57	1.16	0.63	3			81	16	99			1	0	94			1	5	44			3	52	3			1	96	
SE5	GAS488-III	38.73	0.03	0.53	1.12	0.56	2			82	16	99			1	0	95			1	5	46			3	51	2			1	97	
SE6	GAS488-I	42.53	0.04	0.60	1.24	0.50	2			60	37	85			5	10	92			3	5	40			2	59	2			1	97	
SE6	GAS488-II	41.69	0.04	0.60	1.21	0.52	2			69	29	83			5	11	94			3	3	40			2	58	2			1	97	
SE6	GAS488-III	41.45	0.04	0.60	1.24	0.52	2			66	31	86			5	10	92			3	5	40			2	59	2.1			1	97	
SE-Ac5	GAS488 (72)	40.63	0.03	0.57	1.19	0.63	3			74	24	99			0	1	94			2	4	44			3	53	2.8			1	96	72hr acetate
SE-Ox1	GAS488-I	40.77	0.04	0.54	1.24	0.62	2			72	26	93			3	4	92			3	5	41			3	56	2.8			1	96	6 hr, oxic
SE-Ox1	GAS488-II	41.81	0.03	0.58	1.24	0.64	2			70	27	94			2	4	93			3	5	41			3	56	2.7			1	97	6 hr, oxic
SE-Ox2	GAS488-I	39.88	0.03	0.55	1.27	0.63	3			78	19	93			2	4	92			2	7	40			4	56	3.0			1	96	24 hr, oxic
SE-Ox2	GAS488-II	39.86	0.03	0.59	1.27	0.64	3			80	17	94			2	4	93			2	6	40			4	55	2.5			1	97	24 hr, oxic
SE-Ox3	GAS488-I	41.77	0.03	0.54	1.29	0.60	2			60	37	91			1	8	93			2	5	39			2	59	3.1			1	96	6 hr, inert
SE-Ox3	GAS488-II	41.48	0.03	0.53	1.23	0.58	2			60	38	92			0	8	94			2	4	40			2	58	3.1			1	96	6 hr, inert
SE-Ox4	GAS488-I	40.58	0.03	0.55	1.19	0.63	2			67	31	94			0	6	93			2	5	41			3	56	2.5			1	97	24 hr, inert
SE-Ox4	GAS488-II	41.70	0.03	0.54	1.26	0.66	2			64	34	92			0	8	92			2	6	40			2	58	3.1			1	96	24 hr, inert
SE-Ox5	GAS488-I	41.33	0.04	0.54	1.28	0.61	2			49	48	93			0	7	93			3	4	40			2	58	2.8			1	97	6 hr, oxic, dark
SE-Ox5	GAS488-II	41.56	0.03	0.55	1.26	0.61	2			59	39	93			1	6	93			2	5	41			3	57	3.2			1	96	6 hr, oxic, dark
SE-Ox6	GAS488-I	41.57	0.03	0.57	1.31	0.75	3			92	5	94			4	2	92			2	6	40			8	52	3.1			2	95	24 hr, oxic, 50°C
SE-Ox6	GAS488-II	40.60	0.03	0.55	1.23	0.74	3			92	5	96			4	0	93			2	5	42			8	50	2.9			1	96	24 hr, oxic, 50°C
SE7	GAS488	39.75	0.07	0.62	1.10	0.66	2			82	16	64			5	31	91			3	6	44			5	51	3			1	96	
SE7	GAS488	39.37	0.06	0.69	1.12	0.68	2			83	15	62			5	33	78			3	19	43			5	52	3			1	96	
SE7	GAS488	39.08	0.06	0.64	1.09	0.66	2			84	14	60			5	35	84			2	13	44			5	51	3			1	96	
SE7	GAS488	38.79	0.06	0.59	1.14	0.64	2			82	15	62			5	33	89			2	9	42			5	53	3			1	96	
SE7	GAS488	38.69	0.06	0.58	1.10	0.65	2			82	16	60			6	34	92			3	5	44			5	51	3			1	96	
SE7	GAS488	40.23	0.05	0.59	1.16	0.64	2			82	16	62			5	33	90			2	7	41			5	54	3			1	96	
SE7	GAS488	39.26	0.06	0.58	1.14	0.67	2			82	16	60			5	35	92			3	5	42			5	53	3			1	96	
SE7	GAS488	39.40	0.05	0.58	1.15	0.63	2			83	15	62			5	33	93			2	5	42			5	53	3			1	96	
SE7	GAS488	38.03	0.03	0.58	1.19	0.65	2			85	13	89			2	9	92			2	6	41			5	54	3			1	96	

		Fe	Mn	Ca	Mg	Si	Fe - distribution (%)					Mn - distribution (%)					Ca - distribution (%)					Mg - distribution (%)					Si - distribution* (%)					
Extraction	Sample	wt%	wt%	wt%	wt%	wt%	Ac	Hy	Di	Ox	HF	Ac	Hy	Di	Ox	HF	Ac	Hy	Di	Ox	HF	Ac	Hy	Di	Ox	HF	Ac	Hy	Di	Ox	HF	Notes
Bulk-rock	**HEX722**	**25.44**	**3.80**	**3.40**	**2.62**	**10.47**																										
SE1	HEX722-I	20.59	n.d.	n.d.	n.d.	n.d.	51	33	1	5	11																					ICP-OES in Cologne
SE1	HEX722-II	26.18	n.d.	n.d.	n.d.	n.d.	47	41	1	3	8																					ICP-OES in Cologne
SE1	HEX722-III	20.40	n.d.	n.d.	n.d.	n.d.	55	31	1	3	10																					ICP-OES in Cologne
SE2	HEX722-I	26.96	2.72	3.09	2.44	0.18	58	32	0	1	9	67	32	0	1	1	91	8	0	0	0	62	29	0	1	8	2	0	0	0	98	
SE2	HEX722-II	26.98	3.04	3.32	2.45	0.20	58	33	0	1	8	66	33	0	1	1	91	9	0	0	0	62	31	0	1	7	2	0	0	0	98	
SE2	HEX722-III	21.05	2.09	2.07	1.93	0.13	60	31	0	1	8	58	40	0	1	1	88	12	0	0	0	54	36	0	1	9	1	0	0	0	99	
SE3	HEX722-I	27.26	2.89	3.12	2.54	0.18	48	41		2	9	57	41		2	1	89	10		0	0	54	37		2	8	2	0		0	98	
SE3	HEX722-II	27.26	2.89	2.87	2.54	0.16	49	40		2	9	57	40		2	1	89	10		0	0	55	36		1	8	1	0		0	98	
SE3	HEX722-III	27.51	3.06	3.35	2.57	0.19	48	41		2	9	56	41		2	1	90	10		0	0	53	37		2	8	2	0		0	98	
SE4	HEX722-I	25.24	2.77	2.95	2.37	0.29	78	11	1	0	9	92	7	0	0	1	96	4	0	0	0	86	6	0	0	8	3	0	0	0	97	
SE4	HEX722-II	25.29	2.59	2.95	2.38	0.30	82	8	0	0	9	93	6	0	0	1	96	4	0	0	0	87	5	0	0	8	3	0	0	0	97	
SE4	HEX722-III	25.15	2.76	3.28	2.36	0.32	79	10	2	0	9	93	6	0	0	1	96	3	0	0	1	86	6	0	0	8	3	0	0	0	97	
SE5	HEX722-I	24.98	2.82	2.74	2.35	0.26	77			11	11	89			9	2	97			0	3	82			8	10	2			0	97	
SE5	HEX722-II	25.12	2.66	2.72	2.36	0.25	72			16	12	88			9	3	96			0	3	81			8	10	2			0	98	
SE5	HEX722-III	24.98	2.57	2.58	2.35	0.25	82			7	11	92			6	2	97			0	3	85			5	9	2			0	98	
SE6	HEX722-I	26.64	2.87	3.21	2.43	0.26	83			7	10	94			5	1	97			1	3	87			5	9	2			0	98	
SE6	HEX722-II	27.08	2.91	3.21	2.45	0.25	84			6	10	95			4	1	97			1	3	88			4	8	2			0	98	
SE6	HEX722-III	26.85	2.91	3.15	2.44	0.26	85			5	9	95			4	1	98			1	2	88			3	9	2			0	98	
SE-Ac1	HEX722 (0)	26.52	2.95	2.62	2.47	0.14				62	38				56	44				0	100				59	41				1	99	No acetate
SE-Ac1	HEX722 (0)	26.93	2.83	2.48	2.49	0.13				66	34				62	38				0	100				64	36				1	99	No acetate
SE-Ac2	HEX722 (7)	26.33	2.73	2.41	2.46	0.14	48			39	13	57			38	5	91			0	9	54			34	12	1			0	99	7hr acetate
SE-Ac2	HEX722 (7)	26.54	2.91	3.11	2.47	0.19	53			36	11	62			36	2	92			0	8	59			32	10	2			0	98	7hr acetate
SE-Ac3	HEX722 (24)	25.31	2.86	3.07	2.38	0.23	72			17	11	82			16	2	96			0	4	76			14	10	2			0	98	24hr acetate
SE-Ac3	HEX722 (24)	25.72	2.88	3.28	2.42	0.24	72			17	11	82			16	2	95			0	4	76			14	10	2			0	98	24hr acetate
SE-Ac4	HEX722 (48)	25.38	2.73	3.16	2.38	0.28	80			10	11	90			9	2	96			0	3	83			7	9	2.5			0	97	48hr acetate
SE-Ac4	HEX722 (48)	25.57	2.74	3.15	2.40	0.28	80			9	11	90			8	2	97			0	3	84			7	9	2.5			0	97	48hr acetate
SE-Ac5	HEX722 (72)	25.69	2.72	3.04	2.40	0.31	84			5	11	95			4	1	97			0	3	87			3	9	2.8			0	97	72hr acetate
SE-Ac5	HEX722 (72)	25.49	2.77	3.12	2.39	0.31	83			6	11	93			5	1	97			0	3	86			4	9	2.8			0	97	72hr acetate
SE-Ac5	HEX722 (72)	25.83	2.75	3.07	2.42	0.31	83			7	11	93			6	1	97			0	3	86			5	9	2.8			0	97	72hr acetate
SE7	HEX722	25.23	2.87	3.43	2.41	0.28	69			21	10	92			7	1	92			0	7	84			7	10	3			0	97	

		Fe	Mn	Ca	Mg	Si	Fe - distribution (%)					Mn - distribution (%)					Ca - distribution (%)					Mg - distribution (%)					Si - distribution* (%)					
Extraction	Sample	wt%	wt%	wt%	wt%	wt%	Ac	Hy	Di	Ox	HF	Ac	Hy	Di	Ox	HF	Ac	Hy	Di	Ox	HF	Ac	Hy	Di	Ox	HF	Ac	Hy	Di	Ox	HF	Notes
Bulk-rock	**SARM-40**	**1.91**	**0.18**	**34.52**	**1.17**	**1.49**																									
SE2	SARM-40-I	1.66	0.14	35.82	1.10	0.17	7	5	35	33	20	90	8	1	0	1	93	5	0	0	2	37	35	0	1	27	1	7	2	1	89	
SE2	SARM-40-II	1.58	0.13	32.13	1.12	0.13	8	5		60	27	93	6		1	0	94	6		0	0	38	37	0	0	25	1	7		1	91	
SE3	SARM-40-I	1.50	0.13	32.34	1.10	0.17	10	4	35	36	16	98	1	1	0	0	95	5	0	0	0	42	30		0	28	3	7	1	0	89	
SE3	SARM-40-II	1.67	0.13	30.11	1.12	0.07	8			42	49	96			1	3	95			0	5	39	32		0	28	3			2	95	
SE4	SARM-40-I	1.61	0.14	35.14	1.07	0.16	7	5	36	37	15	91	7	1	0	0	93	6	0	0	0	59	16	0	0	24	1	8	1	0	89	
SE4	SARM-40-II	1.53	0.15	36.83	1.06	0.14	8	4		56	32	92	6		1	1	94	6		0	0	59	17	0	0	25	1	7		1	91	
SE5	SARM-40-I	1.36	0.14	33.99	1.06	0.17	10	4	37	35	15	98	1	1	0	0	95	5	0	0	0	60			3	37	3	7	1	0	88	
SE5	SARM-40-II	1.56	0.12	27.05	1.05	0.07	8			38	54	96			1	3	95			0	5	58			3	39	2			2	96	

		Fe	Mn	Ca	Mg	Si	Fe - distribution (%)					Mn - distribution (%)					Ca - distribution (%)					Mg - distribution (%)					Si - distribution* (%)					
Extraction	Sample	wt%	wt%	wt%	wt%	wt%	Ac	Hy	Di	Ox	HF	Ac	Hy	Di	Ox	HF	Ac	Hy	Di	Ox	HF	Ac	Hy	Di	Ox	HF	Ac	Hy	Di	Ox	HF	Notes
Bulk-rock	**HEX836**	**31.18**	**0.21**	**0.22**	**2.91**	**17.85**																									
SE6	HEX836-I	32.08	0.15	0.20	2.73	0.73	33			39	28	80			9	10	52			7	41	44			8	48	2			2	96	
SE6	HEX836-II	32.92	0.16	0.20	2.84	0.74	32			40	28	78			10	11	51			7	42	43			8	49	2			2	96	
SE6	HEX836-III	32.60	0.16	0.21	2.84	0.75	32			41	27	78			12	10	49			8	43	43			9	48	2			2	96	
SE-Ox1	HEX836	32.18	0.15	0.21	2.80	0.84	34			44	23	86			10	5	52			6	43	44			8	48	4			2	94	6 hr, oxic
SE-Ox2	HEX836	32.13	0.15	0.20	2.81	0.95	34			48	18	86			11	3	52			4	45	44			11	45	3			3	94	24 hr, oxic
SE-Ox3	HEX836	32.74	0.15	0.20	2.80	0.84	32			38	30	85			7	8	52			7	41	43			7	50	3			2	95	6 hr, inert
SE-Ox4	HEX836	32.57	0.15	0.20	2.79	0.99	33			39	27	87			6	8	54			4	42	44			9	47	3			3	94	24 hr, inert
SE-Ox5	HEX836	31.97	0.15	0.19	2.80	0.85	34			41	25	86			9	4	55			7	38	44			8	47	3			2	95	6 hr, oxic, dark
SE-Ox6	HEX836	31.81	0.15	0.20	2.79	1.39	34			57	8	87			12	1	54			7	39	45			22	34	3			5	92	24 hr, oxic, 50°C
SE7	HEX836	30.45	0.15	1.42	2.79	0.94	33			34	34	83			8	9	8			1	91	44			10	47	3			2	95	
SE7	HEX836	29.26	0.16	0.41	2.52	0.98	34			51	15	76			11	13	26			4	71	47			13	39	3			2	95	
SE7	HEX836	30.78	0.16	0.20	2.68	0.92	31			45	25	73			12	14	49			5	46	42			11	47	3			2	95	
SE7	HEX836	30.97	0.16	0.22	2.65	0.96	32			47	21	75			11	14	48			5	48	44			12	44	3			2	95	
SE7	HEX836	31.00	0.17	0.21	2.67	0.98	32			46	22	75			9	16	49			7	44	45			11	45	3			2	95	
SE7	HEX836	30.87	0.16	0.20	2.67	0.94	32			49	20	74			12	14	53			5	42	44			12	43	3			2	95	
SE7	HEX836	31.31	0.16	0.21	2.70	0.97	31			47	22	75			11	14	49			6	44	44			12	44	3			2	95	
SE7	HEX836	32.00	0.16	0.24	2.80	0.99	31			50	18	75			15	11	47			4	49	43			14	43	3			3	94	
SE7	HEX836	30.29	0.16	0.20	2.63	0.94	32			49	19	75			13	12	52			5	43	44			13	44	3			2	95	

Appendix IV: Bulk-rock and sequentially extracted data

The following tables contain the elemental concentrations of the different extractions and their bulk-rock values. The fractions (Frac:) are marked A-D, with A: Acetate fraction, B: Oxalate fraction, C: HF fraction and D: Bulk-rock concentrations. Data were calculated to elemental wt% level (Ca - Al; green) or in ppm (Ti - U; orange). Concentrations were measured using a variety of techniques, and in some cases elements (i.e. Mn) were measured with multiple techniques to verify the concentrations. In case of duplicate or replicate measurements the numbers are averaged.

The data in the table were obtained by the following techniques:

Bulk-rock data (D):

- Ca, Fe, Mg, Si, K, Al: XRF fusion bead
- Na XRF pressed pellet
- C, S LECO C-S Analyzer
- Mn, Ti - U ICP-MS

Extracted data (A-C)

- Ca, Fe, Mg, Si, K ICP-OES
- Mn, Al - U ICP-MS

The color codes in the tables are:

Code	Explanation	Treated:
neg.	Either a negative number after background subtraction (ICP) or zero on XRF	Values set to zero
< d.l.	Smaller then detection limit (limit of quantification, LOQ) ICP-MS: LOQ = 10x SD on matrix matched blanks ICP-OES: 3x SD of the background plasma	Approximate value, but used for recovery calculations
< BEC	Smaller then Background Equivalent Concentration (ICP-OES) The BEC gives the lowest concentration which has a uncertainty <10%. The BEC>detection limit	Approximate value, but used for recovery calculations
err.	Erroneous value in the extraction, number removed manually. Concentration is >5x the bulk-rock value or summed recovery is too far of the calibration line.	Values omitted
>l.r.	Value is above the line range defined by the calibration standards (ICP-MS)	Approximate value, but used for interpretation purposes.
n.m.	Not measured. Si in HF fraction and Na, S and C in all extracted fractions.	Si in HF fraction is assumed based on 100% recovery.

Fractions: A= Acetate, B= Oxalate, C: HF, D= Bulk-rock

wt% ppm neg. < d.l. < BEC err. >l.r. n.m.

	ARP484				ARP490				ARP499				ARP509				ARP516				ARP527			
Frac:	A	B	C	D	A	B	C	D	A	B	C	D	A	B	C	D	A	B	C	D	A	B	C	D
Ca	9.95	0.01	0.11	10.35	6.93	0.01	0.03	7.49	1.07	0.01	<0.01	1.19	3.12	0.01	0.06	3.55	2.14	0.01	0.04	2.33	2.73	0.01	0.03	2.95
Fe	9.36	2.58	3.97	16.07	9.45	3.17	10.08	22.16	0.95	20.83	10.82	32.78	7.96	14.03	6.24	28.01	6.55	3.82	2.89	13.78	6.67	4.31	12.25	23.16
Mg	2.10	0.12	0.19	2.85	1.51	0.16	0.59	2.54	0.32	0.01	1.09	1.48	1.45	0.11	0.43	2.24	1.11	0.09	0.39	1.75	1.25	0.09	0.43	1.94
Mn	3.20	0.13	0.08	2.64	1.94	0.07	0.15	2.23	0.15	<0.01	0.05	0.24	1.15	0.07	0.06	1.24	0.96	0.05	0.03	1.12	0.24	0.01	0.01	0.30
Si	0.16	0.03		12.10	0.26	0.10		12.66	0.08	0.15		21.52	0.13	0.08		16.13	0.26	0.04		28.54	0.24	0.03		21.68
K	0.08	0.01	0.02	0.06	0.21	0.03	0.02	0.24	0.02	0.03	0.03	0.02	0.21		0.01	0.20	0.20		0.02	0.19	0.30	0.00	0.03	0.31
Na				0.02				0.08								0.10				0.06				0.12
S				0.08				0.15				0.50				0.08				0.09				0.11
C				7.82				5.99				0.70				4.35				3.03				3.27
Al	0.01	0.04	0.11	0.19	0.03	0.10	0.35	0.59	<0.01	<0.01	0.02	0.01	0.01	0.01	0.24	0.44	0.02	0.03	0.20	0.31	0.02	0.03	0.34	0.41
Ti	2.54	17.18	127.03	117.43	2.46	33.60	424.45	411.87	<0.01	5.18	10.14	17.73	2.41	14.21	114.29	135.17	0.72	13.04	180.66	175.76	1.17	56.78		222.08
Be	0.28	0.04	0.05	0.27	0.28	0.08	0.13	0.43	0.07	0.10	0.09	0.26	0.20	0.04	0.04	0.23	0.16	0.02	0.07	0.24	0.23	0.02	0.10	0.31
Sc	0.56	0.07	0.06	0.47	1.18	0.38	0.44	1.39		0.01	0.03	0.15	0.73	0.08	0.19	0.71	0.63	0.09	0.18	0.63	0.65	0.11	0.26	0.96
V	0.84	1.84	1.60	4.56	2.14	4.98	7.26	14.12	0.89	3.33	0.00	6.21	1.01	4.27	2.17	9.32	2.17	3.10	3.91	9.07	1.46	3.12	4.92	12.63
Cr	2.55	2.38	3.24	7.16	4.11	5.39	9.77	15.49	<0.01		0.06	7.49	5.77	2.83	3.23	11.09	9.13	6.70	4.15	20.89	4.74	4.42	6.03	17.61
Co	0.29	0.04	0.72	0.51	0.29	0.03	1.29	1.36	0.22	0.04	1.25	1.88	0.73	0.25	0.91	1.75	0.48	0.11	0.59	1.07	0.53	0.10	0.77	1.48
Ni	1.41	0.69	1.23	3.03	1.41	1.29	5.13	6.81	1.03	0.42	2.40	4.96	1.67	0.93	2.55	5.16	2.96	0.78	1.82	5.81	2.13	1.02	3.83	7.30
Cu	1.54	0.35	0.72	1.62	3.91	0.02	4.69	5.46	3.29	2.15	3.41	4.47	5.82	1.00	3.78	4.82	4.47	1.57	2.50	5.82	3.29	0.84	4.94	8.35
Zn	4.30	1.55	2.50	3.23	1.60	1.02	5.12	2.83	1.53	<0.01	7.81	4.03	3.53	0.74	2.62	3.06	7.04	1.54	1.92	6.83	2.33	0.47	4.13	2.69
Rb	3.34	0.31	0.85	3.69	13.46	2.49	2.70	17.09	0.18	0.03	0.58	0.65	10.58	1.33	1.38	11.61	8.63	1.32	1.92	11.28	13.83	2.87	3.02	19.47
Sr	18.16		18.90	13.88	17.74		6.65	15.87	5.52	<0.01	0.89	5.69	13.65		13.39	11.89	6.42		12.80	6.43	13.37		5.02	13.41
Y	4.31	0.27	0.42	3.91	4.55	0.40	0.99	5.29	1.96	0.16	0.20	2.39	4.07	0.42	0.44	4.35	1.60	0.27	0.45	2.20	1.81	0.36	0.59	2.70
Zr	0.05	0.51	2.81	2.98	0.22	1.45	8.03	9.31	<0.01	0.18	0.67	0.66	0.05	0.29	3.17	3.68	0.03	0.62	5.38	5.76	0.05	0.68	6.34	6.36
Mo	0.50	0.09	0.21	0.24	0.33	0.12	0.12	0.18	0.18	0.16	0.05	0.40	0.23	0.28	0.20	0.56	0.23	0.69	0.17	0.99	0.17	0.35	0.22	0.74
Cs	0.59	0.12	0.23	0.79	2.69	0.47	0.52	3.35	0.02	0.02	0.04	0.11	2.26	0.30	0.17	2.49	1.90	0.49	0.27	2.62	3.19	0.65	0.42	4.30
Ba	7.38	0.99	3.27	8.93	22.49	1.26	55.44	69.38	0.35	0.68	0.68	2.22	3.04		3.14	7.28	2.08		1.43	5.47	7.99		9.19	17.06
La	1.46	0.03	0.19	1.28	1.72	0.11	0.28	1.93	0.40	0.06	0.10	0.68	1.26	0.19	1.00	2.58	0.63	0.15	0.58	1.41	1.04	0.32	1.04	2.39
Ce	2.14	0.10	0.36	1.96	2.94	0.33	0.72	3.41	0.86	0.11	0.19	1.26	2.87	0.46	1.87	4.89	1.18	0.39	1.08	2.51	1.80	0.68	1.84	3.90
Pr	0.25	0.01	0.05	0.24	0.36	0.04	0.09	0.45	0.12	0.01	0.02	0.17	0.39	0.05	0.19	0.62	0.15	0.05	0.11	0.31	0.21	0.07	0.18	0.47
Nd	0.95	0.06	0.19	0.98	1.43	0.18	0.39	1.87	0.51	0.06	0.07	0.71	1.54	0.21	0.64	2.37	0.56	0.18	0.39	1.17	0.79	0.27	0.60	1.72
Sm	0.20	0.01	0.04	0.22	0.31	0.04	0.08	0.42	0.10	0.01	0.01	0.14	0.39	0.05	0.09	0.51	0.13	0.04	0.06	0.23	0.17	0.05	0.10	0.33
Eu	0.08	<0.01	0.01	0.09	0.10	0.01	0.02	0.14	0.04	<0.01	<0.01	0.05	0.09	0.01	0.02	0.13	0.03	0.01	0.01	0.06	0.05	0.01	0.02	0.09
Gd	0.28	0.02	0.04	0.28	0.39	0.04	0.09	0.47	0.14	0.02	0.02	0.19	0.43	0.05	0.09	0.53	0.15	0.05	0.06	0.26	0.20	0.06	0.09	0.35
Tb	0.04	<0.01	0.01	0.05	0.06	0.01	0.01	0.08	0.02	<0.01	<0.01	0.03	0.07	0.01	0.01	0.08	0.02	0.01	0.01	0.04	0.03	0.01	0.01	0.05
Dy	0.34	0.03	0.04	0.33	0.44	0.04	0.09	0.54	0.16	0.02	0.02	0.20	0.49	0.05	0.06	0.53	0.18	0.04	0.05	0.26	0.21	0.05	0.06	0.33
Ho	0.08	0.01	0.01	0.08	0.10	0.01	0.02	0.11	0.04	<0.01	<0.01	0.05	0.10	0.01	0.01	0.10	0.04	0.01	0.01	0.05	0.04	0.01	0.01	0.06
Er	0.29	0.02	0.04	0.27	0.33	0.02	0.08	0.37	0.13	0.01	0.02	0.15	0.32	0.03	0.03	0.33	0.14	0.02	0.04	0.18	0.15	0.02	0.05	0.20
Tm	0.04	<0.01	0.01	0.04	0.04	<0.01	0.01	0.06	0.02	<0.01	<0.01	0.02	0.05	<0.01	<0.01	0.05	0.02	<0.01	0.01	0.03	0.02	<0.01	0.01	0.03
Yb	0.28	0.01	0.05	0.26	0.28	0.02	0.09	0.34	0.13	0.01	0.02	0.15	0.30	0.02	0.03	0.30	0.14	0.01	0.04	0.18	0.15	0.01	0.04	0.19
Lu	0.04	<0.01	0.01	0.04	0.04	<0.01	0.01	0.05	0.02	<0.01	<0.01	0.02	0.05	<0.01	<0.01	0.05	0.02	<0.01	0.01	0.03	0.02	<0.01	0.01	0.03
Hf	<0.01	0.02	0.07	0.09	<0.01	0.04	0.22	0.26	<0.01	0.01	0.01	0.01	<0.01	0.01	0.08	0.10	<0.01	0.02	0.12	0.16	<0.01	0.03	0.14	0.17
Pb	1.08	0.00	0.13	0.42	0.49	1.25	0.18	0.46	0.63	0.05	0.26	0.83	0.91	0.26	0.18	1.14	0.67	0.14	0.22	0.89	0.57	0.06	0.27	0.90
Th	0.10	0.08	0.14	0.20	0.12	0.16	0.63	0.43	<0.01	<0.01	0.03	0.02	0.12	0.25	0.45	0.42	0.12	0.29	0.54	0.46	0.13	0.56	0.53	0.59
U	0.01	0.01	0.03	0.03	0.03	0.03	0.05	0.10	0.01	<0.01	0.01	0.02	0.04	0.02	0.07	0.13	0.03	0.01	0.06	0.09	0.06	0.03	0.11	0.19

Fractions: A= Acetate, B= Oxalate, C: HF, D= Bulk-rock

wt% ppm neg. < d.l. < BEC err. >l.r. n.m.

	ARP538				ARP542				ARP547				ARP560				ARP571				ARP578			
Frac:	A	B	C	D	A	B	C	D	A	B	C	D	A	B	C	D	A	B	C	D	A	B	C	D
Ca	3.34	0.02	0.08	3.71	5.65	0.01	0.50	6.26	0.58	0.01	0.08	0.74	0.26	0.01	0.34	0.38	0.59	0.01	0.08	0.79	4.09	0.01	0.02	4.45
Fe	6.80	4.11	13.48	22.98	17.06	3.20	2.05	22.55	4.89	1.18	9.37	15.47	7.08	9.97	14.56	30.26	1.22	0.88	15.57	16.55	6.77	3.34	4.94	15.62
Mg	1.53	0.27	1.56	3.59	2.05	0.21	0.17	2.73	0.78	0.15	1.32	2.33	0.63	0.63	1.01	2.39	0.26	0.13	1.93	2.45	1.25	0.10	0.34	1.90
Mn	0.33	0.03	0.04	0.43	1.09	0.11	0.03	1.34	0.69	0.07	0.16	1.14	0.18	0.03	0.07	0.33	0.06	0.01	0.11	0.22	0.12	0.01	0.01	0.15
Si	0.40	0.17		15.98	0.10	0.01		12.09	0.30	0.10		22.34	0.93	0.45		19.72	0.49	0.14		24.26	0.25	0.06		25.36
K	0.74	0.22	0.13	1.00	0.11	0.03	0.02	0.10	0.68	0.21	3.61	4.50	0.04	0.03	0.17	0.21	0.98	0.27	3.29	4.43	0.10	0.01	0.35	0.43
Na				0.26				0.04				0.20				<0.01				0.42				0.09
S				0.12				0.11				0.12				0.07				0.21				0.35
C				3.62				8.29				2.04				1.70				0.45				3.66
Al	0.09	0.19	1.21	1.59	0.01	0.01	0.31	0.09	0.07	0.12	3.58	3.82	0.01	0.06	0.21	0.13	0.10	0.16	3.45	3.92	0.01	0.02	0.15	0.15
Ti	2.38	46.51	842.23	806.62	1.55	8.24	58.06	80.42	3.27	83.30	2059.55	2213.36	1.55	55.18	61.49	113.48	7.80	127.83	2432.94	2538.01	1.85	19.92	139.24	137.65
Be	0.44	0.11	0.31	0.80	0.25	0.01	0.04	0.25	0.32	0.05	0.65	1.01	0.34	0.14	0.13	0.59	0.22	0.04	0.77	0.96	0.06	0.02	0.12	0.17
Sc	2.31	0.42	1.60	3.31	0.55	0.01	0.13	0.40	3.45	0.54	4.16	7.66	1.27	0.47	0.21	0.58	1.21	0.31	6.55	7.45	0.40	0.06	0.58	0.61
V	2.51	6.83	17.36	27.32	1.00	1.02	8.54	4.73	4.12	4.33	46.43	59.82	1.08	2.59	0.66	5.84	3.45	4.07	47.76	56.04	2.56	3.12	3.07	10.16
Cr	1.01	11.08	20.52	34.45	4.08	0.70	3.99	6.53	3.17	5.87	63.39	73.83	0.01	0.75	2.47	8.60	5.52	7.72	68.46	84.82	9.17	5.46	5.01	20.17
Co	0.77	0.37	3.56	4.63	0.39	0.02	1.50	1.48	2.37	0.58	6.71	11.05	0.22	0.27	0.59	1.11	1.70	0.67	8.84	12.45	0.81	0.12	1.72	2.14
Ni	2.01	2.52	10.62	14.99	1.62	0.19	1.64	3.24	3.35	2.77	22.73	34.61	0.77	1.69	1.87	4.82	2.91	2.66	23.60	33.23	3.28	0.81	6.59	10.12
Cu	3.64	0.98	6.22	8.35	5.14	0.22	1.55	2.20	4.69	0.69	14.69	28.55	1.74	1.70	2.91	2.68	9.57	1.25	15.11	44.07	3.45	1.87	5.49	7.97
Zn	4.77	1.90	11.63	11.41	2.97	<0.01	2.04	1.32	5.15	1.38	20.80	22.91	2.49	1.99	5.19	5.89	6.89	2.40		16.53	1.52	0.57	2.57	0.96
Rb	34.52	21.96	15.93	67.83	4.73	0.57	0.66	5.51	32.97	24.18	104.72	169.72	2.31	3.07	21.18	25.72	51.91	31.65	99.48	192.32	5.60	7.47	43.16	51.77
Sr	14.97		16.19	15.61	33.02		30.67	30.69	13.81		28.54	30.32	6.16		20.98	10.08	22.53		25.72	36.45	83.28		4.08	78.42
Y	3.88	1.60	3.91	8.31	5.76	1.41	1.46	7.39	2.14	1.53	8.04	12.47	1.27	1.11	0.96	3.02	1.76	1.19	5.51	8.65	1.38	0.24	0.26	1.77
Zr	0.14	2.44	24.58	24.65	0.06	0.59	2.85	2.76	0.24	2.91	67.88	72.09	<0.01	0.92	3.45	3.85	0.25	5.53	110.48	117.36	0.03	0.53	4.22	4.30
Mo	0.09	0.16	0.23	0.47	0.35	0.20	0.12	0.23	0.23	0.26	0.48	1.13	0.06	0.18	0.12	0.33	0.11	0.47	0.42	1.18	0.45	0.35	0.28	1.01
Cs	8.42	5.43	2.28	15.55	1.09	0.08	0.07	1.14	6.69	3.94	4.46	16.59	0.66	0.68	1.28	2.72	8.88	6.59	5.69	22.50	0.69	0.68	2.72	4.01
Ba	21.70	1.80	23.10	43.34	7.14	0.23	9.81	10.88	36.59	2.19	281.92	356.45	3.87	0.77	4.32	5.92	58.45	4.37	235.72	371.80	7.43	<0.01	3.50	10.55
La	1.79	0.97	6.80	9.42	1.59	0.20	0.98	2.14	0.89	1.69	12.71	17.23	0.34	0.25	0.85	1.23	1.28	1.87	12.49	20.20	0.66	0.14	0.28	1.14
Ce	3.53	2.31	14.39	17.46	2.68	0.45	2.03	3.46	1.86	3.70	26.80	31.06	0.55	0.55	1.75	2.04	2.68	3.92	25.35	35.31	1.19	0.36	0.56	1.97
Pr	0.45	0.27	1.56	2.18	0.32	0.05	0.23	0.47	0.24	0.41	2.90	3.86	0.07	0.06	0.20	0.27	0.34	0.47	2.97	4.48	0.14	0.04	0.06	0.26
Nd	1.77	1.02	5.35	7.98	1.28	0.22	0.93	1.95	0.94	1.46	10.05	13.89	0.24	0.24	0.77	1.09	1.30	1.69	10.21	16.00	0.50	0.17	0.21	0.95
Sm	0.49	0.23	0.90	1.57	0.29	0.05	0.20	0.44	0.25	0.33	1.88	2.66	0.06	0.05	0.15	0.22	0.32	0.37	1.80	2.97	0.11	0.03	0.04	0.19
Eu	0.10	0.05	0.16	0.34	0.11	0.02	0.04	0.17	0.05	0.06	0.37	0.59	0.01	0.01	0.03	0.06	0.07	0.06	0.32	0.59	0.03	0.01	0.01	0.05
Gd	0.57	0.27	0.80	1.52	0.42	0.08	0.21	0.56	0.31	0.36	1.64	2.44	0.08	0.08	0.16	0.28	0.36	0.38	1.47	2.46	0.12	0.04	0.04	0.20
Tb	0.09	0.04	0.10	0.23	0.07	0.01	0.03	0.10	0.06	0.05	0.23	0.35	0.01	0.01	0.02	0.04	0.06	0.05	0.19	0.33	0.02	0.01	<0.01	0.03
Dy	0.61	0.25	0.64	1.39	0.54	0.12	0.18	0.72	0.37	0.30	1.40	2.10	0.11	0.10	0.12	0.31	0.36	0.28	1.13	1.83	0.16	0.04	0.03	0.23
Ho	0.12	0.04	0.12	0.25	0.13	0.03	0.04	0.15	0.08	0.05	0.27	0.37	0.03	0.02	0.02	0.07	0.07	0.05	0.22	0.31	0.04	0.01	0.01	0.05
Er	0.39	0.12	0.40	0.78	0.47	0.08	0.11	0.52	0.24	0.12	0.86	1.15	0.11	0.08	0.07	0.22	0.20	0.11	0.71	0.95	0.13	0.02	0.02	0.16
Tm	0.06	0.01	0.05	0.12	0.07	0.01	0.01	0.08	0.04	0.01	0.12	0.18	0.02	0.01	0.01	0.03	0.03	0.01	0.11	0.15	0.02	<0.01	<0.01	0.03
Yb	0.38	0.07	0.36	0.71	0.47	0.06	0.10	0.50	0.30	0.08	0.81	1.12	0.12	0.06	0.06	0.20	0.22	0.07	0.80	1.01	0.12	0.01	0.03	0.16
Lu	0.06	0.01	0.05	0.11	0.07	0.01	0.01	0.08	0.05	0.01	0.12	0.17	0.02	0.01	0.01	0.03	0.03	0.01	0.12	0.16	0.02	<0.01	<0.01	0.02
Hf	<0.01	0.08	0.71	0.71	<0.01	0.01	0.07	0.08	<0.01	0.10	1.94	2.00	<0.01	0.02	0.08	0.09	<0.01	0.18	3.16	3.28	<0.01	0.02	0.10	0.12
Pb	1.26	0.08	0.81	1.65	0.63		0.80	0.77	1.35	0.12	2.57	3.74	0.42	0.02	0.36	0.58	1.77	0.18	2.70	4.11	0.69	0.09	0.53	1.13
Th	0.67	2.04	4.90	3.25	0.13	0.19	0.66	0.31	0.58	2.68	12.99	7.18	0.06	0.23	0.41	0.24	1.69	1.58	6.92	11.00	0.07	0.18	0.38	0.31
U	0.16	0.14	0.58	0.74	0.02	0.01	0.11	0.06	0.20	0.07	1.68	1.78	0.01	0.02	0.06	0.05	0.24	0.10	2.17	2.31	0.01	0.01	0.06	0.08

Fractions: A= Acetate, B= Oxalate, C: HF, D= Bulk-rock

wt% | ppm | neg. | < d.l. | < BEC | err. | >l.r. | n.m.

	ARP586				ARP596				ARP605				ARP614				ARP619				ARP629			
Frac:	A	B	C	D	A	B	C	D	A	B	C	D	A	B	C	D	A	B	C	D	A	B	C	D
Ca	2.35	0.01	0.06	2.55	0.89	0.01	0.04	1.04	2.77	0.01	0.02	2.94	3.29	<0.01	0.17	3.71	1.41	0.01	0.03	1.52	1.98	0.01		2.12
Fe	9.85	2.68	6.85	19.52	9.46	7.71	11.61	28.76	7.97	8.33	6.05	21.95	3.67	11.92	12.40	27.36	2.38	0.21	6.96	9.63	11.25	11.12	3.02	25.50
Mg	1.26	0.20	0.56	2.24	1.17	0.37	1.32	3.20	1.23	0.16	0.31	1.86	0.70	0.08	0.51	1.45	0.32	0.01	0.44	0.85	1.27	0.18	0.24	1.82
Mn	0.57	0.06	0.02	0.72	0.65	0.08	0.06	0.95	0.42	0.03	0.01	0.52	0.21	0.01	0.01	0.24	0.13	<0.01	0.01	0.16	0.48	0.03	0.02	0.68
Si	0.39	0.14		22.63	0.48	0.38		16.87	0.28	0.12		22.63	0.26	0.18		20.36	0.53	0.02		36.36	0.69	0.14		19.98
K	0.12	0.08	0.39	0.57	0.16	0.34	0.84	1.31	0.13	0.03	0.31	0.44	0.17	0.03	0.14	0.32	0.04		0.03	0.04	0.17	0.01	0.18	0.38
Na				0.44				0.01				0.02				0.71				1.25				0.03
S				0.14				0.08				0.09				0.12				0.09				0.10
C				4.05				3.63				3.45				2.25				0.84				3.79
Al	0.01	0.03	0.13	0.14	0.01	0.08	0.22	0.38	0.01	0.03	0.10	0.12	0.01	0.05	0.13	0.16	<0.01	<0.01	0.01		0.04	0.09	0.15	0.23
Ti	1.98	27.48	94.61	113.17	2.38	71.54	183.96	242.82	1.86	38.36	105.17	136.55	2.09	48.15	124.46	157.98	0.55	3.82	30.16	34.22	4.46	71.13	190.45	246.25
Be	0.11	0.04	0.17	0.29	0.17	0.09	0.25	0.45	0.07	0.03	0.10	0.18	0.13	0.12	0.33	0.54	0.03	<0.01	0.07	0.10	0.24	0.09	0.15	0.53
Sc	0.54	0.12	0.54	0.52	0.74	0.34	0.50	0.88	0.48	0.15	0.24	0.47	0.41	0.11	0.49	0.56	0.55	0.03	0.18	0.19	1.18	0.28	0.21	1.17
V	1.65	1.05	6.97	9.80	0.59	3.95	0.24	7.28	1.83	3.39	0.84	7.55	1.26	2.51	3.78	8.97	5.62	1.03	4.66	11.24	1.89	4.99	1.74	10.12
Cr	5.60	5.32	4.92	15.79		10.38	3.23	15.72	6.84	6.30	3.66	16.29	4.76	5.31	4.71	15.70	25.63	2.08	2.25	30.33	5.17	11.77	2.74	23.27
Co	0.40	0.13	1.01	1.38	0.36	0.24	1.24	1.81	0.67	0.18	0.55	1.34	0.45	0.09	0.73	1.20	1.30	0.03	0.35	1.56	0.72	0.37	0.43	1.63
Ni	1.94	1.11	2.71	5.81	0.63	2.16	3.30	5.71	2.37	1.12	2.29	5.82	1.68	1.06	2.62	5.75	6.84	0.09	1.05	8.29	2.63	2.38	1.93	8.01
Cu	3.04	1.24	4.27	5.53	3.77	1.33	4.42	4.74	4.13	0.47	3.25	5.53	1.87	0.04	2.22	4.47	10.12	0.62	1.66	10.51	3.59	1.72	1.91	6.71
Zn	2.01	0.92	2.16	1.04	2.09	0.81	4.99	3.82	1.63	0.56	1.11		3.65	1.62	2.24	0.70	1.74	0.33	1.94		3.23	1.08	1.94	2.31
Rb	8.56	20.89	56.20	80.32	12.62	62.43	114.98	189.58	7.28	9.31	32.00	47.25	10.20	11.11	16.89	36.86	1.10	0.17	2.36	3.33	16.48	8.19	29.70	58.76
Sr	101.49		15.83	100.72	16.53		13.08	17.98	28.52		9.02	28.00	51.24		28.64	50.10	20.99		0.68	22.83	32.94		2.27	37.05
Y	1.44	0.69	0.64	2.59	1.13	0.77	0.86	2.61	0.91	0.31	0.20	1.37	1.65	0.93	0.81	3.25	0.63	0.05	0.11	0.85	1.18	0.16	0.16	1.61
Zr	0.02	0.99	2.97	3.74	0.03	2.23	4.95	7.07	0.01	0.58	3.42	3.55		1.25	3.60	5.66	<0.01	0.10	0.95	1.14	0.06	2.12	6.10	7.38
Mo	0.33	0.33	0.20	0.72	0.28	0.24	0.07	0.28	0.24	0.33	0.19	0.65	0.20	0.38	0.23	0.76	1.41	0.26	0.16	1.85	0.25	0.44	0.07	0.71
Cs	0.74	1.70	3.32	5.71	0.78	4.33	6.03	11.39	0.86	0.97	2.13	4.04	1.70	1.49	1.35	4.50	0.11	0.02	0.15	0.29	2.73	1.64	2.65	7.91
Ba	7.80	0.27	2.38	11.22	6.84	1.65	2.18	10.67	6.54	0.36	2.00	9.63	8.43	2.99	4.35	14.38	2.69		0.91	4.10	11.09	0.35	2.75	15.91
La	0.68	0.25	0.48	1.42	0.44	0.31	0.56	1.42	0.40	0.11	0.16	0.70	0.52	0.22	0.64	1.41	0.14	0.01	0.02	0.23	0.56	0.07	0.12	0.87
Ce	1.08	0.54	0.96	2.29	0.78	0.75	1.28	2.59	0.65	0.27	0.31	1.15	0.86	0.48	1.23	2.38	0.23	0.05	0.03	0.40	1.11	0.23	0.25	1.62
Pr	0.12	0.07	0.11	0.30	0.10	0.09	0.15	0.35	0.07	0.03	0.04	0.16	0.10	0.06	0.16	0.34	0.03	0.01	<0.01	0.06	0.14	0.03	0.02	0.22
Nd	0.43	0.24	0.43	1.14	0.33	0.33	0.59	1.34	0.27	0.13	0.14	0.58	0.37	0.24	0.65	1.37	0.10	0.03	0.02	0.21	0.53	0.12	0.08	0.85
Sm	0.09	0.05	0.08	0.23	0.07	0.07	0.12	0.28	0.05	0.03	0.03	0.12	0.08	0.06	0.12	0.27	0.02	0.01	<0.01	0.05	0.12	0.02	0.01	0.19
Eu	0.02	0.01	0.01	0.05	0.02	0.02	0.02	0.07	0.02	0.01	0.01	0.04	0.02	0.02	0.03	0.09	0.01	<0.01	<0.01	0.02	0.03	0.01	<0.01	0.05
Gd	0.10	0.07	0.08	0.25	0.09	0.09	0.12	0.30	0.06	0.03	0.03	0.13	0.10	0.08	0.12	0.30	0.03	0.01	<0.01	0.05	0.13	0.03	0.01	0.20
Tb	0.02	0.01	0.01	0.04	0.02	0.01	0.02	0.05	0.01	0.01	<0.01	0.02	0.02	0.01	0.01	0.05	0.01	<0.01	<0.01	0.01	0.02	<0.01	<0.01	0.03
Dy	0.13	0.08	0.06	0.27	0.12	0.10	0.10	0.31	0.08	0.03	0.02	0.14	0.12	0.09	0.08	0.31	0.05	0.01	0.01	0.07	0.14	0.02	0.02	0.20
Ho	0.03	0.01	0.01	0.06	0.03	0.02	0.02	0.06	0.02	0.01	<0.01	0.03	0.03	0.02	0.02	0.06	0.01	<0.01	<0.01	0.02	0.03	<0.01	<0.01	0.04
Er	0.11	0.04	0.04	0.18	0.10	0.06	0.07	0.21	0.07	0.02	0.01	0.09	0.11	0.06	0.05	0.21	0.05	<0.01	0.01	0.07	0.11	0.01	0.02	0.13
Tm	0.02	<0.01	0.01	0.03	0.02	0.01	0.01	0.03	0.01	<0.01	<0.01	0.01	0.02	0.01	0.01	0.03	0.01	<0.01	<0.01	0.01	0.02	<0.01	<0.01	0.02
Yb	0.11	0.02	0.06	0.18	0.11	0.04	0.08	0.22	0.07	0.01	0.02	0.10	0.12	0.03	0.04	0.18	0.05	<0.01	0.03	0.09	0.12	0.01	0.02	0.15
Lu	0.02	<0.01	0.01	0.03	0.02	0.01	0.01	0.04	0.01	<0.01	<0.01	0.02	0.02	<0.01	0.01	0.03	0.01	<0.01	0.01	0.02	0.02	<0.01	<0.01	0.03
Hf	<0.01	0.03	0.07	0.10	<0.01	0.06	0.14	0.20	<0.01	0.02	0.08	0.10	<0.01	0.04	0.08	0.13	<0.01	<0.01	0.02	0.03	<0.01	0.06	0.14	0.19
Pb	0.63	0.08	0.28	0.99	0.78	0.20	0.28	1.17	0.29	0.12	0.08	0.39	0.65	0.14	0.18	0.94	0.31		0.05	0.43	0.49	0.05	0.08	0.86
Th	0.07	0.32	0.30	0.35	0.08	0.48	0.58	0.52	0.05	0.14	0.20	0.20	0.06	0.15	0.08	0.29	0.03	0.01	0.02	0.05	0.11	0.16	0.35	0.35
U	0.03	0.02	0.08	0.14	0.02	0.02	0.08	0.10	0.01	0.01	0.03	0.04	0.01	0.02	0.03	0.05	<0.01	<0.01	<0.01	0.01	0.03	0.01	0.04	0.08

Fractions: A= Acetate, B= Oxalate, C: HF, D= Bulk-rock

wt% | ppm | neg. | < d.l. | < BEC | err. | >l.r. | n.m.

	ARP635				ARP649				ARP656				ARP661				ARP666				ARP670			
Frac:	A	B	C	D	A	B	C	D	A	B	C	D	A	B	C	D	A	B	C	D	A	B	C	D
Ca	3.52	<0.01	0.13	4.06	0.93	0.01	0.03	1.15	1.38	0.01	0.08	1.60	1.45	0.01	0.03	1.64	10.80	0.01	0.03	11.13	1.48	<0.01	0.05	1.71
Fe	3.88	14.96	8.15	26.67	10.47	14.98	1.26	27.74	1.64	25.46	3.86	30.75	8.38	15.93	3.71	28.48	3.81	1.25	1.40	7.08	9.85	13.47	5.56	29.41
Mg	0.74	0.06	0.31	1.26	1.05	0.20	0.09	1.58	0.33	0.02	0.07	0.46	0.92	0.13	0.10	1.30	0.27	0.03	0.03	0.38	1.20	0.16	0.17	1.76
Mn	0.33	0.01	0.01	0.42	0.39	0.05	<0.01	0.56	0.11	<0.01	0.01	0.18	0.35	0.03	0.01	0.33	0.28	0.02	<0.01	0.21	0.14	0.01	0.01	0.14
Si	0.24	0.17		20.58	0.34	0.18		20.53	0.13	0.19		23.75	0.24	0.15		20.97	0.08	0.01		26.64	0.31	0.15		19.57
K	0.11		0.09	0.19	0.06		0.04	0.10	0.06		0.01	0.04	0.04		0.07	0.09	0.03		<0.01	<0.01	0.04	0.00	<0.01	0.02
Na				0.44				0.03				0.02				<0.01				0.06				
S				0.06				0.10				0.09				0.08				0.19				0.07
C				2.37				3.61				0.88				3.10				4.66				3.57
Al	0.02	0.04	0.10	0.13	0.04	0.04	0.04	0.11	0.01	0.01	0.03	0.01	0.01	0.01	0.03		<0.01	<0.01	0.02		0.01	0.01	0.01	0.06
Ti	1.39	37.75	103.17	136.65	0.91	23.03	16.71	126.53	1.79	14.61	41.85	40.07	1.77	22.80	20.10	42.00	0.13	5.18	1.48	22.37	0.38	8.08	5.33	23.50
Be	0.14	0.07	0.16	0.35	0.40	0.08	0.05	0.58	0.07	0.22	0.06	0.43	0.14	0.06	0.08	0.26	0.28	0.34	0.35	0.73	0.21	0.07	0.06	0.32
Sc	0.36	0.15	0.38	0.59	0.66	0.05	0.12	0.55	0.01	0.17	0.05	0.32	0.35	0.15	0.07	0.23	0.17	0.04	0.04	0.20	0.48	0.07	0.04	0.39
V	1.42	3.08	2.99	8.68	1.59	3.73		8.05	2.05	2.40		8.09	1.62	1.85		4.55	2.18	1.37	4.67	4.10	1.42	1.81		4.66
Cr	5.38	5.33	3.91	17.04	5.79	7.57	0.35	18.72	8.22	2.29	0.51	17.89	6.78	5.24	1.05	10.99	9.91	1.61	0.77	11.13	7.26	0.47	0.38	10.58
Co	0.52	0.26	0.63	1.38	0.52	0.25	0.10	1.00	0.45	0.08	0.09	0.80	0.54	0.14	0.17	0.73	0.68	0.07	0.04	0.49	0.39	0.14	0.09	0.58
Ni	2.15	1.46	2.02	6.05	2.30	1.49	0.47	5.27	2.46	0.56	0.53	5.18	2.14	0.61	0.53	3.03	3.33	0.34	1.04	3.83	2.16	0.58	0.46	3.65
Cu	3.60	2.19	2.62	4.94	4.50	2.63	1.84	7.50	3.82	1.40	2.32	5.90	4.22	1.01	1.85	4.08	3.48	0.44	0.34	3.49	2.85	2.04	0.85	3.53
Zn	5.93	1.56	1.85	4.85	4.11	1.16	1.02	2.39	0.92	0.13	1.89		1.87	0.43	0.64	2.20	3.45	1.05	<0.01	1.31	8.47	3.78	0.98	11.20
Rb	6.31	3.85	11.94	22.25	2.61	1.89	5.37	11.85	2.15	0.33	1.25	4.66	1.40	0.97	6.48	7.62	0.04	0.01	0.18	0.33	0.72	0.20	0.40	1.17
Sr	58.62		36.71	66.04	14.08		12.96	16.26	18.07		19.79	25.35	16.90		7.96	15.53				99.12	19.94		17.27	19.29
Y	1.15	0.79	0.64	2.51	1.41	0.41	0.05	2.11	1.49	1.91	1.19	5.27	1.00	0.41	0.17	1.38	4.17	0.24	0.20	3.32	3.00	1.32	0.67	4.52
Zr	0.11	1.48	2.53	3.99	0.35	1.88	0.13	3.51	0.05	0.72	3.78	2.06	0.05	0.43	0.84	1.52	<0.01	0.24	0.37	1.65	0.23	1.64	0.33	2.48
Mo	0.10	0.30	0.12	0.66	0.19	0.50	0.09	0.84	0.27	0.28	0.31	1.03	0.20	0.57	0.09	0.59	0.11	0.72	0.11	0.80	0.06	0.35	0.06	0.65
Cs	1.23	0.68	0.99	3.11	0.43	0.22	0.40	1.33	0.38	0.08	0.14	0.80	0.28	0.16	0.80	1.14	0.01	<0.01	0.01	0.05	0.11	0.03	0.06	0.23
Ba	21.48	4.28	12.30	38.31	10.00	1.65	0.59	15.53	6.84	1.35	5.11	14.74	4.61	0.40	2.00	6.84	20.32	0.96	2.05	17.06	4.23	0.06	1.67	6.71
La	0.35	0.18	0.66	1.20	0.39	0.13	0.10	0.75	0.23	0.19	0.55	1.34	0.28	0.09	0.11	0.47	1.59	0.02	0.06	1.40	0.60	0.21	0.45	1.28
Ce	0.58	0.42	1.25	1.99	0.66	0.32	0.20	1.27	0.40	0.45	1.01	2.17	0.45	0.21	0.20	0.81	2.36	0.04	0.09	2.21	0.96	0.43	0.73	2.05
Pr	0.07	0.05	0.15	0.27	0.08	0.04	0.02	0.17	0.06	0.06	0.12	0.31	0.06	0.03	0.02	0.10	0.27	0.01	0.01	0.26	0.12	0.05	0.09	0.26
Nd	0.28	0.19	0.60	1.09	0.33	0.16	0.11	0.73	0.24	0.28	0.55	1.41	0.22	0.11	0.10	0.41	1.05	0.02	0.06	1.04	0.49	0.24	0.38	1.12
Sm	0.06	0.04	0.11	0.23	0.09	0.03	0.02	0.17	0.06	0.07	0.11	0.32	0.05	0.03	0.02	0.10	0.23	0.01	0.02	0.22	0.12	0.05	0.07	0.23
Eu	0.02	0.01	0.03	0.08	0.03	0.01	<0.01	0.06	0.02	0.02	0.03	0.09	0.02	0.01	<0.01	0.03	0.08	<0.01	0.01	0.08	0.03	0.02	0.02	0.07
Gd	0.08	0.06	0.11	0.26	0.13	0.05	0.02	0.21	0.09	0.14	0.14	0.44	0.08	0.04	0.02	0.13	0.35	0.02	0.02	0.37	0.18	0.09	0.08	0.35
Tb	0.01	0.01	0.01	0.04	0.02	0.01	<0.01	0.04	0.02	0.02	0.02	0.07	0.01	0.01	<0.01	0.02	0.06	<0.01	<0.01	0.05	0.03	0.02	0.01	0.06
Dy	0.11	0.08	0.07	0.26	0.17	0.05	0.01	0.25	0.14	0.18	0.11	0.49	0.10	0.04	0.02	0.15	0.43	0.03	0.03	0.38	0.26	0.12	0.06	0.43
Ho	0.03	0.02	0.01	0.05	0.04	0.01	<0.01	0.05	0.03	0.04	0.02	0.11	0.02	0.01	<0.01	0.03	0.10	0.01	<0.01	0.08	0.07	0.03	0.01	0.10
Er	0.09	0.05	0.04	0.17	0.12	0.03	<0.01	0.16	0.13	0.12	0.08	0.34	0.08	0.02	0.01	0.10	0.34	0.02	0.02	0.28	0.25	0.10	0.05	0.35
Tm	0.01	<0.01	<0.01	0.03	0.02	<0.01		0.03	0.02	0.01	0.01	0.05	0.01	<0.01	<0.01	0.01	0.05	<0.01	<0.01	0.04	0.04	0.01	0.01	0.06
Yb	0.11	0.03	0.04	0.15	0.14	0.02	<0.01	0.17	0.14	0.08	0.06	0.29	0.08	0.02	0.01	0.10	0.34	0.03	0.02	0.30	0.31	0.08	0.04	0.40
Lu	0.02	<0.01	0.01	0.03	0.02	<0.01	<0.01	0.03	0.02	0.01	0.01	0.05	0.01	<0.01	<0.01	0.02	0.06	<0.01	<0.01	0.05	0.05	0.01	0.01	0.07
Hf	<0.01	0.04	0.06	0.10	<0.01	0.06	<0.01	0.09	<0.01	0.01	0.07	0.03	<0.01	0.01	0.02	0.06	<0.01	<0.01	<0.01	0.05	<0.01	0.02	<0.01	0.03
Pb	0.19		0.23	0.48	1.03	0.57	0.08	1.81	0.07		0.15	0.27	0.36	0.04	0.04	0.57	0.54	0.02	0.03	0.58	0.23	0.08	0.10	0.57
Th	0.05	0.14	0.14	0.17	0.09	0.09	0.01	0.16	0.02	0.06	0.09	0.09	0.02	0.04	0.06	0.06	0.01	0.02		0.08	0.05	0.05	0.02	0.08
U	0.04	0.02	0.02	0.08	0.02	<0.01	<0.01	0.03	0.02	<0.01	0.01	0.03	0.01	<0.01	0.01	0.02	0.01	0.01	0.01	0.03	0.02	<0.01	<0.01	0.02

Fractions: A= Acetate, B= Oxalate, C: HF, D= Bulk-rock

wt% | ppm | neg. | < d.l. | < BEC | err. | >l.r. | n.m.

	ERI373				ERI377				ERI387				ERI395				ERI405				ERI415			
Frac:	A	B	C	D	A	B	C	D	A	B	C	D	A	B	C	D	A	B	C	D	A	B	C	D
Ca	3.24	0.01	0.09	3.50	3.46	0.01	0.02	3.82	3.89	0.01	0.02	4.13	2.86	0.01	0.02	3.13	2.11	0.01	0.02	2.26	0.89	0.01	0.09	1.06
Fe	14.59	5.33	5.88	25.14	7.70	20.38	7.84	35.30	5.10	10.77	9.26	24.57	3.43	7.69	3.73	14.92	8.82	1.23	1.51	12.13	7.56	5.33	15.91	27.88
Mg	0.96	0.26	0.36	1.70	1.05	0.05	0.12	1.37	1.06	0.05	0.33	1.56	0.74	0.04	0.17	1.05	1.25	0.05	0.11	1.57	1.04	0.22	1.08	2.36
Mn	1.11	0.15	0.04	1.26	0.80	0.02	0.02	0.79	0.59	0.01	0.03	0.48	0.41	0.01	0.02	0.33	0.41	0.01	0.01	0.32	0.36	0.06	0.05	0.36
Si	0.50	0.13		15.45	0.23	0.18		13.35	0.22	0.09		20.63	0.16	0.06		30.20	0.17	0.01		30.32	0.26	0.04		17.99
K	0.28	0.05	0.03	0.29	0.06	0.01	<0.01	0.05	0.19		0.01	0.20	0.08		<0.01	0.07	0.07		0.02	0.06	0.47	0.12	0.07	0.63
Na				0.08				0.02				0.08				0.05				0.02				0.18
S				0.13				0.11				0.07				0.04				0.12				0.17
C				5.74				3.70				3.12				2.08				3.62				3.26
Al	0.09	0.19	0.39	0.69	0.01	0.02	0.05	0.03	0.02	0.02	0.24	0.27	0.01	0.02	0.11	0.10	0.01	0.01	0.09	0.06	0.03	0.05	0.74	0.86
Ti	3.01	63.82	376.76	464.74	1.07	20.15	26.59	64.44	0.35	13.00	121.22	123.73	0.60	12.04	87.17	84.78	0.42	6.86	67.99	56.51	0.95	112.84	1172.17	697.41
Be	0.72	0.17	0.14	1.09	0.39	0.21	0.07	0.65	0.13	0.05	0.07	0.24	0.08	0.04	0.07	0.15	0.16	0.01	0.06	0.18	0.29	0.09	0.24	0.51
Sc	1.37	0.57	0.43	1.92	0.52	0.28	0.07	0.65	0.79	0.15	0.38	0.97	0.42	0.08	0.16	0.50	0.40	0.06	0.05	0.28	1.74	0.20	1.01	2.16
V	3.80	7.59	7.37	18.12	1.10	2.43		5.06	1.85	2.93	4.11	7.99	3.10	3.73	2.51	7.98	3.84	1.31	1.86	6.52	1.38	6.40	19.42	23.44
Cr	7.77	11.92	11.97	26.03	3.20	3.74	0.57	9.61	7.15	1.82	3.64	11.13	13.26	2.08	3.30	15.50	16.85	1.89	1.98	16.70	<0.01	4.95	14.67	18.71
Co	0.98	0.27	1.90	3.18	0.38	0.16	0.31	0.82	0.48	0.11	0.75	1.14	0.66	0.01	1.02	1.33	0.92	0.03	0.42	1.11	0.27	0.09	4.55	4.20
Ni	2.19	2.50	6.28	9.27	1.37	1.00	1.03	4.10	2.49	0.74	2.80	5.27	3.86	0.65	1.94	5.67	5.08	0.21	0.48	4.93	1.45	0.87	7.02	8.26
Cu	6.27	1.09	5.07	9.38	1.33	0.19	1.04	3.67	5.14	2.24	3.06	3.88	6.67	0.62	2.89	6.10	7.34	0.88	1.20	6.39	2.05	1.23	10.58	13.00
Zn	4.93	1.96	5.95	11.10	5.19	1.45	2.58	4.37	1.82	0.90	3.24	4.12	1.53	1.27	1.78	2.94	2.03	0.31	0.79	2.09	3.00	0.48	9.57	9.51
Rb	21.71	5.14	3.90	32.77	3.42	0.21	0.08	4.10	10.55	1.40	1.52	11.89	3.52	0.31	0.49	3.57	2.34	0.15	1.19	2.63	20.86	9.82	8.46	33.45
Sr	12.61		28.72	14.01	14.77		8.21	15.48	12.94		7.95	11.54	10.56		4.72	9.04	8.45		4.72	7.15	16.32		13.60	15.55
Y	3.47	0.85	1.77	6.22	2.71	0.31	0.21	3.54	2.78	0.24	0.35	3.00	1.54	0.17	0.40	1.76	2.93	0.48	0.44	3.16	2.83	1.27	3.23	5.91
Zr	0.38	2.10	13.46	16.58	0.08	0.61	2.14	3.55	0.05	0.41	3.18	3.91	0.01	0.28	3.97	2.37	<0.01	0.20	2.26	2.01	0.11	1.69	20.67	17.62
Mo	0.36	0.34	0.42	0.99	0.42	0.44	0.08	0.60	0.38	0.23	0.11	0.59	0.63	0.28	0.15	0.94	0.51	0.82	0.07	1.07	0.02	0.21	0.35	0.53
Cs	3.62	0.89	0.85	5.53	0.58	0.07	0.04	0.78	2.19	0.41	0.34	2.64	0.73	0.08	0.12	0.84	0.57	0.04	0.14	0.65	5.97	2.45	1.19	8.30
Ba	14.47	1.19	22.45	37.28	2.10	1.82	2.78	5.88	3.03		5.04	7.46	1.28		2.11	2.98	1.84		3.36	2.84	17.80	1.67	19.37	31.97
La	2.99	0.47	2.81	6.89	1.06	0.13	0.22	1.60	0.82	0.11	0.21	1.06	0.53	0.11	0.64	1.25	0.45	0.12	0.50	0.98	1.12	0.63	3.62	5.02
Ce	4.57	1.05	4.87	11.04	1.70	0.24	0.31	2.59	1.64	0.31	0.43	2.16	0.98	0.24	0.95	2.02	0.89	0.27	0.79	1.69	2.28	1.36	7.22	9.55
Pr	0.51	0.12	0.47	1.21	0.21	0.03	0.03	0.31	0.21	0.04	0.05	0.29	0.12	0.03	0.09	0.23	0.12	0.03	0.08	0.21	0.31	0.16	0.80	1.17
Nd	1.87	0.42	1.54	4.34	0.80	0.13	0.12	1.26	0.85	0.16	0.20	1.18	0.48	0.11	0.29	0.89	0.51	0.14	0.29	0.89	1.25	0.61	2.90	4.51
Sm	0.39	0.09	0.23	0.79	0.17	0.03	0.02	0.25	0.19	0.03	0.04	0.26	0.10	0.02	0.04	0.16	0.13	0.03	0.04	0.19	0.32	0.15	0.55	0.95
Eu	0.13	0.02	0.05	0.25	0.06	0.01	<0.01	0.10	0.04	0.01	0.01	0.06	0.04	0.01	0.01	0.06	0.04	0.01	0.01	0.06	0.07	0.03	0.11	0.23
Gd	0.45	0.11	0.24	0.82	0.22	0.04	0.02	0.31	0.23	0.04	0.04	0.28	0.13	0.03	0.04	0.19	0.19	0.05	0.05	0.25	0.40	0.18	0.53	0.98
Tb	0.07	0.02	0.03	0.13	0.03	0.01	<0.01	0.05	0.04	0.01	<0.01	0.05	0.02	<0.01	0.01	0.03	0.03	0.01	0.01	0.04	0.06	0.03	0.07	0.15
Dy	0.45	0.12	0.21	0.84	0.24	0.03	0.02	0.34	0.26	0.03	0.03	0.31	0.14	0.02	0.04	0.20	0.24	0.05	0.04	0.31	0.42	0.20	0.47	0.94
Ho	0.10	0.02	0.05	0.17	0.05	0.01	<0.01	0.07	0.06	0.01	0.01	0.07	0.03	<0.01	0.01	0.04	0.06	0.01	0.01	0.07	0.08	0.04	0.09	0.18
Er	0.32	0.06	0.16	0.55	0.18	0.02	0.02	0.22	0.20	0.01	0.03	0.22	0.11	0.01	0.03	0.13	0.22	0.03	0.03	0.24	0.28	0.10	0.29	0.54
Tm	0.05	0.01	0.02	0.09	0.02	<0.01	<0.01	0.03	0.03	<0.01	<0.01	0.03	0.02	<0.01	<0.01	0.02	0.04	<0.01	<0.01	0.04	0.04	0.01	0.04	0.08
Yb	0.34	0.05	0.17	0.57	0.16	0.01	0.02	0.20	0.18	0.01	0.03	0.21	0.11	0.01	0.04	0.14	0.25	0.02	0.03	0.27	0.29	0.08	0.27	0.53
Lu	0.05	0.01	0.02	0.09	0.02	<0.01	<0.01	0.03	0.03	<0.01	0.01	0.03	0.02	<0.01	0.01	0.02	0.04	<0.01	<0.01	0.04	0.05	0.01	0.04	0.08
Hf	<0.01	0.06	0.35	0.45	<0.01	0.02	0.04	0.07	<0.01	0.01	0.08	0.11	<0.01	0.01	0.10	0.07	<0.01	<0.01	0.05	0.05	<0.01	0.06	0.55	0.52
Pb	0.91		0.42	1.49	0.18	0.05	0.05	0.40	0.24		0.28	0.59	0.35	0.01	0.17	0.64	0.33		0.15	0.52	0.90	0.22	1.38	2.31
Th	0.34	0.63	1.48	1.33	0.09	0.07	0.06	0.26	0.14	0.20	0.50	0.45	0.06	0.13	0.28	0.23	0.05	0.11	0.17	0.16	0.25	1.09	1.81	1.33
U	0.10	0.09	0.12	0.31	0.02	0.02	0.02	0.06	0.03	0.02	0.05	0.09	0.02	0.02	0.06	0.10	0.01	<0.01	0.03	0.04	0.06	0.09	0.23	0.33

Fractions: A= Acetate, B= Oxalate, C: HF, D= Bulk-rock

wt% | ppm | neg. | < d.l. | < BEC | err. | >l.r. | n.m.

	ERI427				ERI436				ERI450				ERI459				ERI470				ERI476			
Frac:	A	B	C	D	A	B	C	D	A	B	C	D	A	B	C	D	A	B	C	D	A	B	C	D
Ca	0.74	0.01	0.12	0.92	0.19	<0.01	0.74	0.98	1.13	0.01	0.05	1.30	3.56	0.01	0.01	3.84	0.59	0.01	0.06	0.72	1.02	0.01	0.02	1.11
Fe	2.95	1.32	12.66	16.15	9.17	7.65	11.08	26.96	19.46	5.68	1.90	27.66	8.61	0.97	0.79	10.81	5.73	2.56	7.05	15.39	6.89	0.82	1.72	9.86
Mg	0.56	0.21	1.86	2.80	0.76	0.55	0.73	2.16	1.64	0.18	0.13	2.16	1.02	0.06	0.04	1.23	0.60	0.19	0.60	1.49	0.73	0.05	0.11	1.00
Mn	0.50	0.07	0.21	0.68	0.25	0.05	0.07	0.33	0.58	0.06	0.01	0.60	0.71	0.02	0.01	0.52	0.25	0.05	0.05	0.33	0.92	0.06	0.02	0.96
Si	0.31	0.16		22.41	0.73	0.55		20.35	0.36	0.03		14.59	0.36	0.02		30.33	0.22	0.06		30.61	0.19	0.01		34.04
K	0.69	0.22	2.87	3.67	0.04		0.15	0.17	0.19	0.02	0.03	0.18	0.04		0.03	0.05	0.06	0.01	0.45	0.51	0.05		0.14	0.19
Na				0.36				<0.01				0.03				<0.01				0.01				
S				0.14				0.10				0.21				0.12				0.09				0.09
C				1.55				2.88				7.38				3.67				2.29				2.49
Al	0.12	0.20	3.50	4.03	0.01	0.06	0.07	0.10	0.02	0.03	0.11	0.16	0.01	0.01	0.02	<0.01	<0.01	0.01	0.12	0.12	<0.01	<0.01	0.04	0.07
Ti	2.45	50.81	2084.77	2120.86	1.99	52.03	38.15	89.33	0.27	15.91	79.74	94.87	1.35	8.14	15.38	27.31	1.61	22.87	54.93	85.21	1.18	3.15	22.34	37.92
Be	0.30	0.09	0.52	0.84	0.23	0.11	0.14	0.45	0.19	0.02	0.05	0.25	0.05	<0.01	0.02	0.05	0.04	0.02	0.20	0.25	0.02	<0.01	0.05	0.06
Sc	2.72	0.69	4.87	7.64	0.83	0.60	0.10	0.41	0.61	0.02	0.08	0.59	0.35		0.05	0.20	0.13	0.07	0.30	0.55	0.28		0.10	0.25
V	4.35	6.25	48.76	57.29	1.31	2.34		4.64	1.00	2.12	4.84	6.67	5.38	1.21	1.40	7.07	1.52	1.79	0.91	5.87	4.31	0.60	0.29	7.57
Cr	4.64	8.79	64.90	75.83	1.86	3.06	1.40	8.24	5.88	3.50	4.25	14.15	22.56	1.64	1.14	19.37	5.10	4.43	4.75	15.02	18.97	1.21	1.28	23.50
Co	2.36	0.65	6.57	10.06	0.32	0.39	0.53	1.14	0.63	0.21	1.38	2.14	1.25	0.07	0.10	1.11	0.39	0.18	0.76	1.38	0.96	<0.01	0.85	2.04
Ni	3.28	3.56	23.78	33.00	1.24	1.98	1.49	4.69	1.96	1.22	2.68	5.93	6.58	0.39	0.28	6.11	1.62	1.13	2.82	6.52	5.49	0.01	1.06	7.55
Cu	2.51	0.58	13.71	23.37	2.07	1.53	2.29	3.27	4.14	2.84	2.36	7.09	9.43	0.45	0.68	7.74	3.27	1.66	3.53	6.51	7.93	0.60	1.10	10.17
Zn	9.73	3.54	25.42	31.50	3.07	2.18	3.11	7.14			20.51	7.93	3.78	0.57	0.21	3.05	1.98	0.96	1.94	5.00	2.44	0.40	0.07	4.17
Rb	30.45	21.02	69.34	124.21	1.35	1.63	20.94	22.51	7.31	1.19	2.15	11.28	1.90	0.72	3.11	4.53	2.60	4.69	40.87	48.78	1.81	1.03	13.52	17.54
Sr	15.15		20.57	26.90	4.68		72.74	25.01	33.92		19.24	35.53	56.21		0.87	50.36	18.71		7.66	20.67	43.32		1.48	46.02
Y	2.31	1.13	8.11	11.98	1.55	3.16	6.40	9.99	2.18	0.72	0.20	3.08	0.87	0.07	0.03	0.86	0.60	0.35	0.46	1.38	0.54	0.07	0.06	0.74
Zr	0.44	3.82	68.83	69.34		0.47	2.33	2.76	0.09	1.70	2.11	4.02		0.24	0.69	0.96		0.25	2.91	3.18		0.12	0.83	1.19
Mo	0.17	0.22	0.39	0.96	0.27	0.19	0.09	0.31	0.32	0.78	0.23	1.10	0.91	0.75	0.08	1.38	0.24	0.34	0.22	0.77	1.17	0.24	0.05	1.49
Cs	8.59	4.13	3.32	16.03	0.50	0.42	1.19	2.06	1.52	0.20	0.20	1.96	0.24	0.08	0.22	0.47	0.40	0.48	3.35	4.39	0.21	0.09	0.99	1.45
Ba	70.05	4.12	257.62	331.63	2.68		1.90	4.73	15.09	1.23	3.20	18.76	5.42		0.33	6.30	3.41	0.30	1.46	6.04	2.75		0.23	3.68
La	0.82	1.25	12.69	16.89	0.64	0.24	4.68	5.43	0.69	0.22	0.61	1.48	0.27	0.02	0.02	0.58	0.28	0.09	0.25	0.67	0.20	0.03	0.03	0.33
Ce	1.67	2.54	24.96	32.80	0.83	0.42	7.13	7.66	1.16	0.60	1.08	2.69	0.46	0.08		1.17	0.50	0.23	0.51	1.26	0.34	0.09	0.06	0.60
Pr	0.22	0.30	2.93	3.83	0.09	0.04	0.78	0.89	0.14	0.08	0.12	0.34	0.06	0.01	<0.01	0.15	0.06	0.03	0.06	0.16	0.04	0.01	0.01	0.07
Nd	0.85	1.08	10.23	13.96	0.34	0.16	3.02	3.56	0.52	0.32	0.42	1.35	0.21	0.04	0.02	0.62	0.22	0.11	0.24	0.62	0.15	0.05	0.03	0.28
Sm	0.24	0.24	1.89	2.68	0.06	0.04	0.54	0.64	0.13	0.07	0.07	0.27	0.04	0.01	<0.01	0.11	0.04	0.03	0.05	0.13	0.03	0.01	0.01	0.06
Eu	0.06	0.04	0.34	0.55	0.02	0.02	0.17	0.25	0.03	0.02	0.01	0.08	0.01	<0.01	<0.01	0.03	0.01	0.01	0.01	0.04	0.01	<0.01	<0.01	0.01
Gd	0.33	0.27	1.68	2.41	0.09	0.08	0.66	0.82	0.15	0.09	0.06	0.30	0.05	0.01	<0.01	0.11	0.05	0.03	0.05	0.15	0.04	0.01	0.01	0.07
Tb	0.06	0.04	0.24	0.36	0.01	0.02	0.08	0.12	0.03	0.01	<0.01	0.05	0.01	<0.01		0.01	0.01	0.01	0.01	0.02	0.01	<0.01	<0.01	0.01
Dy	0.40	0.22	1.51	2.21	0.11	0.18	0.50	0.79	0.21	0.08	0.03	0.33	0.07	0.01	<0.01	0.09	0.07	0.04	0.05	0.16	0.05	0.01	0.01	0.07
Ho	0.08	0.04	0.30	0.40	0.03	0.05	0.10	0.17	0.05	0.02	<0.01	0.07	0.02	<0.01	<0.01	0.02	0.01	0.01	0.01	0.03	0.01	<0.01	<0.01	0.02
Er	0.24	0.10	0.96	1.22	0.11	0.18	0.30	0.54	0.20	0.04	0.01	0.24	0.06	<0.01	<0.01	0.06	0.05	0.03	0.04	0.12	0.04	<0.01	<0.01	0.05
Tm	0.03	0.01	0.14	0.19	0.02	0.02	0.03	0.07	0.03	<0.01	<0.01	0.04	0.01	<0.01		0.01	0.01	<0.01	0.01	0.02	0.01	<0.01	<0.01	0.01
Yb	0.24	0.07	0.92	1.21	0.11	0.12	0.16	0.38	0.26	0.03	0.01	0.28	0.05	<0.01	<0.01	0.05	0.05	0.02	0.05	0.13	0.04	<0.01	0.01	0.05
Lu	0.03	0.01	0.13	0.18	0.02	0.02	0.02	0.05	0.04	<0.01	<0.01	0.05	0.01	<0.01		0.01	0.01	<0.01	0.01	0.02	0.01	<0.01	<0.01	0.01
Hf	<0.01	0.14	2.01	2.09	<0.01	0.01	0.05	0.07	<0.01	0.04	0.05	0.10	<0.01	<0.01	0.02	0.03	<0.01	<0.01	0.07	0.09	<0.01	<0.01	0.02	0.03
Pb	3.92	0.18	2.43	6.28	0.57		0.29	0.83	0.98	0.18	0.75	1.84	0.47		<0.01	0.56	0.92	0.18	0.14	1.46	0.36		0.21	0.75
Th	0.51	0.91	5.86	7.84	0.04	0.18	0.20	0.22	0.19	0.29	0.32	0.46	0.03	0.02	0.06	0.07	0.02	0.10	0.27	0.19	0.01	0.01	0.10	0.08
U	0.12	0.06	1.81	1.88	0.01	0.02	0.01	0.05	0.04	0.01	0.04	0.09	0.01	<0.01	0.01	0.02	<0.01	<0.01	0.03	0.04	<0.01	<0.01	0.02	0.03

Fractions: A= Acetate, B= Oxalate, C: HF, D= Bulk-rock

wt% ppm neg. < d.l. < BEC err. >l.r. n.m.

	ERI489				ERI499				ERI510				ERI524				ERI535				ERI550			
Frac:	A	B	C	D	A	B	C	D	A	B	C	D	A	B	C	D	A	B	C	D	A	B	C	D
Ca	1.01	0.01	0.01	1.10	1.65	0.01	0.02	1.81	0.57	0.01	0.10	0.72	0.99	0.01	0.01	1.13	1.56	0.01	<0.01	1.70	5.50	<0.01	0.14	5.97
Fe	5.49	3.98	2.81	12.90	7.53	9.87	6.50	24.05	9.19	11.48	8.14	28.40	4.19	9.04	5.55	19.43	4.81	8.33	4.91	18.27	5.43	12.56	8.93	26.72
Mg	0.75	0.14	0.32	1.34	0.97	0.10	0.25	1.41	1.04	0.64	0.64	2.52	0.51	0.07	0.18	0.85	0.69	0.07	0.19	1.07	1.40	0.02	0.07	1.67
Mn	0.15	0.01	<0.01	0.15	0.29	0.02	0.02	0.36	0.23	0.09	0.01	0.30	0.10	0.01	0.01	0.13	0.13	0.01	<0.01	0.17	0.07	<0.01	<0.01	0.06
Si	0.37	0.17		33.27	0.11	0.09		23.46	0.43	0.70		18.20	0.16	0.12		30.10	0.13	0.08		29.80	0.13	0.11		17.78
K	0.12	0.08	0.17	0.36	0.09		0.17	0.24	0.24	0.56	0.66	1.40	0.07		0.06	0.12	0.06		0.06	0.09	0.04		0.02	0.03
Na				0.06				0.04				0.06				0.17				0.02				0.06
S				0.09				0.06				0.06				0.13				0.09				0.09
C				1.83				3.28				3.85				1.63				2.29				3.92
Al	0.01	0.04	0.06	0.09	<0.01	0.01	0.07	0.06	0.01	0.11	0.14	0.24	<0.01	0.01	0.03	0.01	0.01	0.01	0.02	0.01	<0.01	<0.01	<0.01	
Ti	1.53	33.71	45.13	83.91	1.97	23.14	100.22	91.42	1.39	108.42	144.02	222.17	0.77	10.81	15.15	41.94	0.92	14.80	21.83	56.80	0.75	6.66	7.22	22.86
Be	0.06	0.02	0.06	0.14	0.04	0.03	0.07	0.14	0.13	0.11	0.22	0.38	0.03	0.02	0.04	0.09	0.03	0.02	0.05	0.12	0.12	0.05	0.09	0.24
Sc	0.56	0.13	0.24	0.46	0.21	<0.01	0.20	0.51	0.45	0.58	0.70	0.83	0.22	0.10	0.08	0.34	0.14	0.06	0.10	0.34	0.21	0.09	0.13	0.22
V	4.49	1.83	2.06	9.66	1.44	2.30		6.44	0.67	2.79	1.47	5.52	3.11	1.10	1.64	8.05	2.60	1.16	0.20	7.48	1.70	1.37		4.80
Cr	20.40	3.96	2.06	29.48	5.59	2.08	1.42	13.40	2.34	9.98	5.63	19.59	13.44	2.51	2.47	24.46	11.97	2.09	1.31	21.38	7.01	0.04		10.79
Co	1.07	0.03	0.41	1.57	0.56	0.13	0.31	1.19	0.39	0.78	1.27	1.80	0.80	0.19	0.59	1.48	0.69	0.11	0.20	1.28	0.41	<0.01	0.13	0.53
Ni	5.75	0.41	1.09	8.28	1.66	0.66	1.05	4.66	1.25	2.37	5.16	6.34	3.80	0.47	1.08	7.15	3.62	0.46	0.82	6.75	2.30	0.51	0.45	3.74
Cu	7.80	0.49	3.25	10.46	4.39	1.12	2.66	5.02	2.96	1.00	5.38	6.37	4.55	0.70	1.72	9.17	5.01	1.09	1.99	7.85	3.59	1.53	0.80	4.11
Zn	8.09	2.26	0.61	10.77	1.51	0.26	0.86	3.56	13.15	5.42	4.53	17.86	3.60	1.38	0.67	3.97	1.22	0.53	0.20	3.84	3.15	0.68		4.48
Rb	10.38	22.49	21.40	55.70	4.07	4.55	22.80	37.71	22.67	133.08	112.54	262.63	4.71	5.08	8.10	22.48	1.94	1.94	7.10	14.44	0.52	0.27	1.60	2.25
Sr	22.42		1.37	23.03	30.86		3.97	37.12	17.54		15.82	19.77	21.56	0.92	1.13	25.82	24.08		1.47	31.38	69.65		34.69	67.88
Y	0.64	0.21	0.14	1.02	0.56	0.19	0.20	1.09	0.88	0.96	0.96	2.60	0.38	0.17	0.11	0.83	0.59	0.16	0.13	1.17	3.47	1.86	1.07	5.90
Zr	0.01	1.09	1.43	2.73	<0.01	0.26	2.37	2.42	0.06	2.40	4.14	5.57		0.27	0.95	1.21		0.50	0.88	1.90	0.01	0.20	1.01	1.44
Mo	0.55	0.87	1.61	1.60	0.26	0.27	0.20	0.62	0.22	0.37	0.10	0.42	0.66	0.49	0.18	1.34	0.47	0.40	0.11	1.21	0.30	0.21	0.05	0.62
Cs	0.53	1.39	1.15	3.21	0.60	0.39	1.29	2.83	0.57	6.06	4.44	10.92	0.36	0.35	0.43	1.48	0.22	0.14	0.46	1.13	0.06	0.05	0.24	0.36
Ba	5.60	0.23	1.35	7.72	6.76	0.66	3.16	12.84	9.20	2.83	2.85	15.20	3.15	1.91	1.61	7.32	4.19	0.21	3.38	10.56	20.88	0.86	6.27	26.87
La	0.21	0.08	0.15	0.49	0.30	0.06	0.12	0.59	0.35	0.23	0.60	1.19	0.12	0.07	0.05	0.33	0.12	0.05	0.10	0.39	0.60	0.13	0.64	1.42
Ce	0.37	0.21	0.27	0.94	0.53	0.15	0.25	1.09	0.63	0.52	1.26	2.29	0.16	0.11	0.07	0.53	0.20	0.12	0.16	0.67	0.74	0.26	0.89	1.83
Pr	0.05	0.03	0.03	0.11	0.06	0.02	0.03	0.13	0.08	0.06	0.15	0.29	0.02	0.01	0.01	0.06	0.03	0.01	0.02	0.08	0.09	0.03	0.11	0.23
Nd	0.18	0.10	0.10	0.44	0.24	0.07	0.10	0.52	0.29	0.24	0.57	1.14	0.07	0.05		0.24	0.11	0.06	0.07	0.34	0.37	0.13	0.48	1.00
Sm	0.04	0.02	0.02	0.09	0.05	0.01	0.02	0.10	0.06	0.05	0.12	0.25	0.01	0.01	0.01	0.05	0.02	0.01	0.01	0.07	0.08	0.03	0.09	0.19
Eu	0.01	<0.01	<0.01	0.02	0.01	<0.01	<0.01	0.03	0.02	0.02	0.03	0.07	<0.01	<0.01	<0.01	0.01	0.01	<0.01	<0.01	0.02	0.03	0.01	0.03	0.08
Gd	0.05	0.02	0.02	0.11	0.05	0.02	0.02	0.11	0.07	0.08	0.12	0.28	0.02	0.01	0.01	0.07	0.03	0.02	0.01	0.10	0.13	0.07	0.11	0.37
Tb	0.01	<0.01	<0.01	0.02	0.01	<0.01	<0.01	0.02	0.01	0.01	0.02	0.05	<0.01	<0.01	<0.01	0.01	0.01	<0.01	<0.01	0.01	0.02	0.01	0.01	0.05
Dy	0.06	0.02	0.01	0.11	0.05	0.02	0.02	0.10	0.09	0.10	0.10	0.30	0.02	0.01	0.01	0.07	0.05	0.02	0.01	0.10	0.24	0.13	0.09	0.44
Ho	0.01	<0.01	<0.01	0.02	0.01	<0.01	<0.01	0.02	0.02	0.02	0.02	0.06	0.01	<0.01	<0.01	0.01	0.01	<0.01	<0.01	0.02	0.07	0.03	0.02	0.11
Er	0.06	0.01	0.01	0.08	0.04	0.01	0.01	0.07	0.07	0.07	0.07	0.21	0.03	0.01	0.01	0.05	0.05	0.01	0.01	0.09	0.26	0.11	0.06	0.40
Tm	0.01	<0.01	<0.01	0.01	0.01	<0.01	<0.01	0.01	0.01	0.01	0.01	0.03	<0.01	<0.01	<0.01	0.01	0.01	<0.01	<0.01	0.01	0.04	0.01	0.01	0.06
Yb	0.06	0.01	0.02	0.09	0.05	0.01	0.02	0.08	0.08	0.06	0.07	0.20	0.03	0.01	0.01	0.05	0.06	0.01	0.01	0.10	0.31	0.08	0.05	0.40
Lu	0.01	<0.01	<0.01	0.02	0.01	<0.01	<0.01	0.01	0.01	0.01	0.01	0.03	<0.01	<0.01	<0.01	0.01	0.01	<0.01	<0.01	0.02	0.05	0.01	0.01	0.07
Hf	<0.01	0.03	0.03	0.07	<0.01	0.01	0.06	0.06	<0.01	0.06	0.10	0.15		0.01	0.02	0.03	<0.01	0.01	0.02	0.04	<0.01	<0.01	0.01	0.02
Pb	0.51	0.01	0.09	0.87	0.13		0.09	0.42	0.62	0.06	0.13	1.01	0.62	0.48		0.93	0.13		0.02	0.35	0.33		0.11	0.52
Th	0.04	0.12	0.11	0.16	0.02	0.06	0.15	0.12	0.04	0.27	0.21	0.25	0.01	0.03	<0.01	0.05	0.02	0.03	0.05	0.07	0.01	0.03	0.03	0.04
U	0.01	0.01	0.02	0.04	<0.01	<0.01	0.02	0.03	0.01	0.01	0.03	0.05	<0.01	<0.01	<0.01	0.01	<0.01	<0.01	<0.01	0.02	<0.01	<0.01	<0.01	0.01

Fractions: A= Acetate, B= Oxalate, C: HF, D= Bulk-rock

wt% | ppm | neg. | < d.l. | < BEC | err. | >l.r. | n.m.

	ERI562				ERI572				ERI584				ERI603				ERI618				ERI628			
Frac:	A	B	C	D	A	B	C	D	A	B	C	D	A	B	C	D	A	B	C	D	A	B	C	D
Ca	0.09	0.01	0.02	0.16	4.54	0.01	0.07	5.00	0.83	0.01	0.02	0.94	2.83	0.01	0.08	3.12	2.39	0.01	0.03	2.52	2.60	0.01	0.05	2.81
Fe	5.47	6.82	13.62	24.98	3.47	10.02	3.55	17.69	2.39	7.76	8.14	18.95	0.35	14.66	5.20	20.45	0.74	25.61	5.00	32.10	18.05	3.38	7.00	28.26
Mg	0.57	0.51	1.40	2.62	0.89	0.01	0.12	1.09	0.39	0.02	0.34	0.82	0.08	0.03	1.70	1.94	0.17	0.10	1.22	1.68	2.03	0.27	0.62	3.19
Mn	0.05	0.01	0.02	0.07	0.16	<0.01	<0.01	0.12	0.07	<0.01	0.01	0.09	0.10	<0.01	0.03	0.13	0.10	0.01	0.04	0.16	0.22	0.02	0.02	0.26
Si	0.76	0.17		24.64	0.12	0.07		26.08	0.20	0.09		30.80	0.20	0.05		27.49	0.46	0.28		20.92	0.46	0.06		11.97
K	0.05	0.08	0.41	0.49	0.05		<0.01	0.02	0.06		<0.01	0.02	0.08		0.03	0.06	0.17	0.01	0.03	0.19	0.19	0.04	0.08	0.22
Na				0.01				0.28				0.56				0.04				0.04				0.02
S				0.20				0.07				0.05				0.09				0.05				0.06
C				1.51				3.02				1.10				1.01				0.86				7.70
Al	<0.01	0.01	0.04	0.05	<0.01	<0.01	<0.01		0.01	0.01	0.01	0.02	<0.01	0.01	0.03	0.04	0.01	0.02	0.10	0.11	0.02	0.05	0.15	0.29
Ti	0.78	12.15	19.49	37.71	1.82	4.21	16.51	35.11	2.83	1.09	4.80	20.89	2.21	8.88		23.96	2.08	107.85	5.09	142.25	3.84	30.90	92.36	133.52
Be	0.33	0.16	0.78	1.04	0.11	0.14	0.12	0.31	0.10	0.03	0.06	0.23	0.02	0.11	0.04	0.19	0.03	0.69	0.01	0.90	0.39	0.11	0.28	0.73
Sc	0.83	0.07	0.17	0.35	0.73		0.20	0.29	0.91	<0.01	0.08	0.31	0.60		0.06	0.21	0.43	0.17	0.63	1.08	1.20	0.28	0.48	1.35
V	0.94	1.90	0.84	5.52	2.41	2.19	0.56	5.74	2.85	1.13	0.53	8.70	0.38	1.48		3.09	0.71	6.86		10.86	2.21	3.45	8.44	13.40
Cr	0.02	0.22	0.21	6.15	12.78		0.93	11.53	12.75		1.24	22.49	2.84		0.20	6.18	6.03	1.76		12.80	3.52	3.26	3.83	11.44
Co	0.12	0.12	0.21	0.47	0.56	0.04	0.12	0.56	0.68	0.03	0.13	1.14	0.16	0.20	0.74	1.39	0.25	0.28	0.52	1.36	0.84	0.20	2.15	2.27
Ni	0.75	1.22	2.21	4.87	3.03	1.01	1.12	4.41	3.33	0.23	0.88	6.54	0.57	0.09	0.37	1.81	1.24	0.86	1.16	4.68	2.29	1.80	5.09	9.95
Cu	2.13	1.02	1.48	2.15	6.92	0.38	1.71	4.03	11.53	1.70	1.87	8.43	5.50	1.08	2.10	2.54	3.34	1.94	1.70	3.53	6.08	1.51	2.20	4.36
Zn	1.68	1.29	4.72	7.57	2.29	0.09	0.13	2.04	4.46	0.83	0.80	7.71	1.70	0.27	5.33	8.34	2.44	1.35	4.28	9.19	5.45	0.87	5.24	11.70
Rb	4.94	14.05	70.82	85.99	1.20	0.15	0.21	1.18	1.31	0.03	0.18	1.36	1.90	0.27	1.43	3.53	6.66	1.86	2.38	12.86	8.45	2.97	8.59	20.94
Sr	2.73		4.64	3.76	38.42		14.54	32.43	11.23		1.16	14.29	29.75		22.60	38.26	24.80		11.69	36.28	21.56		11.08	22.62
Y	1.46	1.14	1.74	3.99	2.86	0.65	0.85	3.47	0.78	0.35	0.95	1.75	1.72	1.20	0.80	3.93	2.10	1.95	0.66	5.40	3.03	0.66	0.44	4.19
Zr	<0.01	0.79	2.36	3.20	0.01	0.31	2.90	3.16		0.06	10.84	1.37	<0.01	0.12	0.36	0.94	<0.01	1.21	2.61	5.29	0.10	1.90	4.68	6.91
Mo	0.06	0.17	0.04	0.24	0.54	0.08	0.13	0.67	0.57	0.12	0.16	1.27	0.01		0.10	0.30		0.22	0.17	0.82	0.30	0.70	0.81	1.09
Cs	0.59	1.26	4.56	6.26	0.11	0.02	0.02	0.16	0.11	0.01	0.02	0.20	0.30	0.09	0.12	0.61	1.23	0.38	0.29	2.28	2.12	1.00	1.54	4.71
Ba	8.72	2.09	3.29	13.37	8.70	<0.01	0.63	8.77	1.49		0.54	4.30	1.21	0.89	0.60	4.70	2.73	8.37	0.94	15.60	18.50	2.13	6.46	25.58
La	0.15	0.16	0.52	0.95	0.49	0.12	0.48	1.07	0.09	0.06	0.70	0.81	0.38	0.19	0.51	1.27	0.54	0.40	0.54	2.06	1.35	0.22	0.35	2.01
Ce	0.26	0.35	0.87	1.54	0.72	0.33	0.85	1.72	0.15	0.14	1.05	1.29	0.56	0.38	0.83	1.98	0.95	0.85	1.02	3.65	2.43	0.63	0.84	3.92
Pr	0.04	0.05	0.10	0.20	0.09	0.05	0.11	0.22	0.02	0.02	0.11	0.15	0.07	0.04	0.10	0.25	0.13	0.10	0.13	0.47	0.28	0.08	0.10	0.47
Nd	0.16	0.21	0.41	0.86	0.38	0.21	0.44	0.97	0.10	0.11	0.37	0.62	0.28	0.19	0.42	1.05	0.52	0.42	0.50	1.91	1.02	0.32	0.42	1.86
Sm	0.05	0.05	0.08	0.18	0.08	0.05	0.08	0.19	0.02	0.03	0.05	0.12	0.07	0.05	0.09	0.23	0.13	0.10	0.10	0.44	0.20	0.07	0.08	0.39
Eu	0.01	0.01	0.02	0.06	0.03	0.02	0.02	0.07	0.01	0.01	0.01	0.04	0.07	0.03	0.05	0.18	0.03	0.02	0.01	0.09	0.06	0.02	0.02	0.12
Gd	0.08	0.08	0.10	0.25	0.14	0.07	0.09	0.27	0.04	0.04	0.06	0.17	0.11	0.08	0.11	0.36	0.18	0.15	0.10	0.56	0.27	0.09	0.08	0.45
Tb	0.02	0.01	0.02	0.05	0.03	0.01	0.01	0.04	0.01	0.01	0.01	0.02	0.02	0.01	0.01	0.05	0.03	0.03	0.01	0.09	0.05	0.01	0.01	0.07
Dy	0.13	0.11	0.13	0.36	0.22	0.08	0.08	0.32	0.07	0.04	0.06	0.17	0.15	0.11	0.08	0.36	0.22	0.23	0.08	0.63	0.37	0.09	0.06	0.50
Ho	0.03	0.03	0.04	0.09	0.06	0.02	0.02	0.07	0.02	0.01	0.02	0.04	0.04	0.02	0.02	0.08	0.05	0.05	0.01	0.13	0.09	0.02	0.01	0.11
Er	0.14	0.09	0.17	0.36	0.24	0.04	0.06	0.27	0.07	0.02	0.08	0.14	0.12	0.08	0.05	0.25	0.18	0.17	0.05	0.44	0.31	0.05	0.04	0.37
Tm	0.02	0.01	0.04	0.07	0.04	<0.01	0.01	0.05	0.01	<0.01	0.01	0.03	0.02	0.01	0.01	0.04	0.03	0.02	0.01	0.07	0.05	0.01	0.01	0.06
Yb	0.18	0.10	0.32	0.54	0.29	0.02	0.08	0.33	0.09	0.01	0.15	0.23	0.10	0.05	0.05	0.20	0.20	0.16	0.05	0.45	0.36	0.05	0.04	0.41
Lu	0.03	0.01	0.05	0.09	0.05	<0.01	0.02	0.06	0.01	<0.01	0.02	0.04	0.01	0.01		0.03	0.03	0.02	0.01	0.07	0.06	0.01	0.01	0.07
Hf	<0.01	0.01	0.02	0.03	<0.01	<0.01	0.02	0.02	<0.01	<0.01		0.01	<0.01	0.01	0.01	0.02	<0.01	0.03	0.05	0.10	<0.01	0.03	0.09	0.13
Pb	0.25		0.05	0.36	0.13	<0.01	0.09	0.19	0.39		0.05	0.65	0.22	0.63	0.39	1.60	0.38	1.24	0.39	2.43	1.42	0.02	0.45	1.50
Th	0.02	0.06	0.12	0.10	0.02	0.03	0.06	0.05	0.01	<0.01	0.05	0.04	0.01	0.05	0.03	0.06	0.05	0.30	0.22	0.30	0.14	0.32	0.55	0.48
U	0.01	<0.01	0.02	0.03	<0.01		0.01	0.01	<0.01		0.01	0.01	<0.01	0.01	<0.01	0.02	0.03	0.06	0.05	0.15	0.03	0.02	0.09	0.13

Fractions: A= Acetate, B= Oxalate, C: HF, D= Bulk-rock

wt% ppm neg. < d.l. < BEC err. >l.r. n.m.

	ERI637				ERI646				GAS142				GAS150				GAS174				GAS192			
Frac:	A	B	C	D	A	B	C	D	A	B	C	D	A	B	C	D	A	B	C	D	A	B	C	D
Ca	0.84	0.01	0.25	1.13	4.94	<0.01	0.16	5.41	4.15	0.01	0.04	4.43	1.45	0.01	0.09	1.69	0.18	0.01	0.04	0.28	2.72	0.01	<0.01	3.01
Fe	9.46	4.03	19.79	31.63	11.11	3.31	10.03	24.04	8.03	1.27	4.14	13.62	10.43	12.40	7.27	30.40	13.13	9.65	10.64	33.24	8.25	17.46	6.31	32.59
Mg	0.84	0.31	1.13	2.43	0.67	0.19	0.61	1.59	1.21	0.09	0.36	1.83	0.90	0.56	0.47	2.16	1.26	0.34	0.91	2.87	1.31	0.16	0.46	2.23
Mn	0.19	0.04	0.05	0.20	0.16	0.03	0.02	0.19	1.25	0.09	0.05	0.99	0.21	0.03	0.03	0.27	0.41	0.04	0.03	0.39	0.36	0.02	0.02	0.48
Si	0.32	0.09		14.07	0.40	0.06		17.41	0.21	0.02		24.39	0.89	0.68		17.41	0.67	0.16		14.84	0.33	0.31		14.94
K	0.17	0.06	0.94	1.08	0.05	0.02	0.18	0.21	0.21	0.04	0.02	0.23	0.03	0.03	0.07	0.11	0.13	0.07	0.76	0.93	0.17	0.10	0.26	0.51
Na				0.09				0.03				0.10				0.01				0.03				0.07
S				3.75				0.07				0.40				0.08				0.08				0.15
C				4.17				5.59				4.48				2.91				3.85				3.77
Al	0.02	0.07	0.56	0.62	0.01	0.02	0.06	0.08	0.02	0.03	0.40	0.42	0.08	0.27	0.11	0.50	0.03	0.08	0.34	0.51	0.02	0.05	0.19	0.27
Ti	2.34	45.89	297.29	268.08	3.00	17.81	43.26	70.90	0.41	4.73	261.91	182.58	1.34	81.01	318.17	366.65	2.27	61.46	354.50	324.39	2.32	56.08	149.66	253.35
Be	0.27	0.18	0.92	1.00	0.27	0.07	0.60	0.86	0.22	0.03	0.06	0.21	0.27	0.17	0.07	0.52	0.16	0.10	0.37	0.47	0.06	0.05	0.11	0.26
Sc	0.65	0.16	2.42	2.35	0.52	0.05	0.25	0.52	0.83		0.38	0.76	1.54	1.28	0.25	1.72	2.63	0.54	0.52	1.27	1.33	0.17	0.51	0.94
V	1.91	5.30	6.61	11.42	1.22	1.33	0.66	4.51	1.61	1.08	7.74	7.31	4.25	8.78	0.56	15.43	3.13	8.15	0.09	11.05	0.59	6.97		10.71
Cr	0.57	5.82	7.87	14.13	4.00	2.25	1.47	7.91	4.78	2.94	10.10	13.04	2.79	10.50	3.31	20.05	0.30	13.20	3.26	18.58	<0.01	9.86	2.56	22.63
Co	0.32	0.08	4.31	3.99	0.36	0.16	0.50	0.79	1.55	0.51	3.77	4.39	0.83	0.97	1.01	2.86	0.52	0.39	0.88	1.45	0.50	14.86	0.92	2.18
Ni	0.76	0.69	11.51	11.72	1.07	0.71	0.89	2.60	2.43	0.89	6.61	7.79	2.37	4.69	2.88	11.10	1.63	2.35	4.30	7.48	1.11	2.32	2.88	8.91
Cu	0.50	1.23	14.38	13.93	5.43	1.70	0.66	2.39	2.04	2.16	6.38	8.53	1.07	1.13	3.08	4.65	6.07	1.20	4.55	6.53	4.75	2.98	3.03	6.30
Zn	4.46	1.79	7.67	8.02	2.70	1.44	6.82	10.08	7.79	2.52	5.15	6.07	5.72	4.63	6.89	14.58	3.68	1.22	6.23	6.16	1.64	1.89	2.08	5.65
Rb	10.75	8.95	131.59	125.74	2.05	1.93	24.80	28.82	18.80	5.63	3.61	20.02	2.96	3.48	10.57	16.84	10.78	8.90	66.40	67.52	20.20	18.89	37.53	90.89
Sr	15.32		32.52	16.05	33.71		37.88	35.68	35.29		10.14	24.88	14.42		21.50	15.85	4.94		14.21	6.17	126.04		1.28	139.32
Y	2.43	2.06	3.02	6.06	2.62	2.10	1.43	5.82	3.57	0.26	0.86	3.44	1.29	0.98	0.52	2.67	0.89	0.56	0.37	1.40	1.82	0.22	0.18	2.56
Zr	0.05	1.63	15.31	13.80	0.02	0.91	2.02	2.98	0.14	0.95	8.33	6.21	0.13	3.73	6.10	9.70	0.03	1.33	9.33	8.78	0.08	1.26	4.39	7.19
Mo	0.28	0.19	0.41	0.58	0.34	0.19	0.39	0.75	0.49	0.44	0.09	0.46	0.14	0.25	0.11	0.39	0.22	0.26	0.09	0.30	0.20	1.80	0.14	0.54
Cs	2.22	2.15	13.17	15.11	0.37	0.26	1.90	2.58	3.48	0.77	0.53	3.50	1.20	1.41	1.75	4.37	2.21	1.83	7.26	9.09	1.48	1.78	2.43	6.87
Ba	20.11	6.31	12.79	30.34	20.28	1.94	1.72	23.35	79.30	6.48	87.13	127.17	5.07	0.91	1.68	7.37	7.63	2.53	4.93	10.24	11.18	1.59	4.38	18.23
La	1.12	0.55	3.11	4.28	1.02	0.23	0.99	2.22	0.82	0.19	1.88	2.24	1.07	0.40	0.70	2.22	0.65	0.32	0.36	1.21	0.49	0.09	0.56	1.50
Ce	2.04	1.20	6.20	8.12	1.48	0.51	1.78	3.61	1.86	0.42	3.41	4.44	1.76	0.99	1.57	4.19	1.06	0.86	0.83	2.13	0.99	0.23	1.05	2.78
Pr	0.24	0.14	0.74	0.99	0.17	0.06	0.21	0.44	0.26	0.06	0.37	0.54	0.20	0.12	0.19	0.50	0.13	0.11	0.10	0.27	0.13	0.03	0.10	0.33
Nd	0.92	0.53	2.79	3.81	0.62	0.23	0.88	1.81	1.12	0.22	1.23	2.06	0.71	0.45	0.75	1.95	0.47	0.43	0.42	1.08	0.52	0.11	0.32	1.17
Sm	0.19	0.13	0.53	0.74	0.12	0.05	0.17	0.36	0.34	0.05	0.17	0.44	0.14	0.10	0.15	0.40	0.10	0.10	0.08	0.22	0.13	0.02	0.03	0.23
Eu	0.04	0.03	0.11	0.19	0.04	0.02	0.05	0.13	0.15	0.01	0.03	0.18	0.04	0.03	0.03	0.11	0.02	0.02	0.02	0.05	0.03	0.01	0.01	0.06
Gd	0.24	0.18	0.53	0.82	0.18	0.10	0.21	0.49	0.41	0.05	0.15	0.47	0.18	0.14	0.13	0.42	0.12	0.11	0.07	0.23	0.16	0.03	0.04	0.24
Tb	0.04	0.03	0.07	0.12	0.03	0.02	0.03	0.08	0.07	0.01	0.02	0.07	0.03	0.02	0.02	0.06	0.02	0.01	0.01	0.03	0.03	<0.01	<0.01	0.04
Dy	0.29	0.23	0.40	0.79	0.25	0.17	0.15	0.57	0.44	0.04	0.11	0.46	0.18	0.14	0.08	0.39	0.12	0.09	0.05	0.19	0.19	0.03	0.02	0.26
Ho	0.07	0.05	0.08	0.16	0.06	0.04	0.03	0.13	0.09	0.01	0.02	0.09	0.04	0.03	0.02	0.07	0.03	0.02	0.01	0.04	0.04	<0.01	<0.01	0.05
Er	0.22	0.16	0.23	0.49	0.24	0.14	0.09	0.43	0.27	0.02	0.08	0.27	0.13	0.08	0.05	0.24	0.09	0.04	0.04	0.13	0.15	0.02	0.01	0.18
Tm	0.03	0.02	0.03	0.07	0.04	0.02	0.01	0.07	0.04	<0.01	0.01	0.04	0.02	0.01	0.01	0.04	0.02	<0.01	0.01	0.02	0.02	<0.01	<0.01	0.03
Yb	0.23	0.14	0.22	0.47	0.26	0.11	0.09	0.43	0.26	0.02	0.08	0.27	0.16	0.07	0.05	0.25	0.11	0.03	0.05	0.15	0.15	0.01	0.02	0.20
Lu	0.04	0.02	0.03	0.07	0.04	0.01	0.01	0.07	0.04	<0.01	0.01	0.04	0.03	0.01	0.01	0.04	0.02	<0.01	0.01	0.02	0.02	<0.01	<0.01	0.03
Hf	<0.01	0.04	0.33	0.33	<0.01	0.02	0.04	0.07	<0.01	0.03	0.19	0.17	<0.01	0.10	0.15	0.24	<0.01	0.04	0.25	0.22	<0.01	0.04	0.12	0.18
Pb	7.78	0.10	6.96	12.67	0.29		0.16	0.43	2.77	0.40	1.19	3.29	0.89	0.12	0.19	0.94	0.27	0.06	0.24	0.54	0.28	0.43	0.20	0.73
Th	0.15	0.40	1.72	1.23	0.09	0.14	0.22	0.25	0.14	0.11	0.35	0.53	0.19	0.58	0.43	0.57	0.10	0.33	0.87	0.46	0.09	0.20	0.39	0.37
U	0.02	0.04	0.24	0.25	0.02	0.01	0.02	0.05	0.03	0.01	0.13	0.14	0.05	0.06	0.04	0.12	0.02	0.01	0.11	0.10	0.01	0.01	0.05	0.07

Fractions: A= Acetate, B= Oxalate, C: HF, D= Bulk-rock

wt% | ppm | neg. | < d.l. | < BEC | err. | >l.r. | n.m.

	GAS201				GAS212				GAS229				GAS244				GAS259				GAS266			
Frac:	A	B	C	D	A	B	C	D	A	B	C	D	A	B	C	D	A	B	C	D	A	B	C	D
Ca	1.81	<0.01	0.02	1.93	0.78	0.01	0.31	0.95	2.40	0.01	0.07	2.64	0.52	0.01	0.02	0.61	0.09	0.01	0.09	0.15	1.57	0.01	0.01	1.70
Fe	2.80	0.48	5.00	8.33	10.54	9.64	7.82	27.98	2.59	13.48	4.16	20.51	4.41	16.56	8.20	29.48	7.57	20.20	11.90	39.53	12.52	4.49	2.25	20.15
Mg	0.49	0.02	0.42	1.01	1.22	0.28	0.66	2.35	0.55	0.02	0.14	0.78	0.54	0.09	0.54	1.33	0.80	0.22	0.90	2.15	1.39	0.11	0.18	1.79
Mn	0.09	<0.01	<0.01	0.10	0.19	0.01	0.01	0.25	0.11	<0.01	<0.01	0.14	0.11	0.01	0.01	0.16	0.32	0.03	0.03	0.46	0.47	0.02	0.01	0.74
Si	0.46	0.05		36.84	0.67	0.61		19.54	0.24	0.15		28.36	0.49	0.24		23.27	0.55	0.38		13.49	0.36	0.07		23.47
K	0.04	0.01	0.03	0.07	0.27	0.38	0.72	1.31	0.05	0.03	0.03	0.08	0.10	0.06	0.13	0.27	0.21	0.18	0.84	1.22	0.05	0.04	0.14	0.19
Na				0.84				0.08				0.20				0.65				0.03				0.02
S				0.15				0.14				0.11				0.10				0.07				0.06
C				1.11				3.24				1.53				1.32				2.15				4.41
Al	<0.01	0.01	0.02	0.03	0.03	0.10	0.35	0.33	0.01	0.01	0.03	0.01	0.01	0.03	0.06	0.08	0.03	0.08	0.27	0.39	0.01	0.01	0.02	0.03
Ti	1.04	15.98	74.50	92.46	1.73	73.16	229.59	314.53	<0.01	18.95	34.31	82.27	<0.01	28.69	69.20	124.48	1.40	46.74	63.27	144.11	<0.01	9.07	11.37	41.83
Be	0.03	<0.01	0.11	0.15	0.15	0.07	0.23	0.50	0.03	0.03	0.05	0.14	0.07	0.10	0.09	0.36	0.19	0.15	0.44	0.91	0.07	0.02	0.10	0.30
Sc	0.47	0.02	0.16	0.27	1.01	0.42	0.84	1.01	0.06	0.06	0.16	0.38	0.33	0.16	0.31	0.59	0.49	0.35	0.25	0.56	0.25	0.02	0.04	0.20
V	5.98	1.22	4.19	12.81	0.60	3.32	1.15	6.79	3.39	2.46	<0.01	10.03	1.11	4.98	1.29	12.46	0.37	2.57		4.89	1.13	1.19		5.84
Cr	27.78	2.75	3.04	36.26	<0.01	11.83	4.29	23.26	16.75	3.01	0.76	29.25	3.77	7.44	3.63	23.30	1.88	2.99	0.53	9.45	4.82	4.01	0.68	16.72
Co	1.36	0.06	0.33	1.72	0.29	0.12	1.58	2.40	0.85	0.11	0.20	1.52	0.35	0.36	0.55	1.62	0.31	0.34	0.75	1.78	0.55	0.21	0.13	1.40
Ni	8.09	0.42	1.01	10.74	1.42	2.45	3.61	9.10	5.15	0.61	0.74	8.91	1.46	1.76	2.42	8.08	0.47	0.90	0.95	3.53	1.85	1.06	0.39	5.55
Cu	8.22	0.49	0.84	11.75	3.37	2.21	4.26	6.15	3.81	1.38	0.54	10.32	<0.01	1.79	1.97	6.55	0.32	1.46	1.63	3.47	<0.01	1.48	0.51	6.35
Zn	2.60	0.07	1.40	5.28	3.11	1.24	5.11	7.88	1.49	<0.01	0.49	3.35	2.84	0.09	3.51	8.82	7.09	2.07	4.22	13.06	3.70	0.87	0.76	8.18
Rb	3.93	1.82	4.17	9.78	37.06	103.41	139.21	307.25	4.30	2.78	4.46	14.67	12.28	15.31	24.44	66.95	29.44	46.33	135.35	272.99	4.22	5.20	17.92	39.14
Sr	41.01	<0.01	0.35	38.46	17.92		6.31	19.17	50.86		25.28	64.07	10.24		4.80	13.84	1.63		4.98	3.58	27.39		0.84	37.30
Y	0.65	0.02	0.12	0.77	1.34	0.19	0.59	2.01	0.74	0.60	0.17	1.82	0.54	0.29	0.18	1.27	1.21	0.74	0.65	3.20	1.12	0.22	0.19	2.15
Zr	<0.01	0.36	1.55	1.64	0.10	2.96	5.70	9.02	0.01	0.51	1.41	2.44	0.02	1.59	3.69	6.33	0.11	2.98	11.22	18.68	<0.01	0.22	0.83	1.62
Mo	1.68	0.46	0.18	2.39	0.15	0.32	0.17	0.55	0.72	0.51	0.06	1.80	0.13	0.48	0.28	1.16	0.17	0.38	0.07	0.43	0.03	0.67	0.09	1.19
Cs	0.25	0.14	0.25	0.66	0.87	5.90	6.54	14.61	0.35	0.20	0.28	1.09	0.93	1.24	1.48	4.74	2.12	3.72	7.92	17.62	0.25	0.31	1.08	2.35
Ba	4.80	<0.01	0.88	5.49	4.72	1.12	5.59	8.19	8.81	0.50	0.52	12.01	3.81	0.37	0.90	6.89	3.38	1.83	1.14	6.90	4.61	0.16	0.23	7.06
La	0.16	0.02	0.18	0.37	0.37	0.09	1.44	1.85	0.20	0.07	0.18	0.63	0.24	0.13	0.16	0.75	0.42	0.43	1.90	4.14	0.26	0.06	0.09	0.65
Ce	0.30	0.05	0.34	0.67	0.79	0.21	2.80	3.39	0.39	0.26	0.39	1.32	0.47	0.34	0.32	1.53	0.83	0.95	3.60	7.73	0.46	0.15	0.16	1.17
Pr	0.04	<0.01	0.03	0.08	0.12	0.02	0.28	0.39	0.05	0.03	0.05	0.18	0.06	0.04	0.04	0.19	0.10	0.11	0.36	0.83	0.06	0.02	0.02	0.15
Nd	0.17	0.02	0.11	0.30	0.49	0.09	0.90	1.41	0.20	0.15	0.25	0.78	0.23	0.17	0.14	0.77	0.35	0.41	1.06	2.71	0.22	0.08	0.06	0.57
Sm	0.04	<0.01	0.02	0.07	0.15	0.02	0.13	0.26	0.04	0.04	0.05	0.18	0.05	0.04	0.03	0.16	0.07	0.08	0.11	0.39	0.05	0.02	0.01	0.12
Eu	0.01	<0.01	<0.01	0.02	0.03	<0.01	0.02	0.06	0.01	0.01	0.01	0.05	0.01	0.01	0.01	0.04	0.01	0.01	0.01	0.04	0.01	<0.01	<0.01	0.02
Gd	0.05	<0.01	0.01	0.07	0.16	0.02	0.12	0.25	0.06	0.06	0.05	0.21	0.06	0.04	0.03	0.16	0.08	0.09	0.09	0.34	0.06	0.02	0.01	0.13
Tb	0.01	<0.01	<0.01	0.01	0.02	<0.01	0.01	0.04	0.01	0.01	<0.01	0.03	0.01	0.01	<0.01	0.02	0.01	0.01	0.01	0.05	0.01	<0.01	<0.01	0.02
Dy	0.07	<0.01	0.01	0.08	0.16	0.02	0.09	0.24	0.07	0.07	0.02	0.19	0.06	0.04	0.02	0.15	0.11	0.08	0.05	0.30	0.08	0.02	0.01	0.17
Ho	0.01	<0.01	<0.01	0.02	0.04	<0.01	0.02	0.05	0.02	0.01	<0.01	0.04	0.01	0.01	<0.01	0.03	0.03	0.02	0.01	0.06	0.02	<0.01	<0.01	0.04
Er	0.05	<0.01	0.01	0.06	0.11	0.01	0.06	0.15	0.05	0.04	0.01	0.11	0.05	0.02	0.02	0.10	0.10	0.05	0.06	0.24	0.08	0.01	0.01	0.14
Tm	0.01	<0.01	<0.01	0.01	0.02	<0.01	0.01	0.02	0.01	<0.01	<0.01	0.02	0.01	<0.01	<0.01	0.02	0.02	0.01	0.01	0.04	0.01	<0.01	<0.01	0.03
Yb	0.05	<0.01	0.03	0.08	0.10	0.02	0.07	0.16	0.05	0.02	0.01	0.09	0.05	0.02	0.03	0.12	0.12	0.04	0.11	0.31	0.10	0.01	0.03	0.19
Lu	0.01	<0.01	0.01	0.01	0.02	<0.01	0.01	0.03	0.01	<0.01	<0.01	0.01	0.01	<0.01	0.01	0.02	0.02	0.01	0.02	0.05	0.02	<0.01	<0.01	0.03
Hf	<0.01	0.01	0.04	0.04	<0.01	0.08	0.15	0.24	<0.01	0.02	0.04	0.06	<0.01	0.04	0.09	0.15	<0.01	0.09	0.37	0.55	<0.01	0.01	0.02	0.04
Pb	2.30	0.10	0.10	2.48	0.72	0.19	0.51	1.09	0.58		0.10	0.84	0.19	0.03	0.08	0.60	0.34	0.14	0.28	1.03	0.50	0.19	0.01	1.07
Th	0.07	0.04	0.08	0.12	0.15	0.32	0.80	0.52	0.04	0.07	0.06	0.13	0.09	0.15	0.16	0.27	0.47	0.74	2.31	2.63	0.03	0.02	0.04	0.09
U	0.01	<0.01	0.01	0.01	0.03	0.01	0.11	0.10	0.01	0.02	0.01	0.05	0.09	0.01	0.02	0.12	0.08	0.05	0.30	0.45	0.01	<0.01	0.01	0.02

Fractions: A= Acetate, B= Oxalate, C: HF, D= Bulk-rock

wt% | ppm | neg. | < d.l. | < BEC | err. | >l.r. | n.m.

	GAS271				GAS283				GAS296				GAS336				GAS354				GAS367			
Frac:	A	B	C	D	A	B	C	D	A	B	C	D	A	B	C	D	A	B	C	D	A	B	C	D
Ca	3.96	<0.01	0.30	4.63	0.12	<0.01	0.14	0.27	2.96	0.01	0.05	3.23	2.68	0.01	0.02	2.87	1.24	0.01	0.01	1.35	0.67	0.01	0.06	0.85
Fe	3.14	13.65	5.65	22.60	4.79	19.93	5.83	30.57	9.37	12.02	5.08	26.65	2.00	18.74	5.25	25.85	10.60	4.06	6.47	21.58	7.48	15.80	13.01	36.07
Mg	0.91	<0.01	0.05	1.02	0.65	0.33	1.09	2.26	1.63	0.10	0.15	2.03	0.80	0.02	0.47	1.38	1.12	0.24	0.49	2.03	0.93	0.05	0.73	1.94
Mn	0.33	<0.01	<0.01	0.41	0.03	<0.01	<0.01	0.05	0.26	0.01	0.01	0.38	0.20	<0.01	0.01	0.27	0.12	0.01	0.01	0.20	0.28	0.01	0.02	0.42
Si	0.14	0.11		23.42	0.72	0.28		22.37	0.13	0.08		18.39	0.14	0.12		23.52	0.54	0.07		24.24	0.41	0.16		17.07
K	0.02	0.01	<0.01	0.00	0.02	0.01	0.03	0.04	0.06	0.01	0.01	0.04	0.05	0.02	<0.01	0.03	0.06	0.02	0.07	0.11	0.04	0.02	0.08	0.11
Na				0.13				0.01				0.05				0.32				0.03				0.09
S				0.07				0.04				0.10				0.07				0.09				0.08
C				2.49				1.25				4.36				1.67				3.40				2.47
Al	<0.01	<0.01			<0.01	0.01	0.01		0.01	0.01	0.04	0.05	<0.01	<0.01	0.03	0.03	0.01	0.04	0.09	0.13	<0.01	0.01	0.04	
Ti		3.56	1.17	21.28		6.31	6.42	27.03	<0.01	10.99	14.05	39.10	0.40	9.73	15.81	45.05	0.54	18.60	49.51	108.79	1.53	9.53	23.75	55.29
Be	0.06	0.14	0.03	0.29	0.23	0.22	0.17	0.91	0.19	0.12	0.09	0.51	0.12	0.20	0.10	0.53	0.24	0.11	0.19	0.71	0.34	0.13	0.50	1.16
Sc	0.09	0.03	0.07	0.21	0.47	0.21	0.08	0.44	0.23	0.02	0.15	0.49	0.11	0.08	0.22	0.53	0.51	0.14	0.18	0.80		0.03	0.23	0.47
V	1.36	0.77		4.62	0.40	1.71		5.13	0.64	2.27		5.83	1.51	2.47	1.83	10.99	1.18	2.73	0.67	9.54	0.43	2.38		6.05
Cr	5.47	0.24	0.78	11.35	<0.01	0.26		7.27	2.31	0.89	0.52	9.07	6.33	1.62	2.88	20.53	<0.01	2.58	1.56	12.01	2.31		1.56	8.48
Co	0.37	0.04	0.14	0.68	0.10	0.08	0.10	0.46	0.39	0.08	0.17	0.90	0.46	0.63	0.40	1.75	0.32	0.21	0.41	1.50	0.29	0.13	0.52	1.28
Ni	2.02	0.28	0.43	3.69	0.69	0.60	1.19	4.52	1.37	0.65	1.01	4.64	1.77	0.18	1.11	6.77	0.87	1.53	2.04	7.35	0.68	0.31	0.95	2.85
Cu	<0.01	0.49	0.70	4.47		1.90	0.23	2.09	<0.01	1.51	0.46	3.63	1.94	0.55	1.57	11.91		1.10	1.06	4.02	4.67	2.65	2.44	2.36
Zn	2.37	0.14	0.49	7.43	1.99	0.72	2.10	7.39	3.58	0.20	0.87	6.15	4.11	1.22	1.72	6.75	2.35	0.99	4.09	10.61	3.02		4.95	10.71
Rb		0.06	0.21	0.65	0.38	0.73	3.31	6.70	2.75	0.27	1.34	6.10	1.95	0.12	0.29	3.19	2.75	1.14	9.63	18.51	2.93	1.31	13.15	23.75
Sr	56.09		51.18	76.40	1.57		31.29	7.02	41.86		11.33	52.80	32.81	0.32	2.46	40.40	15.20		4.92	20.90	13.68		20.66	21.15
Y	2.28	2.63	1.86	7.86	1.56	2.98	2.36	9.21	2.31	0.69	0.35	4.23	2.06	0.41	0.52	3.69	1.89	0.65	0.46	4.04	2.14	1.79	1.20	6.38
Zr	<0.01	0.08	0.22	0.55	<0.01	1.28	1.18	3.52	0.05	0.34	1.27	2.15		0.27	0.97	2.03	0.04	1.07	3.57	6.89	<0.01	0.56	1.64	3.19
Mo	0.34	0.15	0.07	0.73	<0.01	0.13	0.03	0.36	<0.01	0.33	0.06	0.60	0.39	0.35	0.28	1.30	0.05	0.36	0.13	0.81	0.20	0.18	0.18	0.58
Cs	0.02	0.01	0.02	0.10	0.18	0.18	0.40	1.17	0.51	0.06	0.11	0.93	0.33	0.03	0.04	0.54	0.56	0.23	1.00	2.51	0.34	0.11	0.70	1.61
Ba	8.26	1.09	1.06	12.24	1.34	0.94	0.51	3.83	10.87	1.15	0.87	16.20	1.85	1.77	0.11	3.57	3.43	0.39	1.47	7.45	3.76	1.02	2.09	9.00
La	0.37	0.05	0.66	1.38	0.30	0.28	1.33	2.69	0.41	0.10	0.31	1.26	0.27	0.12	0.92	1.79	0.49	0.25	0.67	2.04	0.42	0.24	0.89	2.32
Ce	0.52	0.14	0.99	2.04	0.42	0.51	1.92	3.74	0.70	0.21	0.47	1.97	0.45	0.22	1.35	2.84	0.94	0.65	1.26	3.92	0.64	0.50	1.38	3.51
Pr	0.06	0.01	0.12	0.26	0.05	0.06	0.22	0.46	0.09	0.03	0.05	0.24	0.06	0.03	0.14	0.32	0.12	0.08	0.13	0.47	0.08	0.06	0.15	0.42
Nd	0.27	0.06	0.53	1.10	0.23	0.28	0.95	2.04	0.39	0.11	0.19	1.00	0.28	0.12	0.45	1.22	0.51	0.31	0.44	1.85	0.34	0.28	0.60	1.78
Sm	0.06	0.02	0.11	0.24	0.05	0.07	0.17	0.40	0.09	0.03	0.03	0.21	0.08	0.03	0.06	0.25	0.13	0.07	0.07	0.37	0.08	0.06	0.10	0.35
Eu	0.02	0.01	0.04	0.09	0.01	0.03	0.05	0.14	0.02	0.01	0.01	0.06	0.03	0.01	0.01	0.07	0.04	0.02	0.02	0.10	0.02	0.02	0.03	0.11
Gd	0.10	0.05	0.17	0.39	0.07	0.15	0.24	0.63	0.14	0.05	0.03	0.29	0.14	0.05	0.06	0.32	0.16	0.09	0.07	0.45	0.13	0.12	0.13	0.51
Tb	0.02	0.01	0.02	0.07	0.01	0.03	0.03	0.10	0.02	0.01	<0.01	0.05	0.02	0.01	0.01	0.05	0.03	0.01	0.01	0.07	0.02	0.02	0.01	0.08
Dy	0.14	0.14	0.15	0.52	0.12	0.24	0.21	0.74	0.20	0.05	0.03	0.35	0.19	0.05	0.05	0.35	0.22	0.09	0.06	0.48	0.18	0.16	0.10	0.67
Ho	0.04	0.04	0.03	0.12	0.03	0.06	0.05	0.17	0.05	0.01	0.01	0.08	0.05	0.01	0.01	0.07	0.05	0.02	0.01	0.10	0.05	0.04	0.02	0.13
Er	0.15	0.14	0.09	0.42	0.13	0.21	0.16	0.60	0.19	0.04	0.02	0.28	0.16	0.03	0.04	0.26	0.18	0.05	0.04	0.33	0.19	0.11	0.08	0.44
Tm	0.02	0.02	0.01	0.06	0.02	0.03	0.02	0.10	0.03	0.01	<0.01	0.04	0.02	<0.01	0.01	0.04	0.03	0.01	0.01	0.06	0.03	0.01	0.01	0.07
Yb	0.16	0.08	0.05	0.34	0.21	0.18	0.14	0.65	0.21	0.03	0.02	0.31	0.16	0.02	0.05	0.27	0.21	0.04	0.04	0.36	0.26	0.07	0.09	0.51
Lu	0.03	0.01	0.01	0.05	0.04	0.03	0.02	0.11	0.04	<0.01	<0.01	0.05	0.02	<0.01	0.01	0.05	0.03	0.01	0.01	0.06	0.05	0.01	0.01	0.09
Hf	<0.01	<0.01	<0.01	0.01	<0.01	0.01	0.01	0.02	<0.01	0.01	0.02	0.04		0.01	0.01	0.03	<0.01	0.02	0.08	0.14	<0.01	0.01	0.02	0.05
Pb	0.29		0.18	0.72	0.84	0.01	0.12	0.77	0.50	0.16	0.07	1.01	1.39	0.20		2.03	0.89	0.15	0.14	1.72	0.75	0.10	0.10	1.44
Th	0.01	0.03	0.01	0.05	0.02	0.03	0.04	0.07	0.03	0.07	0.13	0.15	0.02	0.03	0.02	0.08	0.11	0.19	0.60	0.56	0.03	0.06	0.15	0.17
U	<0.01	<0.01		0.01	0.01	0.01	<0.01	0.02	0.01	0.01	0.02	0.05	0.03	0.03	0.08	0.17	0.03	0.03	0.05	0.13	0.01	<0.01	0.01	0.04

Fractions: A= Acetate, B= Oxalate, C: HF, D= Bulk-rock

wt% | ppm | neg. | < d.l. | < BEC | err. | >l.r. | n.m.

	GAS371				GAS390				GAS404				GAS420				GAS434				GAS441			
Frac:	A	B	C	D	A	B	C	D	A	B	C	D	A	B	C	D	A	B	C	D	A	B	C	D
Ca	2.01	<0.01	0.18	2.32	2.00	<0.01	0.24	2.40	0.76	0.01	0.01	0.91	2.14	0.01	0.15	2.48	0.75	0.01	0.05	0.82	0.47	0.01	0.08	0.55
Fe	7.92	5.62	15.35	27.88	15.52	6.66	8.42	30.44	1.61	20.94	12.44	34.41	8.34	20.69	2.42	32.49	7.04	19.91	4.39	32.11	0.91	26.97	2.87	30.87
Mg	0.52	0.16	0.90	1.68	1.00	0.33	0.48	1.96	0.16	0.04	0.90	1.15	1.34	0.10	0.24	1.89	0.86	0.09	0.17	1.26	0.52	0.08	0.89	1.68
Mn	0.28	0.04	0.04	0.64	0.28	0.02	0.02	0.59	0.01	<0.01	0.02	0.04	0.30	0.02	<0.01	0.42	0.02	<0.01	<0.01	0.04	0.03	<0.01	<0.01	0.04
Si	0.28	0.11		18.76	0.95	0.27		15.37	0.84	0.20		21.41	0.38	0.14		16.29	0.60	0.20		20.77	0.65	0.18		23.89
K	0.03	0.02	0.07	0.08	0.03	0.01	0.02	0.03	0.03	0.03	0.11	0.14	0.07		0.01	0.03	0.06		<0.01	0.01	0.03	0.03	<0.01	0.01
Na				1.21				0.01				0.01				0.04								0.10
S				0.05				0.13				0.12				0.12				0.08				0.06
C				3.34				4.59				0.31				3.50				1.96				0.29
Al	<0.01	0.01	0.02		<0.01	0.01	0.02		<0.01	<0.01	0.01		<0.01	<0.01	0.01		<0.01	<0.01	<0.01		<0.01	<0.01	0.04	
Ti		3.01	13.95	40.61	<0.01	9.33	17.06	39.22	<0.01	4.55	0.52	21.66	1.04	7.85	3.88	31.37	1.33	5.25		24.91	<0.01	2.60	4.31	20.28
Be	0.35	0.11	0.46	1.19	0.61	0.13	0.12	1.36	0.15	0.24	0.33	0.90	0.28	0.24	0.10	0.84	0.19	0.20	0.04	0.54	0.07	0.13	0.03	0.27
Sc	0.21	0.04	0.13	0.41	0.71	0.15	0.02	0.30	0.68	0.06	0.04	0.23	0.13		0.06	0.26	0.76	0.03	0.03	0.32	0.61	0.02	0.04	0.13
V	0.27	0.38	0.11	8.18	0.69	1.01		5.32	0.63	1.75		4.67	0.55	1.70		4.51	1.62	1.70		7.82	2.10	0.93	0.70	5.78
Cr	<0.01	0.94	0.54	12.32	<0.01	0.52	0.42	8.70	<0.01	0.73	0.35	9.91	1.98			8.52	7.88	2.90	1.71	21.23	10.07		0.42	28.49
Co	0.17	0.05	0.45	1.62	0.20	0.12	0.41	1.33	0.11	0.15	0.20	0.61	0.38	0.16	0.52	1.59	0.31	0.23	0.10	0.87	0.50	0.04	0.04	0.91
Ni	0.20	0.11	0.80	5.05	0.36	0.31	0.62	3.29	0.71	0.98	0.86	3.26	1.07	0.68	0.49	3.04	2.06	1.64	0.68	5.97	3.14	0.19	0.26	9.83
Cu		1.35	1.66	8.61		1.10	1.05	3.99	2.13	1.58	1.85	3.84	1.85	2.16	1.27	2.91	6.91	4.14	2.04	7.27	2.32	0.84	0.46	5.83
Zn	1.96	0.69	5.14	13.53	2.90	1.75	5.03	19.00	1.73		9.60	14.16	6.21	0.75	0.78	11.90	4.08	0.98	0.28	8.32	3.68		1.71	8.63
Rb	0.98	0.98	8.21	16.58	0.45	0.73	2.09	5.95	2.92	1.22	16.27	25.90	2.42	0.74	4.06	9.80	0.51	0.18	0.47	1.34	0.31	0.03	0.15	0.67
Sr	46.45		26.77	79.79	32.55		43.01	64.31	17.11		5.93	31.17	32.94		38.58	48.47	14.68		0.95	19.53	5.56		10.80	7.39
Y	2.91	1.52	1.98	10.16	2.91	1.61	1.47	10.28	1.64	0.80	1.07	4.42	2.25	2.41	1.55	7.75	1.13	0.39	0.74	2.37	0.76	0.60	0.78	2.19
Zr	<0.01	0.33	1.49	3.18	<0.01	0.74	0.84	2.78	<0.01	0.41	0.46	1.88		0.28	0.88	1.96		0.34	0.53	1.74		0.18	0.79	1.23
Mo	0.11	0.17	0.09	0.79	0.14	0.10	0.05	0.39	<0.01	0.34	0.09	0.75	0.29		0.08	0.52	0.29	0.49	0.19	1.45	0.46	0.32	0.05	1.06
Cs	0.15	0.14	0.57	1.41	0.18	0.15	0.19	0.96	0.27	0.11	1.04	1.85	0.19	0.05	0.19	0.62	0.05	0.03	0.03	0.19	0.06	0.01	0.01	0.15
Ba	11.85	0.83	2.14	23.54	9.11		1.34	17.10	3.49	2.16	0.84	9.79	13.92	1.54	1.73	24.42	1.84	<0.01	0.09	4.97	1.27	0.43	1.24	2.75
La	0.82	0.19	0.84	3.06	0.80	0.09	0.95	3.12	0.31	0.09	0.56	1.81	0.54	0.14	0.70	1.96	0.19	0.09	0.19	0.77	0.18	0.06	0.33	0.71
Ce	1.10	0.44	1.63	4.90	1.01	0.22	1.63	4.54	0.50	0.25	0.89	3.12	0.69	0.29	1.09	2.82	0.31	0.20	0.27	1.21	0.25	0.16	0.53	1.06
Pr	0.12	0.05	0.21	0.60	0.11	0.02	0.19	0.53	0.07	0.04	0.09	0.39	0.08	0.04	0.14	0.35	0.04	0.02	0.03	0.14	0.03	0.02	0.05	0.13
Nd	0.46	0.22	0.88	2.52	0.42	0.10	0.83	2.19	0.31	0.18	0.33	1.64	0.34	0.15	0.61	1.51	0.17	0.10	0.09	0.57	0.15	0.10	0.21	0.54
Sm	0.09	0.05	0.18	0.51	0.08	0.02	0.16	0.44	0.08	0.05	0.04	0.31	0.07	0.03	0.11	0.30	0.04	0.02	0.01	0.13	0.03	0.02	0.04	0.11
Eu	0.03	0.02	0.05	0.19	0.04	0.01	0.06	0.20	0.03	0.01	0.01	0.09	0.03	0.02	0.04	0.13	0.01	0.01	<0.01	0.05	0.01	0.01	0.01	0.04
Gd	0.14	0.09	0.23	0.71	0.14	0.06	0.20	0.65	0.12	0.08	0.06	0.37	0.11	0.08	0.16	0.48	0.07	0.04	0.03	0.18	0.05	0.04	0.05	0.16
Tb	0.03	0.02	0.03	0.12	0.03	0.01	0.03	0.11	0.02	0.01	0.01	0.05	0.02	0.02	0.02	0.07	0.01	0.01	<0.01	0.03	0.01	0.01	0.01	0.02
Dy	0.22	0.14	0.20	0.85	0.21	0.12	0.16	0.80	0.14	0.08	0.07	0.37	0.15	0.16	0.13	0.56	0.10	0.04	0.05	0.20	0.06	0.05	0.05	0.17
Ho	0.06	0.03	0.04	0.20	0.06	0.03	0.03	0.18	0.03	0.02	0.02	0.08	0.04	0.04	0.03	0.13	0.02	0.01	0.01	0.05	0.01	0.01	0.01	0.04
Er	0.24	0.10	0.14	0.67	0.23	0.11	0.09	0.65	0.12	0.05	0.09	0.29	0.17	0.15	0.09	0.46	0.09	0.03	0.05	0.17	0.05	0.04	0.05	0.14
Tm	0.03	0.01	0.02	0.10	0.04	0.01	0.01	0.10	0.02	0.01	0.02	0.05	0.03	0.02	0.01	0.07	0.02	<0.01	0.01	0.03	0.01	<0.01	0.01	0.02
Yb	0.21	0.07	0.17	0.67	0.28	0.09	0.06	0.67	0.12	0.04	0.13	0.33	0.21	0.11	0.07	0.47	0.12	0.02	0.04	0.21	0.06	0.02	0.05	0.14
Lu	0.03	0.01	0.03	0.11	0.05	0.01	0.01	0.11	0.02	<0.01	0.02	0.06	0.04	0.02	0.01	0.08	0.02	<0.01	<0.01	0.03	0.01	<0.01	0.01	0.02
Hf	<0.01	0.01	0.01	0.03	<0.01	0.01	0.01	0.03	<0.01	0.01	<0.01	0.03	<0.01	0.01	0.01	0.03	<0.01	0.01	0.01	0.04	<0.01	0.01	0.01	0.02
Pb	0.86	0.04	0.16	1.46	2.98	0.02	0.38	5.03	0.36	0.01	0.04	0.86	0.76		0.23	1.74	0.33	0.06	0.01	1.00	0.20		0.08	0.57
Th	0.03	0.06	0.06	0.12	0.03	0.03	0.06	0.11	0.01	<0.01	0.04	0.06	0.02	0.03	0.05	0.09	0.03	0.01	0.04	0.08	0.02	0.02	0.06	0.05
U	0.01	0.01	0.01	0.03	0.01	0.01	0.01	0.03	<0.01		<0.01	0.01	<0.01	<0.01	0.01	0.02	0.01			0.01	<0.01		0.01	0.01

Fractions: A= Acetate, B= Oxalate, C: HF, D= Bulk-rock

wt% | ppm | neg. | < d.l. | < BEC | err. | >l.r. | n.m.

	GAS447				GAS461				GAS474				GAS488				GAS505				GAS513			
Frac:	A	B	C	D	A	B	C	D	A	B	C	D	A	B	C	D	A	B	C	D	A	B	C	D
Ca	0.26	0.01	0.07	0.35	0.77	0.01	0.03	0.99	1.44	<0.01	0.15	1.73	0.50	0.01	0.04	0.59	0.69	0.02	0.07	0.80	1.96	0.01	0.05	2.17
Fe	1.28	25.21	6.97	33.24	1.04	27.93	3.47	33.91	12.97	2.94	13.41	28.45	0.84	32.51	6.09	41.12	0.99	28.67	9.76	39.78	8.91	10.00	9.95	28.34
Mg	0.19	0.03	0.90	1.21	0.38	0.02	0.29	0.97	1.10	0.17	1.05	2.44	0.44	0.06	0.58	1.26	0.42	0.03	0.41	1.04	0.98	0.04	0.01	1.14
Mn	0.01	<0.01	0.01	0.03	0.03	<0.01	<0.01	0.04	0.32	0.03	0.02	0.42	0.03	<0.01	<0.01	0.04	0.03	<0.01	<0.01	0.05	0.05	<0.01	<0.01	0.08
Si	0.57	0.26		23.07	0.24	0.12		21.86	0.71	0.10		17.43	0.49	0.18		17.37	0.38	0.15		18.37	0.17	0.02		20.82
K	0.02	0.02	0.03	0.03	0.02	0.02	<0.01	0.01	0.08		0.08	0.12	0.03	0.01	<0.01		0.02	0.02	0.01	0.01	0.05		<0.01	0.01
Na								0.22				0.02				0.11				0.03				0.01
S				0.06				0.09				0.08				0.11				0.04				0.08
C				0.15				0.57				4.48				0.37				0.45				3.53
Al	<0.01	<0.01	0.01		<0.01	<0.01	<0.01	0.01	0.01	0.03	0.11	0.13	<0.01	<0.01	0.01		<0.01	<0.01	<0.01		0.01	<0.01	0.01	
Ti	0.65	5.48		23.61	0.95	2.19	8.03	18.96	1.89	15.17	88.06	130.73	0.60	5.35	9.22	22.04	<0.01	4.42	4.66	28.68	0.16	4.77	4.26	32.80
Be	0.13	0.15	0.10	0.51	0.07	0.21	0.09	0.52	1.26	0.25	0.61	2.32	0.10	0.33	0.09	0.62	0.12	0.35	0.22	0.68	0.36	0.09	0.31	1.01
Sc		0.11		0.27			0.02	0.12	1.10	0.24	0.30	1.11	0.49	0.08	0.17	0.14	0.06	0.04	0.03	0.45	0.31		0.01	0.38
V	2.41	1.46		7.46	2.92	1.22		8.36	2.25	2.51	3.68	10.41	2.05	1.86	0.39	9.77	2.79	1.56		7.55	2.84	0.98	0.25	9.54
Cr	8.77	<0.01	0.16	21.81	12.79		0.47	26.63	4.17	1.83	2.75	10.49	12.07	0.46	0.42	31.09	17.05		0.39	19.90	16.22	<0.01	9.41	26.81
Co	0.53	0.13	0.05	0.97	0.76	0.05	0.02	1.26	0.52	0.19	0.94	1.88	0.55	0.14	0.06	1.49	0.71	0.03	0.03	0.92	0.69	0.04	0.12	1.38
Ni	3.29	0.59	0.42	5.79	4.54	0.31	0.15	7.34	1.15	0.98	2.81	5.77	3.92	0.51	0.46	8.59	4.38	0.06	0.36	6.18	4.63	0.53	0.58	8.59
Cu	6.72	2.05	1.78	7.26	14.38	1.61	0.66	12.48	3.61	1.88	2.21	3.94	9.83	1.24	1.53	14.25	2.91	0.52	1.46	14.38	6.48	1.01	2.48	8.98
Zn	1.80		2.16	7.78	4.59		1.56	9.20	3.86	0.97	7.31	13.77	7.05	0.55	4.50	10.84	1.50	<0.01	2.31	12.46	3.51	0.50	<0.01	8.18
Rb	0.22	0.04	0.49	1.07	0.30	0.05	0.07	0.40	3.07	0.46	2.85	7.31	0.36	0.05	0.16	0.45	0.02	0.04	0.04	0.72	0.42	0.04	0.31	0.98
Sr	5.45		18.34	8.72	13.61		10.85	18.61	9.50		38.56	12.28	7.60		6.64	21.82	8.20		16.95	10.94	7.82		19.53	12.49
Y	0.76	0.78	0.96	2.82	1.05	0.72	0.45	2.92	4.62	2.26	3.44	11.37	0.99	0.81	2.69	3.44	1.25	1.15	1.20	4.47	2.94	0.67	0.55	6.41
Zr		0.33	0.34	1.32	<0.01	0.19	0.50	1.04	0.01	0.90	5.93	9.14	<0.01	0.30	1.17	1.25		0.27	0.33	2.21		0.15	0.69	1.86
Mo	0.52	0.50	0.10	1.43	0.52	0.64	0.07	1.74	0.29	0.09	0.10	0.48	0.33	0.61	0.07	2.00	0.28	0.80	0.09	1.14	0.19	0.78	0.87	1.70
Cs	0.02	0.01	0.03	0.13	0.03	0.01	0.01	0.11	0.66	0.10	0.43	1.43	0.09	0.01	0.03	0.13	0.05	0.02	0.02	0.22	0.03	0.01	0.06	0.21
Ba	0.95	0.31	2.46	1.84	1.12	1.10	0.64	3.91	1.84		1.02	4.06	1.23	1.40	3.25	4.57	1.15	1.37	0.93	5.25	2.03		1.44	6.53
La	0.19	0.11	0.41	1.16	0.17	0.08	0.24	0.80	1.12	0.39	2.39	4.79	0.23	0.13	0.73	0.94	0.34	0.18	0.63	1.61	0.64	0.08	0.23	1.51
Ce	0.33	0.27	0.61	1.82	0.28	0.19	0.35	1.24	2.05	0.99	5.06	9.33	0.37	0.26	1.14	1.48	0.48	0.38	1.00	2.45	0.85	0.20	0.35	2.23
Pr	0.05	0.03	0.07	0.22	0.04	0.02	0.04	0.15	0.27	0.12	0.61	1.18	0.05	0.03	0.13	0.18	0.07	0.05	0.11	0.30	0.10	0.03	0.04	0.27
Nd	0.20	0.16	0.26	0.93	0.18	0.11	0.14	0.66	1.10	0.52	2.47	4.91	0.23	0.16	0.48	0.79	0.31	0.22	0.43	1.27	0.38	0.13	0.19	1.14
Sm	0.04	0.04	0.04	0.18	0.04	0.02	0.03	0.14	0.27	0.14	0.49	1.04	0.06	0.04	0.07	0.16	0.07	0.06	0.07	0.25	0.08	0.03	0.04	0.22
Eu	0.01	0.01	0.01	0.06	0.01	0.01	0.01	0.06	0.08	0.04	0.12	0.33	0.01	0.01	0.02	0.07	0.02	0.02	0.02	0.07	0.03	0.01	0.01	0.08
Gd	0.06	0.07	0.06	0.25	0.06	0.05	0.03	0.20	0.38	0.23	0.55	1.36	0.08	0.06	0.11	0.22	0.11	0.09	0.09	0.33	0.13	0.05	0.04	0.34
Tb	0.01	0.01	0.01	0.04	0.01	0.01	<0.01	0.03	0.07	0.04	0.07	0.22	0.01	0.01	0.02	0.03	0.02	0.01	0.01	0.04	0.02	0.01	0.01	0.05
Dy	0.07	0.07	0.06	0.25	0.08	0.06	0.03	0.22	0.53	0.30	0.47	1.50	0.08	0.07	0.14	0.25	0.11	0.11	0.09	0.30	0.18	0.05	0.04	0.40
Ho	0.02	0.02	0.02	0.05	0.02	0.01	0.01	0.05	0.12	0.06	0.10	0.30	0.02	0.01	0.04	0.06	0.02	0.02	0.02	0.07	0.05	0.01	0.01	0.10
Er	0.06	0.05	0.06	0.18	0.07	0.04	0.03	0.17	0.45	0.18	0.31	1.00	0.06	0.05	0.15	0.20	0.08	0.07	0.08	0.23	0.17	0.03	0.03	0.34
Tm	0.01	0.01	0.01	0.03	0.01	<0.01	<0.01	0.03	0.07	0.02	0.04	0.16	0.01	0.01	0.02	0.03	0.01	0.01	0.01	0.04	0.03	<0.01	<0.01	0.05
Yb	0.06	0.03	0.07	0.17	0.08	0.03	0.04	0.17	0.57	0.13	0.26	1.04	0.07	0.04	0.17	0.20	0.09	0.05	0.09	0.29	0.18	0.02	0.03	0.34
Lu	0.01	<0.01	0.01	0.03	0.01	<0.01	0.01	0.03	0.09	0.02	0.03	0.16	0.01	0.01	0.03	0.03	0.02	0.01	0.01	0.05	0.03	<0.01	0.01	0.05
Hf	<0.01	0.01	<0.01	0.02		0.01	0.01	0.02	<0.01	0.02	0.09	0.17	<0.01	0.01	0.02	0.02	<0.01	0.01	<0.01	0.03	<0.01	0.01	0.01	0.03
Pb	0.35	0.05	0.28	0.80	0.88	0.09	0.11	1.57	0.28		0.19	0.69	0.71	0.21	0.28	1.84	0.73	0.14	0.18	1.53	0.32		0.49	1.44
Th	0.02	<0.01	0.03	0.05	0.02	0.01	0.01	0.04	0.11	0.20	0.51	0.49	0.02	0.03	0.04	0.05	0.02	0.01	0.02	0.07	0.02	0.02	0.02	0.08
U	<0.01		<0.01	0.01	<0.01		<0.01	0.01	0.03	0.01	0.03	0.08	<0.01	<0.01	<0.01	0.01	<0.01		<0.01	0.01	<0.01	<0.01	<0.01	0.01

Fractions: A= Acetate, B= Oxalate, C: HF, D= Bulk-rock

wt% | ppm | neg. | < d.l. | < BEC | err. | >l.r. | n.m.

	HEX648				HEX651				HEX653				HEX656				HEX661				HEX667			
Frac:	A	B	C	D	A	B	C	D	A	B	C	D	A	B	C	D	A	B	C	D	A	B	C	D
Ca	4.35	0.01	0.02	4.64	1.14	0.01	0.09	1.35	3.04	0.01	0.09	3.29	4.12	0.01	0.04	4.54	7.22	0.01	0.03	7.85	3.09	0.01	0.06	3.31
Fe	8.28	9.36	2.39	20.19	14.64	10.10	5.01	29.47	16.49	6.23	8.15	30.63	15.87	1.46	2.69	20.49	14.56	3.13	3.39	21.74	3.02	18.40	3.92	25.37
Mg	0.64	0.02	0.02	0.74	1.09	0.25	0.19	1.69	1.69	0.25	0.53	2.65	1.81	0.08	0.23	2.35	2.12	0.14	0.21	2.80	0.87	0.03	0.27	1.31
Mn	0.46	0.02	0.01	0.32	0.35	0.05	0.04	0.45	0.52	0.06	0.03	0.53	1.78	0.06	0.02	1.69	2.06	0.08	0.04	1.72	0.26	<0.01	0.01	0.27
Si	0.22	0.05		23.50	0.38	0.14		16.19	0.52	0.08		9.31	0.33	0.02		16.01	0.40	0.05		10.54	0.49	0.13		23.11
K	0.03	0.01	<0.01	0.02	0.01	0.01	0.02	0.01	0.39	0.05	0.04	0.40	0.20	0.04	0.03	0.17	0.14	0.02	0.02	0.09	0.10	0.02	0.02	0.10
Na				0.02				0.01				0.11				0.06				0.03				0.03
S				0.57				0.06				0.10				0.11				0.08				0.20
C				4.18				5.97				7.75				7.52				7.72				1.86
Al	0.01	<0.01	0.02		0.03	0.11	0.04	0.16	0.05	0.11	0.47	0.69	0.03	0.03	0.17	0.25	0.02	0.04	0.12	0.21	0.03	0.03	0.08	0.15
Ti		6.81	22.68	28.55	1.56	35.44	195.11	228.56	0.41	37.10	554.78	538.69	2.27	8.93	165.69	158.25	2.34	17.67	113.25	108.14	<0.01	25.75	76.72	117.25
Be	0.35	0.04	0.06	0.33	1.15	0.38	0.18	1.82	1.06	0.27	0.23	1.32	0.33	0.01	0.07	0.39	0.32	0.03	0.07	0.32	0.16	0.08	0.05	0.29
Sc	0.23	0.09	0.01	0.15	0.82	0.45	0.17	0.99	2.06	0.68	0.79	2.56	0.97	<0.01	0.13	0.56	0.86	0.06	0.07	0.43	0.68	0.13	0.12	0.55
V	1.66	2.49	1.80	4.05	1.73	9.60	2.96	13.72	2.87	11.67	22.08	31.27	1.56	1.43	5.47	7.08	1.23	2.56	5.30	5.24	2.97	4.12	1.58	9.65
Cr	13.06	4.98	3.16	9.80	4.00	6.82	2.58	13.97	3.14	6.70	15.42	25.44	4.30	2.94	5.45	10.74	3.63	3.47	3.02	7.55	17.79	3.85	2.97	24.24
Co	0.42	0.17	1.30	1.42	0.24	0.13	1.07	1.36	1.11	0.23	2.79	3.76	0.73	0.22	0.69	1.30	0.46	0.10	2.90	2.23	0.72	0.18	0.53	1.47
Ni	3.03	1.27	5.76	7.40	2.41	3.35	4.07	10.34	5.30	3.48	14.22	22.35	1.59	0.90	1.86	4.14	2.04	1.06	2.55	4.03	5.55	1.59	1.52	7.97
Cu	8.59	2.90	8.90	4.71	4.79	1.65	2.90	6.01	9.90	2.56	6.35	17.50	6.16	1.45	1.00	2.77	6.27	0.67	2.90	4.19	9.76	2.45	5.12	10.34
Zn	10.96	0.88	0.02	2.51	3.70	2.01	3.16	10.56				31.22	1.48		1.62	7.58	2.74	0.67	2.20	3.34	2.15	0.73	1.06	5.19
Rb	1.50	0.02	0.02	0.90	0.56	0.26	0.31	1.32	23.71	5.71	3.76	30.91	10.09	1.51	2.01	12.79	5.60	0.58	0.71	5.74	5.54	0.47	0.90	6.95
Sr	26.83		11.01	20.40	4.32		25.57	5.44	9.44		26.33	9.73	12.32		15.00	11.34	21.33		10.98	17.09	12.78		6.90	13.40
Y	3.22	0.25	0.20	2.76	5.71	2.07	1.85	9.92	9.63	1.33	3.47	13.96	2.39	0.31	0.46	2.92	5.49	0.30	0.40	5.06	2.07	0.53	0.29	3.05
Zr	0.01	0.20	1.27	2.47	0.12	1.21	7.91	10.06	0.36	3.77	25.38	28.40	0.09	0.85	3.92	4.56	0.05	0.55	3.00	3.39	<0.01	0.54	2.95	3.96
Mo	0.82	0.56	0.52	1.06	0.23	0.31	0.14	0.49	0.57	0.47	0.08	0.82	0.38	0.41	0.17	0.69	0.32	0.27	0.39	0.28	0.64	0.52	0.15	1.42
Cs	0.15		0.01	0.15	0.25	0.17	0.11	0.61	3.65	1.19	1.02	5.48	2.01	0.36	0.47	2.60	1.02	0.13	0.14	1.08	0.94	0.12	0.11	1.30
Ba	1.67		0.66	2.11	1.45	0.18	0.28	2.14	3.20	2.74	6.47	8.72	3.05	<0.01	1.85	4.49	2.91	<0.01	0.81	3.07	2.06		0.44	3.06
La	1.34	0.09	0.50	1.60	1.31	0.26	0.78	2.55	2.29	0.37	2.92	5.67	1.13	0.05	0.12	1.21	2.58	0.08	0.13	2.25	0.90	0.37	0.82	2.47
Ce	1.83	0.20	0.72	2.33	2.27	0.69	1.63	4.78	4.07	0.84	4.97	10.09	1.78	0.20	0.27	2.06	4.26	0.25	0.29	3.89	1.65	0.72	1.36	4.21
Pr	0.20	0.02	0.07	0.25	0.30	0.09	0.20	0.64	0.52	0.12	0.55	1.21	0.20	0.02	0.04	0.26	0.51	0.03	0.04	0.48	0.20	0.08	0.13	0.47
Nd	0.76	0.09	0.22	1.00	1.27	0.39	0.88	2.87	2.23	0.51	1.92	4.82	0.77	0.11	0.15	1.00	1.99	0.13	0.16	1.94	0.76	0.27	0.39	1.72
Sm	0.15	0.02	0.03	0.18	0.29	0.10	0.19	0.66	0.56	0.13	0.29	1.01	0.16	0.03	0.03	0.21	0.44	0.03	0.03	0.43	0.17	0.05	0.05	0.31
Eu	0.05	<0.01	0.01	0.06	0.09	0.03	0.04	0.20	0.14	0.03	0.06	0.27	0.06	0.01	0.01	0.08	0.12	0.01	0.01	0.13	0.04	0.01	0.01	0.08
Gd	0.23	0.03	0.03	0.24	0.47	0.17	0.21	0.93	0.83	0.18	0.33	1.30	0.21	0.03	0.04	0.26	0.57	0.03	0.04	0.51	0.20	0.07	0.05	0.37
Tb	0.03	<0.01	0.01	0.04	0.08	0.03	0.03	0.15	0.15	0.03	0.05	0.23	0.03	<0.01	<0.01	0.04	0.09	<0.01	0.01	0.08	0.03	0.01	0.01	0.06
Dy	0.24	0.03	0.02	0.24	0.64	0.22	0.19	1.13	1.16	0.19	0.41	1.77	0.23	0.03	0.04	0.29	0.59	0.03	0.04	0.56	0.23	0.06	0.04	0.37
Ho	0.06	<0.01	0.01	0.06	0.15	0.05	0.04	0.25	0.28	0.04	0.10	0.40	0.05	0.01	0.01	0.06	0.13	0.01	0.01	0.11	0.05	0.01	0.01	0.08
Er	0.20	0.01	0.02	0.19	0.56	0.16	0.17	0.88	0.99	0.13	0.44	1.46	0.19	0.02	0.03	0.22	0.42	0.02	0.03	0.37	0.16	0.04	0.03	0.24
Tm	0.03	<0.01	0.01	0.03	0.09	0.02	0.03	0.14	0.16	0.02	0.07	0.25	0.03	<0.01	0.01	0.03	0.06	<0.01	<0.01	0.06	0.02	<0.01	0.01	0.03
Yb	0.19	0.01	0.02	0.19	0.65	0.15	0.17	0.99	1.16	0.14	0.54	1.78	0.19	0.01	0.04	0.23	0.38	0.01	0.04	0.36	0.15	0.02	0.04	0.23
Lu	0.03	<0.01	0.01	0.03	0.10	0.02	0.03	0.16	0.19	0.02	0.08	0.29	0.03	<0.01	0.01	0.04	0.06	<0.01	<0.01	0.06	0.02	<0.01	0.01	0.03
Hf	<0.01		0.03	0.05	<0.01	0.03	0.14	0.20	<0.01	0.09	0.53	0.61	<0.01	0.02	0.10	0.13	<0.01	0.01	0.08	0.10	<0.01		0.07	0.11
Pb	2.47	0.27	1.66	3.82	0.97	0.13	0.27	1.59	3.76	0.23	0.98	2.37	0.24		0.14	0.45	1.70	0.13	0.35	1.98	0.26		0.13	0.64
Th	0.04	0.02	0.09	0.09	0.15	0.24	0.36	0.45	0.45	0.28	1.08	1.95	0.13	0.06	0.35	0.32	0.17	0.06	0.29	0.30	0.10	0.16	0.35	0.38
U	0.01	<0.01	0.02	0.03	0.04	0.04	0.03	0.12	0.07	0.05	0.18	0.29	0.02	0.01	0.03	0.05	0.02	<0.01	0.03	0.05	0.03	0.02	0.06	0.12

Fractions: A= Acetate, B= Oxalate, C: HF, D= Bulk-rock

wt% | ppm | neg. | < d.l. | < BEC | err. | >l.r. | n.m.

	HEX672				HEX685				HEX694				HEX706				HEX722				HEX733			
Frac:	A	B	C	D	A	B	C	D	A	B	C	D	A	B	C	D	A	B	C	D	A	B	C	D
Ca	3.43	0.01	0.03	3.87	0.43	0.02	0.03	0.51	6.50	0.01	0.02	6.83	2.82	0.01	0.02	3.09	3.16	0.01	0.22	3.40	0.59	0.01	0.06	0.69
Fe	2.95	16.07	7.40	25.94	4.24	9.58	9.20	21.79	5.38	10.03	14.37	28.23	10.71	1.45	1.56	14.11	17.74	5.24	2.73	25.44	13.78	6.76	8.04	28.30
Mg	0.86	0.03	0.49	1.52	0.96	0.35	1.74	3.12	1.46	0.03	1.44	3.14	1.07	0.04	0.06	1.25	2.01	0.16	0.22	2.62	1.36	0.27	0.59	2.43
Mn	0.40	0.01	0.03	0.39	0.39	0.03	0.10	0.44	0.47	<0.01	0.05	0.44	0.53	0.02	0.01	0.52	2.66	0.18	0.02	2.50	0.23	0.03	0.01	0.25
Si	0.31	0.15		21.92	0.76	0.31		23.28	0.46	0.11		13.66	0.22	0.01		27.63	0.31	0.03		10.47	0.61	0.10		17.33
K	0.06	0.01	0.02	0.06	0.67	0.19	0.11	0.89	0.03	0.01	0.07	0.07	0.06	0.01	0.02	0.04	0.22	0.03	0.04	0.23	0.15	0.07	0.65	0.83
Na				0.02				0.24								0.02				0.06				0.03
S				0.29				0.13				0.05				0.08				0.20				0.09
C				2.17				1.20				3.94				4.12				7.92				4.61
Al	0.01	0.01	0.06	0.05	0.17	0.37	0.96	1.56	<0.01	<0.01	0.06		0.01	0.01	0.07	0.03	0.03	0.04	0.27	0.27	0.02	0.05	0.22	0.28
Ti	<0.01	16.63	74.05	99.46	1.91	101.76	945.39	897.43	<0.01	4.72	53.30	28.27		12.19	82.64	62.90	0.36	8.12	167.73	176.97	0.27	36.91	185.85	200.92
Be	0.19	0.08	0.09	0.36	0.32	0.05	0.17	0.48	0.21	0.03	0.09	0.28	0.13	<0.01	0.04	0.14	0.35	0.02	0.04	0.34	0.17	0.04	0.44	0.57
Sc	0.37	0.08	0.14	0.37	2.60	0.65	1.79	3.32	0.47	0.06	0.03	0.18	0.25	0.02	0.05	0.35	0.86		0.19	0.82	0.70	0.08	0.70	0.85
V	1.27	3.15	1.23	5.96	4.32	17.41	8.14	26.31	0.48	1.43	0.79	2.66	2.55	1.84	3.13	7.96	0.75	1.68	8.29	7.29	1.00	3.54	2.31	6.57
Cr	8.38	2.11	1.96	11.64	5.22	19.58	10.55	29.93	3.59	0.03	0.41	4.09	12.59	3.98	4.64	17.54	0.86	2.59	6.27	11.65	4.31	7.07	2.67	14.51
Co	0.30	0.07	1.23	1.59	1.11	0.76	3.06	4.59	0.13	0.03	0.15	0.27	0.75	0.15	0.36	1.13	0.37	0.12	2.61	3.07	0.46	0.23	0.85	1.40
Ni	2.08	1.10	4.32	7.60	3.45	4.12	8.03	14.75	0.94	0.31	2.16	3.07	3.79	0.90	0.98	5.71	1.40	0.65	2.91	5.73	1.57	1.78	3.99	7.02
Cu	4.41	1.50	4.95	5.43	2.67	2.15	4.37	7.25	3.46	1.37	1.72	1.34	6.96	1.40	2.70	7.48	0.25	1.99	4.97	8.09	3.98	2.46	3.93	4.46
Zn	0.02	0.54	3.54	4.40	5.37	1.86	10.24	13.12	0.70	0.36	6.84	5.91	3.76	0.50	1.64	4.16	7.92	2.39	4.26	6.84	1.99	1.37	3.75	6.41
Rb	3.02	0.17	0.66	3.46	35.22	19.71	12.38	60.77	0.46	0.05	1.62	1.57	2.44	0.16	0.97	2.89	10.70	2.23	3.04	15.36	9.95	9.96	66.98	83.61
Sr	14.77		13.08	14.62	13.54		10.43	13.63	27.71		7.10	24.99	41.10		9.43	39.81	78.92		30.68	75.15	14.70		15.50	15.89
Y	1.81	0.26	0.25	2.31	1.81	1.04	2.53	4.58	6.25	0.21	0.50	6.31	3.85	1.07	0.83	5.47	6.27	1.12	0.73	7.78	1.81	0.77	0.58	3.02
Zr		0.21	2.16	2.37	0.09	3.38	27.79	26.87	<0.01	0.11	1.30	0.66	0.01	0.23	3.56	1.86	0.05	1.45	4.47	5.56	0.02	1.13	7.00	7.52
Mo	0.36	0.22	0.15	0.72	0.21	0.29	0.18	0.52	0.26	0.10	0.05	0.26	0.38	0.84	0.24	1.24	0.83	0.36	0.04	0.38	0.45	0.35	0.16	0.54
Cs	0.53	0.05	0.08	0.68	7.94	6.22	2.16	15.01	0.05	0.01	0.07	0.16	0.42	0.02	0.09	0.55	2.11	0.36	0.30	2.66	1.13	1.12	4.83	7.07
Ba	0.89		0.62	1.50	32.02	2.76	8.43	38.44	0.82	<0.01	0.88	1.24	3.26		3.95	4.25	11.50	2.45	5.46	15.57	6.56	0.36	1.67	9.05
La	0.50	0.08	0.16	0.76	0.69	0.69	2.30	3.63	1.35	0.04	0.21	1.46	0.56	0.18	0.55	1.35	2.07	0.38	0.86	3.19	0.63	0.26	0.80	1.76
Ce	0.90	0.20	0.29	1.44	1.50	1.72	4.93	7.60	1.69	0.10	0.42	1.93	0.99	0.37	0.86	2.21	3.43	0.89	1.82	5.93	1.30	0.66	1.64	3.54
Pr	0.12	0.02	0.04	0.18	0.20	0.21	0.58	0.94	0.20	0.01	0.04	0.24	0.14	0.04	0.09	0.29	0.40	0.12	0.24	0.73	0.17	0.08	0.18	0.44
Nd	0.46	0.11	0.14	0.79	0.82	0.81	2.02	3.67	0.87	0.06	0.14	1.05	0.58	0.20	0.35	1.24	1.49	0.50	0.96	2.94	0.68	0.33	0.63	1.75
Sm	0.11	0.02	0.03	0.17	0.22	0.19	0.39	0.78	0.19	0.01	0.02	0.23	0.15	0.05	0.06	0.27	0.33	0.12	0.19	0.63	0.17	0.07	0.11	0.38
Eu	0.04	0.01	0.01	0.06	0.04	0.04	0.06	0.16	0.05	<0.01	<0.01	0.07	0.04	0.01	0.01	0.08	0.09	0.03	0.04	0.19	0.03	0.02	0.02	0.07
Gd	0.15	0.03	0.03	0.22	0.25	0.21	0.36	0.76	0.32	0.02	0.03	0.37	0.22	0.08	0.07	0.38	0.43	0.16	0.18	0.74	0.20	0.10	0.10	0.40
Tb	0.02	<0.01	0.01	0.03	0.04	0.03	0.06	0.12	0.05	<0.01	<0.01	0.06	0.04	0.01	0.01	0.06	0.08	0.02	0.02	0.12	0.03	0.01	0.01	0.06
Dy	0.17	0.03	0.03	0.24	0.28	0.17	0.38	0.75	0.42	0.02	0.04	0.48	0.29	0.09	0.07	0.48	0.57	0.16	0.11	0.84	0.23	0.10	0.07	0.42
Ho	0.04	0.01	0.01	0.05	0.06	0.03	0.08	0.14	0.11	<0.01	0.01	0.12	0.08	0.02	0.02	0.11	0.14	0.03	0.02	0.18	0.05	0.02	0.01	0.08
Er	0.14	0.02	0.02	0.17	0.17	0.08	0.30	0.46	0.43	0.01	0.03	0.44	0.28	0.07	0.06	0.38	0.52	0.07	0.06	0.60	0.16	0.06	0.05	0.27
Tm	0.02	<0.01	0.01	0.03	0.03	0.01	0.04	0.07	0.06	<0.01	0.01	0.07	0.04	0.01	0.01	0.06	0.08	0.01	0.01	0.10	0.02	0.01	0.01	0.04
Yb	0.13	0.01	0.03	0.18	0.19	0.05	0.33	0.49	0.46	0.01	0.04	0.48	0.32	0.04	0.05	0.41	0.59	0.04	0.05	0.65	0.16	0.05	0.07	0.26
Lu	0.02	<0.01	0.01	0.03	0.03	0.01	0.05	0.07	0.08	<0.01	0.01	0.09	0.05	0.01	0.01	0.07	0.09	0.01	0.01	0.10	0.02	0.01	0.01	0.04
Hf	<0.01		0.05	0.06	<0.01	0.12	0.82	0.80	<0.01		0.03	0.02	<0.01		0.09	0.05	<0.01	0.05	0.12	0.16	<0.01	0.01	0.18	0.22
Pb	0.39	0.01	0.21	0.85	0.77	0.12	0.38	1.34	0.29		0.06	0.30	1.21	0.24	0.15	1.85	1.57	0.22	0.88	2.51	0.46	0.03	0.29	0.97
Th	0.06	0.06	0.18	0.17	0.76	1.26	3.31	2.53	0.02	0.01	0.17	0.08	0.07	0.15	0.25	0.25	0.30	0.28	0.25	0.83	0.14	0.31	0.62	0.58
U	0.01	<0.01	0.02	0.03	0.15	0.07	0.42	0.54	0.02	<0.01	0.03	0.04	0.01	<0.01	0.04	0.05	0.05	0.02	0.14	0.18	0.02	0.01	0.08	0.11

Fractions: A= Acetate, B= Oxalate, C: HF, D= Bulk-rock

wt% | ppm | neg. | < d.l. | < BEC | err. | >l.r. | n.m.

	HEX744				HEX753				HEX767				HEX780				HEX792				HEX802			
Frac:	A	B	C	D	A	B	C	D	A	B	C	D	A	B	C	D	A	B	C	D	A	B	C	D
Ca	1.81	0.01	0.21	2.08	0.89	0.01	0.01	0.98	2.43	0.01	0.03	2.62	3.57	0.01	0.01	3.95	1.91	0.01	<0.01	2.02	0.54	0.01	0.08	0.66
Fe	13.71	2.36	6.22	22.72	12.47	6.23	8.13	26.89	11.57	4.76	7.46	23.28	6.48	17.18	5.50	29.16	12.00	11.34	2.51	25.73	6.52	23.24	8.03	39.11
Mg	1.31	0.17	0.47	2.13	1.23	0.41	0.57	2.29	1.37	0.13	0.58	2.23	1.24	0.11	0.31	1.88	1.47	0.11	0.16	1.87	0.62	0.08	0.32	1.13
Mn	0.38	0.05	0.02	0.50	0.27	0.02	0.02	0.30	1.72	0.10	0.10	1.95	0.33	0.01	0.02	0.32	0.32	0.02	<0.01	0.34	0.37	0.02	0.02	0.41
Si	0.22	0.02		19.46	1.09	0.21		19.71	0.30	0.06		18.03	0.30	0.22		17.29	0.38	0.16		19.95	0.47	0.25		15.31
K	0.25	0.04	0.11	0.34	0.11	0.08	0.41	0.53	0.08	0.05	0.64	0.70	0.22	0.09	0.21	0.46	0.11	0.06	0.13	0.28	0.22	0.07	0.08	0.33
Na				0.26				0.01				0.01				0.07				0.05				0.26
S				0.08				0.12				0.08				0.08				0.07				0.05
C				5.30				3.27				4.88				3.35				4.10				1.98
Al	0.01	0.02	0.25	0.28	0.01	0.04	0.10	0.14	0.01	0.02	0.17	0.18	0.02	0.06	0.18	0.23	0.02	0.03	0.07	0.09	0.03	0.06	0.13	0.25
Ti	2.62	8.65	176.94	210.13	2.69	62.89	76.15	135.83	1.47	20.21	141.04	177.86	1.91	49.74	159.53	196.59	0.02	36.85	110.03	150.87	2.23	36.40	78.39	133.11
Be	0.06	0.01	0.13	0.23	0.09	0.02	0.12	0.20	0.04	0.01	0.21	0.25	0.07	0.05	0.09	0.21	0.13	0.04	0.13	0.27	0.06	0.05	0.07	0.21
Sc	0.17		0.68	0.89	1.08	0.21	0.30	0.53	0.30	0.02	0.36	0.64	0.47	0.24	0.58	0.80	0.43	0.12	0.23	0.44	0.44	0.15	0.46	0.64
V	0.68	0.46	5.78	9.85	1.69	2.81	3.78	6.63	0.90	4.05	0.07	7.09	0.66	7.05	0.41	8.73	1.39	3.60	1.24	7.24	1.01	5.97		9.26
Cr	4.70	1.78	8.01	15.99	5.34	4.59	3.99	12.86	4.46	5.81	3.56	13.47	1.91	13.36	3.59	18.10	8.68	8.88	3.09	22.30	5.89	12.84	4.31	24.45
Co	0.50	0.09	1.20	1.97	0.37	0.26	0.60	1.18	0.60	0.17	0.97	1.79	0.50	0.42	1.34	1.96	0.70	0.29	0.75	1.72	0.44	0.26	0.78	1.54
Ni	1.57	0.53	3.48	6.32	1.30	1.85	1.95	5.48	1.42	0.68	2.37	4.72	1.19	2.42	2.98	6.61	2.66	2.14	1.36	7.04	1.65	2.89	2.33	6.97
Cu	5.31	1.03	1.98	4.92	4.18	1.09	4.21	4.94	0.42	0.61	1.60	4.11	1.49	1.05	4.56	8.61	5.52	2.63	3.78	8.38	4.11	3.47	4.07	9.11
Zn	2.67	0.40	4.53	7.81	1.50	2.92	3.12	5.58	1.04		3.23	4.31	3.04	1.32	1.67	3.02	2.39	1.00	1.50	4.39	1.47		3.07	4.12
Rb	10.21	2.59	13.32	30.46	7.05	12.46	41.03	61.17	4.19	5.01	61.55	74.85	14.48	16.44	28.16	59.13	12.18	10.29	17.73	44.09	16.28	11.94	12.04	43.79
Sr	156.71		17.53	185.96	28.64		3.29	30.17	42.84		7.78	45.31	84.93	2.82	0.53	80.30	40.12		0.53	42.62	14.90		19.76	18.82
Y	2.14	0.80	0.69	4.15	1.06	0.39	0.25	1.71	1.43	0.33	0.33	2.19	1.87	0.11	0.08	2.04	0.99	0.10	0.06	1.26	0.86	0.77	0.19	1.93
Zr	0.07	0.99	5.82	7.80		0.65	3.07	3.72	0.02	0.70	4.35	5.25	0.05	1.50	4.44	6.29	0.08	1.06	2.46	3.58	0.03	1.73	3.00	5.17
Mo	0.23	0.23	0.15	0.45	0.39	0.32	0.17	0.78	0.28	0.26	0.10	0.53	0.23	0.45	0.16	0.52	0.35	0.76	0.20	1.21	0.22	0.54	0.13	0.82
Cs	2.10	0.45	1.10	4.25	0.66	1.21	3.00	5.07	0.55	0.49	4.50	5.96	1.67	1.90	1.74	5.47	0.74	0.93	1.06	3.10	1.98	1.36	0.95	4.69
Ba	9.47	1.42	6.31	18.89	5.70	0.12	1.70	7.82	9.41	0.20	1.37	12.11	10.70	2.62	4.06	16.57	9.65	0.39	2.60	12.80	9.81	2.14	3.41	15.74
La	0.71	0.32	0.80	2.33	0.52	0.15	0.13	0.85	0.66	0.12	0.16	1.07	0.64	0.06	0.43	1.31	0.49	0.05	0.16	0.81	0.32	0.18	0.36	0.99
Ce	1.26	0.77	1.60	4.31	0.75	0.37	0.29	1.49	1.14	0.36	0.36	2.05	1.17	0.10	0.60	2.15	0.79	0.12	0.24	1.30	0.59	0.49	0.70	1.97
Pr	0.15	0.09	0.18	0.51	0.09	0.05	0.04	0.18	0.13	0.04	0.04	0.25	0.16	0.01	0.06	0.26	0.10	0.01	0.02	0.15	0.08	0.06	0.09	0.26
Nd	0.55	0.35	0.67	1.99	0.32	0.18	0.13	0.73	0.45	0.18	0.18	0.94	0.64	0.05	0.18	0.99	0.37	0.06	0.07	0.60	0.28	0.27	0.33	1.05
Sm	0.11	0.08	0.13	0.41	0.07	0.04	0.02	0.15	0.09	0.04	0.03	0.21	0.17	0.01	0.02	0.22	0.08	0.01	0.01	0.12	0.06	0.06	0.06	0.22
Eu	0.03	0.02	0.03	0.10	0.02	0.01	0.01	0.04	0.02	0.01	0.01	0.05	0.06	<0.01	<0.01	0.08	0.03	<0.01	<0.01	0.04	0.02	0.02	0.01	0.06
Gd	0.14	0.09	0.12	0.41	0.08	0.05	0.03	0.17	0.12	0.05	0.04	0.21	0.22	0.02	0.02	0.26	0.10	0.01	0.01	0.14	0.08	0.09	0.06	0.25
Tb	0.03	0.01	0.01	0.07	0.01	0.01	<0.01	0.03	0.02	0.01	<0.01	0.03	0.03	<0.01	<0.01	0.04	0.01	<0.01	<0.01	0.02	0.01	0.01	<0.01	0.04
Dy	0.20	0.09	0.08	0.45	0.10	0.04	0.02	0.19	0.14	0.04	0.03	0.23	0.20	0.01	0.01	0.24	0.10	0.01	0.01	0.13	0.09	0.09	0.02	0.24
Ho	0.05	0.02	0.02	0.09	0.02	0.01	0.01	0.04	0.03	0.01	0.01	0.05	0.04	<0.01	<0.01	0.05	0.02	<0.01	<0.01	0.03	0.02	0.02	<0.01	0.04
Er	0.18	0.05	0.05	0.31	0.08	0.03	0.02	0.14	0.11	0.02	0.03	0.16	0.14	0.01	0.01	0.15	0.07	0.01	0.01	0.09	0.06	0.05	0.01	0.14
Tm	0.03	0.01	0.01	0.05	0.01	<0.01	<0.01	0.02	0.02	<0.01	<0.01	0.03	0.02	<0.01	<0.01	0.02	0.01	<0.01	<0.01	0.01	0.01	<0.01	<0.01	0.02
Yb	0.21	0.03	0.07	0.34	0.09	0.02	0.03	0.15	0.11	0.01	0.05	0.17	0.14	0.01	0.01	0.16	0.08	0.01	0.01	0.10	0.06	0.02	0.01	0.10
Lu	0.03	<0.01	0.01	0.06	0.01	<0.01	0.01	0.02	0.02	<0.01	0.01	0.03	0.02	<0.01	<0.01	0.03	0.01	<0.01	<0.01	0.02	0.01	<0.01	<0.01	0.02
Hf	<0.01	0.02	0.15	0.22	<0.01		0.07	0.10	<0.01	0.02	0.12	0.15	<0.01	0.04	0.10	0.18	<0.01	0.01	0.06	0.10	<0.01	0.05	0.09	0.15
Pb	0.53		0.46	1.34	1.00	0.10	0.10	1.51	1.15		0.14	1.54	0.58	0.14	0.04	0.87	0.38	0.06	0.05	0.75	0.45	0.12	0.14	0.99
Th	0.15	0.50	0.81	0.84	0.05	0.11	0.25	0.23	0.06	0.11	0.47	0.36	0.09	0.10	0.11	0.35	0.07	0.07	0.12	0.19	0.07	0.16	0.13	0.23
U	0.02	0.01	0.10	0.14	0.01	<0.01	0.03	0.05	0.01	<0.01	0.06	0.07	0.02	0.01	0.03	0.07	0.01	0.01	0.02	0.04	0.02	0.01	0.02	0.05

Fractions: A= Acetate, B= Oxalate, C: HF, D= Bulk-rock

wt% | ppm | neg. | < d.l. | < BEC | err. | >l.r. | n.m.

	HEX814				HEX827				HEX836				HEX849				HEX864				HEX872			
Frac:	A	B	C	D	A	B	C	D	A	B	C	D	A	B	C	D	A	B	C	D	A	B	C	D
Ca	0.02	0.01	0.03	0.07	1.10	0.01	<0.01	1.17	0.46	0.01	0.11	0.22	0.09	0.01	0.02	0.12	0.87	0.01	0.06	1.07	0.13	0.01	0.01	0.16
Fe	1.00	2.20	17.94	19.23	4.73	14.50	6.72	25.84	8.75	14.23	6.45	31.19	10.45	23.10	2.99	37.58	7.35	21.28	3.23	31.98	8.65	11.87	5.70	26.97
Mg	0.11	0.06	1.15	1.34	0.70	0.10	0.72	1.65	1.13	0.33	1.15	2.91	1.17	0.26	0.42	2.01	1.04	0.10	0.53	1.87	0.95	0.27	0.63	1.98
Mn	0.01	0.01	0.03	0.04	0.13	0.01	0.01	0.13	0.13	0.02	0.01	0.10	0.34	0.02	0.01	0.29	0.04	<0.01	<0.01	0.04	0.04	0.01	<0.01	0.05
Si	0.60	0.10		30.57	0.41	0.24		23.98	0.56	0.45		17.85	1.00	0.63		15.15	0.39	0.19		19.65	0.58	0.13		22.73
K	0.07	0.03	0.15	0.22	0.11	0.09	0.55	0.72	0.16	0.25	0.45	0.86	0.29	0.24	0.26	0.73	0.04	0.03	0.08	0.10	0.03	0.02	0.06	0.07
Na				2.23				0.16				0.05				0.01				0.09				
S				0.07				0.10				0.12				0.09				0.08				0.90
C				0.05				1.68				3.18				2.68				2.52				2.47
Al	<0.01	0.02	0.10	0.09	0.01	0.02	0.12	0.11	0.01	0.07	0.12	0.18	<0.01	0.02	0.02	0.03	<0.01	<0.01	0.03		<0.01	0.01	0.02	0.02
Ti		27.85	120.08	154.39	0.16	25.24	107.36	117.50	1.18	47.65	152.50	133.48	1.15	23.49	25.27	45.65	<0.01	3.42	16.25	17.89	<0.01	7.95	14.52	27.16
Be	0.07	0.02	0.17	0.29	0.07	0.05	0.38	0.44	0.21	0.14	0.36	0.55	0.15	0.08	0.20	0.37	0.12	0.07	0.35	0.52	0.37	0.18	0.37	0.93
Sc	0.44	0.13	0.30	0.46	0.39	0.15	0.40	0.46	0.62	0.36	0.67	0.65		0.48	0.07	0.16	0.30	0.06	0.15	0.31	0.62	0.09	0.16	0.42
V	0.79	2.67	9.33	12.16	2.12	3.42	1.38	6.57	0.91	3.46	0.46	3.98	0.61	2.21		3.13	1.00	1.79		4.22	0.66	2.17	0.13	4.56
Cr	<0.01	9.81	18.79	26.39	11.25	5.46	3.09	17.28	4.35	7.69	1.22	9.66	4.89	1.75	0.02	7.11	7.45		0.43	8.89	4.12	1.04	0.81	8.67
Co	0.55	0.70	1.33	1.74	0.64	0.24	0.56	1.21	0.44	0.24	0.65	0.92	0.34	0.29	0.30	0.81	0.26	0.08	0.11	0.42	0.09	0.09	0.48	0.77
Ni	0.96	2.38	5.23	8.15	2.83	1.09	2.30	5.87	1.63	1.13	2.99	4.18	0.96	1.27	0.23	2.16	1.67	0.74	1.08	3.79	1.16	1.23	4.78	8.53
Cu	<0.01	3.47	8.10	15.11	7.19	2.13	3.70	5.32	3.11	1.36	3.83	3.62	2.43	4.09	1.39	2.75	5.57	2.18	0.37	2.73	3.17	1.04	4.98	5.94
Zn	8.84	2.16	5.06	9.84	0.26	0.81	2.67	4.01	3.63	0.78	3.76	3.94	2.01	1.43	1.19	3.42	0.21	0.72	0.68	2.28	1.33	1.41	1.68	4.45
Rb	3.11	2.99	19.82	29.12	12.00	15.91	70.62	96.51	18.48	65.22	82.19	140.37	49.44	60.71	29.75	127.12	1.66	1.27	7.60	10.56	1.24	0.92	6.13	8.76
Sr	0.89	2.62	2.29	3.06	24.17		1.13	23.65	8.06		22.86	6.46	1.85		8.83	2.92	10.34		24.64	12.02	2.70		5.49	4.04
Y	0.47	0.43	0.56	1.71	0.98	0.25	0.69	1.76	1.73	1.80	1.53	3.96	1.42	0.71	0.37	2.18	1.61	1.82	2.13	4.87	1.70	1.22	2.53	4.14
Zr	0.03	0.50	2.61	3.24		0.44	4.05	3.08	0.04	2.24	3.08	4.30	<0.01	0.48	0.92	1.23		0.42	2.68	2.54	0.02	1.07	6.53	4.06
Mo	0.51	0.66	1.10	1.48	0.48	0.35	0.22	0.91	0.33	0.16	0.21	0.29	0.25	0.30	0.03	0.39	0.45	0.11	0.06	0.60	0.30	0.18	0.12	0.51
Cs	0.62	0.38	1.71	3.11	0.43	0.95	3.78	5.27	0.68	3.83	3.76	6.99	0.82	3.01	1.78	5.28	0.14	0.12	0.81	1.17	0.26	0.20	0.86	1.50
Ba	3.51	1.58	4.23	9.23	4.00	<0.01	2.48	5.69	7.17	1.58	2.48	9.78	5.13	0.90	0.90	5.74	6.04	<0.01	0.86	7.39	3.89	0.41	1.31	6.16
La	0.12	0.19	0.29	0.79	0.15	0.07	0.39	0.66	0.33	0.31	1.03	1.42	0.30	0.10	0.10	0.47	0.32	0.32	1.17	1.64	0.31	0.26	1.47	2.41
Ce	0.23	0.45	0.55	1.57	0.30	0.16	0.70	1.16	0.65	0.68	1.94	2.66	0.40	0.21	0.17	0.72	0.43	0.50		2.23	0.48	0.53	2.14	3.44
Pr	0.03	0.06	0.07	0.20	0.04	0.02	0.07	0.15	0.09	0.08	0.23	0.34	0.05	0.02	0.02	0.09	0.06	0.06	0.15	0.27	0.06	0.07	0.22	0.41
Nd	0.13	0.25	0.27	0.83	0.19	0.08	0.25	0.59	0.38	0.34	0.88	1.42	0.17	0.10	0.08	0.37	0.25	0.27	0.57	1.19	0.29	0.32	0.78	1.68
Sm	0.03	0.06	0.06	0.18	0.05	0.02	0.03	0.12	0.10	0.08	0.17	0.31	0.04	0.02	0.01	0.08	0.06	0.06	0.09	0.22	0.07	0.07	0.10	0.28
Eu	0.01	0.02	0.01	0.05	0.01	<0.01	0.01	0.03	0.03	0.02	0.04	0.09	0.01	0.01	<0.01	0.03	0.02	0.02	0.02	0.07	0.02	0.02	0.03	0.09
Gd	0.04	0.07	0.06	0.20	0.08	0.02	0.04	0.15	0.14	0.12	0.18	0.38	0.06	0.04	0.02	0.11	0.09	0.12	0.19	0.35	0.11	0.12	0.14	0.39
Tb	0.01	0.01	0.01	0.03	0.01	<0.01	0.01	0.02	0.02	0.02	0.02	0.06	0.01	0.01	<0.01	0.02	0.01	0.02	0.02	0.05	0.02	0.02	0.02	0.06
Dy	0.05	0.06	0.06	0.20	0.09	0.03	0.05	0.17	0.18	0.17	0.16	0.44	0.08	0.04	0.02	0.15	0.12	0.16	0.14	0.42	0.15	0.13	0.18	0.41
Ho	0.01	0.01	0.01	0.04	0.02	0.01	0.01	0.04	0.04	0.04	0.03	0.09	0.02	0.01	<0.01	0.04	0.03	0.04	0.04	0.09	0.04	0.03	0.05	0.09
Er	0.04	0.03	0.05	0.13	0.07	0.02	0.06	0.14	0.14	0.12	0.11	0.30	0.09	0.04	0.02	0.13	0.13	0.12	0.15	0.33	0.16	0.09	0.18	0.34
Tm	<0.01	<0.01	0.01	0.02	0.01	<0.01	0.01	0.03	0.02	0.01	0.02	0.05	0.01	<0.01	<0.01	0.02	0.02	0.01	0.02	0.05	0.03	0.01	0.03	0.07
Yb	0.03	0.01	0.06	0.12	0.06	0.02	0.12	0.19	0.14	0.08	0.11	0.28	0.08	0.03	0.04	0.14	0.18	0.08	0.16	0.38	0.32	0.08	0.19	0.54
Lu	<0.01	<0.01	0.01	0.02	0.01	<0.01	0.02	0.03	0.02	0.01	0.02	0.04	0.01	<0.01	0.01	0.03	0.03	0.01	0.03	0.07	0.06	0.01	0.03	0.10
Hf	<0.01	0.01	0.06	0.08	<0.01		0.09	0.08	<0.01	0.05	0.07	0.12	<0.01	0.01	0.02	0.03	<0.01		0.03	0.02	<0.01		0.17	0.04
Pb	1.21	0.08	0.13	1.70	0.15		0.06	0.40	0.56	0.01	0.14	0.64	0.11	0.03	0.01	0.27	0.05		0.04	0.23	0.68		0.23	1.23
Th	0.05	0.05	0.04	0.15	0.03	0.05	0.23	0.16	0.07	0.23	0.21	0.26	0.04	0.05	0.05	0.09	0.02	0.01	0.07	0.06	0.03	0.03	0.14	0.10
U	0.01	0.01	0.03	0.03	<0.01	<0.01	0.03	0.04	0.02	0.01	0.02	0.05	0.01	<0.01	<0.01	0.02	<0.01	<0.01	0.01	0.01	0.01	<0.01	0.03	0.02

Fractions: A= Acetate, B= Oxalate, C: HF, D= Bulk-rock | wt% | ppm | neg. | < d.l. | < BEC | err. | >l.r. | n.m.

	HEX887				HEX899				HEX920				HEX934			
Frac:	A	B	C	D	A	B	C	D	A	B	C	D	A	B	C	D
Ca	2.11	<0.01	0.01	2.17	1.38	<0.01	0.04	1.49	1.82	0.01	<0.01	1.94	2.08	0.01	<0.01	2.26
Fe	5.30	17.87	4.61	27.02	3.10	11.55	16.24	28.88	8.24	9.54	2.70	21.31	3.88	16.31	1.79	22.91
Mg	1.20	0.03	0.32	1.68	0.56	0.07	1.15	1.84	1.37	0.13	0.58	2.32	0.93	0.06	0.38	1.55
Mn	0.27	<0.01	<0.01	0.30	0.04	<0.01	0.01	0.05	0.23	0.01	0.01	0.27	0.17	<0.01	<0.01	0.19
Si	0.26	0.11		20.10	0.44	0.13		22.74	0.34	0.08		23.86	0.54	0.13		25.87
K	0.06	0.01	0.01	0.08	0.05		0.04	0.06	0.09		0.01	0.06	0.11		0.01	0.08
Na				0.38				0.01				0.02				0.15
S				0.07				0.09				0.16				0.11
C				2.53				1.34				3.45				1.78
Al	0.01	0.01	0.03		<0.01	<0.01	0.02		0.01	0.01	0.04	0.04	0.01	0.02	0.05	0.05
Ti	<0.01	3.58	17.86	28.77	1.03	4.69	0.43	16.30	1.83	10.26	24.46	63.76	0.71	17.82	54.64	85.34
Be	0.17	0.07	0.12	0.40	0.26	0.06	0.24	0.53	0.31	0.11	0.12	0.65	0.13	0.17	0.09	0.47
Sc	0.15	0.03	0.10	0.26	0.58	0.02	0.08	0.26	0.50	0.02	0.11	0.45	0.58	0.05	0.50	0.80
V	1.99	1.48	0.26	6.59	0.66	1.83		4.00	1.09	3.12		7.34	3.20	3.97	4.05	12.26
Cr	10.94	0.95	1.53	16.62	5.57	<0.01	<0.01	6.29	6.88	1.29	0.47	13.23	17.00	4.04	1.28	28.59
Co	0.60	0.17	0.25	1.19	0.14	0.05	0.10	0.33	0.46	0.17	0.20	1.11	0.99	0.28	0.33	1.89
Ni	2.86	0.55	0.74	5.32	0.86	0.44	0.98	2.74	1.66	0.59	0.80	4.90	4.96	0.84	0.69	8.49
Cu	6.03	1.57	1.41	5.95	3.54	1.90	1.59	1.81	4.91	1.60	1.82	5.17	4.23	1.40	2.54	9.97
Zn	1.40	0.40	1.24	4.52	2.08	0.48	1.32	4.21	3.27	0.61	2.54	9.07	10.05	1.48	1.86	10.39
Rb	2.29	0.15	0.70	3.59	0.57	0.10	2.30	2.87	3.38	0.29	0.70	5.30	4.16	0.41	0.89	6.67
Sr	36.21		0.47	43.42	31.56		16.68	33.59	16.81		3.71	21.44	27.23	1.29	0.43	31.69
Y	1.54	0.09	0.62	2.20	1.70	1.21	1.69	3.73	1.60	0.34	0.60	2.81	1.99	0.22	0.20	2.88
Zr		0.10	1.01	1.19		0.37	1.20	1.87	0.01	0.58	1.21	2.72	<0.01	1.04	2.73	4.37
Mo	0.45	0.45	0.14	1.17	0.11	0.16	0.04	0.38	0.27	0.24	0.19	0.82	0.71	0.71	0.22	2.07
Cs	0.48	0.03	0.05	0.74	0.06	0.02	0.17	0.31	0.65	0.09	0.11	1.17	0.80	0.11	0.09	1.26
Ba	5.85	0.29	1.30	9.29	1.28		0.04	1.99	2.01		0.56	4.11	4.60	0.88	0.95	7.42
La	0.26	0.04	0.33	0.78	0.22	0.15	1.01	1.78	0.22	0.12	0.49	1.25	0.33	0.17	0.56	1.42
Ce	0.39	0.06	0.45	1.07	0.37	0.36	1.51	2.69	0.39	0.27	0.80	2.08	0.63	0.35	0.95	2.48
Pr	0.05	0.01	0.05	0.12	0.05	0.05	0.16	0.33	0.06	0.04	0.08	0.25	0.09	0.05	0.10	0.31
Nd	0.20	0.03	0.15	0.48	0.23	0.25	0.63	1.38	0.24	0.16	0.29	1.00	0.39	0.18	0.34	1.22
Sm	0.05	0.01	0.02	0.09	0.05	0.06	0.09	0.25	0.07	0.03	0.04	0.21	0.11	0.03	0.04	0.25
Eu	0.01	<0.01	<0.01	0.02	0.02	0.02	0.03	0.09	0.02	0.01	0.01	0.07	0.03	0.01	0.01	0.07
Gd	0.07	0.01	0.02	0.13	0.09	0.11	0.12	0.35	0.11	0.05	0.05	0.27	0.17	0.04	0.04	0.37
Tb	0.01	<0.01	<0.01	0.02	0.02	0.02	0.02	0.05	0.02	0.01	0.01	0.04	0.03	0.01	<0.01	0.05
Dy	0.10	0.01	0.04	0.16	0.14	0.12	0.12	0.37	0.15	0.04	0.05	0.28	0.22	0.03	0.02	0.34
Ho	0.03	<0.01	0.01	0.04	0.03	0.03	0.03	0.08	0.04	0.01	0.01	0.06	0.05	0.01	<0.01	0.07
Er	0.11	<0.01	0.04	0.15	0.14	0.08	0.12	0.27	0.13	0.02	0.04	0.21	0.18	0.01	0.02	0.25
Tm	0.02	<0.01	0.01	0.03	0.02	0.01	0.02	0.04	0.02	<0.01	0.01	0.03	0.03	<0.01	<0.01	0.04
Yb	0.11	<0.01	0.05	0.18	0.20	0.05	0.10	0.31	0.16	0.01	0.03	0.24	0.18	0.01	0.03	0.24
Lu	0.02	<0.01	0.01	0.03	0.04	0.01	0.02	0.05	0.03	<0.01	<0.01	0.04	0.03	<0.01	<0.01	0.04
Hf	<0.01		0.02	0.03	<0.01	0.01	0.01	0.02	<0.01	0.01	0.03	0.05	<0.01	0.02	0.06	0.09
Pb	0.26	0.03	0.01	0.50	0.56	0.01	0.06	0.79	0.13	0.08	0.08	0.38	0.87	0.15	0.15	1.56
Th	0.04	0.03	0.07	0.10	0.01	<0.01	0.07	0.06	0.04	0.04	0.18	0.17	0.08	0.06	0.17	0.26
U	0.01	<0.01	0.01	0.03	0.01	<0.01	<0.01	0.02	0.01	<0.01	0.02	0.04	0.03	0.01	0.03	0.07

APPENDIX V: LA-ICP-MS DATA

The following tables contain the LA-ICP-MS data sorted per mineral. For mineral in a sample the 1-9 accepted analyses (n=) were averaged. Concentrations for the oxides (SiO_2 - K_2O) are in wt% and the elements (P - U) in ppm. The internal standards were CaO for ankerite and FeO for other minerals. Values in red cells are below the detection limit and should be treated cautiously.

	Ankerite								Greenalite					Minnesotaite				
n=	1	5	3	3	3	4	2	6	1	9	1	4	5	3	4	4	4	
Sample:	ARP499	ARP578	ARP605	ERI387	GAS224	HEX694	HEX827	HEX899	ERI387	ERI562	HEX694	HEX899	ARP499	ARP605	GAS367	HEX899		
SiO_2	2.41	19.37	42.69	9.03	2.97	4.79	17.88	12.31	155.78	94.51	38.76	86.84	90.11	145.22	184.16	118.92		
Al_2O_3	<0.01	0.04	0.05	<0.01	0.01	0.15	0.01	<0.01	1.11	0.22	0.24	0.09	0.22	0.20	0.30	0.11		
CaO	27.55	27.55	27.55	27.55	27.55	27.55	27.55	27.55	2.26	0.67	0.59	1.17	1.79	0.43	2.55	3.35		
FeO	14.20	19.94	22.76	17.88	19.84	21.53	21.68	23.05	49.68	49.68	49.68	49.68	34.74	34.74	34.74	34.74		
MnO	3.34	0.41	1.32	2.59	0.88	1.85	0.79	0.35	2.30	0.20	2.08	0.12	0.54	0.87	0.53	0.14		
MgO	8.31	7.34	8.31	5.91	6.93	6.37	7.73	7.86	4.91	7.05	4.77	5.86	9.66	3.42	6.95	6.75		
Na_2O	<0.01	0.02	<0.01	<0.01	0.10	0.01	0.44	<0.01	0.23	0.03	0.01	0.12	0.03	0.06	0.11	0.13		
K_2O	<0.01	0.06	0.07	<0.01	0.01	0.07	0.03	<0.01	0.25	1.07	0.01	0.08	0.14	0.28	0.38	0.16		
P	9.26	25.80	102.85	15.69	9.26	12.22	19.57	223.87	916.11	708.74	113.69	460.90	280.35	480.30	966.09	782.00		
Sc	0.33	0.39	0.51	0.30	0.15	1.07	0.20	0.16	5.03	2.07	1.31	2.10	1.37	2.95	2.23	1.94		
Ti	0.49	16.26	31.49	0.64	22.37	3.66	22.47	5.15	123.07	54.95	27.45	60.57	4.92	109.07	22.15	19.61		
V	1.76	0.87	0.73	0.13	0.31	1.02	0.93	0.11	1.95	6.60	3.42	3.03	1.08	4.99	0.35	0.56		
Cr	0.90	2.13	1.94	0.69	1.18	0.93	1.18	0.74	3.79	2.04	0.92	1.06	2.03	3.50	1.78	0.90		
Co	0.05	0.60	0.21	0.05	0.10	0.06	0.21	0.06	1.79	0.58	0.08	0.09	0.11	0.52	1.03	0.11		
Ni	2.86	3.54	5.78	2.80	2.34	2.97	5.20	3.79	8.61	5.61	4.36	5.20	6.39	11.01	7.66	6.47		
Cu	0.21	0.32	0.45	0.21	0.32	0.25	0.34	0.26	2.88	1.44	0.30	0.68	2.76	3.28	6.53	1.20		
Zn	2.92	1.94	3.72	3.29	1.59	3.74	2.25	1.13	18.73	12.93	9.66	7.45	34.92	4.47	28.58	7.76		
Rb	0.04	5.94	6.70	0.19	1.09	2.59	2.46	0.08	17.28	163.32	1.02	4.31	3.14	26.31	42.23	6.01		
Sr	103.91	355.86	177.41	74.26	424.31	89.26	360.58	364.32	7.64	11.59	1.49	27.71	6.35	3.82	38.15	65.91		
Y	93.95	2.61	3.48	10.74	4.71	63.36	6.16	13.41	6.05	10.66	10.81	5.42	2.75	0.69	7.22	6.06		
Zr	0.10	0.91	0.99	0.10	0.54	0.18	0.25	0.13	5.64	5.99	0.33	6.02	1.26	2.65	9.39	4.59		
Mo	0.06	0.09	0.12	0.07	0.05	0.07	0.11	0.08	0.18	0.10	0.09	0.10	0.12	0.25	0.17	0.13		
Cs	0.02	0.45	0.60	0.02	0.11	0.50	0.15	0.03	3.22	12.40	0.38	0.97	0.20	2.65	2.55	0.41		
Ba	0.08	24.86	20.40	2.75	34.32	0.80	36.86	10.76	18.63	25.31	0.28	2.63	0.32	11.51	5.92	1.69		
La	12.85	1.20	1.11	6.28	1.45	8.37	1.07	3.15	2.56	1.95	0.66	0.47	0.85	0.32	1.16	0.64		
Ce	29.88	2.05	1.90	8.72	2.75	13.84	2.02	2.09	4.42	3.56	0.81	0.87	1.12	0.43	2.06	1.11		
Pr	3.96	0.21	0.19	0.91	0.31	1.65	0.26	0.26	0.55	0.49	0.11	0.12	0.14	0.05	0.25	0.15		
Nd	18.91	0.80	0.79	3.63	1.23	7.71	1.15	1.32	2.44	2.48	0.44	0.60	0.63	0.16	1.11	0.85		
Sm	4.15	0.17	0.16	0.62	0.26	1.63	0.32	0.32	0.47	0.56	0.09	0.14	0.14	0.04	0.38	0.18		
Eu	1.43	0.09	0.08	0.28	0.08	0.58	0.09	0.15	0.20	0.16	0.04	0.09	0.06	0.02	0.10	0.11		
Gd	6.15	0.19	0.23	0.75	0.27	2.78	0.39	0.59	0.70	0.82	0.32	0.27	0.18	0.11	0.44	0.37		
Tb	0.94	0.04	0.03	0.12	0.05	0.43	0.07	0.11	0.09	0.13	0.06	0.05	0.03	0.01	0.08	0.06		
Dy	6.84	0.27	0.27	0.84	0.43	3.43	0.51	0.92	0.62	0.96	0.51	0.37	0.24	0.04	0.54	0.47		
Ho	1.65	0.06	0.07	0.19	0.11	0.99	0.12	0.27	0.13	0.25	0.17	0.10	0.05	0.02	0.19	0.12		
Er	5.25	0.20	0.23	0.61	0.38	3.55	0.36	1.01	0.46	0.93	0.85	0.46	0.18	0.04	0.57	0.41		
Tm	0.66	0.03	0.03	0.09	0.06	0.54	0.05	0.17	0.06	0.16	0.17	0.10	0.03	0.01	0.09	0.06		
Yb	4.30	0.16	0.20	0.48	0.43	3.87	0.24	1.33	0.38	1.27	1.60	1.12	0.17	0.08	0.88	0.49		
Lu	0.62	0.02	0.03	0.07	0.06	0.69	0.04	0.24	0.06	0.23	0.31	0.22	0.03	0.01	0.16	0.09		
Pb	0.29	0.25	0.33	0.33	0.53	1.47	0.34	0.24	0.69	0.54	0.12	0.28	0.87	0.18	0.84	0.28		
Th	0.01	0.10	0.06	0.05	0.03	0.10	0.03	0.02	0.87	0.20	0.11	0.07	0.05	0.10	0.51	0.07		
U	<0.01	0.01	0.01	<0.01	<0.01	0.03	<0.01	<0.01	0.54	0.07	0.10	0.05	0.08	0.06	0.13	0.02		

	Magnetite										Riebeckite					Siderite			Stilpnomelane					
n=	6	2	4	6	4	4	3	5	4	4	5	4	5	20	15	1	3	4	3	4	4	1	2	4
Sample:	ARP499	ARP578	ARP605	ERI387	ERI562	GAS224	GAS367	HEX694	HEX827	HEX899	GAS224	HEX827	HEX899	ARP609*	HEX814*	ERI387	HEX694	HEX653	ARP578	ARP605	GAS224	HEX694	HEX827	HEX653
SiO_2	1.39	1.19	1.13	1.80	1.28	11.63	1.88	2.83	7.07	4.93	129.28	402.10	56.05			65.96	10.35	21.55	122.31	64.61	331.35	57.24	89.98	41.66
Al_2O_3	<0.01	0.02	0.01	0.01	<0.01	0.05	<0.01	0.04	0.10	<0.01	0.13	0.12	0.01			0.08	0.01	0.06	1.95	1.19	1.12	2.42	1.32	2.91
CaO	<0.01	<0.01	<0.01	0.02	0.01	0.01	0.03	0.02	0.01	0.01	0.19	0.24	0.37			0.43	16.67	13.48	0.99	1.07	0.38	0.19	0.05	2.71
FeO	90.05	90.05	90.05	90.05	90.05	90.05	90.05	90.05	90.05	90.05	33.18	33.18	33.18			49.53	49.53	49.53	34.81	34.81	34.81	34.81	34.81	34.81
MnO	0.01	<0.01	0.01	0.02	<0.01	<0.01	0.01	0.02	0.02	<0.01	0.02	0.10	0.01			4.09	3.69	1.46	0.07	0.48	0.07	0.46	0.13	0.41
MgO	0.06	0.04	0.03	0.03	0.03	0.44	0.09	0.11	0.40	0.19	3.88	4.30	4.32			5.11	8.46	6.44	4.15	4.70	3.15	3.71	5.26	3.73
Na_2O	<0.01	<0.01	<0.01	<0.01	0.01	0.04	0.05	0.01	<0.01	0.10	6.06	5.35	6.57			<0.01	<0.01	<0.01	0.05	0.02	0.40	0.42	0.08	0.47
K_2O	0.01	0.02	0.02	<0.01	<0.01	0.07	0.01	0.01	0.28	0.01	0.16	0.28	0.08			<0.01	<0.01	0.02	3.74	3.34	1.23	1.08	4.09	1.22
P	13.64	15.25	27.08	26.28	27.73	26.21	63.71	54.61	43.92	33.83	340.76	1571.78	214.11			258.60	605.21	792.69	191.55	85.26	1099.14	11.49	176.02	234.69
Sc	0.14	0.11	0.11	0.10	0.15	0.36	0.13	0.15	0.14	0.44	4.62	6.96	11.56			1.56	0.91	2.00	2.09	1.56	9.37	1.22	2.74	2.83
Ti	4.56	94.40	49.38	70.30	100.71	28.86	30.13	45.64	53.97	19.39	242.90	225.11	105.00			11.44	15.94	35.41	272.19	244.45	150.88	31.67	420.52	17.17
V	15.27	52.06	24.36	6.15	15.53	10.03	8.42	30.50	11.40	7.97	8.26	6.94	7.05			0.37	0.49	3.22	3.45	1.05	4.64	9.35	0.98	57.04
Cr	0.36	165.21	51.44	3.91	10.48	16.35	3.96	3.48	22.07	0.95	3.01	3.68	0.29			1.80	1.46	2.16	8.76	2.56	5.42	2.65	4.23	26.21
Co	0.07	0.24	0.44	0.07	0.07	0.09	0.09	0.09	0.22	0.07	0.92	1.10	0.07			0.11	0.08	0.35	1.15	1.74	0.83	0.07	2.21	0.42
Ni	4.04	4.19	4.25	3.94	3.87	3.38	4.83	4.87	5.88	4.08	5.03	32.89	2.87			6.72	4.53	6.85	12.96	10.01	15.91	3.63	6.89	48.92
Cu	0.29	0.56	2.70	1.28	0.64	0.59	1.25	0.42	0.48	0.46	1.53	2.64	0.31			0.48	0.32	0.55	0.49	0.39	6.47	0.41	0.51	0.70
Zn	1.19	0.54	0.97	0.85	1.09	1.83	5.95	1.33	2.43	2.15	8.60	9.55	4.61			11.48	7.69	10.30	12.80	10.11	12.74	14.44	17.13	15.29
Rb	0.42	2.59	1.50	0.24	0.44	10.80	0.61	0.68	33.30	0.28	9.57	15.47	0.32			0.12	0.11	1.41	411.79	279.83	166.33	55.67	467.78	79.92
Sr	0.70	0.53	0.13	0.57	0.16	0.68	0.72	0.67	0.70	0.63	1.69	1.56	1.13			1.41	70.61	25.72	15.70	9.25	7.50	2.18	1.76	7.66
Y	0.25	0.13	0.05	0.35	0.17	0.29	0.38	0.61	0.31	0.23	0.76	1.86	2.19	0.61	1.06	1.62	16.73	29.92	1.05	1.33	2.94	2.91	3.72	6.80
Zr	0.42	0.49	1.48	1.45	0.20	2.33	0.27	10.88	1.37	1.65	6.52	2.55	28.42			0.72	1.25	2.15	8.34	4.63	33.05	0.67	15.46	2.87
Mo	0.22	1.02	0.23	0.29	0.75	0.23	0.18	0.11	0.19	0.08	0.10	0.71	0.06			0.14	0.10	0.25	0.14	0.14	1.18	0.09	0.15	0.11
Cs	0.28	0.23	0.15	0.06	0.04	0.97	0.05	0.16	2.18	0.04	1.11	1.10	0.03			0.08	0.04	0.24	24.39	19.44	15.53	12.35	26.70	13.25
Ba	14.31	5.15	4.42	1.01	2.32	1.77	3.39	1.38	13.44	0.80	4.78	6.63	1.63			0.71	1.65	2.64	9.64	8.12	3.61	4.81	7.13	14.82
La	0.07	0.10	0.04	0.18	0.02	0.13	0.09	0.17	0.07	0.04	0.05	0.10	0.07	0.04	0.15	1.02	4.09	8.43	0.25	0.47	1.59	0.41	0.29	2.26
Ce	0.13	0.27	0.08	0.33	0.04	0.29	0.14	0.32	0.14	0.07	0.14	0.19	0.14	0.22	0.38	1.37	7.25	15.28	0.50	0.81	3.79	0.57	0.62	4.18
Pr	0.01	0.02	0.01	0.03	<0.01	0.04	0.02	0.04	0.01	0.01	0.02	0.04	0.02	0.03	0.05	0.12	0.88	1.75	0.05	0.09	0.49	0.07	0.08	0.54
Nd	0.06	0.05	0.03	0.15	0.04	0.17	0.09	0.17	0.07	0.06	0.10	0.15	0.12	0.13	0.24	0.47	3.78	8.01	0.20	0.34	1.95	0.34	0.41	2.37
Sm	0.02	0.01	0.01	0.03	0.01	0.04	0.02	0.05	0.03	0.02	0.03	0.08	0.04	0.03	0.06	0.08	0.78	1.87	0.05	0.07	0.50	0.05	0.11	0.55
Eu	0.01	0.01	0.01	0.01	0.01	0.01	0.01	0.02	0.01	0.01	0.02	0.06	0.02	0.01	0.02	0.02	0.21	0.57	0.02	0.02	0.13	0.03	0.03	0.16
Gd	0.03	0.04	0.03	0.04	0.03	0.04	0.04	0.07	0.06	0.04	0.04	0.25	0.07	0.04	0.08	0.08	0.90	2.62	0.11	0.08	0.54	0.10	0.19	0.77
Tb	<0.01	<0.01	<0.01	<0.01	<0.01	0.01	0.01	0.01	0.01	<0.01	0.01	0.02	0.02	0.01	0.01	0.02	0.14	0.44	0.01	0.01	0.06	0.02	0.04	0.11
Dy	0.03	0.02	0.01	0.04	0.02	0.04	0.04	0.06	0.04	0.03	0.07	0.17	0.17	0.05	0.10	0.14	1.05	3.13	0.13	0.11	0.37	0.16	0.21	0.80
Ho	0.01	<0.01	<0.01	0.01	<0.01	0.01	0.01	0.01	0.01	0.01	0.02	0.04	0.05	0.01	0.03	0.04	0.38	0.76	0.02	0.02	0.10	0.05	0.07	0.17
Er	0.04	0.02	0.01	0.03	0.02	0.03	0.03	0.04	0.03	0.02	0.09	0.19	0.21	0.05	0.09	0.12	1.13	2.59	0.09	0.09	0.25	0.18	0.30	0.56
Tm	0.01	<0.01	<0.01	<0.01	<0.01	<0.01	<0.01	0.01	0.01	<0.01	0.02	0.05	0.05			0.02	0.19	0.38	0.01	0.02	0.04	0.04	0.07	0.08
Yb	0.05	0.02	0.01	0.03	0.02	0.03	0.04	0.04	0.05	0.03	0.30	0.33	0.77	0.08	0.13	0.20	1.36	2.55	0.14	0.14	0.20	0.28	0.54	0.55
Lu	0.01	<0.01	<0.01	<0.01	0.01	0.01	0.01	0.01	0.01	0.01	0.06	0.06	0.27	0.01	0.02	0.03	0.25	0.45	0.02	0.03	0.04	0.06	0.10	0.09
Pb	0.16	0.65	0.30	0.36	0.39	0.54	0.59	0.46	0.49	0.29	0.41	0.22	0.13			0.06	0.42	0.39	0.57	0.32	0.66	0.14	0.46	0.18
Th	0.01	0.07	0.03	0.20	<0.01	0.08	0.02	0.13	0.08	0.01	0.60	0.16	0.02			0.19	0.32	0.18	0.90	0.33	0.96	0.15	0.70	0.45
U	0.01	0.07	0.01	0.02	<0.01	0.01	0.01	0.06	0.02	<0.01	0.03	0.02	<0.01			0.05	0.04	0.04	0.44	0.10	0.22	0.21	0.22	0.12

* Two riebeckite samples measured by Van den Brug (in prep.)